Ceramic Processing of Magnesium Diboride

Claire Dancer

Trinity Term 2008



A thesis submitted for the degree of

Doctor of Philosophy at the University of Oxford

Abstract

Ceramic Processing of Magnesium Diboride

Claire Dancer, Linacre College

A thesis submitted for the degree of Doctor of Philosophy at the University of Oxford

Trinity Term 2008

This thesis describes the fabrication and characterization of *ex situ* magnesium diboride (MgB_2) bulk material to study its sintering behaviour. Since the discovery of superconductivity in magnesium diboride in 2001, many research studies have identified the attractive properties of this easy-to-fabricate, low cost superconductor which can attain high critical current density even without heat-treatment. However there is little consensus in the literature on the processing requirements to produce high quality MgB_2 material with low impurity content and high density. In this work, the key parameters in the production of dense *ex situ* MgB_2 produced from Alfa Aesar MgB_2 powder are established by examining the effect of modifying the characteristics of the starting material and the processing parameters during pressureless and pressure-assisted heat-treatment.

The particle size distribution, impurity content and particle morphology of Alfa Aesar MgB_2 powder were determined using laser diffraction, X-ray diffraction, X-ray photoelectron spectroscopy, electron dispersive spectroscopy, scanning electron microscopy and transmission electron microscopy. This powder was also modified by separation (sieving and sedimentation) and milling (ball milling and attrition milling), with changes made to the powder determined by the same techniques.

A pressureless heat-treatment method using a magnesium diboride powder bed was developed. This minimised MgO formation in samples produced from as-purchased MgB_2 powder to less than 8 wt.% for heat-treatment at 1100 °C. MgO content was determined by X-ray diffraction using calibrated standards. MgB_2 bulk material was produced from as-purchased and modified powders by pressureless heat-treatment under Ar gas, and characterized using Archimedes' density method, X-ray diffraction, Vickers hardness testing, scanning electron microscopy, and magnetization measurements. Very limited densification was observed for all samples prepared by pressureless heat-treatment, with only limited increases in connectivity observed for some samples heat-treated at 1100 °C.

Pressure-assisted bulk samples were prepared from as-purchased MgB_2 and selected modified powders using resistive sintering, spark plasma sintering, and hot pressing. These were characterized using the same techniques, which indicated much more extensive densification with similar levels of impurity formation as for pressureless heat-treatment at 1100 °C. The results indicate that densification and applied pressure are strongly correlated, while the effect of temperature is less significant. The optimum processing environment (inert gas or vacuum) was dependent on the technique used. These results indicate that pressure-assisted heat-treatment is required in order to produce dense bulk MgB_2.

Acknowledgements

I would like to thank my supervisors, Chris Grovenor and Richard Todd, for guidance throughout my project, for giving me the freedom to pursue my project in the directions which most interested me, and for encouraging me to attend conferences, teach undergraduates, and pursue collaborative projects, which has made a huge difference to my postgraduate experience.

I could not have made it through my DPhil without help from many people in the Department of Materials; thanks to Susie Speller, Gabriella Chapman, Ron Doole, Steve Lett, Chris Salter, Alison Crossley, Frank Cullen, Laurie Walton, Bob Lloyd, and Paula Topping for help with a huge variety of equipment and training. Particular thanks to Khalid Schofield for rescuing my ageing laptop from a hard-drive failure a month after I started writing up! I also owe particular thanks to Katie Moore and Ben Britton to introducing me to the joys of LyX, and for remaining calm even when my thesis was refusing to compile.

I would like to thank my collaborators; Pavol Kováč at the Slovak Academy of Sciences in Bratislava, Mike Reece and Haixue Yan at Queen Mary, University of London, Alex Bevan, Pavlo Mikheenko and Stuart Abell at the University of Birmingham, Ekrem Yanmaz at the Karadeniz Technical University, Turkey, Gilliane Sills of the Department of Engineering at the University of Oxford, and Dharmalingham Prabhakaran at the Clarendon Laboratory, University of Oxford for all their assistance, advice and hospitality.

I would also like to thank the all members of the CRMG and RIT groups throughout my time in Oxford. I have learnt so much from all of you, and you've been great company over the last 4 years. Thanks in particular to Sarah Haigh, Marty Rust, Dave Armstrong, Helen Marsh, Ellie Clarke and John Murphy for making my time in the department such a happy and stimulating period. I would also like to thank Sian Alexander and Freija Glansdorp for writing up at high speed just before I started and giving me lots of good tips and encouragement. Thanks also to Isobel Barry for her invaluable and authoritative grammar tips (though I will be very happy to never have another conversation about the use of the hyphen!), and for distracting me with crafting and wine.

I would also like to thank my London/Cambridge friends for putting up with my never-ending student-hood, from block-bookings of the cheap "seats" at the opera to the aborted attempt at Diplomacy, every weekend I've spent with you has been an intense distraction from my DPhil and sent me back to Oxford revived and ready to start over.

I would like to thank my family for all their support and understanding, particularly over the last few months. In particular, to my parents - thank you for the sacrifices you made for my education - after 22 years I think I'm finally done!

Finally - I would like to thank James, for his support, encouragement and his willingness to understand (and even explain!) superconductivity even if law sometimes sends me to sleep; I couldn't have got here without you.

Preface

This thesis is an account of the work carried out by the author in the Department of Materials, University of Oxford, under the supervision of Prof. C.R.M. Grovenor and Dr. R.I. Todd between October 2004 and May 2008. No part of this work has been previously submitted for a degree at this or any other university. The work of other authors has been freely drawn upon and is duly acknowledged in the text. A list of references has been given at the end of the thesis. Some of the research presented in this thesis has previously been presented at conferences or in articles, and a list of these appears below in chronological order.

7th European Conference on Applied Superconductivity, Vienna, Austria, Sept. 2005, Poster Presentation

How Can We Quantify Magnesium Oxide Content in Magnesium Diboride using X-ray Diffraction? C.E.J. Dancer, F.L. Cullen, R.I. Todd and C.R.M. Grovenor.

Applied Superconductivity Conference, Seattle, USA, Aug. 2006, Poster Presentation

Does Magnesium Diboride Sinter?

C.E.J. Dancer, P. Mikheenko, A.L. Bevan, J.S. Abell, R.I. Todd and C.R.M. Grovenor.

Applied Superconductivity Conference, Seattle, USA, Aug. 2006, Oral Presentation

Resistive Sintering of MgB_2 Bulk Material

C.E.J. Dancer, P. Mikheenko, A.L. Bevan, J.S. Abell, R.I. Todd and C.R.M. Grovenor.

Superconductivity Group Annual Group Meeting, Institute of Physics, London, UK, Nov. 2006, Poster Presentation

Does Magnesium Diboride Sinter?

C.E.J. Dancer, P. Mikheenko, A.L. Bevan, J.S. Abell, R.I. Todd and C.R.M. Grovenor.

8th European Conference on Applied Superconductivity, Brussels, Belgium, Sept. 2007, Oral Presentation

Improved Dispersion, Consolidation and Heat Treatment of Ex Situ Magnesium Diboride Powders

C.E.J. Dancer, D. Prabhakaran, R.I. Todd and C.R.M. Grovenor.

Superconductivity Group Annual Group Meeting, Institute of Physics, London, UK, Nov 2007, Poster Presentation

Improved Dispersion and Heat Treatment of Ex Situ Magnesium Diboride Powders

C.E.J. Dancer, D.Prabhakaran, R.I. Todd and C.R.M. Grovenor.

Materials Research Society Spring Meeting 2008, San Francisco, USA, Mar 2008, Oral Presentation

Densification Processes in Ex Situ Magnesium Diboride Bulk Material Fabricated by Pressureless and Pressure-Assisted Heat-Treatment

C.E.J. Dancer, A.L. Bevan, P. Mikheenko, H.Y. Yan, D. Prabhakaran, M.J. Reece, J.S. Abell, R.I. Todd, and C.R.M. Grovenor.

Article submitted to Superconductor Science and Technology, May 2008

Does Magnesium Diboride Sinter?

C.E.J. Dancer, P. Mikheenko, A.L. Bevan, J.S. Abell, R.I. Todd and C.R.M. Grovenor.

Nomenclature

Symbols

η	- dynamic viscosity
2θ	- Bragg (diffraction) angle
κ	- Ginsburg-Landau Ratio
λ	- penetration depth (Superconductivity)
λ	- wavelength of X-ray radiation (XRD)
ξ	- coherence length
ρ	- measured density of the solid including all porosity
ρ_0	- density of fluid (Stokes's Law)
ρ_{liquid}	- density of liquid dispersant
ρ_{solid}	- density of solid
$\rho_{theor.}$	- theoretical density of solid calculated from the lattice parameters
Ω	- molecular volume
B	- constant in the Beer-Lambert law related to molecular weight
C	- concentration of solid phase in a solid/liquid dispersion
d	- characteristic dimension of sample (Bean model)
d_h	- length of base diagonals of a pyramidal indent
d_{lp}	- interplannar lattice spacing
d_{max}	- maximum diameter
d_{sieve}	- sieve diameter
$d_{spherical}$	- diameter of a spheical particle
d_{St}	- Stokes's diameter
d_v	- diameter of a sphere with equal volume to the particle
$d_{v,90}$	- 90 vol.% of the particles are smaller than $d_{v,90}$
$d_{v,50}$	- median particle diameter
$d_{v,10}$	- 10 vol.% of the particles are smaller than $d_{v,10}$

E_0 - Young's Modulus

E_b - binding energy

F_d - drag force on a particle falling vertically in a fluid

g - gravitational constant

H - applied magnetic field

H_c - critical magnetic field

H_{c1} - magnetic field at which perfect diamagnetism is lost in Type II superconductors

H_{c2} - magnetic field at which the sample loses all superconductivity

H_{irr} - magnetic field at which magnetisation behaviour becomes irreversible

HV - Vickers hardness

h - distance travelled by a falling particle (Stokes's Law)

hv - energy of the incident photon (XPS)

I - intensity of X-ray which has passed through the solid/liquid dispersion of concentration C

I_0 - intensity of X-ray which has passed through only the dispersing liquid

I_c - critical current

J_c - critical current density

$J_{c,trans}$ - critical current density measured by the transport method

$J_{c,mag}$ - critical current density measured by the magnetic method

k - Boltzmann Constant

M - magnetization

m_{air} - mass of pellet when weighed in air

m_{damp} - mass of pellet when all internal pores are filled with liquid

m_{liquid} - mass of liquid

m_{solid} - mass of the solid component

m_{wet} - mass of a pellet when immersed in liquid

P - load

Re - Reynolds number

T - temperature

T_c - critical temperature

T_m - melting temperature

T/T_m - homologous temperature (heat-treatment temperature divided by melting temperature)

ΔT_c - temperature range of transition from normal to superconducting behaviour

$T_{c,onset}$ - temperature at start of transition normal to superconducting behaviour

t - time

V - volume

v - terminal velocity of a falling particle (Stokes's Law)

v - dispersion unit stirring speed (Mastersizer S)

Abbreviations

AC	Alternating Current
BCS	Bardeen, Cooper and Schrieffer
BSE	Back-Scattered Electrons
CIP	Cold Isostatic Pressing
DC	Direct Current
EDX	Energy Dispersive X-ray Spectroscopy
HIPing	Hot Isostatic Pressing
HP	Hot Pressing
HTS	High Temperature Superconductor
MRI	Magnetic Resonance Imaging
MPMS	Magnetic Property Measurement System
PCS	Photon-Correlated Spectroscopy
PIT	Powder-In-Tube
POM	Polarised Optical Microscopy
RS	Resistive Sintering
SE	Secondary Electrons
SEM	Secondary Electron Microscopy
SPS	Spark Plasma Sintering
SQUID	Superconducting Quantum Interference Device
TEM	Transmission Electron Microscopy
XPS	X-ray Photoelectron Spectroscopy
XRD	X-Ray Diffraction

Contents

1 Superconductivity **1**

1.1 Characteristics of Superconducting Materials 1
1.2 Type I and Type II Superconductors 2
1.3 Measurement of Superconductivity 5
1.3.1 Superconductivity Parameters 5
1.3.2 Critical Temperature 6
1.3.3 Critical Current Density 6
1.3.4 Critical Magnetic Fields 8
1.4 Theories of Superconductivity 8
1.5 Superconducting Materials 9
1.5.1 Low-Temperature Superconductors 9
1.5.2 High Temperature Superconductors 10
1.5.3 Magnesium Diboride 10

2 Magnesium Diboride **12**

2.1 Crystallographic Structure 12
2.2 Characteristic Properties of Ceramic Materials 13
2.3 Materials Used for Production of Magnesium Diboride 19
2.3.1 *Ex Situ* Processing 19
2.3.2 *In Situ* Processing 20
2.3.3 Mechanical Alloying 22
2.4 Fabrication of Magnesium Diboride Artefacts 24
2.4.1 Magnesium Diboride Bulk Artefacts 24
2.4.2 Magnesium Diboride Wires and Tapes 25
2.5 Factors affecting the Superconducting Properties of *Ex Situ* Magnesium Diboride Artefacts 26
2.5.1 Heat-Treatment 26
2.5.2 Particle Size 29
2.5.3 Pressure 35
2.5.4 Impurity Phases 39
2.5.4.1 Impurity Phases Which Form During Heat-Treatment . . 41
2.5.4.2 Doping of the Magnesium Diboride Crystal Lattice 44
2.5.4.3 Improvement of Microstructure by Addition of Impurity Phases 45
2.5.4.4 Improved Flux Pinning by Finely Dispersed Impurity Phases 46
2.6 Conclusions and Aims of This Work 48

3 Experimental Methodology **49**

3.1 Fabrication: Powders . . . 49
3.1.1 Sieving . . . 50
3.1.2 Sedimentation . . . 51
3.1.3 Ball milling . . . 54
3.1.4 Attrition Milling . . . 57
3.2 Fabrication: Bulk Samples . . . 58
3.2.1 Pressureless Heat-Treatment . . . 58
3.2.2 Resistive Sintering . . . 59
3.2.3 Spark Plasma Sintering . . . 60
3.2.4 Hot Pressing . . . 61
3.3 Characterization: Macroscopic Physical Properties . . . 62
3.3.1 Density Measurements . . . 62
3.3.2 Vickers Hardness . . . 64
3.4 Characterization: Size and Shape of Particles and Grains . . . 64
3.4.1 Particle Sizing . . . 64
3.4.1.1 X-ray Sedimentation . . . 67
3.4.1.2 Laser Diffraction . . . 68
3.4.2 Optical Microscopy . . . 69
3.4.3 Polarised Optical Microscopy . . . 70
3.4.4 Scanning Electron Microscopy . . . 70
3.4.5 Transmission Electron Microscopy . . . 73
3.5 Characterization: Impurity Content Determination . . . 75
3.5.1 X-Ray Diffraction . . . 75
3.5.2 Energy Dispersive X-ray Spectroscopy . . . 77
3.5.3 X-Ray Photoelectron Spectroscopy . . . 78
3.6 Characterization: Magnetic Measurements . . . 79

4 Processing Commercial Magnesium Diboride Powder 80
4.1 Characterization of Commercial Powder . . . 80
4.1.1 Impurity Content Prior to Heat-Treatment . . . 80
4.1.1.1 X-Ray Diffraction . . . 81
4.1.1.2 Energy-Dispersive X-Ray Spectroscopy . . . 82
4.1.1.3 Back-scattered Scanning Electron Microscopy . . . 88
4.1.1.4 X-Ray Photoelectron Spectroscopy . . . 88
4.1.2 Particle Size . . . 92
4.1.2.1 SEM and TEM . . . 92
4.1.2.2 X-Ray Sedimentation . . . 93
4.1.2.3 Laser diffraction . . . 99
4.1.3 Summary . . . 108
4.2 Pressureless Heat-Treatment . . . 109
4.2.1 Measurement of increase in MgO content using XRD . . . 109
4.2.2 Establishing the method for pressureless heat-treatment . . . 111
4.2.3 Standard method for pressureless heat-treatment . . . 114
4.2.4 Impurity Content post-Heat-Treatment . . . 114
4.2.4.1 XRD . . . 114
4.2.4.2 EDX . . . 121

4.2.5 Density and Connectivity . . . 122
4.2.6 Magnetic Measurements . . . 125
4.2.7 Summary . . . 127

5 Modification of Magnesium Diboride Powder 131
5.1 Sieving . . . 131
5.1.1 Impurity Content . . . 132
5.1.2 Particle Sizing . . . 132
5.2 Sedimentation . . . 136
5.2.1 Impurity Content . . . 139
5.2.2 Particle Sizing . . . 140
5.3 Ball Milling . . . 143
5.3.1 Impurity Content . . . 144
5.3.2 Particle Sizing . . . 146
5.3.3 Magnetization Measurements . . . 157
5.4 Attrition Milling . . . 159
5.4.1 Impurity Content . . . 159
5.4.2 Particle Sizing . . . 163
5.4.3 Magnetization Measurements . . . 165
5.5 Summary . . . 167

6 Pressureless Heat-Treatment of Modified Powders 168
6.1 Pellets Produced from Sieved Powders . . . 168
6.1.1 Density . . . 168
6.1.2 Hardness . . . 169
6.1.3 Impurity Content by XRD . . . 170
6.1.4 SEM Microscopy . . . 173
6.2 Pellets Produced from Sedimented Powders . . . 175
6.2.1 Density . . . 177
6.2.2 Hardness . . . 177
6.2.3 Impurity Content . . . 180
6.2.4 Microscopy . . . 183
6.3 Pellets Produced from Ball Milled Powders . . . 188
6.3.1 Density . . . 189
6.3.2 Impurity Content . . . 189
6.3.3 Hardness . . . 202
6.3.4 SEM the presence of . . . 204
6.3.5 Magnetization Measurements . . . 204
6.4 Pellets Produced from Attrition Milled Powder . . . 212
6.4.1 Density . . . 212
6.4.2 Impurity Content . . . 213
6.4.3 Hardness . . . 218
6.4.4 SEM . . . 219
6.4.5 Magnetization Measurements . . . 220
6.5 Summary . . . 224

7 Pressure-Assisted Heat-Treatment 225

7.1 Resistive Sintering . . . 225
7.1.1 Density . . . 226
7.1.2 Hardness . . . 227
7.1.3 Impurity Content . . . 229
7.1.4 Microscopy . . . 238
7.1.5 Summary . . . 243
7.2 Spark Plasma Sintering . . . 244
7.2.1 Density . . . 248
7.2.2 Hardness . . . 250
7.2.3 Impurity Content . . . 250
7.2.4 Microscopy . . . 257
7.3 Hot Pressing . . . 269
7.3.1 Density . . . 269
7.3.2 Hardness . . . 271
7.3.3 Impurity Content . . . 273
7.3.4 Microscopy . . . 275
7.4 Summary . . . 276

8 Conclusions and Suggestions for Further Work 278
8.1 Conclusions . . . 278
8.2 Further Work . . . 281

References 283

1 Superconductivity

1.1 Characteristics of Superconducting Materials

In 1911 at the University of Leiden, Heike Kamerlingh Onnes observed that mercury lost all resistance when immersed in liquid helium (boiling point 4.2 K) [1–3]. Kamerlingh Onnes and his co-workers rapidly discovered mercury was not unique in this respect, observing the same effect in tin, lead and mercury-tin amalgam [4]. This phenomenon whereby materials conduct electricity with no resistance below a material-characteristic transition temperature became known as *superconductivity* and those materials which demonstrate the effect as *superconductors*.

The difference between normal electrical conductivity and superconductivity is best demonstrated by the change in resistance with temperature. In normal metallic conductors, resistance decreases monotonically with temperature as scattering mechanisms become less influential. In superconducting materials cooled below a certain temperature (T_c, the transition or critical temperature) a sudden rapid decrease in resistivity is observed such that below the transition temperature the material has effectively no resistance [5] (Figure 1.1).

This property means that superconducting materials are very efficient conductors of electricity. In addition, superconductors display the *Meissner Effect* when exposed to magnetic fields. Meissner and Ochsenfeld [7] performed measurements of the magnetic flux distribution around tin and lead samples below their transition temperatures, whilst exposing them to a magnetic field. They observed that below T_c the samples became spon-

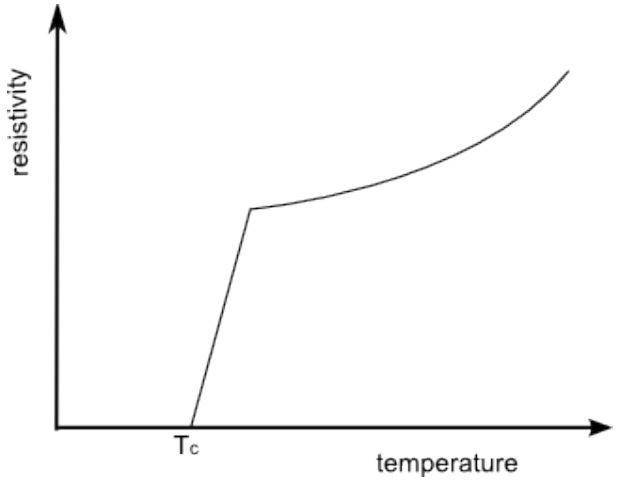


Figure 1.1: Variation in resistivity of a superconductor with temperature (after Rose-Innes and Rhoderick [6])

taneously diamagnetic, *i.e.* magnetic flux within the body of the specimen was excluded. In order to prevent magnetic flux lines passing through the superconductor, screening currents are set up on the surface of the material, creating an equal and opposite flux density to that applied externally. The magnetic flux density *within* the material is therefore zero [6]. The Meissner effect shows that in external magnetic fields superconducting currents flow preferentially through a small volume near the surface. The distance into the superconductor to which flux can penetrate is called the *penetration depth*, the value of which varies depending on whether the superconductor is Type I or Type II (see below), and whether it is a high or low temperature superconductor. This is discussed in more detail in Section 1.2. The Meissner effect allows the levitation of permanent magnets above the surface of superconductors which has a number of potential industrial applications, including magnetic levitating trains and bearings [8].

1.2 Type I and Type II Superconductors

Superconductors can be categorised by their superconducting properties as *Type I* or *Type II*. In Type I superconductors the Meissner effect is observed as described in Section 1.1, with no flux penetration of the material in the superconducting state, providing there

is no demagnetizing factor due to the shape of the body [6]. However, magnetic flux lines can penetrate the body of a Type II superconductor, existing at equilibrium in normal cores within the superconducting matrix. Normal cores in Type II superconductors are prevented from moving through the superconducting matrix by impurities or other imperfections in the material. This is known as *flux pinning* [9] and is an intrinsic material property regardless of the shape of the sample [6]. Without effective pinning, the flux lines will move when current is passed through the superconducting matrix, resulting in dissipation and loss of the low resistance state. The normal cores in a Type II superconductor, with the current vortices around each one, are depicted in Figure 1.2.

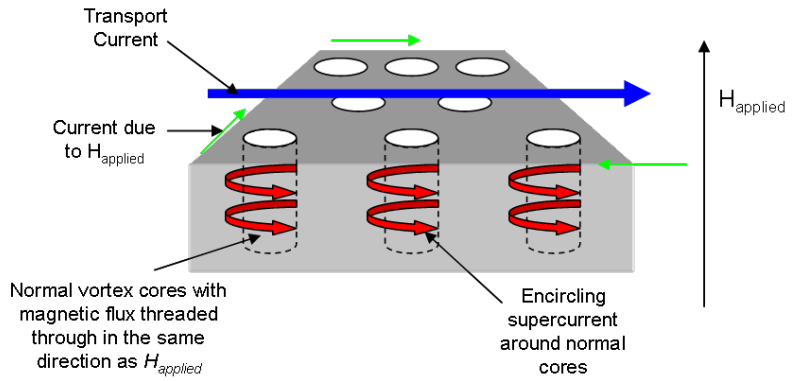


Figure 1.2: Normal cores in Type II superconductors (based on a diagram from [6])

A key property of Type II superconductors is the coherence length, which is the limiting distance over which pairs of electrons can interact [10; 11]. The relationship between the coherence length and the penetration depth determines whether a superconductor is Type I or Type II. In Type I materials the coherence length is larger than the penetration depth, while in Type II superconductors this relationship is reversed (Figure 1.3). In Type I materials, because the penetration depth is much smaller than the coherence length, externally applied magnetic fields cannot penetrate far enough to affect the superconductivity [11] (for example, in aluminium, the coherence length is 1.6 μm and the penetration depth is 0.05 μm [10]). In Type II materials, the superconductivity cannot exist outside the small coherence distance. It is therefore unaffected by magnetic fields

beyond this distance which have entered the material in the mixed state [11]. Values of both the coherence length and penetration depth vary significantly for Type II materials. For the widely used low-temperature superconductor Nb-Ti, the penetration depth is 60 nm and the coherence length 45 nm, while for $YBa_2Cu_3O_7$, a commonly used high-temperature superconductor, the penetration depth is 400 nm and the coherence length 1 nm [10]. The ratio of the penetration depth (λ) and the coherence length (ξ) is known as the Ginsburg-Landau ratio (κ) (Equation 1.1). The limiting value of κ is 0.707; above this value the superconductor is defined as Type II, below it as Type I [11].

$$\kappa = \frac{\lambda}{\xi} \tag{1.1}$$

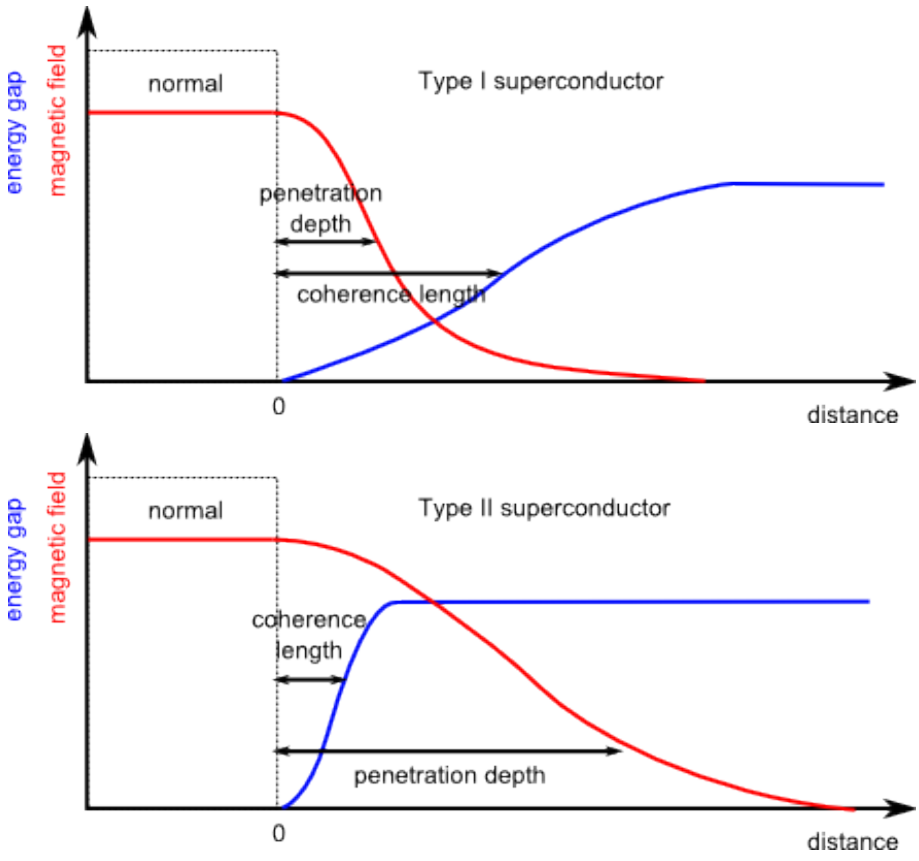


Figure 1.3: Schematic diagram showing the relationship between penetration depth and coherence length for Type I and Type II superconductors (adapted from diagrams in Sheahen [11])

The magnetization behaviour of Type I and Type II superconductors is compared in

Figure 1.4. For Type I materials the behaviour is straightforward: at $H = H_c$ the superconductivity disappears abruptly. For Type II materials, the behaviour is more complex. For $0 < H < H_{c1}$ the material behaves as a Type I superconductor. At H_{c1} the magnetic flux lines begin to penetrate and normal cores form. As the magnetic field increases, more normal cores form and the magnetization (the difference between the density of flux lines inside and outside the sample) becomes less negative until at $H = H_{c2}$ the magnetic flux penetrates the whole sample. The sample then reverts to its normal conducting behaviour, with zero magnetization [6].

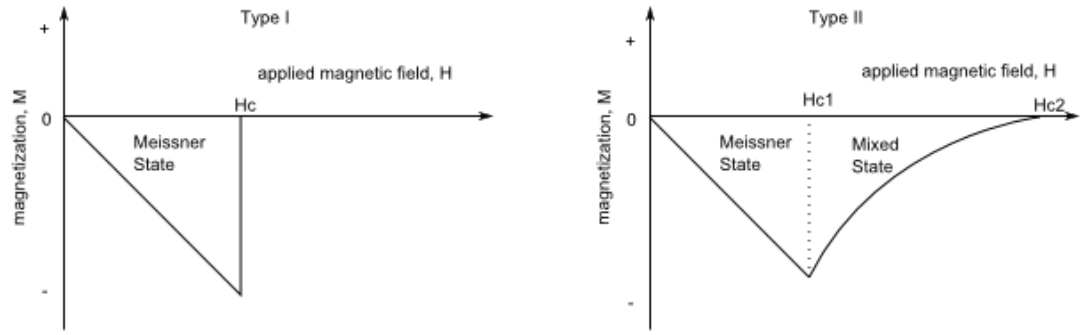


Figure 1.4: Magnetization behaviour for ideal Type I and Type II superconductors (after Sheahen [11] and Cyrot and Pavuna [10])

1.3 Measurement of Superconductivity

1.3.1 Superconductivity Parameters

The key parameters associated with superconductivity in a particular material are the critical temperature (T_c), critical current density (J_c), and critical magnetic field (H_c). In all cases, *critical* refers to the maximum value of that property before the material ceases to be superconducting. These parameters are closely related to each other as shown in Figure 1.5, although the exact relationship depends on both the material and the method by which it was prepared, and on the contribution of other effects such as strain, impurities and connectivity between grains in polycrystalline materials.

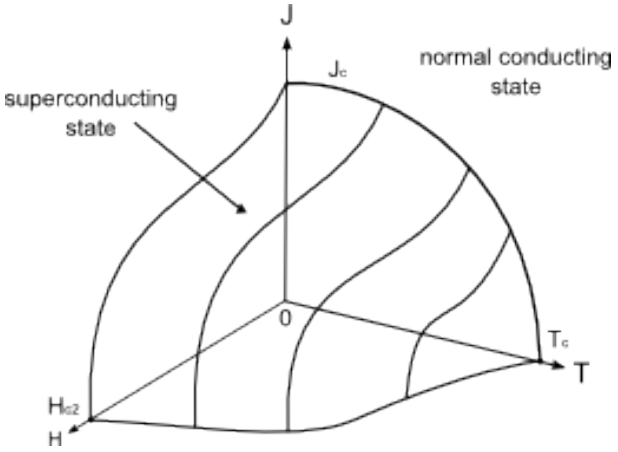


Figure 1.5: Schematic relationship between temperature, magnetic field and current density for superconducting materials (after Goodrich and Bray [12]). The superconducting region is beneath the surface indicated.

1.3.2 Critical Temperature

T_c is generally measured using the four-point probe or van der Pauw method [9] with resistance recorded as the temperature decreases. This temperature can be reported using various criteria (see Figure 1.6). The temperature at which a sharp drop in resistance occurs is known as the onset critical temperature ($T_{c,onset}$). The critical temperature itself (denoted T_c) is defined as the temperature at which the resistance becomes impossible to measure. The width of this transition (ΔT_c) varies with the impurity level and the extent of crystalline lattice disorder of the sample [6]; for example, an undoped single crystal of magnesium diboride had $T_c = 38.2\,\mathrm{K}$ and $\Delta T_c = 0.5\,\mathrm{K}$, while a similar carbon-doped single crystal ($Mg(B_{0.948}C_{0.052})_2$) had $T_c = 35.0\,\mathrm{K}$ and $\Delta T_c = 3.3\,\mathrm{K}$ [13].

1.3.3 Critical Current Density

The critical current density, J_c, is determined by magnetization or transport measurements. The magnetization critical current density ($J_{c,mag}$) can be measured from magnetization variations with applied magnetic field, for example by using DC magnetometry (a Superconducting Quantum Interference Device {SQUID}* combined with pickup coils to measure the voltage induced by the moving magnetic moment of the sample in a con-

*A SQUID can be used to detect very small magnetic fields

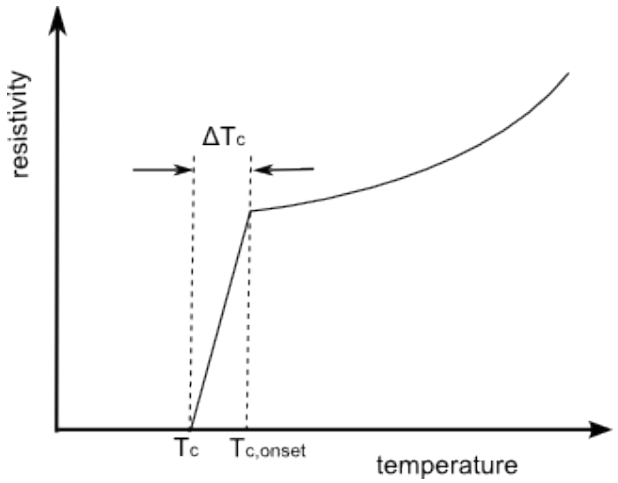


Figure 1.6: Schematic Resistance-Temperature curve showing indicating the various measures of critical temperature

stant applied magnetic field) or AC magnetometry techniques (similar to DC technique but using an AC drive to induce a time-dependent magnetic moment in the sample) [9]. $J_{c,mag}$ is calculated from measured magnetization loops (magnetization M vs. applied magnetic field H) using the Bean model [14]. A typical analysis carried out to calculate $J_{c,mag}$ for MgB_2 bulk material is given in Hsieh *et al* [15]. The Bean model should be used with care, as it is only applicable to homogeneous samples, and the shape of the sample must also be taken into account [8].

The transport critical current is measured by directly passing current along the sample, and is the preferred method of determining J_c values for superconducting wires and tapes. Using a predefined critical voltage criterion (normally $1\,\mu$V/cm [9]), the critical current I_c is determined. By dividing this value by the cross-sectional area of the wire or tape, the transport critical current density ($J_{c,trans}$) can be calculated. For low magnetic fields there are sometimes problems with measuring the critical current because wires are insufficiently stabilised to carry the very high currents (see, for example, Kováč *et al* [16]). In this case $J_{c,trans}$ is often predicted by extrapolating high magnetic field measurements to low magnetic fields, but the accuracy of this method is questionable as the J *vs.* H plots are generally non-linear when experimentally measured. However, it does assist with comparisons of wires and tapes produced by different methods.

Because $J_{c,trans}$ and $J_{c,mag}$ are measured according to different criteria they are not necessarily equivalent. $J_{c,trans}$ depends on connectivity in the core of the wire, and the ability to measure it accurately is often affected by the thermal stabilization of the wire for high values of critical current. $J_{c,trans}$ is a more accurate measurement of the current-carrying ability of a wire or tape [11], but cannot usually be performed for bulk samples. $J_{c,mag}$ can only be accurately measured for regularly-shaped bulk samples, and is affected by the size and granularity of the sample [17].

1.3.4 Critical Magnetic Fields

The critical magnetic field is defined as the highest magnetic field in which the material remains a superconductor. It is measured by recording the magnetization in the sample when placed in a systematically varied magnetic field (*e.g.* using a SQUID magnetometer) [9]. From this curve, we can obtain H_{c2} (the upper critical magnetic field - the magnetic field at which the magnetization becomes zero [18]), and H_{irr} (the magnetic field at which the magnetization behaviour becomes irreversible, *i.e.* the point at which the curves for increasing magnetic field and decreasing magnetic field diverge). H_{c1} is defined as the applied magnetic field at which perfect diamagnetism is lost; for real Type II superconductors it is dependent on the extent of flux pinning in the sample. Critical magnetic fields can also be determined from measurements of resistance with changing applied magnetic field [9].

1.4 Theories of Superconductivity

Superconductivity in some superconducting materials can be described by the Bardeen, Cooper and Schrieffer (BCS) theory [19]. This states that superconducting electrons travel through the material in pairs (Cooper pairs) and interact with each other via lattice vibrations (phonon mediation). The formation of these Cooper pairs leads to a gap in the allowed energy levels between the superconducting and normal states and so the

Cooper pairs are unable to individually gain or lose small amounts of energy [6]. At low temperatures there is not enough energy resulting from collisions with imperfections in the lattice to overcome this energy gap, and thus the pairs can move through the material with no loss of energy (zero resistance). At temperatures above the critical temperature the energy gap can be overcome and the normal conducting state is restored.

However, BCS theory is not entirely applicable to the cuprate high-temperature superconductors [18], and to date no one acceptable theory has been found to explain their behaviour. Modifications of the BCS theory that take the structure of cuprates into account have been proposed, as well as many new models. For more information on superconducting theories, the reader is directed to the books by Buckel and Kleiner [8] and Waldram [18].

1.5 Superconducting Materials

1.5.1 Low-Temperature Superconductors

Thanks in part to the low temperatures required, but also to the discovery that the application of relatively small magnetic fields destroyed the superconductivity, practical applications for superconducting materials were not immediately obvious following Kamerlingh Onnes' discovery of superconductivity [9]. For many years research on superconducting materials focused on the search for new superconducting elements and compounds, and on developing theories to explain the behaviour. In the 1950s, improved purification and synthesis methods, and the availability of commercially produced helium liquifiers, made the search for new superconducting materials more straightforward. Until 1986, superconductors with the highest critical temperatures all belonged to the class which contains Nb_3Sn, the A15 family of superconductors [9]. Nb_3Sn was the first superconductor to maintain high current-carrying ability in high magnetic fields [9]. Nb_3Sn has $T_c \backsimeq 17\,\mathrm{K}$ and $H_{c2}(T = 0\,\mathrm{K})$ of $28\,\mathrm{T}$ [20] and so can be used to make windings for high field magnets. One of the most widely-used superconductors is Nb-Ti, a low-temperature

superconductor with $T_c \backsimeq 9.2\,\mathrm{K}$ and $H_{c2}(T = 0\,\mathrm{K})$ of 14.4 T; it is used in both magnetic resonance imaging (MRI) machines and magnets for particle accelerators [8].

1.5.2 High Temperature Superconductors

In 1986, Bednorz and Mueller's discovery of the high-temperature superconductors [21] revitalised research into superconductivity. To date, all superconductors with transition temperatures above 50 K belong to the same family of perovskite copper oxides, though the phases which are superconducting are often non-stoichiometric and have very carefully controlled dopants and oxygen content [9]. However development of commercial applications for high-temperature superconductors has been slow, due to the cost and technical difficulties of fabricating wires with very highly aligned microstructures to overcome their anisotropic properties [8; 22]. Examples of well-studied HTS compounds with commercial applications include $Bi_2Sr_2Ca_2Cu_3O_{10}$ (BSCCO, $T_c = 110\,\mathrm{K}$) and $YBa_2Cu_3O_7$ (YBCO, $T_c = 92\,K$) [9]. These materials are produced commercially by companies including American Superconductor [23], THEVA [24], and SuperPower [25].

1.5.3 Magnesium Diboride

Until 2001 magnesium diboride (MgB_2) was primarily used for synthesising other materials, such as boron nitride [26], and other metal diboride compounds [27; 28]. But in January 2001 the announcement by Jun Akimitsu of the discovery of superconductivity in MgB_2 [29] led to an explosion of research on the material, and renewed the search for superconductivity in non-cuprate systems. Superconductivity has since been discovered in a number of related compounds including non-stoichiometric niobium diboride [30].

MgB_2 is a Type II phonon-mediated BCS superconductor, as indicated by the observation of the boron isotope effect (an increase in T_c by 1 K on substitution of ^{10}B for ^{11}B in MgB_2) [31]. MgB_2 has two superconducting energy gaps (between the occupied and unoccupied electronic states) [32], which has not been observed in any previously known superconductor. The two energy gaps, denoted π and σ, develop simultaneously

at the critical temperature and are of different widths. This means that conventional BCS theory does not exactly fit the behaviour of MgB_2.

The critical temperature of MgB_2 is 39 K, which is within the range of commercial cryocoolers, and is the highest yet recorded for a non-copper-oxide compound. The compound can be easily synthesised by reacting elemental Mg and B at high temperature in a closed environment. Alternatively, it can be purchased from chemical companies. MgB_2 can show significant superconductivity even when it is extremely porous and has a high impurity content. Early wires showed such high critical current values in low magnetic fields that MgB_2 was quickly being discussed as a replacement for Nb_3Sn in magnetic resonance imaging scanners [33]. Progress has been rapid; just four years after the discovery of superconductivity in MgB_2, wire of 1 km lengths was being produced commercially [34], and the production of MgB_2 magnets is becoming a reality [35]. While improvements must still be made to improve the performance, many researchers feel that MgB_2 has potential to be a practical commercial superconductor [36–38].

2 Magnesium Diboride

2.1 Crystallographic Structure

The preparation of magnesium diboride was first reported by Jones and Morton in 1953 after they determined its crystallographic structure by X-ray diffraction (XRD) [39]. Magnesium diboride has a relatively simple AlB_2-type crystal structure, consisting of boron atoms in a graphitic configuration interlaced with a hexagonal magnesium lattice, as shown in Figure 2.1. The space group of MgB_2 is P6/mmm.

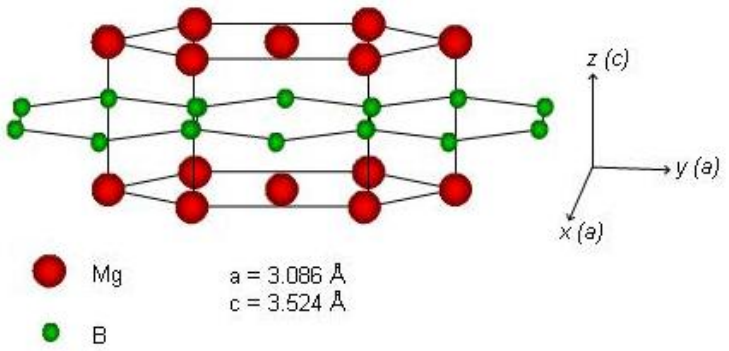


Figure 2.1: The crystal structure of magnesium diboride

The simple structure means that MgB_2 is easily synthesised from the elements, unlike many high-temperature superconductors that require complex reaction processes from specific precursors with precise stoichiometry. Commercial magnesium diboride powder contains significant amounts of oxygen-based impurities [40], but despite this, wires and tapes made from these powders readily attain high critical current values without extensive heat-treatment or purification.

Investigations of superconductivity in niobium diboride have found that, despite the lack of superconductivity above 3 K in stoichiometric NbB_2, non-stoichiometric $Nb_{(1-x)}B_2$ ($x > 0.04$) is superconducting, with $7\,\mathrm{K} < T_c < 9\,\mathrm{K}$ depending on composition and processing [30]. The similar crystal structures of NbB_2 and MgB_2 indicate the possibility that non-stoichiometric composition is also an important factor in the superconducting properties of magnesium diboride. This may explain some of the widely differing results of research groups working on similar samples [33].

2.2 Characteristic Properties of Ceramic Materials

Ceramic materials are inherently brittle [41], and are stronger in compression than in tension. The tensile strength of ceramic materials is dependent on the size of small flaws in the microstructure [42]. The flaws are too small to be observed by non-destructive testing, which means the behaviour of an individual ceramic artefact is not predictable; the tensile strength can only be described by a statistical distribution. Some common flaws which lead to failure are pores, foreign matter, damage during processing, and grain boundaries between large grains [42]. Magnesium diboride is a brittle (fracture toughness $K_{1c} = 4\,\mathrm{MPa\,m^{1/2}}$ [43], similar to magnesia with $K_{1c} = 3\,\mathrm{MPa\,m^{1/2}}$ [44] and alumina with $K_{1c} = 4 - 5\,\mathrm{MPa\,m^{1/2}}$ [44]) strong solid with a high melting point, characteristics of a ceramic material, and densifies by sintering mechanisms.

Pores are present in many ceramic artefacts because it is very difficult to press ceramic powders to high density due to the high coefficient of friction between the particles. A lubricant must be added to reduce porosity to low levels by pressing alone. This can be burnt out during subsequent heat-treatment, but doing this may cause impurity phases or further porosity to form. Porosity can also be caused by agglomeration of the ceramic powders prior to pressing [45]; this occurs when powder particles stick together due to van-der-Waals forces or to the formation of impurity phases between particles. Agglomeration can be reduced by ball milling the powder in a fluid, or using a deflocculant which separates

the powder particles (for example by immersion in water adjusted to an appropriate pH) [42].

Most applications require that porosity be removed from ceramic materials. High porosity leads to lower strength, a lack of transparency, and low thermal conductivity [46]. Porosity is removed by heat-treatment at high temperature, a process known as *sintering*. There are six main processes which can occur during sintering:

1. Diffusion along the particle surface;
2. Lattice diffusion from the surface;
3. Vapour transport from the surface;
4. Diffusion along the grain boundaries;
5. Lattice diffusion from the grain boundaries; and
6. Lattice diffusion from dislocations.

The first three mechanisms lead to changes in shape of the pores due to material transport, but no change in pore volume occurs, *i.e.* no true densification is observed. The other mechanisms (4-6) cause densification. Material is moved to the neck region between particles, shown schematically in Figure 2.2. The driving force for these densification processes is the reduction in the surface area by transforming grain surfaces into grain boundaries, which results in a lowering of the surface free energy due to the removal of solid/vapour interfaces in the material [45].

Sintering diagrams have been developed which correlate sintering temperature with some measure of the changes in the microstructure, such as the ratio of the neck radius to particle radius or the relative density. Fields superimposed on the diagram indicate the dominant sintering mechanisms under those conditions. Examples of these maps are shown in References [47; 48]. At low temperatures and ambient pressure, grain boundary diffusion dominates because it has a significantly lower activation energy compared to

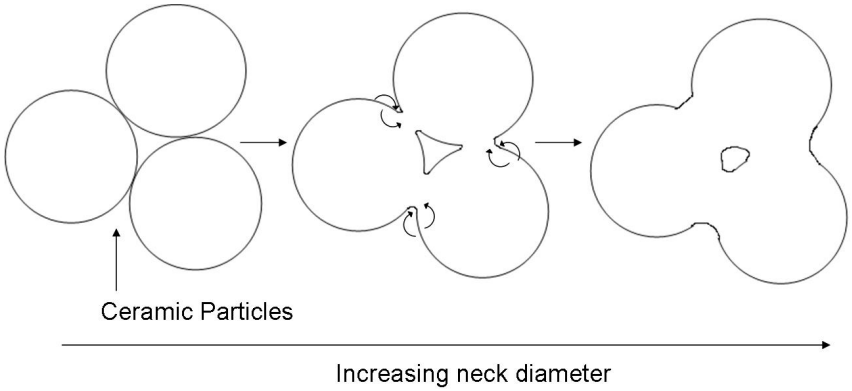


Figure 2.2: Schematic diagram showing densification of ceramic powders by neck formation. Arrows indicate movement of material through the bulk, along the surface, or through the vapour phase

lattice diffusion in most materials [49]. These diagrams are extremely useful in visualising the processes which occur during sintering under various conditions, and hence in understanding the effect of changes to processing parameters. However each map is limited to a specific material system and particle geometry, and vary significantly with impurity content [47].

The effects of applying pressure during heat-treatment can be shown using maps of applied pressure versus relative density [47]. These maps indicate the ranges of applied pressure in which processes such as plastic flow, power-law creep and yield contribute to the densification, and those in which diffusion is the main process. The maps also indicate the effect of time on the densification processes in operation. In general, the higher the applied pressure, the shorter the densification time as densification occurs more rapidly.

The stages in the process of pressureless sintering have been described by Kingery [46] (3 stages) and Reed [50] (4 stages) amongst others. First (Kingery *Stage 0*; Reed *Initial Stage*), adhesion of particles occurs, this is virtually instantaneous on commencement of sintering; Reed states that this stage also involves diffusion of impurity phases, removal of particle surface roughness, and some initial processes such as pore rounding. The second stage (Kingery *Stage 1*; Reed *Intermediate Stage*) is the significant growth of necks between particles and shrinkage of pores as material is transferred from the surface of adjacent particles to the neck region where two particles meet (see Figure 2.2). This

process is driven by the difference in chemical potential, which leads to transport of atoms from the convex to concave region of the neck. Once the material density is $\gtrsim 92\,\%$ (Kingery *Stage 2*; Reed *Final (1) Stage*) the isolated pores which remain once the particles have formed a continuous network shrink until the compact reaches its maximum density. Initially the rate of densification in this phase is rapid, but slows as porosity decreases. Reed adds another stage (*Final (2)*) not included in Kingery's model during which the isolated pores within grains are removed, and grain growth is rapid. The typical expected densification rates in each stage are shown schematically in Figure 2.3. While these stages are generally described as occurring successively, for inhomogeneous green compacts where the packing density varies, the stages may occur concurrently in different regions [51].

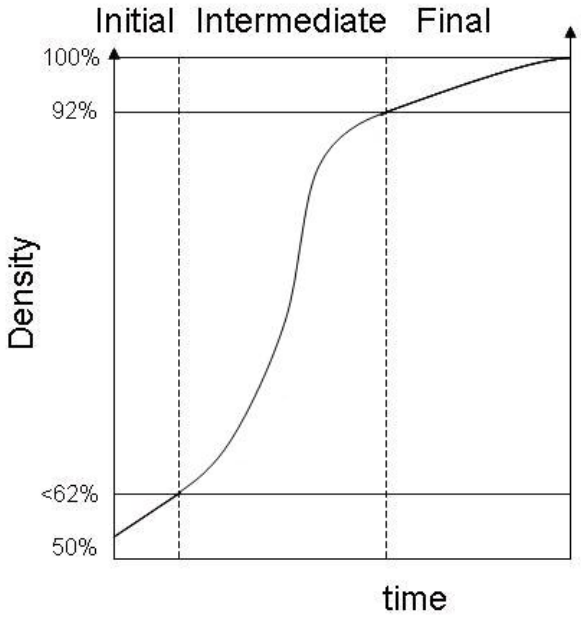


Figure 2.3: Densification rates during the three stages of sintering (drawn by the author from information in Reed [50])

Ceramic materials do not often reach 100 % density because a careful balance between grain growth and the removal of gases from pores by diffusion is required for this to occur. If the diffusion of gases from pores along grain boundaries is not rapid, pores can become trapped within grains. These pores are particularly difficult to remove. The addition of impurity phases is a straightforward way of improving the density as the impurity phases introduce lattice defects which can allow easier diffusion of gases [46]. If the gases are

insoluble in the solid, they can become trapped. As the pores containing the gas shrink, the pressure of the gas in the pore rises until pore shrinkage stops [45].

Sintering rate decreases with time; for this reason, Kingery states that extension of sintering time does not result in significantly greater densification. The key parameters affecting sintering rate are temperature and particle size (see Kingery [46] p. 376). Typical optimum sintering temperatures for ceramics are between $50 - 70\,\%$ of the melting temperature [50]; sintering rate increases with temperature but too high a temperature can cause melting or undesired impurity formation. In addition, during the final stage of sintering high temperatures (and hence high sintering rates) can lead to a more porous end-product due to discontinuous grain growth [50]. Densification rate is inversely proportional to particle size to the power n ($n > 1$ but depends on the transport mechanisms) [50] because smaller particles have a greater surface curvature, leading to a larger driving force for neck growth.

As MgB_2 decomposes before melting (see the phase diagram in Figure 2.11 on page 42), the melting temperature cannot be measured experimentally. The melting temperature of compounds can be estimated by comparison to their Young's modulus, as described by Frost and Ashby [52]. For many materials, the correlation between Young's modulus at room temperature, E_0, and the melting temperature, T_m, was empirically determined as that given in Equation 2.1.

$$E_0 = \frac{100kT_m}{\Omega} \tag{2.1}$$

where Ω is the molecular volume, defined as the molecular weight divided by the bulk density.

The Young's modulus of magnesium diboride has been measured by a number of researchers using hardness testing methods. The measured values of Young's modulus in the peer-reviewed literature vary from 50.2 GPa to 411 GPa [43; 53–57] due to the variation of measured hardness with porosity. Using Equation 2.1 these values give an estimated melting temperature range of 782 °C to 8359 °C. However as the original empirical cor-

relation was based on polycrystalline and presumably fully dense samples, it seems most reasonable to calculate the melting temperature based on a similar sample. Using the Young's moduli measured by Prikhna *et al* [43] gives a melting temperature of 4201 °C for polycrystalline dense MgB_2; similar samples examined by Nesterneko *et al* [57] have calculated melting temperatures ranging from 4094 °C to 5469 °C.

The homologous temperature (the heat-treatment temperature divided by the melting temperature, T/T_m) is used in deformation maps by Frost and Ashby [52] to determine the dominant sintering mechanisms in operation during pressure-assisted heat-treatment by correlating the heat-treatment temperature with the applied stress. Given the high melting temperature of MgB_2, by comparison to maps of known systems such as MgO and alumina-type oxides, it seems likely that at any reasonable working temperature (below the decomposition temperature of 1700 °C [58], giving a homologous temperature around 0.3) the deformation mechanism will be dominated by grain boundary-mediated diffusional flow at low applied pressures and power law creep or plastic flow at higher applied pressures. However it should be noted that these estimated melting temperatures are significantly higher than other diborides with the same AlB_2-type crystal structure as MgB_2 (e.g. HfB_2, TiB_2 and ZrB_2 have melting temperatures of 3100 °C, 2980 °C and 3040 °C respectively [59]), indicating the possibility of inaccuracy in the method of estimating the melting temperature, and also that the maps have not been calculated for any similar materials to MgB_2, which has an unusual combination of properties (hexagonal crystal structure, covalent bonding, and metallic room temperature conductivity) and therefore does not intuitively fit into any of the established isomechanical groups (see Frost and Ashby [52] for details of these). As no deformation map for the magnesium diboride system has been calculated to date it is difficult to make a valid conclusion as to the accuracy of these calculations.

The relatively recent discovery of a useful application for magnesium diboride, beyond its use as a precursor material, means that little is known about the intrinsic ceramic properties of MgB_2. Establishing properties such as the appropriate sintering temperature

and conditions is essential to optimise processing methods which produce artefacts with consistent properties. This is the main focus of this thesis.

2.3 Materials Used for Production of Magnesium Diboride

2.3.1 *Ex Situ* Processing

Ex situ processing uses pre-reacted MgB_2 powder, either purchased from chemical companies or made in the laboratory. Once prepared, samples already contain the superconducting material, so *ex situ* MgB_2 artefacts can superconduct without heat-treatment. However heat-treatment has been shown to improve the superconducting properties of *ex situ* wires. This will be discussed further in Section 2.5.1.

Commercially-produced MgB_2 powder is used by many research groups to produce *ex situ* MgB_2 polycrystalline bulks, wires, and tapes. MgB_2 powder is manufactured by Pfalz and Bauer (99 % purity) [40], Furuuchi Chemical (99 % purity) [60], H.C. Starck ($\sim$ 99 % purity [61]) [62], Aldrich (99 % purity) [63], and Alfa Aesar (98 % purity). The most commonly-used powder is that produced by Alfa Aesar. The powder is described by the manufacturer as "sieve size –325"; this corresponds to a particle diameter of $\leq 40\,\mu m$, assuming spherical particles. Several groups using the powder have questioned this specification; a significant fraction of particles larger than 100 μm in diameter have been observed in the powder using granulometric techniques [64; 65].

Birkedal *et al* [40] compared the Alfa Aesar MgB_2 powder (denoted AA) and the Pfalz and Bauer MgB_2 powder (denoted PB). PB contained 30 wt.% impurity phases including MgO and MgB_4 (detected using high resolution synchrotron powder diffraction measurements). The only impurity detected in the AA powder was around 5 wt.% MgO, suggesting that the impurity content (98 %) specified by the manufacturer may be inaccurate. No superconducting parameters were measured during this study. Despite the wide use

of the Alfa Aesar powder, there are conflicting reports of its purity. Vogt *et al* [66] report it as "without any impurities visible in a high-resolution X-ray powder diffraction pattern", disagreeing with the observation of 5 wt.% MgO content made by Birkedal *et al* [40]. This may be due to differences in impurity levels between different batches of the powder, as observed by Kováč *et al* [67] for Alfa Aesar MgB_2 powder batches #04032/99 and #06051/01 which they determined contained 5 wt.% and 1 wt.% MgO respectively. Otherwise identical wires produced from these powders were found to vary in both T_c and I_c values before and after heat-treatment. As the batch number for the Alfa Aesar MgB_2 powder is rarely stated in published articles, this means it is difficult to compare the performance of samples produced by different groups.

Commercial MgB_2 powder degrades in ambient environment at room temperature, particularly in humid conditions. This can introduce unexpected impurities such as $Mg(OH)_2$, $MgCO_3$ and B_2O_3 if the MgB_2 has been exposed to air and/or water during storage [68]. This has also been cited as a factor in the variable properties of *ex situ* MgB_2 artefacts produced by different groups [69].

2.3.2 *In Situ* Processing

In situ processing uses non-MgB_2 precursors that are reacted during the processing to form the artefact. *In situ* processing is often carried out using elemental magnesium and boron in solid form. However, a number of other precursors have also been used to good effect. There are two major advantages of using such compounds. One is that additives can be incorporated into the lattice, which can perform useful functions such as grain refinement during heat treatment, fine distributions of normal material to aid pinning of magnetic flux lines in the superconducting material, reaction with deleterious impurities such as oxygen to allow more MgB_2 to be formed, and doping of the MgB_2 lattice (for example with carbon [70]). Secondly, using these compounds can allow solid, liquid, gas and sol-gel processing to be performed at lower temperatures compared to those required to improve the superconductivity of *ex situ* MgB_2 samples. The following is a list of

reactions that have been shown to produce MgB_2 as a major product:

1. $Mg_{(s)} + 2B_{(s)} \rightarrow MgB_{2(s)}$[39]
2. $Mg_{(s)} + B_6Si_{(s)} \rightarrow 3MgB_{2(s)} + Mg_2Si_{(s)}$ [71]
3. $12Mg_{(s)} + 3B_2O_{3(s)} \rightarrow 3MgB_{2(s)} + 2B_{(s)} + 9MgO_{(s)}$ [72]
4. $MgCl_{2(s)} + 2NaBH_{4(s)} \rightarrow MgB_{2(s)} + 2NaCl_{(s)} + 4H_{2(g)}$ [73]
5. $MgCl_2 + KCl + Na_2B_2O_4$ (Electrolysis) [74]
6. $MgCl_2 + NaCl + KCl + MgB_2O_4$ (Electrolysis) [75]
7. $MgCl_2 + NaCl + MgB_2O_4 + LiCl$ (Electrolysis) [74]
8. $MgCl_2 + NaCl + MgB_2O_4 + NaCl$ (Electrolysis) [74]
9. $MgCl_2 + NaCl + MgB_2O_4 + Na_2B_2O_4$ (Electrolysis) [74]
10. $Mg_4Ag_{(s)} + B_{(s)} \rightarrow MgB_{2(s)} + MgAg_{(s)} + MgAg_{3(s)}$ after reaction above 850 °C [76]
11. $Mg_2Cu_{(s)} + B_{(s)} \rightarrow MgCu_{2(s)} + MgB_{4(s)} + MgB_{2(s)}$ [77]
12. $MgH_{2(s)} + B_{(s)} \rightarrow MgB_{2(s)} + H_{2(g)}$ [78]

The main disadvantage of *in situ* processing is that the microstructures of artefacts produced via this route are significantly more porous than those produced by *ex situ* processing. This can be seen in SEM images by Kováč *et al* [79] comparing MgB_2 wires produced by similar *ex situ* and *in situ* processing (Figure 2.4).

Zhou *et al* [80] suggest that the reason for the difference in porosity is the density change between MgB_2 and mixed $Mg + B$. The density change on formation of MgB_2 means that the *in situ* method can only produce a core with a maximum density of 74 % of the density of MgB_2 (2.63 g/cm^3 as calculated from the lattice parameters). This does not allow for the removal of Mg by evaporation or reaction with other materials present (such as impurity phases or the sheath material in the case of wires), which will prevent

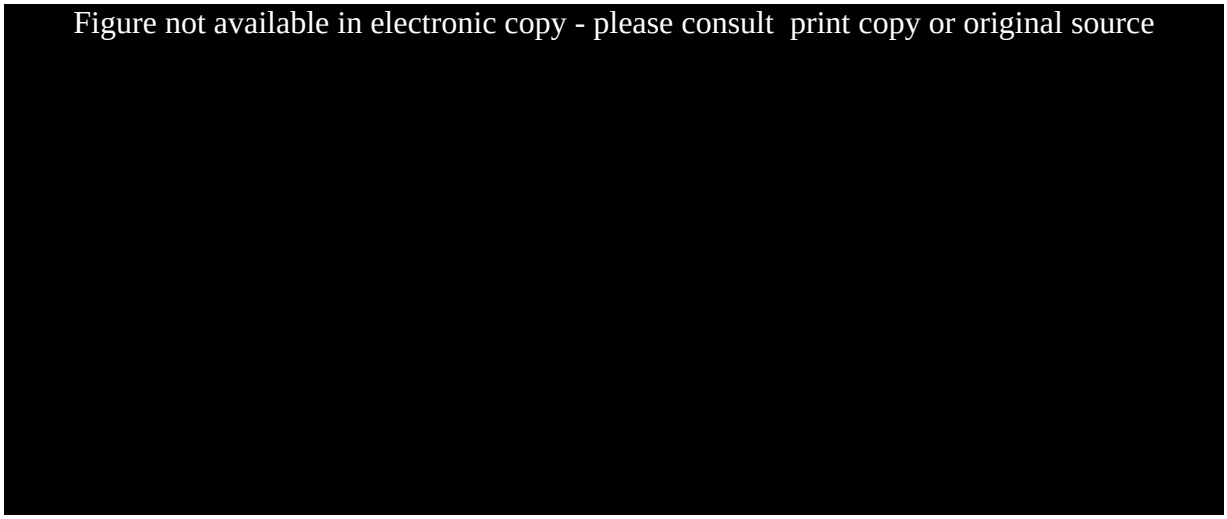


Figure 2.4: Comparison of the microstructure of (a) in situ and (b) ex situ MgB_2 wires taken from Kováč et al [79], reproduced with permission of IoP Publishing

the material reaching even this limited maximum density. Porosity can have a highly detrimental effect on the superconducting properties of MgB_2 artefacts; Grinenko *et al* [81] have shown that T_c is inversely proportional to the density of MgB_2 polycrystalline bulk samples.

2.3.3 Mechanical Alloying

A third processing route for producing MgB_2 artefacts uses powder produced by milling elemental powders. This is called mechanical alloying as the prolonged mixing and fracture of particles causes a reaction between the elemental powders. Some of the precursors remain after milling, leaving a mixture of MgB_2 + Mg + B; this route can therefore be considered as a mixture of *ex situ* and *in situ* processing. However this powder mixture has a higher density than Mg + B and hence lower porosity is expected after heat-treatment to form MgB_2, leading to denser material and hence improved superconducting properties compared to *in situ* wires. In comparison to *ex situ* processing, powder produced by mechanical alloying has a smaller particle size, corresponding to a finer grain size in the final MgB_2 artefact. This is expected to improve the critical current density at high magnetic fields, as the greater concentration of grain boundaries enhances the pinning force [82].

Contamination of the powder often occurs due to wear of the milling media and from impurities formed due to the prolonged exposure to oxygen and organic lubricants during the milling procedure [83]. Ball milling only produces MgB_2 after long milling times of at least 50 h [84], but in at least one study wires produced from powder milled for long periods have a porous, poorly-connected grain microstructure, with correspondingly poor superconducting properties [83]. The optimum time and processing conditions depend on the milling parameters, particularly the speed of the milling, the shape and composition of the milling media, and the ball-to-powder ratio, and this accounts for the different optimum milling times presented in different studies [82]. Copper-sheathed wires made from powders produced by mechanical alloying and annealed at 730 °C for 3 h have $T_c \simeq 30\,\mathrm{K}$, a narrow transition width ΔT of 1.4 K, and $J_{c,mag}$ (4.2 K, 1 T) of $3 \times 10^4\,\mathrm{A/cm^2}$. A decrease in $J_{c,mag}$ to $1.5 \times 10^4\,\mathrm{A/cm^2}$ was observed for tapes prepared using a longer (10 h) annealing process [85]. Tapes using the same mechanical deformation with more conventional precursors (such as MgB_2 powder or Mg + B) were not prepared so it is difficult to establish whether this is a true improvement in the superconducting properties. Copper is infrequently used as a sheath material due to the deleterious reaction of Mg and Cu so equivalent tapes are difficult to find in the literature. However *in situ* Cu-sheathed wires have been prepared by Glowacki *et al* [86] with a 1 h heat-treatment at 700 °C which attain $J_{c,mag} \simeq 3 \times 10^5\,\mathrm{A/cm^2}$ at the same temperature and magnetic field (the transition temperature was not measured). This indicates that the mechanical alloying process may not yet be optimised. Iron- and copper/niobium-sheathed wires have attained high critical currents at high magnetic fields (both attain $J_{c,trans} = 10^4\,\mathrm{A/cm^2}$ at 10 T) [87], perhaps due to the increased mechanical deformation possible using these much harder sheath materials compared to copper.

2.4 Fabrication of Magnesium Diboride Artefacts

MgB_2 artefacts have been produced in the form of polycrystalline bulk, single crystals, thin films, wires, and tapes. As the research reported in this thesis focuses on processing methods suitable for polycrystalline bulks and MgB_2 wires and tapes, the methods for producing MgB_2 thin films and single crystals will not be discussed here.

2.4.1 Magnesium Diboride Bulk Artefacts

Polycrystalline bulks can be manufactured by cold-pressing MgB_2 powder (*ex situ* samples) or precursors (*in situ* samples) in metal or graphite dies using uniaxial [88] or isostatic pressing [89], followed by heat-treatment. Most methods used involve some kind of shielding during the heat-treatment; these methods vary considerably but include sealing the samples in evacuated quartz tubes [90]; packing the samples in tantalum [91], iron [92], or zirconium foil [93]; and heat-treating the samples in high-purity argon [94], or a reducing atmosphere such as $Ar - H_2$ gas mixtures [95]. Elaborate combinations of all these procedures (see, for example, Luo *et al* [96]) are also used. There is no consensus in the literature on the efficacy of these procedures, and little justification is made for which is chosen beyond the general aim to avoid loss of magnesium through evaporation or exposure to oxygen during heat-treatment, although Agrestini *et al* [97] state that contact with quartz tubes causes the formation of MgO during heat-treatment at high temperatures, and suggest encapsulation in tantalum instead. Extra sources of magnesium are sometimes added as powder mixed with the precursors or flakes surrounding the bulk sample to mitigate the loss by evaporation [96]. MgB_2 samples are often made in this form to observe the effects of various heat-treatments [98] and additives [99]. In addition, hot isostatic pressing (HIPing) [60], hot pressing [15], and spark plasma sintering [100] have been used to produce very dense samples by simultaneous application of heat and pressure (see Section 2.5.3).

2.4.2 Magnesium Diboride Wires and Tapes

MgB_2 wires have several potential practical applications including solenoids (electromagnets) used in MRI scanners, power cables, and fault current limiters [101].

Six ways of producing MgB_2 wires have so far been developed:

1. Diffusion of magnesium vapour into boron filaments [102];

2. Powder-in-tube (PIT) technique [103];

3. Suspension spinning using MgB_2 powder suspended in a mixed poly(vinyl alcohol) solution of dimethylsulfoxide and hexamethylphosphoric triamide. [104; 105];

4. Pyrolysis of $Mg/B/MgB_2$ using infrared radiation to produce nanowires of MgB_2 [106];

5. Reaction of boron nanowires with MgO substrates using the thermal vapour transport process to form MgB_2 nanowires [107; 108]; and

6. Boron vapour diffusion into magnesium rods forming hollow wires [109].

The powder-in-tube (PIT) technique is the most widely used method for production of MgB_2 wires. The expertise developed through research on BSCCO superconducting PIT wires [110] meant that the PIT technique was rapidly implemented for production of MgB_2 wires after the discovery of superconductivity in magnesium diboride in 2001 [103]. In addition, the PIT method is the most realistic for production of commercially useful lengths of MgB_2 wire, and at present is used by companies including Columbus Superconductors (Italy) and Hypertech (USA) to produce commercial MgB_2 multifilamentary cables using the *ex situ* processing method [101].

PIT wires are produced by a series of fabrication steps (Figure 2.5). Sintering aids and dopants can be added to the precursor powders before they are packed into a metal tube, either by hand or by using a uniaxial press. The tube is sealed at both ends by crimping (pressing) [111], welding [112], or using metal plugs [113; 114]. This procedure is carried out in air [115] or in an inert-gas glove box [91]. Once sealed, the tube is drawn or swaged to give a round wire of around $1-2\,\mathrm{mm}$. For a flat tape, round wire is rolled to the desired thickness. The wire can be heat-treated in vacuum [116] or inert gas [117] if

required. Wires containing *ex situ* [118; 119], *in situ* [78; 120], and mechanically-alloyed [121] powders have all been successfully fabricated using the PIT technique.

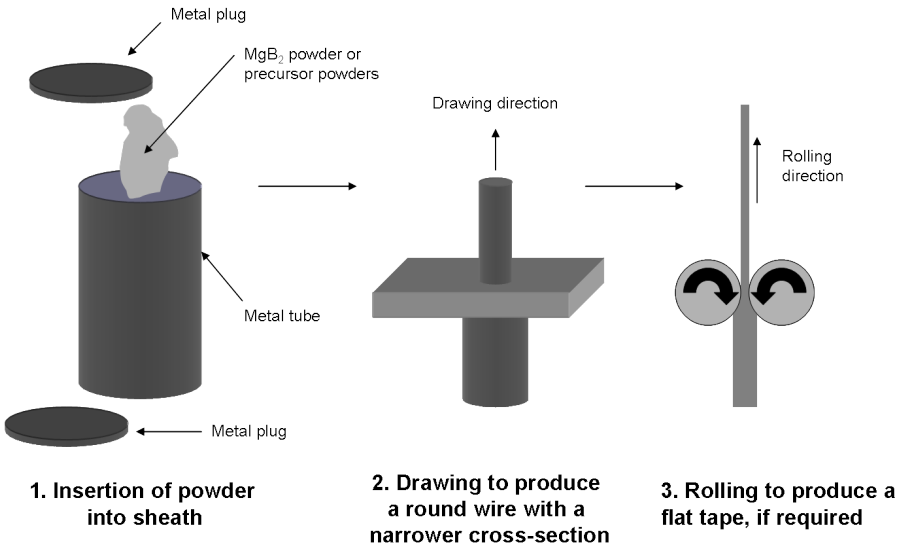


Figure 2.5: Process for fabrication of powder-in-tube wires and tapes

2.5 Factors affecting the Superconducting Properties of *Ex Situ* Magnesium Diboride Artefacts

2.5.1 Heat-Treatment

Heat-treatment of *ex situ* artefacts is not essential for the material to superconduct unlike *in situ* wires where synthesis of superconducting MgB_2 must be accomplished. Grasso *et al* [122] have shown that *ex situ* wires superconduct after mechanical deformation alone without heat-treatment, as the wire already contains powder of the superconducting phase, providing sufficient cold welding of grains occurs during deformation. However, heat-treatment is normally carried out on *ex situ* artefacts as this narrows the temperature range of the normal-superconducting transition (ΔT_c) and raises J_c values [65]. Various explanations have been offered for this including the densification of the MgB_2 core by sintering [115], and "recrystallization" of the lattice [115; 123]. The question of what happens in this heat-treatment is one of the central issues in this thesis.

Ex situ wires are generally heat-treated above 800 °C to achieve the best superconducting properties. Braccini *et al* [124] state that a high heat-treatment temperature is required to allow the material to recover from cold work and restore high T_c, and that generally *ex situ* heat-treated wires achieve higher T_c than *in situ* wires. They prepared a series of Ni-Cr alloy-sheathed wires annealed at peak temperatures between 200 °C and 950 °C, and found that T_c increases with peak heat-treatment temperature, as does $J_{c,mag}$ in low magnetic fields ($H < 5\,\mathrm{T}$). Fujii *et al* [125] found that heat-treatment of *ex situ* stainless steel- and iron-sheathed wires below 700 °C did not significantly improve the $J_{c,trans} - H$ performance compared to wires prepared with no heat-treatment. However, heat-treatment above 800 °C improved the $J_{c,trans}$ performance significantly. $T_{c,onset}$ values of the tapes are all $37 - 38\,\mathrm{K}$, though the width of the superconducting transition (ΔT_c) varies considerably. The widest transition is found in the as-rolled iron-sheathed tape ($\Delta T_c \simeq 25\,\mathrm{K}$), while the heat-treated iron-sheathed tape and both stainless steel-sheathed tapes had much narrower transitions ($\Delta T_c \simeq 4 - 5\,\mathrm{K}$). High ΔT_c values are indicative of weak-link behaviour at powder particle contacts, which is alleviated by heat-treatment of the iron-sheathed tape. The authors ascribe this to improved connectivity between grains caused by the heat-treatment [125], but whether this occurs by a sintering process is not determined.

Another important parameter in the heat-treatment procedure is the rate of heating and cooling. Serquis *et al* [116] studied the effect of varying these rates by preparing *ex situ* MgB_2 Fe-sheathed PIT wires heat-treated at 900 °C with 5 at.% additional Mg to account for vaporization during heat-treatment. The first was heated in Ar gas at 10 °C/min, maintained at the peak temperature for 15 min, cooled to 500 °C at 0.5 °C/min, and thereafter furnace cooled. The second was heated in vacuum at 35 °C/min, maintained at the peak temperature for 30 min and gas quenched with Ar. The preparation of these samples varies in more than just the heating and cooling rate, making it difficult to separate the effects of atmosphere, time at the peak temperature and heating and cooling rates. Comparison to an as-rolled wire showed that the first heat-treatment lowered the

J_c* by an order of magnitude, while the second raised J_c by an order of magnitude (at 4 K, self-field, $J_c = 5 \times 10^4 \mathrm{A/cm^2}$, $J_c = 3 \times 10^3 \mathrm{A/cm^2}$ and $J_c = 10^6 \mathrm{A/cm^2}$ respectively). Further investigations would ascertain which of the processing parameters causes this remarkable effect.

The disadvantage of heat-treating *ex situ* conductors is that the MgB_2 powder reacts with the sheath material in many cases, forming a non-superconducting reaction layer between the core and the sheath [126]. This reduces the cross-sectional area of the wire which is able to superconduct, as the reaction layers are not composed of superconducting material. Additionally vaporization of the magnesium from MgB_2 at elevated temperatures leads to formation of impurity phases such as MgO [127], MgB_4 [38; 128], and MgB_7 [38] in the core (the two borides being observed in non-stoichiometric form by Eyidi *et al* [129]). Processing using heat-treatment places limitations on the sheath materials that can be used, or, conversely, the temperature at which heat-treatment can be carried out is limited by the sheath material. The optimum sheath material is inert with respect to reactions with magnesium, boron and oxygen at high temperatures, while also possessing excellent ductility in order to allow maximum deformation of the wire. Kováč *et al* [123] found that the thickness of the interfacial reaction layer in iron-sheathed *ex situ* wires increases with increasing heat-treatment temperature for samples heated above 950 °C in argon gas for 30 min. The thickness of this layer (25.4 μm for a wire heat-treated at 1100 °C) places limitations on the thickness of MgB_2 filaments in multifilamentary wires, so minimising the heat-treatment temperature whilst maximising the performance of the wires is a priority. Grasso *et al* [130] found similar increases in reaction layer thickness with temperature for nickel-sheathed *ex situ* wires, in which a reaction layer of 20 μm formed for heat-treatment at 940 °C.

The reaction layer can be eliminated by using a composite sheath architecture where a metal which is inert with respect to MgB_2 is used as an inner sheath (*e.g.* Nb, Ta) and a stronger metal (*e.g.* stainless steel) [131] is used as an outer sheath. Cu is also used

*In this paper both $J_{c,trans}$ and $J_{c,mag}$ were measured, with good agreement for the two values for homogeneous samples.

as an outer sheath to increase the quench protection of these wires [67; 126]. The choice of sheath material, while clearly extremely widely-studied in the literature, will not be discussed further as it is not the focus of this thesis. The interested reader is directed to reviews by Buzea and Yamashita [33], Vinod *et al* [132], and Flükiger *et al* [133]. Ultimately, the choice of sheath material will vary according to the intended application [132].

The optimum heat-treatment for PIT wires depends on the sheath material and the extent of deformation (*i.e.* the processing steps to form the wire or tape), as well as any preliminary powder processing carried out (*e.g.* ball milling) because these variables can potentially affect the sintering rate (see Section 2.2).

2.5.2 Particle Size

The particle size distribution of a ceramic powder influences the green packing density, and therefore the final density and grain size of the artefacts produced from it. For *in situ* processing, precursor powders with small particle size (*e.g.* boron powder with particle size $< 5\,\mu$m can be purchased from Alfa Aesar) and narrow particle size range are available. No similarly fine MgB_2 powders are produced commercially, so reduction of the particle size of as-purchased MgB_2 powders is typically carried out to produce fine precursors for the *ex situ* processing route.

Ball milling [134] is often used to reduce the size of powder particles suspended in a liquid or in a gas, and is used in MgB_2 processing to create finer material(s) from coarse, commercially available products. It can also be used to mix precursors. The powder particles (and liquid if required) are placed in a container with a number of balls. These can be made of a variety of materials and shapes. The balls and powder are then mixed by rotating the vessel containing them. Particles trapped between the balls are broken up, and over time the average particle size is reduced.

Successful ball milling requires a good combination of milling media, speed, and time, and an appropriate ball-to-material ratio. Milling can be carried out in gas or under

liquid, both of which can introduce impurities into the powder. During a long milling process the exposure to oxygen can be considerable if measures are not taken to exclude it. Fe-sheathed tapes prepared from commercial MgB_2 powder ball milled in air contained significantly increased amounts of oxygen in the core compared to tapes produced from the same powder without ball milling [126].

Goldacker *et al* [64] compare the microstructures of wires made by using an *in situ* reaction, *ex situ* commercial powder, and *ex situ* ball milled commercial powder (Figure 2.6). The *in situ* MgB_2 wire consists of unreacted B-rich regions of $\sim 20\,\mu$m diameter surrounded by fine regions of MgB_2. The *ex situ* wire is inhomogeneous containing some regions of more than $50\,\mu$m diameter. The ball milled *ex situ* wire has a finer microstructure than either *in situ* or *ex situ* processed wires. In a fine-grained microstructure proportionally more of the material consists of grain boundaries, which act as flux pinning centres in MgB_2. This is expected to improve the wire's performance in high magnetic fields; however, the measurements given in [64] indicate that the superconducting properties of the ball milled powder are worse than that of the precursor powder; the reason for this is not established in this paper. A fine microstructure is more likely to evolve from a starting powder consisting of grains of similar sizes, as there is no driving force for abnormal grain growth, whereby large grains grow by assimilation of small grains [50].

MgB_2 cannot be ball milled in water, as it reacts to produce $Mg(OH)_2$, $MgCO_3$ and B_2O_3 [68]. Organic liquids such as isopropanol can be used without reaction, but this may result in carbon contamination [133]. Another source of contamination is the milling media itself. It is likely that during milling small fragments of the balls will break off (this was exploited by Chen *et al* to study the effect of adding ZrO_2 to MgB_2 [99]). This can lead to an enhancement of the flux pinning in the material, as the fragments are likely to be small, but means it is difficult to separate the effects of addition of the fine distribution of impurities and reduction in particle size on the superconducting properties. If enhancements in superconducting behaviour are primarily due to the impurity phases, it may be easier and cheaper to mix impurity phases into the starting powder, and eliminate

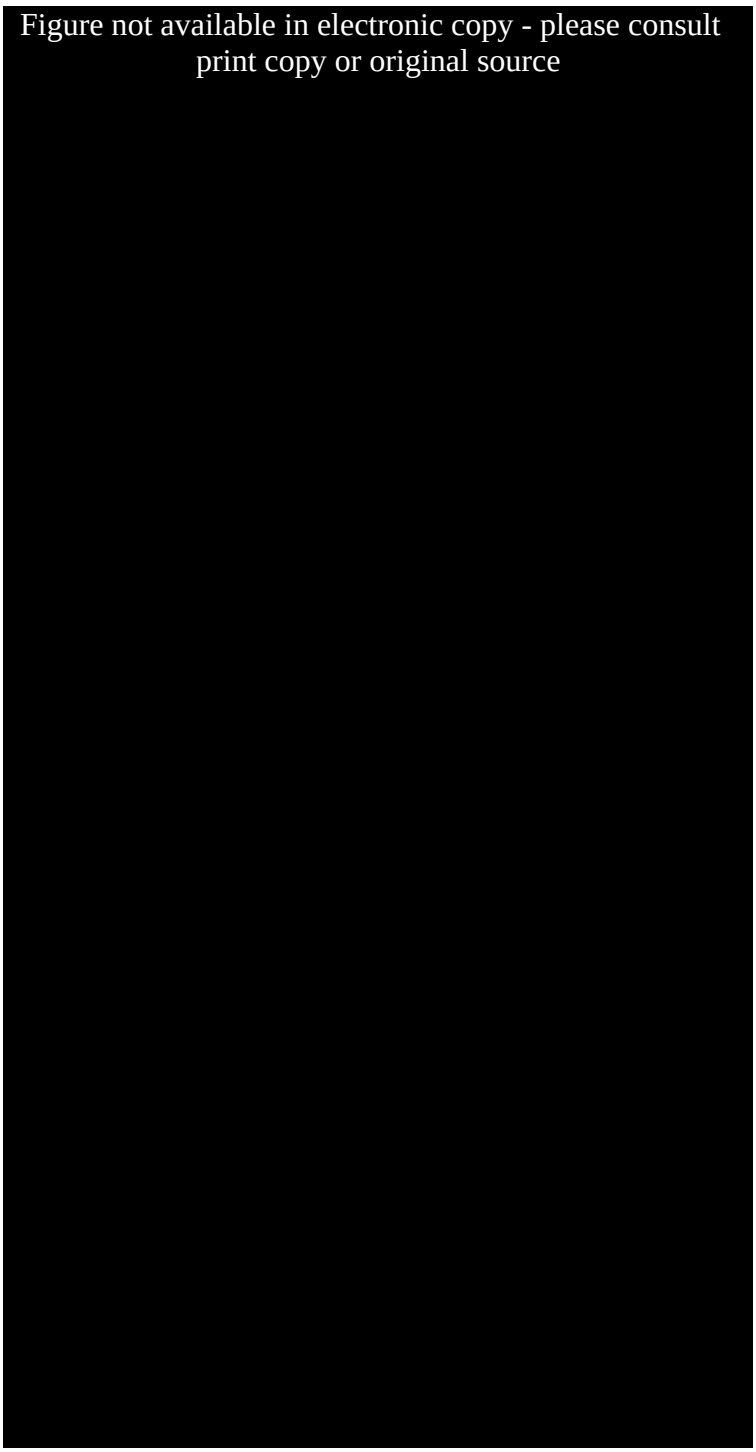


Figure 2.6: Comparison of typical microstructures of (a) in situ and (b) ex situ wires, and (c) an ex situ wire produced from ball milled powder (from Goldacker et al [64], reproduced with permission of IoP Publishing)

the ball milling. For further discussion on the effect of impurity phases on superconducting properties see Section 2.5.4.

Flükiger *et al* [65] ball milled Alfa Aesar MgB_2 powder, measuring the particle sizes using an unspecified granulometric technique (Figure 2.7). Iron-sheathed tapes were produced from this powder and heat-treated for 0.5 h in Ar gas at 950 °C. This tape attained $J_{c,trans} = 7 \times 10^3 \mathrm{A/cm^2}$ at 7 T and 4.2 K; in comparison a tape produced from ball milled powder but not heat-treated attained $J_{c,trans} = 1 \times 10^2 \mathrm{A/cm^2}$ and a tape produced from as-purchased powder which was not heat-treated attained $J_{c,trans} = 2 \times 10^3 \mathrm{A/cm^2}$ under the same conditions. The $J_c - H$ data for the tape made from as-purchased powder without heat-treatment is not given, so it is not possible to separate the effects of ball milling and heat-treatment, so it is unclear which process has the largest effect on the $J_c - B$ behaviour. Additionally the authors did not examine the effect on the superconducting behaviour of impurities from the milling media. XRD carried out on a crushed sample of the tape core detected peaks due to MgB_2 and MgO only [65], but this technique is unlikely to detect low levels of doping which may nonetheless have a significant effect on the behaviour. The milling media are not specified.

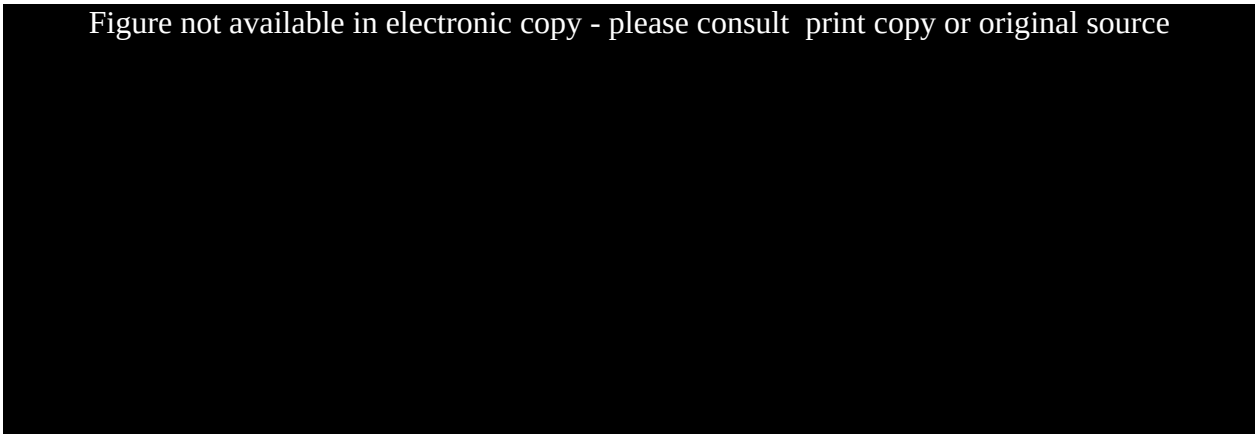


Figure 2.7: Particle size distributions of (a) as-purchased and (b) milled powders from [65]

A later paper from the same group shows the effect of longer milling times [135], comparing tapes made from powders ball milled for 100 h and 3 h, annealed at 920 °C in Ar gas for 0.5 h. At 5 T the 100 h tape has J_c of $3 \times 10^4 \mathrm{A/cm^2}$ while that of the 3 h tape is $2.5 \times 10^4 \mathrm{A/cm^2}$. At 10 T the values are $1 \times 10^3 \mathrm{A/cm^2}$ and $2.5 \times 10^2 \mathrm{A/cm^2}$ respectively.

The temperature at which these measurements were made is not given, so it is not possible to compare them directly to other studies. The difference at high magnetic fields is considerable, but whether this is due to flux pinning by the greater concentration of grain boundaries in the small-grained microstructure, damage to the lattice, or to flux pinning by impurity phases from ball milling is not clear.

Different researchers have reported significantly different rates of reduction in particle size during ball milling. This is likely to vary depending on specific equipment setup, and also on the particle sizing technique employed. For example, Li *et al* [63] ball milled commercial MgB_2 for 60 h and found a reduction in "crystal size" to 2.5 nm, whereas the research done by Lezza *et al* [136] shows that after 100 h similar samples still contain "grains" (*i.e.* particles) over 10 μm in diameter. There is significant confusion in the literature between particle size and grain size. In this thesis, grain size is defined as the size of an individual crystallite within a bulk material, while particle size refers to the individual powder particle dimensions, noting that a particle can be made of several grains. A particle shown to consist of one grain only will be referred to as a crystal.

Lezza *et al* [136] state that they used a granulometric technique to determine particle size distributions in the study cited above, but do not specify the technique. Granulometric techniques cannot distinguish between agglomerates of particles and single particles. They also normally return a single number to describe the size of the particle, the diameter of a sphere with the same volume as the measured particle (*i.e.* the equivalent spherical radius). For non-spherical particles this can be misleading.

Li *et al* used high-resolution TEM observations to determine the crystal size in their ball milled samples [63]. TEM observations are dependent both on whether sufficient particles are observed to obtain an average crystal size and if a suitable sampling protocol is used to select samples from the original ball milled material to ensure the full distribution of particle sizes is represented in the TEM specimen. Reliable chemical analysis is also necessary to make sure that the observed particles are MgB_2 and not an impurity phase. Li *et al* found that for very small MgB_2 crystals of around 2.5 nm, superconductivity is

completely lost, and that the transition temperature is significantly decreased for crystals below 11.8 nm in size. This was ascribed to variation in the Mg-Mg and B-B bond lengths for the smallest crystals.

Gao *et al* [62] ball milled MgB_2 powder obtained from HC Starck (sieve size –100 mesh, *i.e.* particles have a maximum size of 150 μm) for up to 20 h under argon gas using steel milling media. They found that an intermediate compound formed during the ball milling process, indicated by an extra peak in the XRD spectrum, but this compound could not be identified. After 20 h milling however, the XRD spectrum was featureless indicating that the entire mixture had become amorphous. The disappearance of the extra peak indicates that it was not due to contamination by the steel. On annealing in vacuum at 700 °C, crystalline MgB_2 was restored. The formation of this amorphous structure after such a short milling time may be due to use of a particularly highly powered ball mill.

There is extreme variation in the nature of the powders produced by milling processes by different research groups. This causes difficulty with comparing the results, as it seems unlikely that we are comparing like with like. Ball milling studies are better described by the changes in impurity and crystalline material content, and the change in particle size distribution, rather than by comparing the milling time.

An alternative method of varying the particle size is to use sieves of various aperture sizes to separate the powder in various size fractions. This should cause less contamination than ball milling, but the particle size range available is limited to that of the starting powder. Matsumoto *et al* [137] sieved commercial MgB_2 powder into five size fractions. By estimating $J_{c,mag}$ from magnetization data using the Bean critical state model they found that there is no $J_{c,mag}$ dependence on particle size within experimental uncertainty, but because the particle size distribution in each size fraction was considerable there is a large error in the calculated $J_{c,mag}$ as the calculation uses one single value for the particle size (the mean). Sieving can be an inaccurate method of division by particle size, as particles are divided according to their smallest dimensions, and so for non-spherical particles the range of particle sizes in each sieve is large [134]. No verification of the

particle size by a method other than sieving was made in this study.

2.5.3 Pressure

Pressure can be applied to MgB_2 samples either prior to heat-treatment ("cold"), or during heat-treatment ("hot"), either uniaxially or isostatically. Isostatic pressing techniques exert additional pressure on the pellet or wire by applying pressure from all directions, unlike uniaxial pressing where pressure is applied in one direction only. Both methods can be carried out for bulks and for wires and tapes produced from MgB_2. Production of wires involves mechanical deformation which can be considered as another method of applying pressure prior to heat-treatment.

Uniaxial pressing is a quick and simple method of producing green compacts from ceramic powders. Powder is loaded into a die and pressure applied in one direction only. Applying a higher pressure generally increases the density though a large increase in pressure does not result in a proportionally large increase in density [50]. The maximum pressure is limited by the strength of the die itself. There are also limitations on the density of pellets produced by this method due to the ductility of the powder particles and the friction between them [50]. Powder flow can also be limited by the size of the particles. This process is used for a wide number of materials and hence has been carefully studied; for more information the reader is directed to the following standard texts; Ring [138] and Jones [139].

The PIT process was explained in Section 2.4.2. There are a number of additional steps that can be carried out during processing to obtain denser, narrower, or differently shaped filaments. These include two-axial rolling, rotary swaging, and groove rolling, which were compared by Kováč *et al* [119]. They found that two-axial rolling gives the densest microstructure in the core, but also observed a decrease in the pinning force. These techniques can only be used for strong sheath materials, but have the advantage that the core undergoes greater mechanical stresses during processing, leading to greater deformation of the lattice and a reduction in the average grain size, improving inter-grain

connectivity [119].

Round, square and rectangular wires and flat tapes have been produced in a number of sheath materials. "Tapes" are thin flat ribbon-like artefacts, while "wires" have a similar thickness to their width. In order to make these artefacts, special processing techniques must be used. Greater densification due to a greater degree of deformation is likely to produce a finer microstructure. However, "flat" shapes can have anisotropic critical current density at high applied magnetic fields, which limits their applications. Preferential orientation of the MgB_2 grains (texture) can occur only for rolled artefacts such as tapes, and may give higher J_c values depending on the orientation of the tape to the magnetic field, as it does in other superconductors [140]. A slight preferential texture in the [001] direction has been observed by XRD in the core of iron-sheathed tapes by Lezza *et al* [135].

Kováč *et al* compared the performance of 10 wt.% tungsten-doped iron–sheathed four-filament multifilamentary wires with square, circular and rectangular cross-sections [141]. The original wire formed was rectangular; a section was then deformed to a square wire using two-axial rolling, and similarly circular and rectangular cross-sections were obtained by drawing and two-axial rolling respectively. Measured at 4.2 K, the square wire had the best performance, achieving the highest $J_{c,trans}$ over the entire applied magnetic field range, while the round wire had the poorest $J_c - H$ relationship. The explanation for the difference in performance is that the processes to form each shape of wire involve differing degrees of deformation. Particularly, unlike two-axial rolling, the drawing process to produce round wires exerts axial tension on the wires, increasing the chance of transverse cracking. Two-axial rolling may produce denser material in the core, leading to an improved microstructure. Microhardness measurements (indicative of the density of the material [119; 142]) were made and compared to the measured $J_{c,trans}$. The square wire had an average microhardness of 410 HV/0.03 and $J_{c,trans}(4.2\,\mathrm{K},\, 3\,\mathrm{T}) = 6 \times 10^4\,\mathrm{A/cm^2}$ while the round wire had average microhardness of 310 HV/0.03 and $J_{c,trans}(4.2\,\mathrm{K},\, 3\,\mathrm{T}) = 1 \times 10^4\,\mathrm{A/cm^2}$. However this study does not de-

termine whether the difference in $J_{c,trans}$ is solely due to the density difference indicated by the hardness, as other factors such as the size of the wires also varied. The two-axially rolled wire had the highest hardness (680 HV/0.03) and $J_{c,trans}$ between that of the rectangular and circular wires ($J_{c,trans}(4.2\,\mathrm{K},\,3\,\mathrm{T}) = 4 \times 10^4\,\mathrm{A/cm^2}$). Microstructural observations using electron microscopy would help ascertain the differences in the grain shape, size and connectivity between the variously shaped samples, and to correlate these with the performance.

Cold isostatic pressing (CIP) at 0.7 GPa and 1.5 GPa in argon for 10 min has been carried out on two short pieces of MgB_2 square wire prepared by two-axial rolling [143]. No subsequent heat-treatment was carried out. The CIP improves inter-grain connectivity as shown by an improved $I-V$ characteristic from $I = 15\,\mathrm{A}$ (average of several tapes with no CIP) to $I = 24\,\mathrm{A}$ (CIP at 0.7 GPa) and $I = 25.5\,\mathrm{A}$ (CIP at 1.5 GPa) using a voltage criterion of $1\,\mu\mathrm{V}$ at 4.2 K and 0 T. $J_{c,trans}$ for these wires were calculated from the $I-V$ characteristic to be $7.1 \times 10^3\,\mathrm{A/cm^2}$, $1 \times 10^4\,\mathrm{A/cm^2}$ and $1.1 \times 10^4\,\mathrm{A/cm^2}$ respectively. SEM images revealed several cracks and voids in the microstructure caused by the CIP process. The authors suggest that CIP in a non-Cu sheath would be useful in preventing stress relaxation following removal of pressure, which leads to formation of these cracks and voids [143]. CIP has not been widely studied or exploited, despite the advantages in improving superconducting properties without heat-treatment.

Hot pressing involves simultaneous application of uniaxial pressure and heat to produce dense samples. Bulk *ex situ* MgB_2 has been produced using this method by Hsieh *et al* [15], Tampieri *et al* [144] and Kumakura *et al* [60]. Spark plasma sintering has also been used [100; 145; 146]; this has the potential to act as a very similar technique to hot pressing as the experimental set-up is similar, though heating originates from current passed through the die and sample rather than the die being surrounded by an induction coil, which leads only to heating of the die. In conductive powders the current also passes through the powder [147]. Whether MgB_2 has sufficiently high room-temperature electrical conductivity to allow this is not discussed in the studies carried out to date. If

so the connectivity would be expected to increase and the effects of local sparks would be visible in SEM images of the post-heat-treatment artefacts. Otherwise SPS can be expected to have a similar effect to hot pressing. *Ex situ* MgB_2 wires have not yet been produced by spark plasma sintering, though *in situ* PIT wires produced by Suo *et al* [148] using SPS have J_c of almost two orders of magnitude higher than a conventionally heat-treated wire of the same type in low magnetic fields, indicating that the SPS process is very effective in improving the superconducting properties.

Hot isostatic pressing (HIPing) combines the isostatic pressing of CIP with simultaneous heat-treatment. This gives highly dense MgB_2 bulks, in some cases reaching the theoretical maximum density calculated from lattice parameters ($2.63\,g/cm^3$). The densest pellets have been obtained using high pressures of around 3 GPa and temperatures of 775 °C to 1000 °C [60; 149–153]. These pellets can be used for a number of studies including determination of the Vickers hardness [149], specific heat measurements [154], and calculation of "phase" diagrams relating applied magnetic field, critical current density and temperature [150]. It is also easier to measure transport properties using dense samples [152]. HIPed pellets have also been found to be more stable to degradation in ambient environment due to their dense microstructure, and maintain a sharp superconducting transition even after several months in air [155].

The high densities and well-connected microstructures obtained in these MgB_2 pellet studies means that HIPing is a very attractive process for improving the quality of MgB_2 wires. Liao *et al* [156] prepared HIPed wires in stainless steel sheaths at 900 °C with a pressure of 200 MPa. Lower porosity was observed by TEM in hot-pressed samples compared with conventionally heat-treated wires. However, some porous areas are still visible in TEM micrographs of these samples. J_c values in HIPed wires are high due to improvement of flux pinning (due to a high concentration of subgrain boundaries in the crystallites) and lower porosity, $J_c > 10^6\,A/cm^2$ at 5 K and 0 T, and achieving $J_c > 10^5\,A/cm^2$ up to 3 T at 5 K [157].

A comparison of the microstructure of the densest MgB_2 bulk samples produced by

hot pressing and spark plasma sintering and a wire produced by hot isostatic pressing is shown in Figures 2.8, 2.9 and 2.10 with images taken from [144; 146; 156]. The grain size (length) is $1-2\,\mu$m for hot pressed sample [144], for spark plasma sintered sample around $1\,\mu$m [146] and for the HIPed wire sample around $0.2-0.5\,\mu$m [156]. No micrographs of *ex situ* HIPed bulk MgB_2 could be found in the literature.

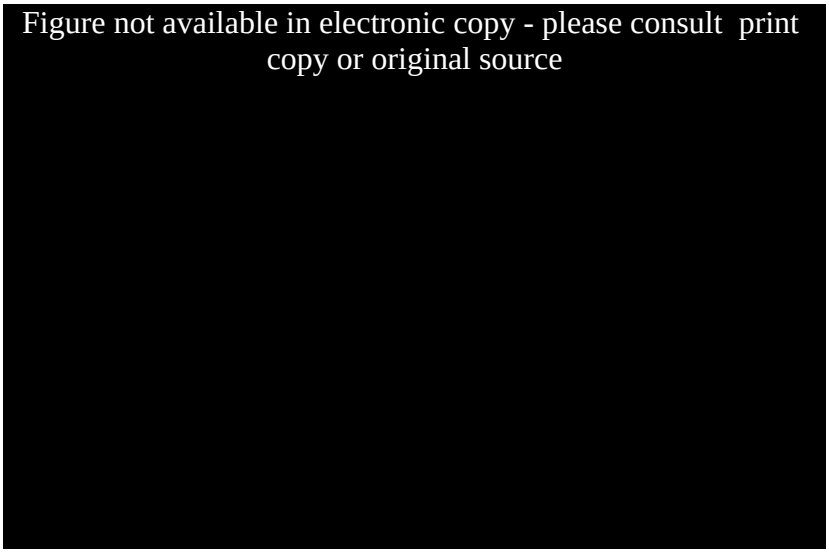


Figure 2.8: SEM micrograph of the fracture surface of ex situ MgB_2 bulk hot pressed at 1190 °C and 30 MPa under vacuum (taken from Tampieri et al [158])

2.5.4 Impurity Phases

There are three main reasons why impurity phases are desirable for MgB_2 artefacts: doping (replacement of Mg and B ions with other elements) of the MgB_2 lattice, improvement of microstructure, and increasing flux pinning. All of these may improve the superconducting properties. Doping of the MgB_2 lattice leads to changes in the electronic structure of the material, introducing extra allowed-energy levels in the energy gap, and decreasing the electron mean free path. This increases the normal state resistivity and hence increases both H_{irr} and H_{c2} [159; 160]. Improving the microstructure, in particular increasing the density of the material, leads to increased connectivity between grains and hence to a narrower ΔT transition and a larger superconducting cross-sectional area. Increasing the flux pinning results in artefacts with higher J_c in high magnetic fields.

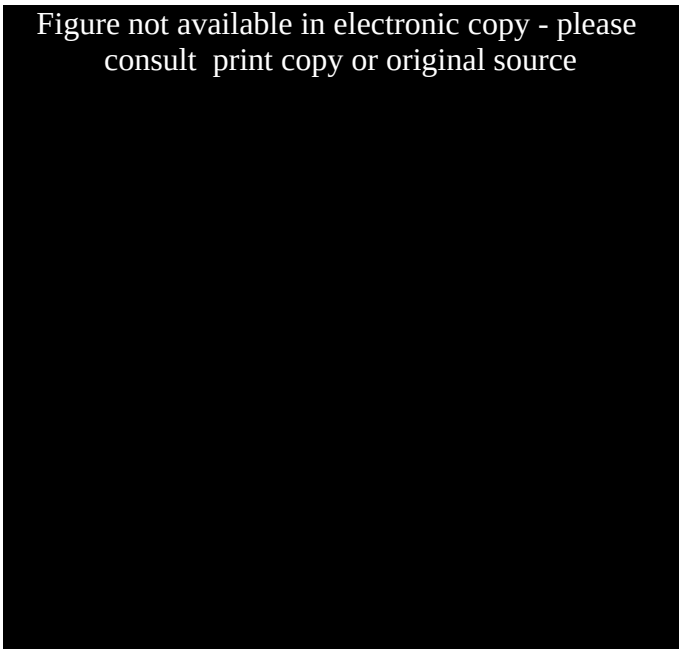


Figure 2.9: SEM micrograph of the fracture surface of ex situ MgB_2 bulk spark plasma sintered at 1050 °C and 50 MPa in Ar (taken from Shim et al [146]). The authors state that the arrows in this image indicate impurity particles.

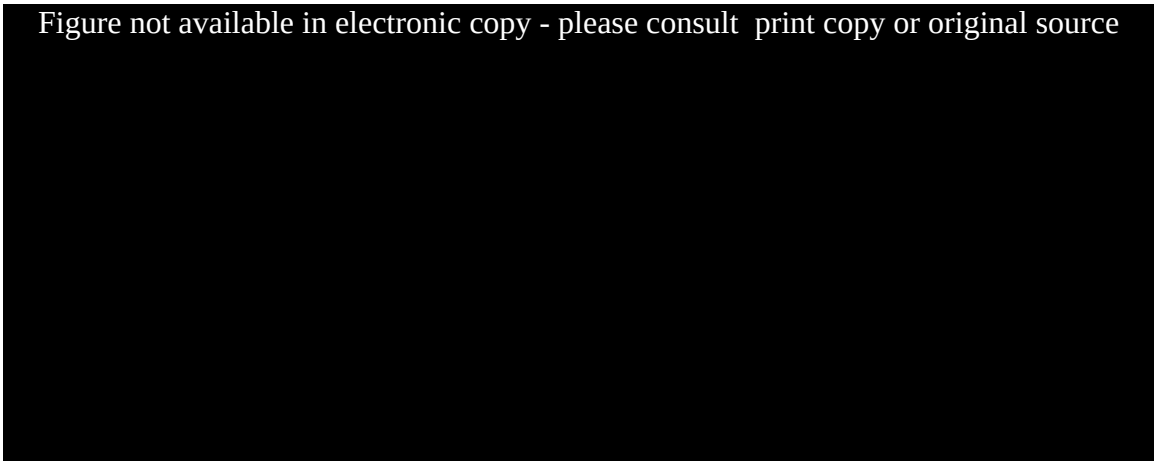


Figure 2.10: TEM micrograph of a HIPed ex situ PIT wire produced by HIPing at 900 °C and 200 MPa (taken from Liao et al [156], reproduced with permission of IoP Publishing)
a) Dense region, grain size $\sim 0.2\ \mu m$
b) Porous region, grain size $\sim 0.5\ \mu m$

Impurity phases are often deliberately added to the precursor powders in both *in situ* and *ex situ* processing. In addition, impurity phases often form during heat-treatment of MgB_2 due to the volatility and reactivity of magnesium at high temperatures; ideally these will also enhance the superconductivity. This means that the concentrations must be low; high levels of non-superconducting phases reduce the current-carrying volume of the sample and reduce the J_c values. Powders can be added by simple hand mixing, or by ball milling with MgB_2 or other MgB_2-forming powders, using a short milling process of around 1 h. Zirconium diboride [161; 162], niobium diboride [162], titanium diboride [162], carbon [162], silicon carbide [161; 162], zirconium oxide [99], and zinc [163] are among the impurity phases that have been introduced in this way. Carbon has also been mechanically alloyed with MgB_2 by a 10 h ball milling process [164]. The particle size of the added impurity phases is not always stated, however Mikheenko *et al* have shown that nanoscale additions are most effective at reducing grain size, and hence enhancing critical current density and flux pinning [165].

2.5.4.1 Impurity Phases Which Form During Heat-Treatment

The magnesium-boron phase diagram has been recently updated by Balducci *et al* [58] (Figure 2.11) to include more data on the stability of the various higher borides, so this diagram is included here in preference to the older diagram published in the standard compendium of phase diagrams edited by Massalski [166]. This diagram estimates the decomposition temperature of MgB_2 to $Mg_{(g)}$ and MgB_4 as 1888 ± 124 K at a magnesium partial-pressure of 1 bar.



Figure 2.11: Equillibrium phase diagram calculated by Balducci et al [58] using Thermo-Calc software and experimental data. Reproduced with permission.

Decomposition of MgB_2 by evaporation of magnesium has been observed during heat-treatment above 560 °C [167], indicating that the partial pressure of magnesium vapour is significantly lower than 1 bar, as indicated by the pressure-temperature phase diagram developed by Brutti *et al* [168]. Evaporation of magnesium occurs during heat-treatment at temperatures as low as 425 °C in an *in situ* MgB_2 powder mixture [169]. This leads to the formation of impurity phases including MgO, MgB_4, and sometimes higher borides [170], and encourages the formation of a reaction layer at the sheath-core interfaces, as discussed in Section 2.5.1. The exact impurities which form depend on the processing environment (vacuum, inert gas, or air) and the magnesium vapour partial pressure. The formation of MgO is difficult to avoid, so it is a crucial consideration in planning an optimised processing technique. Ideally the amount of MgO which forms is controlled

and kept at a level where it can improve or at least not worsen the superconducting properties of the MgB_2 artefact.

Serquis *et al* [116] found that adding 5 wt.% magnesium powder to commercial MgB_2 powder provides magnesium to replace vaporization losses during heat-treatment, improving the microstructure. For *in situ* samples, they have shown that the Mg deficiency introduces significant strain (measured by X-ray diffraction) into the lattice, and that any lattice strain remaining after heat-treatment lowers the critical temperature of the material [171]. By contrast, Lezza *et al* [136] carried out a similar procedure for *ex situ* Fe-sheathed tapes, and compared a tape made with powder ball milled for 100 h with no additions and a tape made with powder ball milled for 100 h with 5 %[†] Mg addition (both annealed at 920 °C in Ar gas for 0.5 h), finding no variation in $J_c - B$ behaviour. The reason for this is unclear, but it is possible that impurities introduced during ball milling (*e.g.* from the milling media) react with the additional Mg hence removing it from the system. For such a long milling time, it is also possible that the Mg may have reacted in a mechanical alloying process to form MgB_4.

Kováč *et al* [67] have investigated the effect of different concentrations of MgO by producing identical Fe/Cu composite PIT wires from two different batches of Alfa Aesar MgB_2 powder; one powder contained around 5 wt.% MgO and the other around 1 wt.% MgO. Both samples contained metallic Mg impurities, and the sample with less MgO contained some MgB_4. The wire sample produced from the batch containing more MgO had a lower T_c by ~ 1 K both before and after heat-treatment. Critical current measurements showed a similar trend, with a higher I_c measured for the sample with a lower level of MgO. However, the pinning force was higher for the sample with higher oxide content, probably due to the distribution of fine MgO particles. This indicates that high MgO content may be especially useful to improve the performance of the MgB_2 wires in high magnetic field, where the pinning force becomes important.

The distribution of MgO in the MgB_2 powder also contributes to the J_c performance

[†]Whether this is at.%, wt.% or mol.% is not stated by the authors

of wires. Fujii *et al* [172] used TEM to examine two commercial powders produced by different (unidentified) companies. One contained MgB_2 grains covered with thick layers of MgO. In the other powder these layers were thinner and only partially covered the MgB_2 particles. The Cu-sheathed wire produced from the MgB_2 powder with thick layers of MgO had no J_c at 4.2 K, while the powder with thinner layers of MgO on the MgB_2 grains achieved a J_c value of $1 \times 10^4 A/cm^2$ in the same conditions. This difference is attributed to the weak link effect, whereby impurity phases between grains of the superconducting phase block current flow. For *in situ* PIT wires, Jiang *et al* [173] found that adding 1.25 wt.% MgO (particle size $\simeq$ 10 nm) improves the critical current density at 10 T, 4.2 K to $3.6 \times 10^3 A/cm^2$, compared to $2.3 \times 10^3 A/cm^{-2}$ for a similar non-doped sample. The authors attribute this improvement to flux pinning by the nanoscale particles of MgO. These studies indicate that the formation of MgO is not necessarily deleterious to the superconducting properties of MgB_2 wires.

2.5.4.2 Doping of the Magnesium Diboride Crystal Lattice

To date only a handful of elements have been shown to actually dope MgB_2 (*i.e.* substitute for Mg or B in the crystal lattice) and improve superconducting properties, rather than merely forming impurity phases or acting as pinning centres. Doped elements replace either Mg or B atoms, and there are three kinds of doping; *electron doping*, where the valency of the doped atom is more positive than that of the Mg or B; *isovalent doping*, where the valency is the same; and *hole doping*, where the valency is less positive than that of the original atom. Aluminium (electron doping on Mg site) has been shown to improve the critical current density in MgB_2 [174] and carbon (electron doping on B site) has been shown to improve H_{c2} [175] and $J_{c,mag}$ [93] for MgB_2. Measuring the change in lattice parameters indicates that manganese (isovalent doping) [176], lithium (hole doping) [177], beryllium [178] and copper (electron doping) [158] can also substitute onto the Mg site, but these materials have yet to show an improvement in superconducting properties.

Typical doping levels are a few at.% as there is a limit to the solid-solubility of elements

in the MgB_2 lattice, and high doping levels often lead to significant depression of T_c [179]. In many doping studies, the composition is examined using $\theta - 2\theta$ XRD measurements, which are not able to detect the very low levels of added impurities used. Substitution for Mg or B is detected by shifts in the MgB_2 peak positions due to changes in the lattice parameters because the substituent atoms are of a different size to those they replace. In some cases the impurity may have been incorporated into the lattice but still not be visible in the peak positions in the $\theta - 2\theta$ XRD spectrum. This is particularly likely if the lattice parameters have not changed outside experimental errors. True doping can also be distinguished from flux pinning enhancement by examining the pinning force [174].

All the substitutions carried out so far have led to a decrease or no change in T_c [160; 174], but improvements in J_c and H_{c2} have been observed. Doping of MgB_2 by 1 at.% Al increases $J_{c,mag}$ of uniaxially-pressed *in situ* pellets by a factor of 20 at 5 T, 5 K [174]. An increase in H_{c2} (extrapolated to 0 K) from 18 T to 21 T has been observed for 5 at.% Al-doped MgB_2 [159]; however this resulted in a decrease of T_c to around 30 K. Doping of MgB_2 by 10 wt.% C in the form of nanoparticles of diamond increases J_c across the magnetic field range 2 T to 6 T by up to an order of magnitude at 20 K [180].

2.5.4.3 Improvement of Microstructure by Addition of Impurity Phases

A second reason to add impurity phases to MgB_2 is to improve the connectivity of the grains. These phases are often described as "sintering aids". Matsumoto *et al* [181] found that the addition of 2.5 at.% SiO_2 produces a denser MgB_2 microstructure with well-connected grains and improved J_c, while flux pinning properties were not changed. Silver has also been suggested as a possible sintering aid, which Kumar *et al* claim prevents Mg loss during sintering by forming temporary intermediate Mg-Ag compounds during heat-treatment, which partially break down again during cooling to room temperature [182]. No direct evidence is presented for this mechanism, though peaks attributed to $AgMg_3$ were observed in a XRD spectrum recorded post-heat-treatment. Added compounds may also preferentially react with impurities such as oxygen, water, or the sheath

material, thus preserving a greater proportion of the superconducting phase [141]. This occurs with titanium-doped MgB_2 when exposed to water and air [183–186]. Titanium forms very thin TiB_2 layers around each grain, observed using TEM by Cheng *et al* [184], which are thought to protect the MgB_2 from reaction by enhancing the chemical stability of grain boundaries [183]. When exposed to water, Ti-doped samples showed a lower degradation in $J_{c,mag}$, compared to undoped samples, although T_c remained unchanged at 38 K for all samples both before and after exposure to water for 124 h [183]. However, in other work exposure of MgB_2 pellets to water for 72 h has been found to completely destroy superconductivity [68], although during the course of this study the pellets broke up into loose powders. The density of the samples, and hence the surface area, is critical in controlling the severity of the reaction with water. Titanium may cause greater densification of the pellet samples used for these studies, preventing water from reaching the MgB_2 inside the pellet. Haigh *et al* [187] have shown that titanium hydride forms in HIPed MgB_2 bulks produced with titanium additions, as Ti preferentially reacts with deleterious impurities such as hydrogen (in this case the source of the hydrogen is probably associated with the HIPing process). This supports the conjecture of Kováč *et al* that all reactive metals improve critical current density values in MgB_2 artefacts by a similar protective mechanism [188].

When impurity particles are fine and gather at grain boundaries they also prevent grain growth by the Zener Effect. The maximum grain size is inversely proportional to the volume fraction of impurity particles, and directly proportional to the size of the impurity particles [189]. Hence a large volume fraction of small particles, randomly distributed through the bulk of the material, will help stabilise a fine-grained microstructure.

2.5.4.4 Improved Flux Pinning by Finely Dispersed Impurity Phases

The improvement of J_c in MgB_2 by introducing disorder using proton irradiation was first proposed by Bugoslavsky *et al* [190]. Since proton irradiation is impractical for commercial applications, research attention has focused on the use of impurity phases to

introduce disorder. Finely distributed impurity phases act as flux pinning centres in the same way as other features such as grain boundaries and dislocations. This gives better performance at high magnetic fields. Many impurity phases have been added to MgB_2 since it was shown to superconduct in 2001, and most of these have some effect on the superconducting properties.

The addition of nanoscale silicon carbide particles has been shown to give significant improvements in superconducting performance whilst minimising the decrease in T_c [179]. The wires with highest J_c values in magnetic fields at 20 K so far produced contain 10 wt.% SiC. The J_c increased over that of the undoped sample by factors of 32 at 5 K, 8 T and of 42 at 20 K and 5 T, and these wires have $J_c > 10^5$ A/cm^2 for magnetic fields up to 6 T at 4.2 K [179; 191; 192]. This is within the performance criteria for fault current limiters, larger motors, and generators, and at the lower end for superconducting magnetic energy storage (SMES) devices [193]. High H_{c2} values have also been reported, with $H_{c2} = 37$ T for a SiC doped bulk MgB_2 sample [179].

Addition of 10 wt.% nanoscale yttria (Y_2O_3) particles has been shown to improve J_c by a factor of 3 for *in situ* MgB_2 pellets, whilst retaining T_c of 39 K [194]. Doping of *in situ* pellets by 10 wt.% Si leads to formation of Mg_2Si, which acts as a pinning centre, improving J_c by one order of magnitude at 8 T and 5 K [195]. Other phases reported to lead to improvement in J_c or H_{irr} are ZrB_2 [162], NbB_2 [162; 196], TiB_2 [162], lanthanum [197], nanoparticles of diamond [180], carbon powder (at high doping levels carbon forms Mg_2C_3 and MgB_2C_2 which act as pinning centres) [198], vanadium [199], and zirconium, titanium, and hafnium [200]. Many other studies have been carried out which find that doping does not affect the lattice parameters or the transition temperature, without examining the critical current and magnetic field behaviour. This is useful in ascertaining which elements dope the MgB_2 crystal lattice, but does not reveal whether flux pinning is enhanced with these additions.

2.6 Conclusions and Aims of This Work

Magnesium diboride has attracted a great deal of interest from the superconducting research community since the discovery of superconductivity in MgB_2 in 2001. Many promising processing routes have been established and a great deal of empirical evidence amassed in particular regarding the effect of impurity phases on superconductivity.

However there are difficulties in this field assessing the relative merits of different processing routes and additives. Comparisons between the results of different research groups are often impossible because there are a large number of variables in the processing methods used. It would be useful for the community as a whole to understand the conditions which lead to the formation of dense MgB_2 material with good superconducting properties. In addition, greater understanding of the materials properties is necessary in order to establish industrial processing routes which produce artefacts with improved superconducting properties comparable to those produced on a small scale in the laboratory.

This work focuses on the sintering behaviour of magnesium diboride, with the goal of establishing the conditions under which dense MgB_2 material can be produced. As there is a considerable density change involved in the reaction to form the superconducting phase using the *in situ* processing route (see Section 2.3.2), this work exclusively examines *ex situ* MgB_2 processing. By taking a traditional ceramics approach to this superconducting material, the microstructural properties can be correlated with superconducting properties to establish the key parameters to obtain high quality MgB_2 artefacts.

3 Experimental Methodology

The experimental procedures used in this work are described below. The techniques carried out by the author fall under the following categories:

- Fabrication of Powders
- Characterization of Powders
- Fabrication of Bulk Samples
- Characterization of Bulk Samples

This work was carried out at the University of Oxford, University of Birmingham, and at Queen Mary, University of London.

3.1 Fabrication: Powders

It is well known that careful selection of the particle size distribution of powders used to produce ceramic artefacts can radically affect the sintering behaviour of the material during heat treatment and therefore the final density [50]. For this reason, in addition to using as-supplied MgB_2 powder (Alfa Aesar, 98 % purity, -325 mesh) to produce MgB_2 bulks and wires, I also used modified powders produced by milling (ball milling and attrition milling) and separating (sedimentation and sieving) the commercial powder. The resulting powders have different particle size distributions and impurity content depending on their processing history. The techniques used to determine these properties are described in Sections 3.4, 3.5 and 3.6.

3.1.1 Sieving

Sieving rapidly fractionates large volumes of powder into broad size categories. Standard wire sieves have square apertures. During sieving the powder can be manipulated mechanically by brushing or vibration, or dispersed by a liquid, ensuring that all particles with breadth and thickness less than the diameter of the aperture pass through the sieve (Figure 3.1). The particle length is excluded from the analysis *unless* the particles are elongated to the extent where it is impossible that they can be shaken to a position where they lie at the correct orientation with respect to the sieve opening [134].

Alfa Aesar MgB_2 powder was sieved by David Hyslop during his Part II project [201] and these powders were then used by the author to make bulk samples. Sieving was performed manually using a brush to aid the dispersion of the powder until no more powder would pass through the sieve. MgB_2 powder in the following size fractions was produced (where d_{sieve} is the sieving diameter, taken as the larger of the breadth or width of the particle as indicated in Figure 3.1):

- $d_{sieve} > 106\,\mu m$
- $80\,\mu m < d_{sieve} < 106\,\mu m$
- $50\,\mu m < d_{sieve} < 80\,\mu m$
- $d_{sieve} < 50\,\mu m$

Because the physical basis of separation during sieving is the sieve diameter, it is difficult to compare particle size measurements from the sieving process with the results from other particle sizing techniques based on the equivalent spherical diameter. Conversion between these requires an independent measurement of the length of the particles in order to establish the volume of the sieved particle (see Figure 3.1). For this reason, the particle size distributions of sieved powders were measured using laser diffraction (see Section 3.4.1.2) in order to make a meaningful comparison between these powders and the other powders produced by separation and milling.

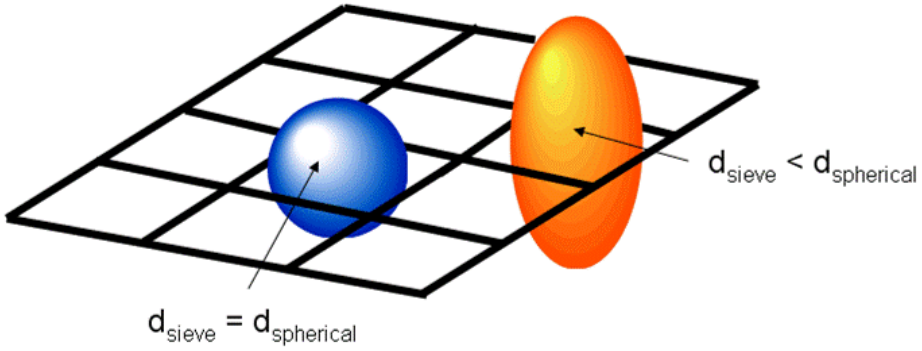


Figure 3.1: Illustration of the geometrical constraints on particles passing through a square-aperture sieve. The particles shown have the same sieve diameter, but their different volumes result in differences in their spherical equivalent diameters

3.1.2 Sedimentation

Sedimentation involves separation of particles on the basis of their size. In an appropriately sized vessel*, the drag force F_d on a particle of diameter d_{St} falling at terminal velocity v in a medium of dynamic viscosity η is given by Stokes's Law [203] (Equation 4.2).

$$F_d = 3\pi d_{St} v \eta \tag{3.1}$$

This drag force is balanced by the weight of the particle and the upthrust from the displaced liquid (according to Archimedes' Principle) (see Figure 3.2). From this an expression for the velocity at which the particle falls can be obtained (Equation 3.2).

*The diameter of the vessel should be greater than $100 \times d_{max}$ in order for the size of the vessel to have no effect on the sedimentation rate [202].

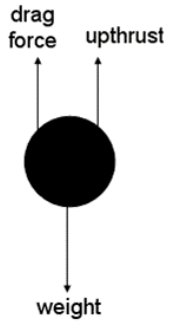


Figure 3.2: Forces on a particle falling at its terminal velocity in a medium of viscosity η and density ρ_{liquid}

$$
\begin{aligned}
F_d + m_{liquid}g &= m_{solid}g \\
(m_{solid} - m_{liquid})g &= 3\pi d_{St} v \eta \\
\rho_{solid} V g - \rho_{liquid} V g &= 3\pi d_{St} v \eta \\
(\rho_{solid} - \rho_{liquid}) \cdot \frac{4}{3}\pi \left(\frac{d_{St}}{2}\right)^3 g &= 6\pi \frac{d_{St}}{2} v \eta \\
v &= \frac{d_{St}^2}{18} \frac{(\rho_{solid} - \rho_{liquid})}{\eta} g
\end{aligned} \tag{3.2}
$$

To separate the particles by size, particles larger than the required size are allowed to fall to the bottom of the container. When the upper layer of liquid is removed, it will contain only particles smaller than the required diameter d_{max}. The time, t, required for the particle to fall a given height, h, can be obtained by solving Equation 3.3.

$$
v = \frac{h}{t} = \frac{d_{max}^2 \cdot (\rho_{solid} - \rho_{liquid}) \cdot g}{18 \cdot \eta} \tag{3.3}
$$

Sedimentation in this work was carried out using a modified version of Pryor's method [204] adjusted for small volumes. The procedure was as follows; 75 ml of isopropanol was added to 5 g of MgB_2 powder in an 100 ml beaker such that the level of the liquid was 50 mm above the base of the beaker. The mixture was vigorously stirred using a spatula then allowed to settle for the time determined by Stokes's Law (see Table 3.1). For the final 15 s of settling the beaker was tapped gently using a plastic stirring rod in order to compact the layer of large particles in the bottom of the beaker. Once the required time had elapsed, the upper layer containing the finer fraction of particles was poured into a

second beaker. Fresh isopropanol was then added to the heavy fraction, the mixture was stirred again, and the method repeated. This process was repeated five times to ensure that the minimum number of small particles remained in the heavy fraction. Because of concerns that agglomeration might be caused by the drying procedure, each fraction obtained was split into three parts and treated as follows: One part was retained as a slurry; one part was dried in a beaker at room temperature; and one part was dried at 75 °C using a hot plate. For fine fractions, multiple samples were combined to produce sufficient powder to form bulk material.

Table 3.1: Settling time required for different particle size fractions in isopropanol calculated from Stokes's Law

Particle Size Fraction (μm)	Settling Time (s)
$d_{St} > 100$	2.5
$d_{St} > 10$	252
$d_{St} > 1$	25205 ($\sim$7 h)

The choice of dispersant liquid for sedimentation is critical. A dispersant liquid needs to be readily available, to act as a dispersant and deflocculant (and most importantly to not cause coagulation and flocculation during sedimentation), and to have an appropriate density and viscosity such that the times for sedimentation are not so short or so long as to be impractical. For drying, the dispersing liquid must evaporate at low temperatures with minimal residue; however too rapid evaporation at room temperature would be inappropriate because of the length of some of the experiments aimed at extracting very fine powders. Selected properties of the liquids considered for this role in this study are given in Table 3.2. Water cannot be used as it reacts vigorously with MgB_2 powder at room temperature, producing $Mg(OH)_2$, $MgCO_3$ and B_2O_3 [68].

Visual inspection of dispersions of MgB_2 in various liquids revealed that some solvents have a radical and rapid flocculation effect, inconsistent with their expected Stokes's Law behaviour. To quantify this observation, sedimentation was carried out using a range of liquids to produce two fractions of $d_{St} > 10\,\mu$m and $d_{St} < 10\,\mu$m. Liquids which caused significant flocculation would be expected to return more coarse material than

Table 3.2: Properties of liquids considered as dispersants for MgB_2 for sedimentation taken from the "CRC Handbook of Chemistry and Physics" [59]

Liquid	Density g/cm^3	Dynamic Viscosity at 25 °C Pa · s	Boiling Point °C
Butan-2-ol	0.8070	0.003096	99.5
Propan-2-ol	0.7855	0.002038	82.2
Cyclohexane	0.7785	0.000894	80.7
Ethanol	0.7893	0.001074	78.5
Ethylene Glycol	1.1088	0.016100	198.0
Methanol	0.7914	0.000544	64.6
Acetone	0.7899	0.003400	56.1

liquids which allow dispersion, even after allowing for slight variations between samples. As shown in Figure 3.3, acetone and cyclohexane appear particularly unsuitable for dispersion. Ethylene glycol was not utilised because it is extremely viscous which would make obtaining small particles very time-consuming. The alcohols (methanol, ethanol, isopropanol and butan-2-ol) have the best combination of properties. Of these isopropanol was chosen on the basis of its ready availability and moderate evaporation rate at room temperature.

3.1.3 Ball milling

Ball mills range in scale from plastic bottles with diameters of a few centimetres to industrial mills with diameters of several metres. The milling set-up used has a radical effect on the efficiency of milling and therefore the rate of reduction of particle size. All ball mills basically consist of a cylindrical or conical bottle or jar approximately half-filled with milling media (in a range of materials, shapes and sizes) and the powder to be milled. The container is rotated horizontally and the powder particles are broken down by grinding caused by the milling media impacting the particle surfaces [50]. The rate of particle size reduction is dependent on the size of the mill, the speed of rotation, the initial particle size (small particles are harder to break up due to agglomeration), and the size and hardness of the milling media. Where milling is carried out in a liquid, the rate is also dependent on the viscosity of the resulting slurry of dispersant and powder

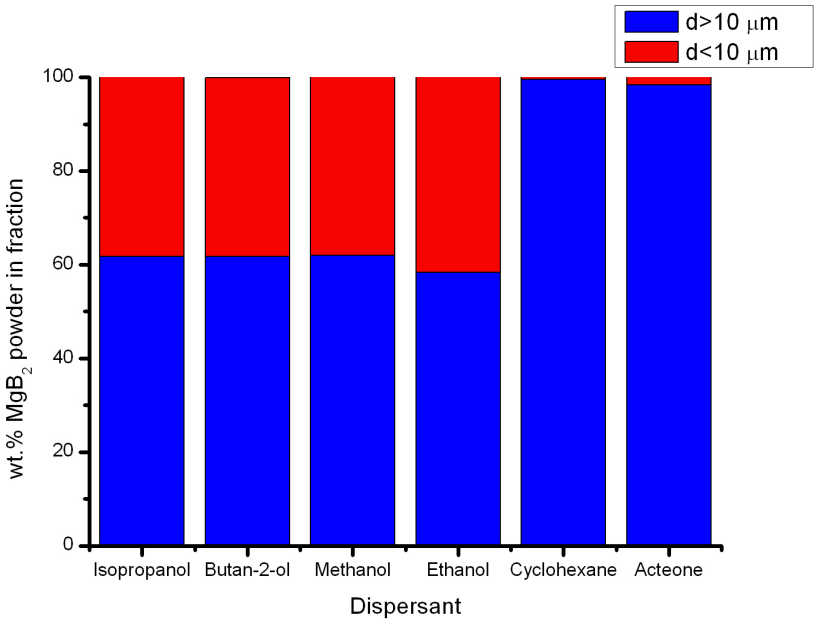


Figure 3.3: Yield of different size fractions from sedimentation in various liquids using the same powder

and the degree of agglomeration of the powder in the liquid. Milling in a liquid decreases the rate of introduction of lattice defects being introduced into crystalline samples, and using a deflocculating liquid can decrease the rate of formation of agglomerates as milling progresses [50]. The overall motion of media during the ball milling process is shown in Figure 3.4.

In this project, ball milling was carried out using isopropanol as a dispersant. The optimum solid loading is at the concentration where every ball-on-ball collision traps a particle and leads to effective average particle size reduction. In a low solid concentration slurry, energy is wasted by ball-on-ball collisions which do not break up the powder particles; in a slurry with high solid loading the viscosity is increased significantly, and therefore the flow rate decreases. The optimum solid loading was determined by viscosity measurements of MgB_2/isopropanol slurries of various concentrations using a Gallenkamp Torsion Viscometer (VHA-200-M, cylinder size 3) (Figure 3.5). The optimum solid loading is the concentration at which the viscosity rises above the plateau level for low solid loading, this being where the two factors described above are balanced. The viscosity of

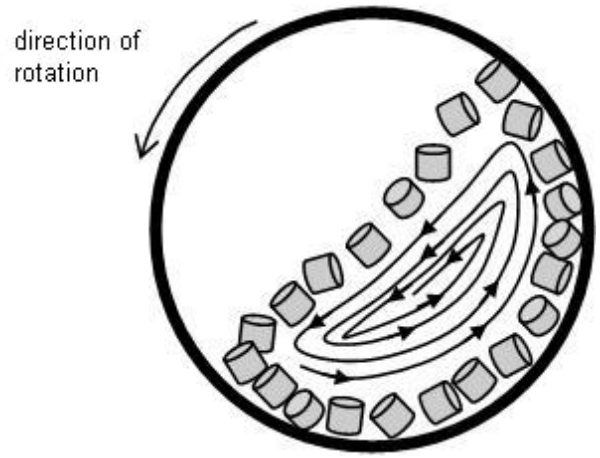


Figure 3.4: Schematic diagram indicating the motion of milling media during ball milling (after [50])

the slurry increases as particle size decreases, and as significant particle size decrease was anticipated for some milling processes, 35 vol.% was chosen as an appropriate concentration to maximise the solid loading while reducing the likelihood that the viscosity would dramatically increase during milling.

Ball milling was carried out as follows: A low-density polyethylene ball milling bottle (Nalgene Inc., 250 ml) was loaded with yttria-stabilised zirconia (YSZ) grinding media (Inframat Advanced Materials; cylindrical - 10 mm diameter, 10 mm height) such that 50 vol.% of the container was filled. A slurry of 35 vol.% MgB_2 powder in isopropanol was then added until the slurry just covered the ball milling media. The bottle was sealed and a rubber O-ring placed around the centre of the bottle in order to ensure maximum agitation during milling by simultaneous tumbling and rotation, and greater friction between the rollers and the bottle. The bottle was loaded horizontally into the ball mill and rotated for a predetermined time. The maximum efficiency of milling is achieved by rotating the bottle at a speed such that the sound produced by the collisions in the mill is at its maximum volume.

Ball milling containers were either packed in air, or in a nitrogen glove box (PlasLabs, Lansing, Michigan). When ball milling containers were packed in nitrogen, Alfa Aesar MgB_2 powder permanently stored in the N_2 glove box was used.

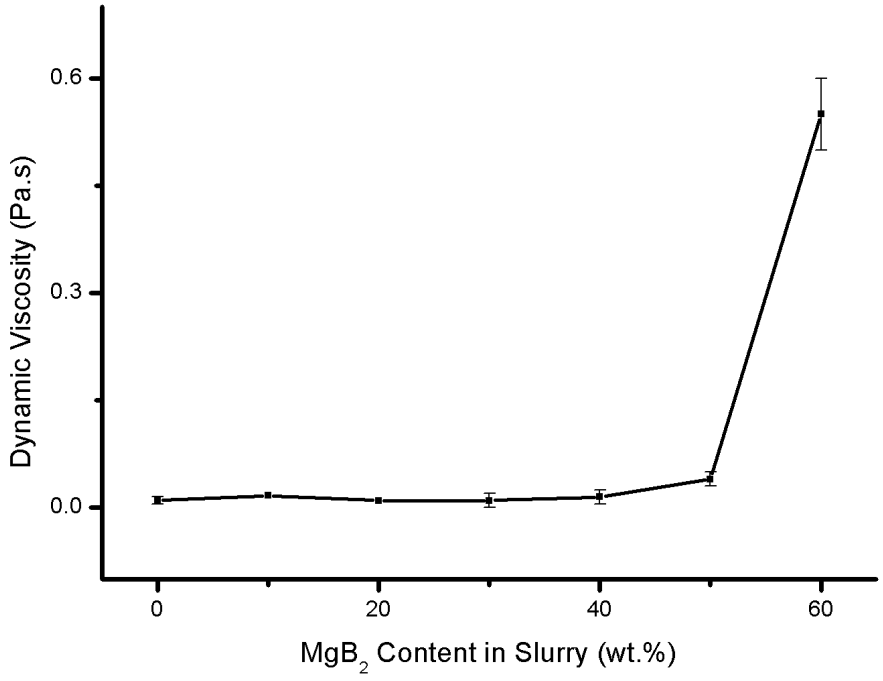


Figure 3.5: Viscosity of magnesium diboride/isopropanol slurries

3.1.4 Attrition Milling

The attrition milling process wears away the edges of particles due to impact by shear during milling. Attrition milling is a more severe mechanical process than ball milling, and results in a more rapid reduction in the average particle size [50].

Milling was carried out in air using a commercially available attrition mill (Union Process Szegardi Attritor System Model 01HD, Size 01). A schematic of the mill is shown in Figure 3.6. The parts of the mill which come into contact with the milled powder during milling are made of alumina (tank lining and blade), plastic-coated stainless steel (shaft of the blade), and plastic (cover, type unstated). Spherical YSZ milling media (Inframat Advanced Materials; 3 mm diameter beads) were used to facilitate stirring in the mill. Once the blade and most of the milling media was in position, a total volume of 35 vol.%-MgB_2/isopropanol slurry was loaded into the tank to $^1/_{16}{}^{\text{th}}$ of the volume of the tank as per the manufacturers recommendation. The remaining milling media was then

placed in the tank and the tank covered to prevent loss of material during milling. Milling was carried out at 500 rpm for 2 h. The slurry was then removed from the tank. All parts were rinsed with isopropanol to recover as much milled MgB_2 powder as possible. The isopropanol was evaporated from the slurry using a hot plate set at 75 °C.

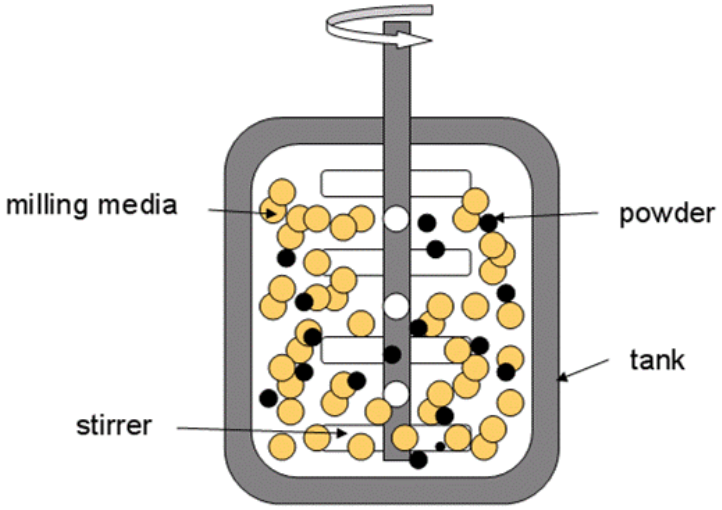


Figure 3.6: Schematic diagram of the attrition mill

3.2 Fabrication: Bulk Samples

3.2.1 Pressureless Heat-Treatment

Pressureless heat-treatment was carried out with the furnace either open to air, or under flowing gas. The basic method of pressureless heat-treatment was as follows: 0.5 g of MgB_2 powder was placed in a steel die and pressed using a uniaxial press at a pressure of 100 bar. Pellets were then heat-treated at a range of temperatures. Further details of these experiments, and the steps taken to establish a reliable protocol to avoid excess oxidation,will be discussed in Chapter 4.

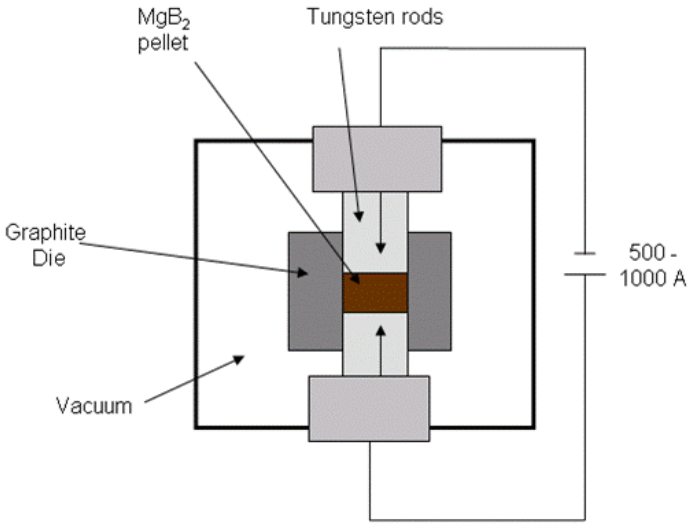


Figure 3.7: Resistive sintering apparatus used at the University of Birmingham

3.2.2 Resistive Sintering

MgB_2 bulk samples were also produced using Alfa Aesar MgB_2 powder using a resistive sintering apparatus which has previously been used to produce dense MgB_2 bulks [205]. The apparatus was built by Dr Alex Bevan, and my samples were produced with his assistance and that of Dr Pavlo Mikheenko, both of the Department of Metallurgy and Materials at the University of Birmingham. A schematic diagram of the resistive sintering apparatus is shown in Figure 3.7.

100 mg of MgB_2 powder was placed in a 5 mm graphite die and placed inside the furnace, supported by the tungsten plungers to which are attached electrodes which allow current to pass through the die. The chamber was then evacuated to a vacuum of 4×10^{-5} mbar. Once this vacuum was obtained (after $\sim$ 2 h), the powder in the die was pressed at 50 MPa applied pressure. The current was then switched on and increased such that the die temperature increased at a rapid, steady rate, with the ram displacement monitored throughout. Typical pressure and temperature ranges measured at the graphite die are $420-550$ bar and $900-980$ °C, but only represent average values across the whole sample. The optimum heat-treatment temperature was assessed by monitoring the thickness of

the specimen during heat-treatment. The temperature was held at the level at which a rapid decrease in the height of the specimen occurred; *i.e.* at the temperature at which effective densification began. Once the height of the specimen stabilised, the sample was held at that temperature for a few minutes to ensure that the densification was complete. The apparatus was allowed to return to ambient temperature and pressure before the sample was removed from the die using a uniaxial press.

3.2.3 Spark Plasma Sintering

Spark plasma sintering was carried out at Queen Mary, University of London with the assistance of Dr Haixue Yan using a Dr Sinter 2050 manufactured by the Sumitomo Coal Mining Company Ltd, Japan. During spark plasma sintering, DC current is passed through the die plungers leading to rapid heating and densification of the pellet [206]. Pressure is applied simultaneously with high temperature. It is unclear whether spark plasma sintering causes densification by passing current through the ceramic causing local heating, or whether it occurs merely due to the high temperature of the die. The balance of influence of these possible effects is strongly dependent on the conductivity of the ceramic. Spark plasma sintering was discussed in more detail in Chapter 2, and a thorough overview of the process can be found on the Sumitomo Coal Mining Company website [206].

A schematic diagram of the experimental setup is shown in Figure 3.8. The process is broadly similar to the resistive sintering technique, but being a commercial instrument is capable of greater variation in the heating rate and temperature, pressure and atmosphere. Powder was placed at the centre of a graphite die which was then heated by passing high current through the die with uniaxial pressure simultaneously applied. The temperature was typically around $1200 - 1300\,^{\circ}\mathrm{C}$, but varied according to the applied pressure ($16 - 80\,\mathrm{MPa}$) and the starting powder. The uniaxial pressure was varied in order to establish the optimum heat-treatment conditions to obtain dense bulk MgB_2. During each run, the vacuum pressure, uniaxial pressure, temperature, and sample height were monitored and

logged automatically.

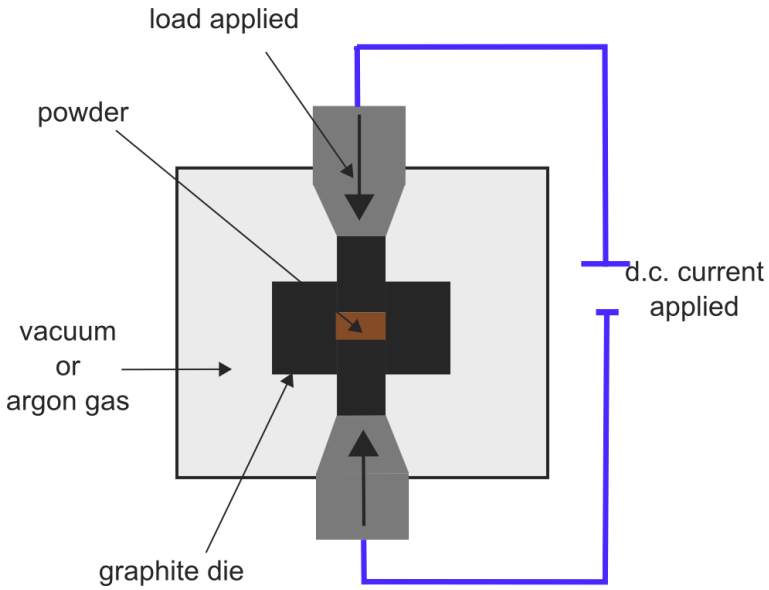


Figure 3.8: Schematic diagram of the spark plasma sintering apparatus

3.2.4 Hot Pressing

Hot pressing was carried out at the University of Oxford using equipment built by Dr Richard Todd and with the assistance of Apichart Limpichaipait. MgB_2 powder was loaded into a graphite die and placed inside the hot press. The die was lined with graphite foil in order to protect it from enhanced reaction with the MgB_2 to enable reuse, and to prevent the sample sticking to the die faces. Inside the hot press, the die is surrounded by a water-cooled induction coil which is heated by applying AC current. Simultaneously, uniaxial pressure is applied to the die. The pressure is limited to 30 MPa due to the limited strength of the graphite die. The temperature in the chamber was monitored using a thermocouple. The heating rate was monitored manually throughout the test. A schematic diagram of the hot press is shown in Figure 3.9.

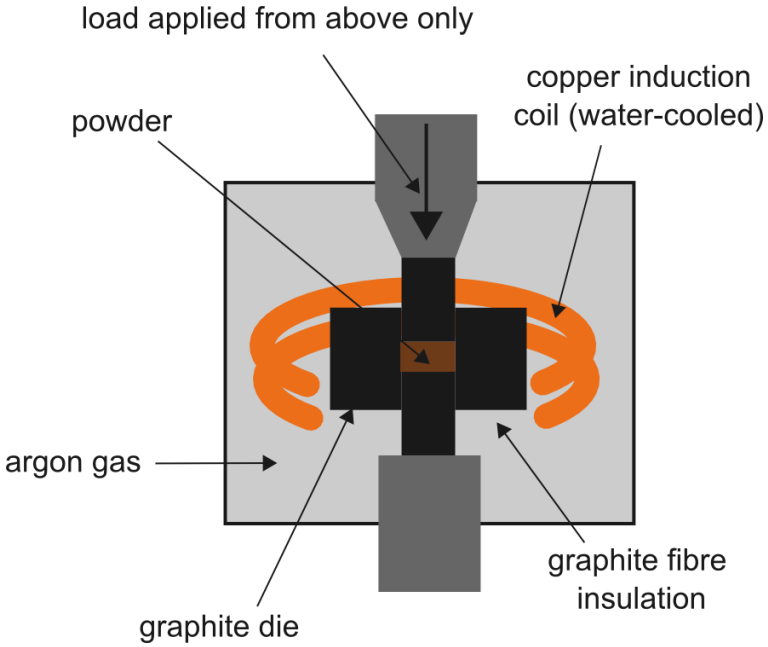


Figure 3.9: Schematic diagram of the hot press

The hot pressing is carried out under argon; though the non-closed system mean it is likely that some air is present. However the reducing atmosphere provided by the graphite die provides additional protection from oxidation and so impurity content was not expected to significantly increase.

3.3 Characterization: Macroscopic Physical Properties

3.3.1 Density Measurements

Density measurements were carried out on all bulk samples using Archimedes' method. All immersion was carried out using isopropanol, rather than water which reacts with MgB_2. The density of isopropanol was taken as $0.78\,g/cm^3$ for all calculations [59]. Measurements were repeated 3 times. Density measurements were made before and after heat-treatment so that the change in density could be readily established.

MgB_2 pellets were weighed in air using a standard balance and then immersed in isopropanol for several hours to ensure full penetration into open pores. The displacement force was measured by weighing the pellet with isopropanol still inside the pores in a

basket suspended from a balance, such that the mass of the liquid displaced by the pellet was measured (wet mass, m_{wet}). The pellet was then removed and wiped on filter paper to remove the surface isopropanol, and weighed again to obtain the total mass of the solid pellet and the isopropanol contained in the pores (damp mass, m_{damp}). The density of the pellet was calculated using Equation 3.4.

$$\rho = \rho_{liquid} \cdot \frac{m_{air}}{(m_{damp} - m_{wet})} \tag{3.4}$$

The relative density can be calculated, but requires accurate knowledge of the true density of the material (for example, from lattice parameters measured by X-ray diffraction). For samples which contain a significant volume fraction of impurity phases, the density must be adjusted using a rule of mixtures to obtain meaningful measurement of the ceramic pellet density. In this thesis, bulks are generally assumed to consist of pure MgB_2 before heat-treatment. After heat-treatment, calculation of the relative density has taken into account the increase in MgO content. This will be explained further in the following chapters.

There are various sources of error in the density calculations. Isopropanol is a low density liquid and wets MgB_2 readily, but may not penetrate into the smallest open pores. The calculation of porosity necessarily excludes any closed porosity (pores which are not open to the atmosphere) unless the true theoretical density can be accurately calculated. Using a liquid which readily evaporates at room temperature means that the damp mass measurements must be carried out very quickly. For this reason fluctuations in density for similar samples are to be expected. However there is no doubt that these density measurements can differentiate between the low densities of the as-pressed green compact (typically for ceramic powders these have a maximum density of 70 % of the theoretical density) and the high density of a sintered bulk ceramic.

3.3.2 Vickers Hardness

Hardness measurements were carried out using a Mitutoyo Vickers Hardness Indenter with a 2 kg load (P). The Vickers indenter is a standard pyramidal indenter where the angle between faces is 136^o. The illumination system in the hardness tester was insufficiently bright to image the surfaces of the samples, which are matte dark brown in colour, so the size of the indents was measured using a standard optical microscope.

The lengths of the diagonals of the indents (d_h) are inversely proportional to the hardness of the sample. The hardness (HV) is calculated using Equation 3.5 [207]. The number given immediately after the HV (e.g. HV/2) indicates the load used in kg. Ten indentations were made on all samples and the mean calculated. Significantly distorted intentations were rejected; this can occur if the surface of the sample is not perpendicular to the indenter due to areas of roughness, or the presence of local distributions of impurity phases with different hardness values.

$$HV = \frac{2P \sin(136^o/2)}{d_h^2} \tag{3.5}$$

3.4 Characterization: Size and Shape of Particles and Grains

3.4.1 Particle Sizing

Particle size distribution is known to affect the density of ceramic materials, both prior to heat-treatment (by affecting the packing density in the green compact) and during heat-treatment (as the curvature of the particle surface affects the activation energy for vapour and surface diffusion of material, and hence the densification rate). For this reason, significant time was committed during this project to developing a reliable and rigorous method of particle size measurement.

It is important to consider what it meant by particle size. While the size of a perfect

sphere can be defined by its diameter, the shape of many ceramic powder particles is more complex. In "Powder Sampling and Particle Size Determination" [134], Allen describes 13 different diameters which can be used to define particle size, including the diameter of a sphere having the same volume as the particle (the spherical equivalent diameter) and the diameter of a sphere having the same external surface area as the particle.

There are a large number of particle size measurement techniques. In chosing a suitable technique, consideration was given to the particle size range which could be measured and the measure of particle size returned. In addition it is important to consider the number of measurements which must be taken to obtain statistically significant results. The properties of techniques available during the course of this project are summarised in Table 3.3. The techniques selected are discussed in the following sections.

Optical microscopy was felt to have no advantages over scanning electron microscopy, which offered a large size range and a larger depth of field (this allowing easier determination of the edge of the particles).

Photon correlated spectroscopy (PCS) requires that particles are light enough that they can be set in motion by bombardment by liquid molecules; therefore the upper particle size limit is typically just a few micrometres [134]. The presence of larger particles dramatically skews the results, so it is not possible to measure a partial particle size range – the entire particle size range must lie within the limits. Initial tests using the PCS with the assistance of Alex Eggeman determined that the particle size range in the MgB_2 powder far exceeded the upper limit, making it inappropriate for measurements.

While sieving was found to be a useful and rapid method of separation of large volumes of MgB_2 powder (see Section 3.1.1 on page 50), it was not considered suitable for rigorous particle size analysis. The difficulties associated in sieving are discussed in detail by Allen [134]. In this project, the difficulties of reproducibility (particularly with small samples of powder), and the fact that nanometer-sized particles were known to be present in the powder (from PCS measurements and microscopy) were the key problems.

Table 3.3: Properties of Particle Sizing Techniques

Technique	Typical Size Range Measured	Size/Property Measured
Optical Microscopy	$0.8 < d < 150\,\mu$m	Any which can be taken from an image *e.g.* perimeter diameter, longest dimension, etc.
Scanning Electron Microscopy	Dependent on sample preparation and microscope resolution. Wide range of sizes can be measured.	
Transmission Electron Microscopy	Dependent on sample preparation and instrument; large powder particles fall off grids but could be mounted differently; this limits the measurable particle size range.	
Sieving (wire)	$20\,\mu\text{m} < d < 125\,\text{mm}$ [134, p. 213]	Sieve diameter d_{sieve}
Photon-Correlated Spectroscopy (or Dynamic Light Scattering)	$d < 3\,\mu$m [134, p. 591]	Diffusion coefficient for particles in Brownian motion from which can extrapolate the equivalent spherical volume diameter (d_v) by the Stokes-Einstein relation ($D = \frac{k_B T}{3\pi\eta d_v}$)
X-Ray Sedimentation	$1 < d < 300\,\mu$m	Stokes's Diameter (d_{St})
Laser Diffraction	$0.05 < d < 900\,\mu$m [134]	Equivalent spherical volume diameter (d_v)

3.4.1.1 X-ray Sedimentation

In this work, X-ray sedimentation was carried out using a Micromeritics Sedigraph 5100. This technique measures the particle size of a large number of particles over a wide range of sizes. X-ray sedimentation measures the size of the particles by measuring the intensity (I) of a scattered X-ray after passing through a suspension of the sample in a liquid, and comparing this to the intensity of an unscattered X-ray which has passed through the suspending liquid only (I_0). The X-ray intensity is proportional to the concentration of powder in the beam path (C) according to the Beer-Lambert law[†] (Equation 3.6).

$$I = I_0\, exp(-BC) \tag{3.6}$$

The concentration of powder in the beam path gives the relative intensities of the various particle size fractions measured. As the powder sediments according to Stokes's Law during the test, the Sedigraph measures the change in the particle position within the cell compared to its starting position to establish the particle size using Stokes's Law (Equation 4.2 on page 95). This concentration can be converted into a measurement of the cumulative mass percentage, and hence a curve indicating mass percentage as a function of the Stokes's particle size can be generated.

If the atomic number is low, the signal will be weak *unless* the concentration is high. This can cause problems when the concentration reaches a level whereby hindered settling begins (*i.e.* the sedimentation has fallen outside the Stokes's Law regime).

The basic operating proceedure of the Sedigraph is as follows. First, dispersing liquid of known density and viscosity is loaded into the system and pumped into the analysis cell. A baseline scan is then taken measuring the X-ray intensity after it has passed through the dispersing liquid in the cell as a function of height in the cell. This X-ray intensity level should be constant over the position in the cell; if it is not this indicates a problem with bubbles or impurities in the dispersing liquid. Next, a slurry of solid mixed

[†]In this equation B is a constant related to the atomic number of the solid

with the same dispersing liquid is loaded into the cell. A second baseline of intensity versus position in the cell is taken while the slurry is pumped around the cell. Again this intensity should be constant, but lower than that measured with only dispersing liquid in the cell. If the intensity is not constant this indicates a problem with the dispersion, such as flocculation or breakup of agglomerates, or a reaction causing bubbles or change of particle size. Once this baseline has been measured, the pump is switched off and the particles allowed to sediment such that their particle size can be measured. The size of the particles is calculated using Stokes's law (Equation 4.2 on page 95) as the distance moved in the cell and the time taken can both be readily measured, giving the velocity of the particle which is proportional to the square of the particle diameter. In order to measure the size of small particles within a reasonable analysis time, the cell can be moved vertically so that the actual sedimentation distance is very small. The intensity of X-rays transmitted through the cell is measured at a certain height in the cell. As the particles sediment to the bottom of the cell, the intensity increases and so the mass fraction of particles in a particular small size range can be determined easily. The mass fraction of particles is then plotted as a histogram versus particle size by the analysis software. The particle size ranges used for each bin of the histogram can be specified by the user.

Details of the precise methodology used for the tests in this work will be given in Section 4.1.2.2 on page 93.

3.4.1.2 Laser Diffraction

Laser diffraction uses either the Fraunhofer or Mie theory of light scattering in order to measure the particle size. Mie theory requires knowledge of the absorption and refractive index of the particle; Fraunhofer theory assumes particles are perfectly opaque.

Laser diffraction is fast and accurate. According to Malvern, who manufacture the system used in this work, measurements are highly reproducible; most problems come from inconsistent sample preparation techniques. Therefore significant time was spent optimising the sample preparation; this is discussed in Chapter 4.

The angle through which incident light is scattered is proportional to the volume of the particles. The intensity of scattered light is measured by an array of sensors over a wide angular range. The subsequent calculations to obtain the particle size assume that particles are spherical. The presence of plate-like particles results in an overestimation of the volume concentration. Also, Allen [134] states that "Non-spherical particles cause a broadening in the particle size distribution because they are measured over all orientations".

In this work, laser diffraction was carried out using a Malvern Mastersizer S laser diffraction system. This was loaned to me by the Engineering and Physical Sciences Research Council Scientific Loan Pool for 3 months from January to March 2007.

3.4.2 Optical Microscopy

Bright-field optical microscopy was carried out on selected bulk samples using an Olympus BX60M optical microscope with an AxioCam MRc Camera. Image processing was carried out using the AxioVision 4.2 software package (Zeiss). When these samples had been in contact with graphite foil during heat-treatment, they were ground on a flatbed grinder in order to remove the graphite foil and obtain a flat surface with a surface finish estimated at 115 μm. Samples were then cut using a diamond blade (Buehler 45HC) into sections appropriate for analysis. An Isomet 5000 was used for the densest samples ($> 90\,\%$) and an Isomet Slow Saw for more porous samples. Selected dense MgB_2 samples were cold-mounted in planar- and cross-sections using Met Prep Kleer-Set Type FF polyester casting resin mixed with Kleer Set hardener. Samples were polished using a Motopol 2000 grinder/polisher with a Kemet electronic dispenser equipped with various grades of diamond paste mixed with oil-based Kemet lubricant. No water-based polishing slurries were used due to the known reaction of water with MgB_2. The final polishing stage, using $^1/_4\,\mu$m polishing media, was carried out just before images were taken in order to minimise the impurities which could form prior to analysis.

3.4.3 Polarised Optical Microscopy

Polarised optical microscopy can be used to reveal the grain structure of materials by optical microscopy without etching. Plane-polarised light is used to illuminate the specimen; polarisation of the reflected light depends on the orientation of the grains of the sample. For flat polished samples, examination using polarised light gives grain contrast as either a variation of brightness (for monochromatic light) or a variation of colour (for white light). While high angle grain boundaries are readily distinguished using this technique, the contrast difference between two grains with relatively little difference in orientation is slight, and hence these grains may appear as one grain when using polarised light microscopy but may be separated using techniques such as electron back-scattered diffraction [208–210].

Polarised optical microscopy was carried out on selected bulk samples using an Olympus BX60M optical microscope with a Polaroid filter placed in the light path before the vertical illuminator and an analyser placed in the objective lens. Samples were prepared for optical microscopy as described previously in Section 3.4.2.

3.4.4 Scanning Electron Microscopy

Scanning electron microscopes (SEMs) are routinely used to examine a wide variety of samples including bulk material, powders, and thin films. SEMs can be used to look at thick bulk specimens because the electron signals used to form images are generated by electron interactions with the sample surface rather than by transmission, as in TEM. Additionally, the depth of field is much larger than for optical light microscopy, and the obtainable resolution is significantly higher [211].

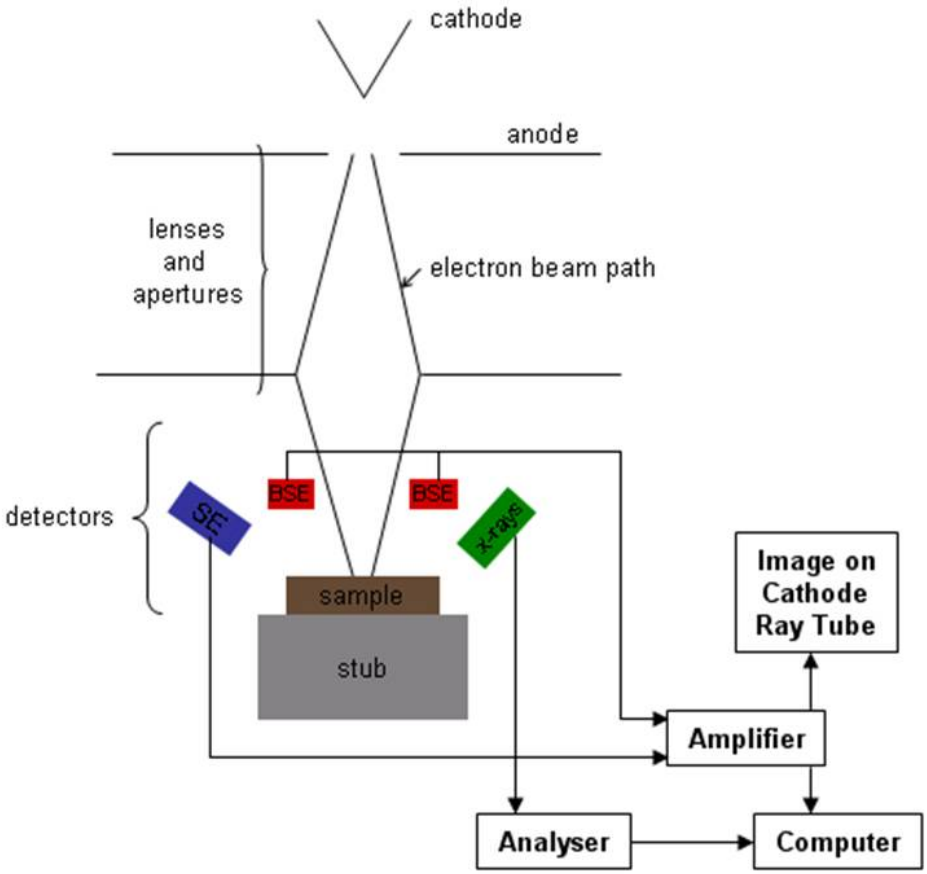


Figure 3.10: Schematic diagram of an SEM (after Reimer [212] and Goodhew et al [211])

A schematic diagram of a typical SEM is shown in Figure 3.10. Electrons are generated in the cathode, and accelerated due to a voltage difference between the cathode and anode of $0.1 - 50\,\mathrm{keV}$ [212]. The electron beam is focused using a series of electromagnetic lenses forming a probe on the sample surface. These incident electrons generate several electromagnetic signals which may then be used to obtain information about the sample. Those used for this work are secondary electrons, back-scattered electrons, and X-rays. Back-scattered electrons are primary electrons which are scattered out of the specimen after one or more scattering events. Each back-scattering event can lead to transfer of energy, forming secondary electrons; however the secondary electrons formed by the original incident electrons are more numerous and dominate the signal. Because they have low energies, they generally originate from an area little larger than that of the incident

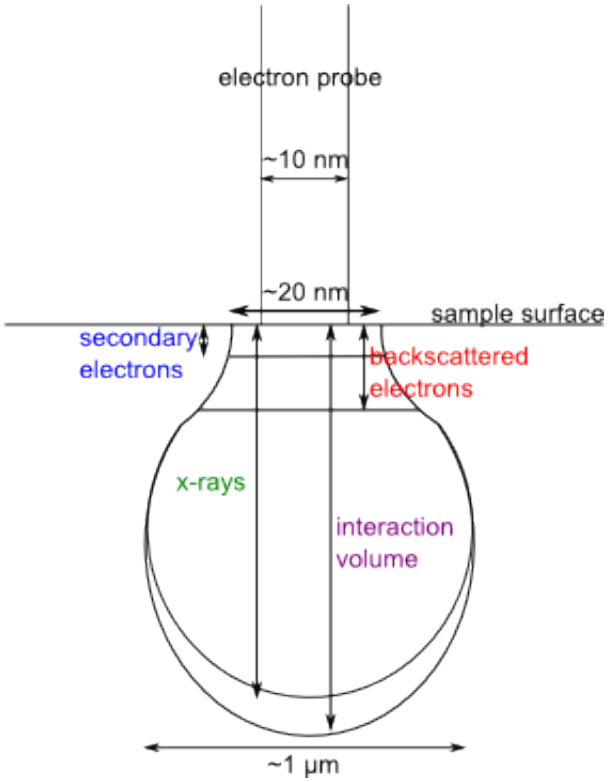


Figure 3.11: Spatial origin of specimen-electron interaction region (after Goodhew et al [211])

electron probe on the sample surface. Back-scattered electrons have a larger interaction volume, so the resolution in back-scattered images is worse than that of secondary electron images.

X-rays are generated when an incident electron removes an inner-shell electron from an atom in the sample; a high-energy electron from an outer shell replaces it, and an X-ray of characteristic energy is released. By measuring the energy of these X-rays, chemical analysis can be carried out (see Section 4.2.4.2). X-rays are generated from a large volume; they are not easily absorbed by the sample and can escape even if generated deep in the sample. The expected volume of the X-ray generation region is similar to that of the total sample interaction region (see Figure 3.11). These signals are detected by various types of detector and converted into an image or spectrum. For more information on scanning electron microscopy, the reader is directed to the extremely thorough texts on this topic by Goodhew *et al* [211] and Reimer [212].

Secondary electron images were obtained using a JEOL 840F SEM[‡] which generates electrons using a field emission gun. High resolution images can be obtained on this microscope by using a small probe current (typically 1×10^{-12} A) and small working distance (~ 12 mm). The microscope was operated at an accelerating voltage of 5 kV to minimise charging of the samples.

Powder samples were prepared by dispersing powders in isopropanol, then pipetting this mixture onto a carbon sticky tab mounted directly onto an aluminium stub. This method ensured that particles were well separated on the carbon tab, as otherwise the individual particle shapes and sizes could not be readily observed. These samples were dried for 24 h prior to examination in order to ensure full evaporation of the solvent. Bulk samples were attached to aluminium stubs using silver conductive paint (Electrolube).

3.4.5 Transmission Electron Microscopy

In transmission electron microscopy, electrons are generated at the cathode (*e.g.* using a tungsten filament, LaB_6 crystal, or field emission gun), and accelerated by a voltage difference between the cathode and the anode. Electrons are transmitted through the specimen and either pass straight through, or interact with it by either elastic or inelastic scattering. For this to occur, the sample must be sufficiently thin for the electrons to pass through the sample. Samples are therefore normally limited in thickness to less than 500 nm[§][209]. A schematic diagram of a TEM is given in Figure 3.12.

[‡]Note that images associated with Energy Dispersive X-ray Spectroscopy were obtained using another instrument; see Section 4.2.4.2 for details.

[§]This is dependent on both the atomic number of the material and the accelerating voltage of the electrons.

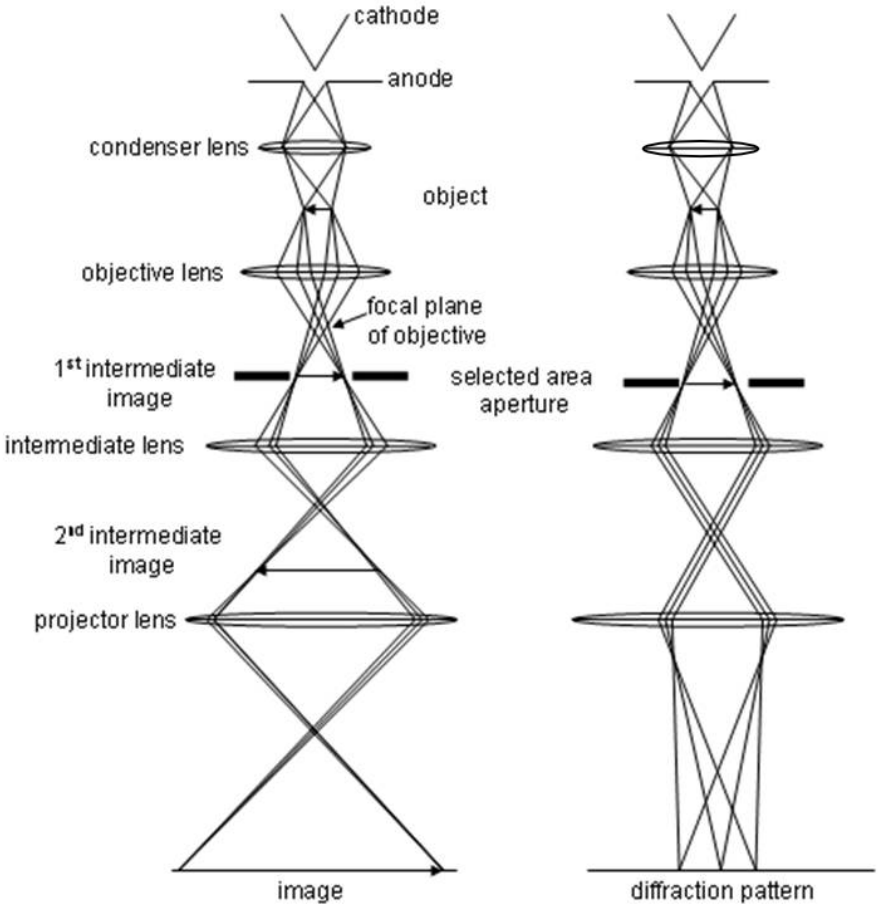


Figure 3.12: Schematic diagram of a TEM in imaging and diffraction mode (after Hirsch et al [213])

Bright-field images are formed by using the objective aperture to exclude all diffracted beams except the direct beam. Dark-field images are obtained by selecting a diffracted beam using the objective aperture. Standard techniques for imaging and obtaining diffraction patterns by selected-area diffraction were used throughout this work, so further details of the technique will not be given here. For more information about all aspects of transmission electron microscopy, the reader is directed to Hirsch *et al* [213] and Williams and Carter [214].

Transmission electron microscopy was used to examine fine particles in powder samples[¶]. Samples were prepared by dispersing them in isopropanol and pipetting them onto

[¶]Bulk samples were not examined using TEM due to the difficulties of preparing sufficiently thin samples of porous ceramics.

a holey carbon film attached to a copper grid of diameter 3 mm (Agar Scientific). TEM was then carried out using a JEOL 200CX or a JEOL 2000FX, both operated at 200 kV.

3.5 Characterization: Impurity Content Determination

3.5.1 X-Ray Diffraction

In X-ray diffraction, X-rays are fired at the surface of a crystalline material. The regular spacing of the lattice planes in the crystal causes the incident X-rays to be diffracted through a characteristic angle 2θ. This is illustrated in Figure 3.13.

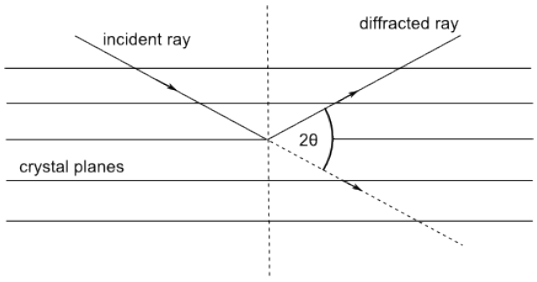


Figure 3.13: Diffraction from a crystal

The principle of X-ray diffraction is defined by Bragg's Law (Equation 3.7).

$$\lambda = 2d_{lp}\, sin\theta \tag{3.7}$$

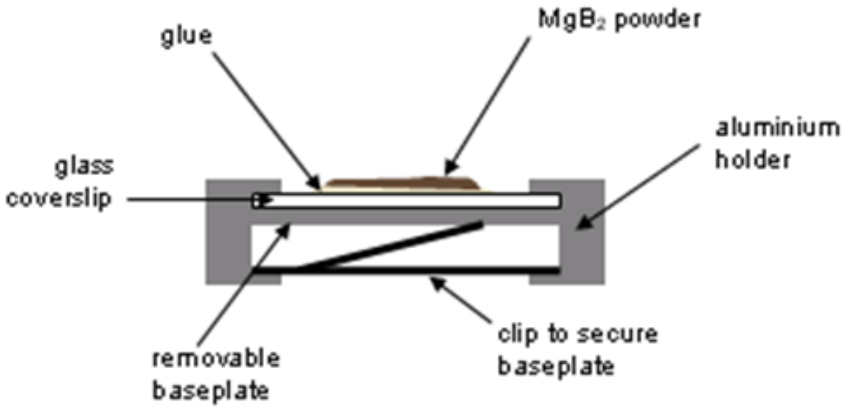
where d_{lp} is the inter-planar spacing, λ is the wavelength of the incident X-rays, and θ is half of the diffraction angle. Hence, for X-rays of a fixed wavelength, λ, a crystalline material will generate a number of peaks in X-ray intensity at characteristic values of 2θ (equivalent to characteristic values of d_{lp}). This is the basis of $\theta - 2\theta$ X-ray diffraction.

The position of peaks in the $\theta - 2\theta$ XRD spectrum varies due to instrumental factors (dependent on the quality of instrument calibration), the height of the specimen in the sample chamber, and stress in the crystal lattice causing variations in inter-planar spacing. The height of peaks in an XRD spectrum is not a reliable indicator of the quantity of crystalline material present in a sample. Yield of X-rays from different phases can vary

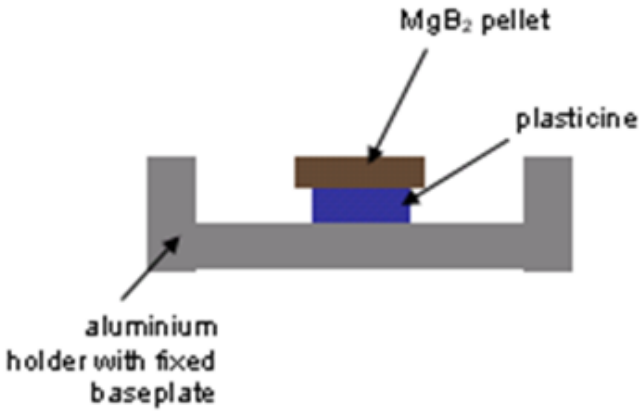
substantially. Also, strain between grains in the polycrystalline material can cause peak broadening, reducing the height below that of an unstrained sample (*e.g.* the reference sample). Materials exclusively made up of very small crystallites also have broader peaks (this effect is generally only observed for materials with a sub-micrometre grain size). It is therefore more illuminating to examine the peak area rather than the height when attempting to make quantitative analysis of impurity content. It is also important that there is no preferential texture of the sample; in this case some planes in the crystal dominate and the peak heights and areas vary accordingly. This is generally only the case for polycrystalline materials where the material has been subject to some preferential rolling or stress, which can cause alignment of crystals in certain preferred directions [215].

$\theta - 2\theta$ XRD was used extensively in this work to identify impurity phases before and after heat-treatment. The instrument used was a Philips $\theta - 2\theta$ diffractometer, which consists of a Philips PW1729 generator, PW1710 control unit, PW1820 detector and an APD system for collecting data. Cu$-$Kα radiation generated at 35 kV and 50 mA was used as the X-ray source, and a curved graphite monochromator is used in the primary optics. Data was processed using the Philips X'pert HiScore software package. Phases were identified by referring to the appropriate JCPDS powder diffraction files.

XRD was carried out on bulk and powder samples. Bulk samples were placed in an aluminium holder on top of a small piece of plasticine, which was completely covered by the sample. This was then pressed down using a glass slide so that the top of the sample was at the exact height of the top of the sample holder. This minimises the peak shifts due to variations in sample height. For powder samples, a square glass cover-slip was placed in an appropriate aluminium holder such that the glass was in the same position for each sample. The powder was attached to the glass slide using a proprietary paper glue (5 Star Office Glue Stick) taking care to cover the entire glued area with powder. Background scans were taken in each case so that peaks due to the holder, plasticine or glue could be identified and eliminated. Sample mounting methods are shown in Figure



(a)



(b)

Figure 3.14: Sample mounting methods for X-ray diffraction measurements(a) powder(b) bulk

3.14.

X-rays only penetrate $50 - 100\,\mu$m into the surface, so in order to establish whether the impurity levels were constant through the depth of the sample, depth profiling was carried out. XRD scans were taken at the surface and then subsequently on the new surface created following removal of a layer of material using SiC paper. Typically around $200\,\mu$m were removed each time; this change was measured using a Mitutoyo micrometer.

3.5.2 Energy Dispersive X-ray Spectroscopy

Energy dispersive X-ray spectroscopy (EDX) is a chemical analysis method which uses characteristic X-ray signals generated in an SEM or TEM to measure the concentration

of elements present in the surface of a sample. This was discussed in Section 3.4.4.

EDX is a quick and easy technique for detecting elemental composition. However, it has low spatial resolution because the X-ray generation volume in the sample is large (see Figure 3.11). In addition, an angled or rough surface can give misleading results. A particular significant problem for this work is the difficulty of detecting light elements such as boron.

EDX was carried out on selected samples using a JEOL 840A operated at 10 kV. Samples were mounted as for SEM imaging (see Section 3.4.4). EDX analysis was carried out using the INCA Energy Microanalysis System (Oxford Instruments).

3.5.3 X-Ray Photoelectron Spectroscopy

X-ray photoelectron spectroscopy (XPS) is used to study surface chemistry and the bonding in both crystalline and amorphous materials. The energy (hv) of a photon incident on the sample is absorbed by an electron with binding energy E_b which is then ejected from the sample (provided that $E_b < hv$). Since the energy of the ejected electron is characteristic of the atom from which it originated, measurement of the energy of the ejected electrons can be used to identify both elements and specific bonds (because the transfer of electrons involved in bonding means electrons ejected from atoms bonded to different neighbours have different energies from those which are in the atomic state). The mean free path of the ejected electron is typically very small, so ejected electrons originate only from the first few atomic layers at the surface of the sample. Ar^+ ion sputtering can be used to remove layers to minimise surface contamination which can lead to misleading results. For more details on XPS, the reader is directed to Briggs and Seah [216].

XPS measurements were taken of selected powder samples by Dr Alison Crossley of the Department of Materials, University of Oxford. Interpretation of these spectra was considered with reference to XRD data, EDX results and knowledge of the sample preparation method (*i.e.* by considering which materials were in contact with the powders during processing).

3.6 Characterization: Magnetic Measurements

Magnetization measurements were made by Dr Dharmalingham Prabhakaran of the Department of Physics, University of Oxford, using a Quantum Design Magnetic Property Measurement System (MPMS). This uses a SQUID to detect the magnetization response of the sample to an applied magnetic field. Bulk samples were cut into small cuboids using a wire cutter. They were then loaded into plastic capsules and placed in the MPMS such that the long axis of the sample was parallel to the applied magnetic field. When powders were examined these were loaded directly into the capsules.

All tests were carried out at 4 K and 20 K. The applied magnetic field was $-7 < H\,(\mathrm{T}) < 7$, with an increment of 0.05 T for $0 < H\,(\mathrm{T}) < 2$ and 0.2 T for $2 < H\,(\mathrm{T}) < 7$ (and similarly for the negative region).

The shape of the magnetization loop is indicative of whether the tested sample is superconducting. In addition, it is possible to obtain information about the critical current density, to establish the coercive field, and to measure the extent of connectivity in the sample by examining the slope of the loop in the region $0 - 7$ T. This will be discussed in more detail in subsequent chapters.

4 Processing Commercial Magnesium Diboride Powder

4.1 Characterization of Commercial Powder

Magnesium diboride powder produced by Alfa Aesar has been widely used for studies of *ex situ* MgB_2 artefacts. It is apparent from the literature that the impurity content of the powder can vary considerably between batches (see Section 2.5.4.1 on page 41 for more extensive discussion). At the time of our purchase of MgB_2 powder (batch #20031; the group had earlier obtained a smaller amount of batch #06051 which was only used in this study during tests to examine the variation between batches) Alfa Aesar described the powder as MgB_2, 98 % pure and -325 mesh size, corresponding to a sieve diameter of around 40 μm. I thoroughly investigated the impurity content and particle size of my batch of Alfa Aesar MgB_2 powder to establish the accuracy of this specification and to establish a baseline for later studies of modified powders and heat-treated samples.

4.1.1 Impurity Content Prior to Heat-Treatment

The phase purity of the MgB_2 powder was investigated using electron dispersive X-ray spectroscopy, X-ray diffraction, and X-ray photoelectron spectroscopy.

4.1.1.1 X-Ray Diffraction

The crystalline phases present in the starting powder were determined by reference to the MgB_2 JCPDS file (Reference Number 38-1369). All of the peaks present in the XRD scan of the Alfa Aesar powder (Figure 4.1) were assigned to MgB_2. It is difficult to distinguish MgB_2 and MgO (JCPDS File Reference Number 45-0946) because the latter phase has very few major peaks in its spectrum, and the largest peak (200) ($2\theta = 42.916°$) is only $0.5°$ apart from the strongest MgB_2 peak (101) ($2\theta = 42.411°$). The second strongest MgO peak is (220) ($2\theta = 62.302°$) whose position is indicated in Figure 4.1. Establishing quantified composition using X-ray diffraction can be difficult because peaks for minor phases (<5 wt.%) can be impossible or difficult to discern from the baseline, and because the peak positions and heights can be affected by many factors including texture, strain, and instrumental broadening and misalignment (see Section 3.5.1 on page 75).

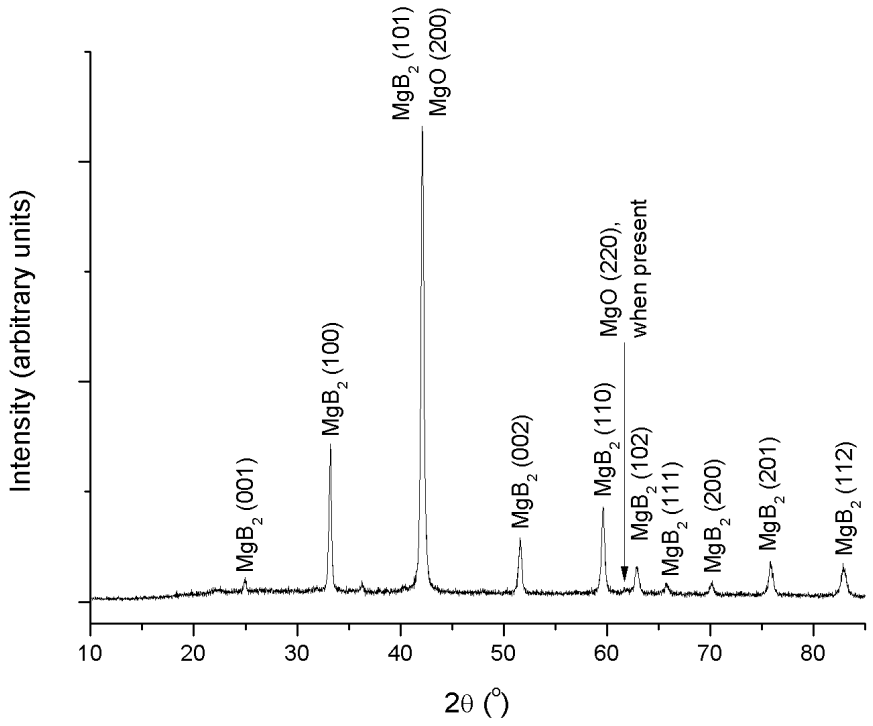


Figure 4.1: X-Ray diffraction spectrum for as-purchased MgB_2 powder

The precise MgO content in the starting powder was not determined because of the dif-

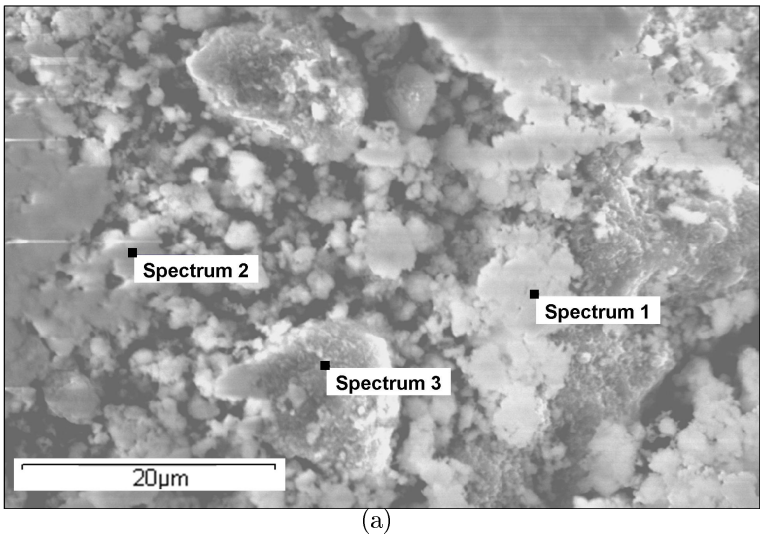
ficulty of obtaining truly pure MgB_2 samples due to the extreme reactivity of magnesium with oxygen. It is more relevant to this project to observe the changes in impurity content in the powder following heat-treatment, and as such the MgO content of the starting powder is treated as a baseline value. In Section 4.2.4 I will discuss how the increase in MgO content of MgB_2 artefacts following heat-treatment was quantified using XRD.

4.1.1.2 Energy-Dispersive X-Ray Spectroscopy

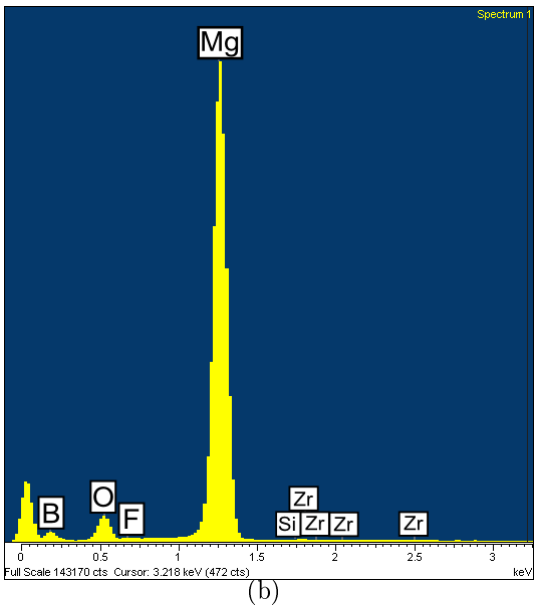
As XRD can only be used to determine the phase purity of powders, and has a low detection limit, the presence of minor impurities was investigated using alternative methods.

Energy dispersive X-ray spectroscopy (EDX) was carried out on a sample of MgB_2 powder using the JEOL 840A and Inca Analysis Software (Oxford Instruments). A typical scan is shown in Figure 4.2 along with a secondary electron (SE) image of the sample. In order to obtain a reasonably flat sample for analysis, powder was pressed firmly onto a carbon sticky tab before removing loose particles using compressed air. This produced a thick coating of powder unsuitable for examining individual particles but providing a large volume of material for compositional analysis.

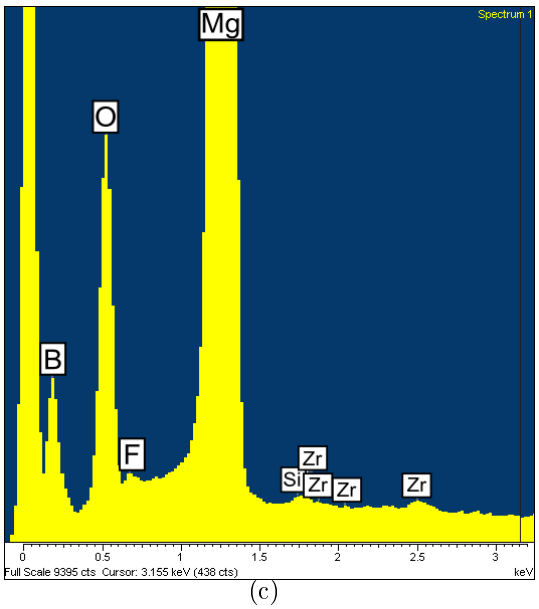
EDX gives information only about the characteristic X-ray emission peaks of individual elements. It was primarily used to establish the presence or absence in our batch of Alfa Aesar powder of impurities reported in other studies. EDX spectra were taken at ten points on the sample using spot analysis mode; three typical points are shown in the SE image (Figure 4.2a). Points on the sample were selected because the sample appeared fairly flat and dense in their vicinity. Large peaks due to Mg and O were detected for all points; a peak due to B at lower energy were also seen in most spectra. The resolution of EDX is more limited for low-atomic weight elements such as boron, so quantification was not attempted. Very small peaks which could be attributed to silicon, fluorine or zirconium were detected in some regions; these were calculated to comprise less than 0.5 wt.% of the Mg content.



(a)



(b)



(c)

Figure 4.2: a) SEM image indicating typical points chosen for scans b) and c) Typical EDX spectrum of MgB_2 powder

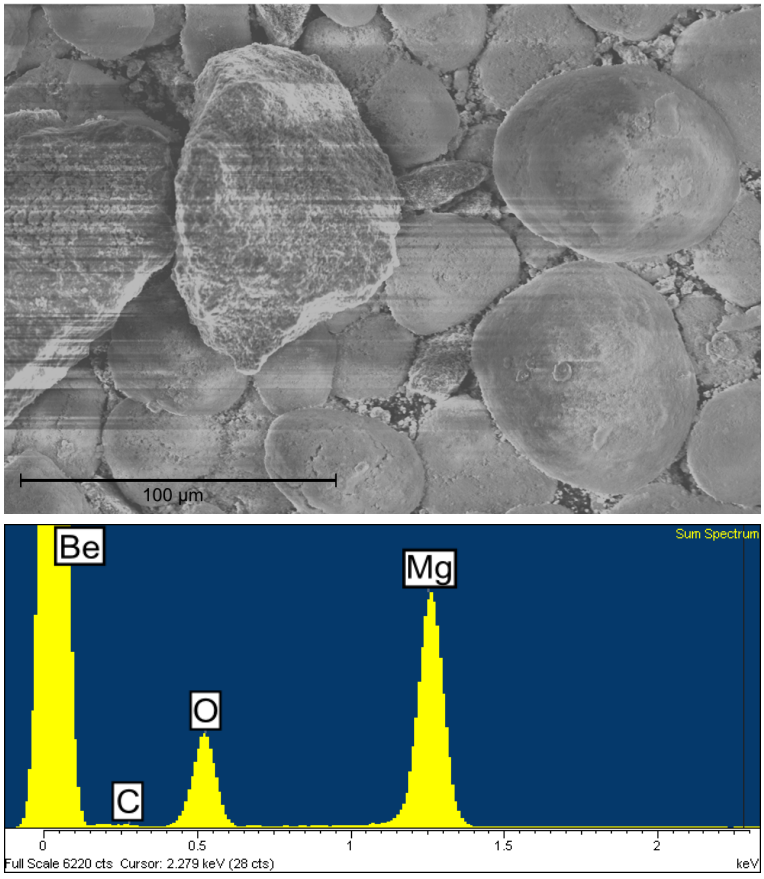


Figure 4.3: Low magnification secondary electron image and corresponding sum EDX spectrum for 50 % MgO/MgB_2 standard powder mixture

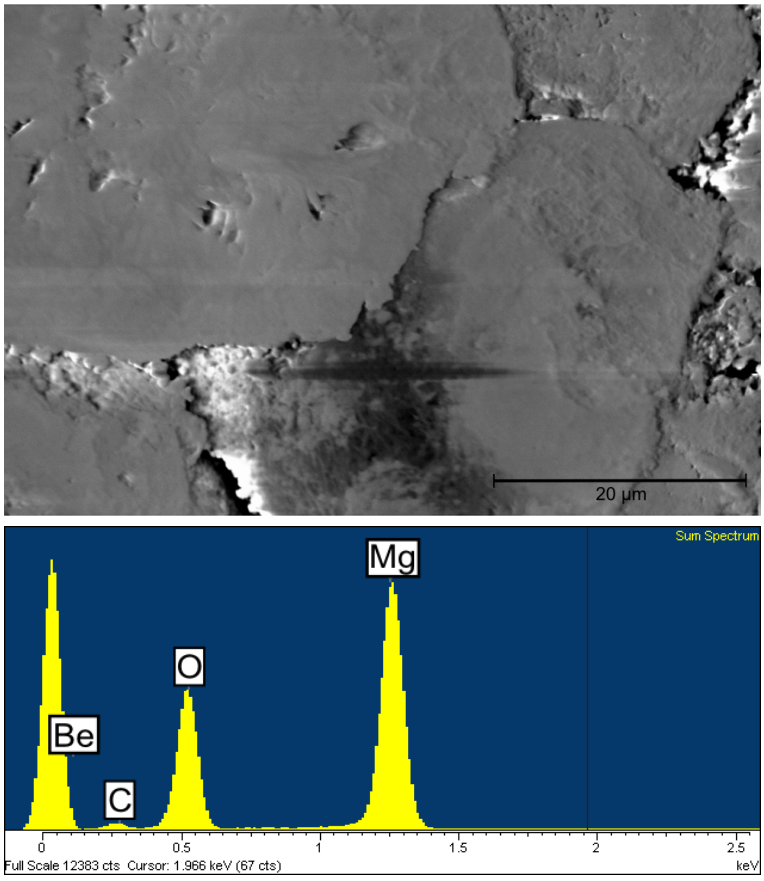


Figure 4.4: High magnification secondary electron image and corresponding sum EDX spectrum for 50 % MgO/MgB_2 standard powder mixture

In order to calibrate the MgO content of samples using EDX, standard samples of known MgO/MgB_2 ratio were examined by EDX in the SEM. Powders of MgO (BDH Ltd) and MgB_2 (Alfa Aesar) were weighed in appropriate proportions and thoroughly mixed. Samples suitable for examination by EDX were prepared as described above. EDX maps were taken of various areas on the surface. At low magnification (field of view approximately $200 \times 150\,\mu m^2$, typically covering ten or more particles) the areas were chosen at random (see Figure 4.3 for a typical secondary electron image and sum spectrum). At high magnification (field of view approximately $60 \times 40\,\mu m^2$, typically covering one or two particles) to avoid misleading results due to topographic variations, the areas were chosen such that the scanned region was roughly at the same height across the entire map (see Figure 4.4).

In mapping mode in EDX, the same number of scans is taken for every map, regardless of magnification. A sum spectrum of all the points in the map was obtained from the software. The ratio of the height of the O peak in the sum spectrum to that of the Mg peak was measured and plotted against the known MgO content for each standard. The graphs are shown in Figure 4.5 (low magnification) and Figure 4.6 (high magnification). The data have been fitted with a straight line in both graphs.

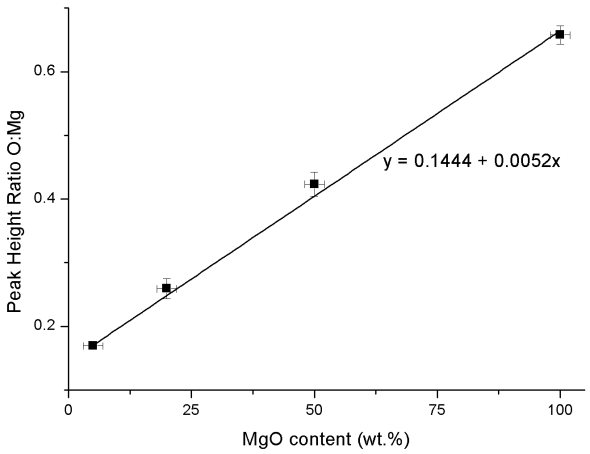


Figure 4.5: EDX calibration curve using the sum spectrum from low magnification maps (see Figure 4.3) of known MgO/MgB_2 standard powder mixtures

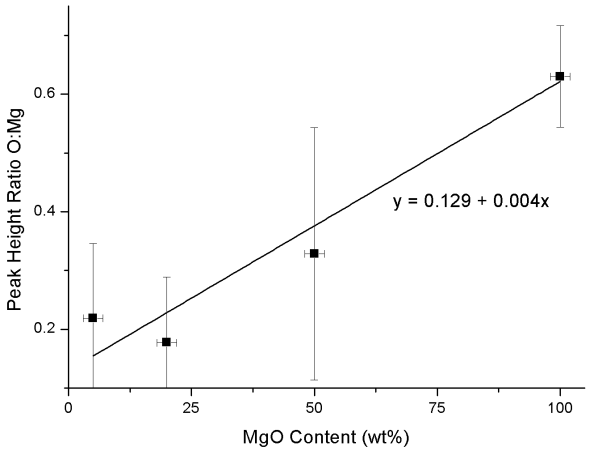


Figure 4.6: EDX calibration curve using the sum spectrum from high magnification maps (see Figure 4.4) of known MgO/MgB_2 standard powder mixtures

When EDX spectra were obtained at high magnification, the standard deviation of the ratios was very high (indicated by the error bars). Using the best fit line equations for each graph to calculate the MgO content for a given O:Mg peak height ratio, the difference between the predicted MgO content is significant. This has been tabulated in Table 4.1. The O:Mg peak height ratio was calculated for a given MgO content from the sum spectrum for the high magnification maps, and input into the equation for the calibration from low magnification maps, and *vice versa*.

Table 4.1: Difference in MgO content (in wt.% throughout) calculated from sum spectra from low and high magnification maps

Known MgO Content (wt.%)	MgO Content Calculated from Calibration Equation for Low Magnification Maps using Ratio measured from High Magnification Sum Spectrum	MgO Content Calculated from Calibration Equation for High Magnification Maps using Ratio measured from Low Magnification Sum Spectrum
5	10	14
20	33	6
50	74	35
100	132	99

The peak ratio measured from the high magnification maps but calculated using the low magnification data consistently overestimates the MgO content compared to the known

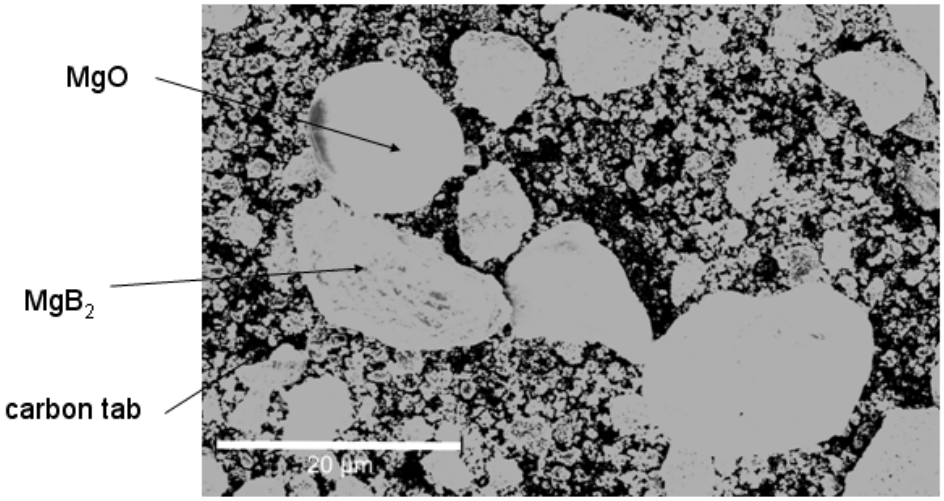
content of MgO. For the opposite scenario, the estimate of MgO content is very inaccurate at low MgO contents, but becomes increasingly accurate as the MgO content increases. The high magnification maps varied significantly in the proportion of MgO to MgB_2, because each map typically contained fewer than 5 particles. At low magnification the results were more consistent. This indicates that EDX can obtain accurate MgO contents for samples providing the MgO is well distributed through the sample. But the results from Table 4.1 indicate that if the MgO is distributed inhomogeneously through the sample the MgO content measured from the calibration equation from the low magnification maps will likely be a serious overestimate.

4.1.1.3 Back-scattered Scanning Electron Microscopy

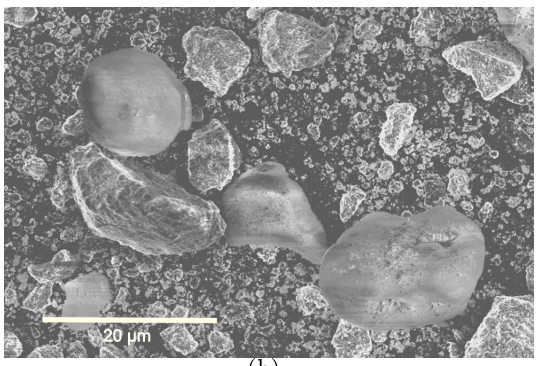
Back-scattered SEM can be used to distinguish between areas of different composition (see Section 3.4.4 on page 70) based on their atomic or molecular mass. This technique has been used by Prikhna *et al* on dense MgB_2 samples to distinguish both added impurities and oxygen-rich phases from MgB_2 [217]. I examined a sample of mixed MgO and MgB_2 powders to determine the contrast level between the two powders. As shown in Figure 4.7a, the difference between the MgO (rounded smooth particle by comparison to Figure 4.7c) and the MgB_2 particles (rough angular particle) is negligible. This is perhaps not surprising considering the small difference in atomic number between boron and oxygen. Also, the topography of rough samples such as these (and the fracture surfaces examined later) affects the contrast even in back-scattered imaging mode, so that the atomic number contrast is less significant. For these reasons, back-scattered SEM imaging was not used for my samples.

4.1.1.4 X-Ray Photoelectron Spectroscopy

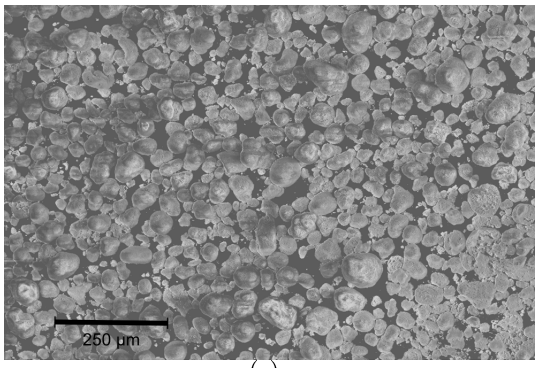
The powder was also examined using XPS with the assistance of Dr. Alison Crossley (the yellow spectrum in Figure 4.8). This technique is highly surface-sensitive, with electrons only generated from the top few atomic layers of the crystals [209; 216]; hence



(a)



(b)



(c)

Figure 4.7: a) Back-scattered image of MgB_2/MgO powder mixture, indicating negligible back-scattered contrast between the two compounds
b) Secondary electron image of the same area
c) Secondary electron image of MgO particles

it is excellent at establishing the nature of surface contamination, but any quantitative analysis cannot be taken as representative of the bulk material.

The XPS scan was used by Alison Crossley to quantify the elemental impurity content (Table 4.2). This revealed extensive surface hydrocarbon contamination, indicated by a large carbon and oxygen content. Boron and magnesium were present in large proportions. Minor elements detected were fluorine, nitrogen, silicon, and argon. Nitrogen and argon have probably been adsorbed onto the surface at some point during processing (powders are often packed and processed under inert gases such as nitrogen and argon) and/or sample preparation for XPS. The sources of the silicon and fluorine have not been established, but are common impurities detected by surface-sensitive methods from contact with polymers in particular. At the levels detected on the surface, these impurities are unlikely to be detected in the bulk by EDX or XRD.

Table 4.2: Quantified surface content (at.%) of as-purchased MgB_2 powder measured using XPS

Mg	**B**	**O**	**C**	**F**	**N**	**Si**	**Ar**
14.2	10.8	33.1	34.7	4.0	2.5	0.7	0.1

Phase analysis can be carried out using scans over smaller energy ranges, but was difficult due to a large number of overlapping peaks in the spectra. Both B_2O_3 and MgB_2 were detected in the narrow energy scan for the boron 1s scan (Figure 4.9a), but only 1 peak could be detected in the Mg 2p peaks (Figure 4.9b), though this peak is made up of contributions from Mg and MgB_2. No MgO was detected in this sample, the peak for which would be expected at $\sim 54\,\text{eV}$ (labelled as Mg^{2+} in Figure 4.9b).

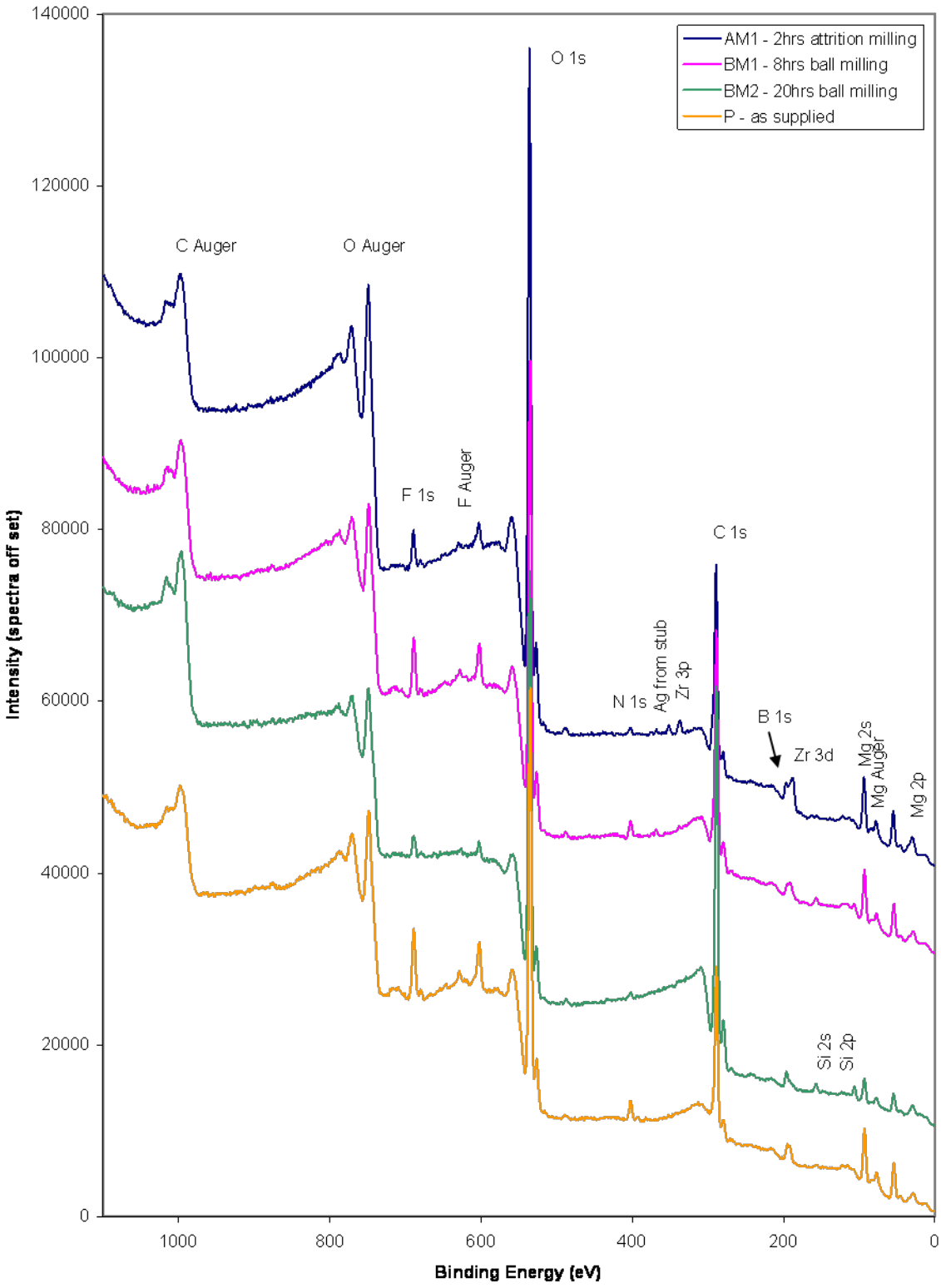
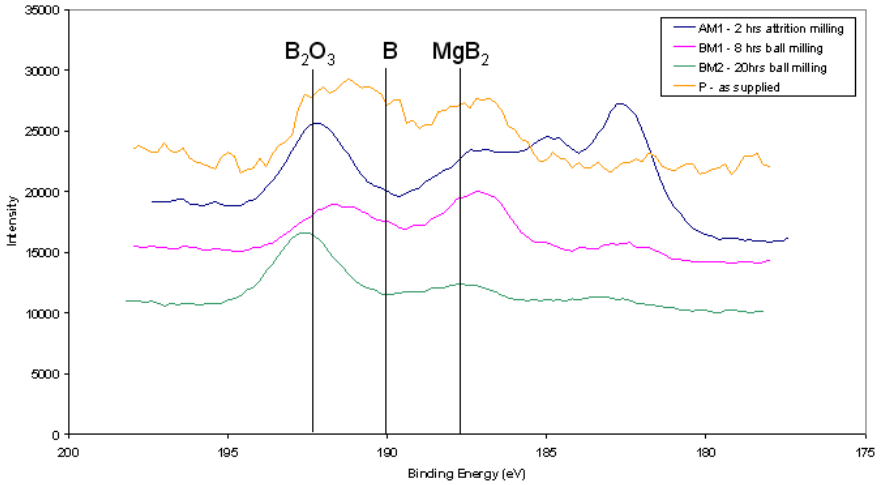
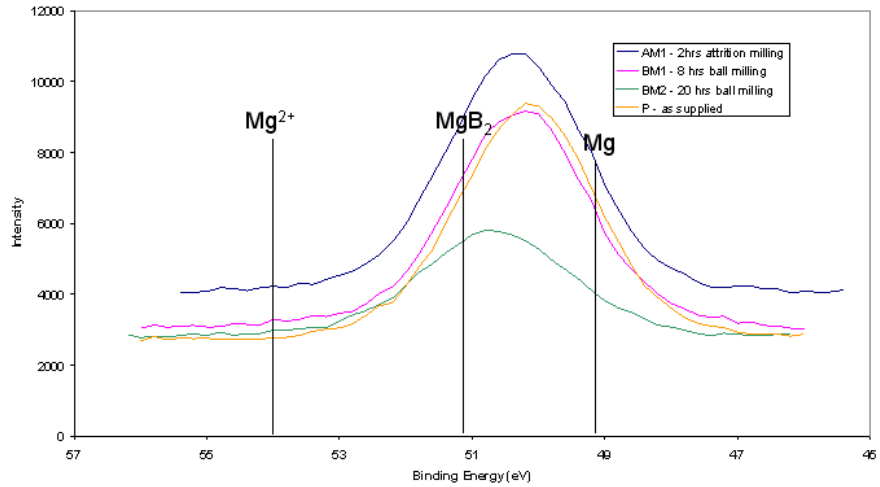


Figure 4.8: XPS wide-energy scan. The scan for the as-purchased MgB_2 powder is the yellow line.



(a)



(b)

Figure 4.9: Narrow range energy XPS scan. The scans for the as-purchased MgB_2 powder are the yellow lines.
a) Boron 1s peaks
b) Magnesium 2p peaks

4.1.2 Particle Size

4.1.2.1 SEM and TEM

Particle size and shape in powders can be readily observed using electron microscopy. SEM and TEM were both performed on the starting powder because the particle size range involved is extremely wide (see examples in Figure 4.10). The MgB_2 powder is extremely inhomogeneous, containing particles and agglomerates of a wide range of sizes

($d \simeq 150\,\mu$m in Figure 4.10b to $d \simeq 0.4\,\mu$m in Figure 4.10d). Particles have varying shape from rectangular (Figure 4.10f) and elongated to highly rounded shapes (Figure 4.10d).

It was impossible to obtain an accurate value of the particle size of the powder by simply measuring the sizes of a number of particles; to obtain a meaningful value would require an extremely large number of measurements to be made due to the wide range of sizes. In addition, large particles were poorly sampled in TEM as they fell off the grids or were too large to image effectively, and smaller particles were difficult to see in SEM due to charging and poor contrast against the background. This resulted in poor sampling for both techniques in the middle of the particle size range ($1 \lesssim d\,(\mu\text{m}) \lesssim 30$) For these reasons, a method which measures the particle size of a large number of particles simultaneously was sought.

4.1.2.2 X-Ray Sedimentation

X-ray sedimentation measures particle size using the settling rate of particles of known density in a liquid of known density and viscosity. The sedimentation rate of a solid in a given liquid is governed by Stokes's law, providing the sedimentation occurs within the laminar flow limit. This is determined by calculating the Reynolds number, which takes into account the maximum diameter of the particles to be measured, and the properties of the fluid. X-ray sedimentation measurements were carried out using a Micromeritics Sedigraph 5100 in the Soil Laboratory courtesy of Prof. Gilliane Sills of the Department of Engineering at the University of Oxford. The standard proceedure for measuring particle size distributions using this machine was described in Section 3.4.1.1 on page 67.

The Sedigraph manual states that the calculations of particle size are accurate for $Re \leqslant 0.3$ and are accurate within a 3 % error for $0.3 \leqslant Re \leqslant 0.5$. For $Re > 0.5$ the errors become significantly higher. This means that it is possible to use the limit of the Reynolds number to calculate the maximum particle size (d_{max}) accurately measurable for any liquid of known density and viscosity. The liquids were chosen on the basis of availability and reactivity when in contact with both MgB_2 and the wetted materials

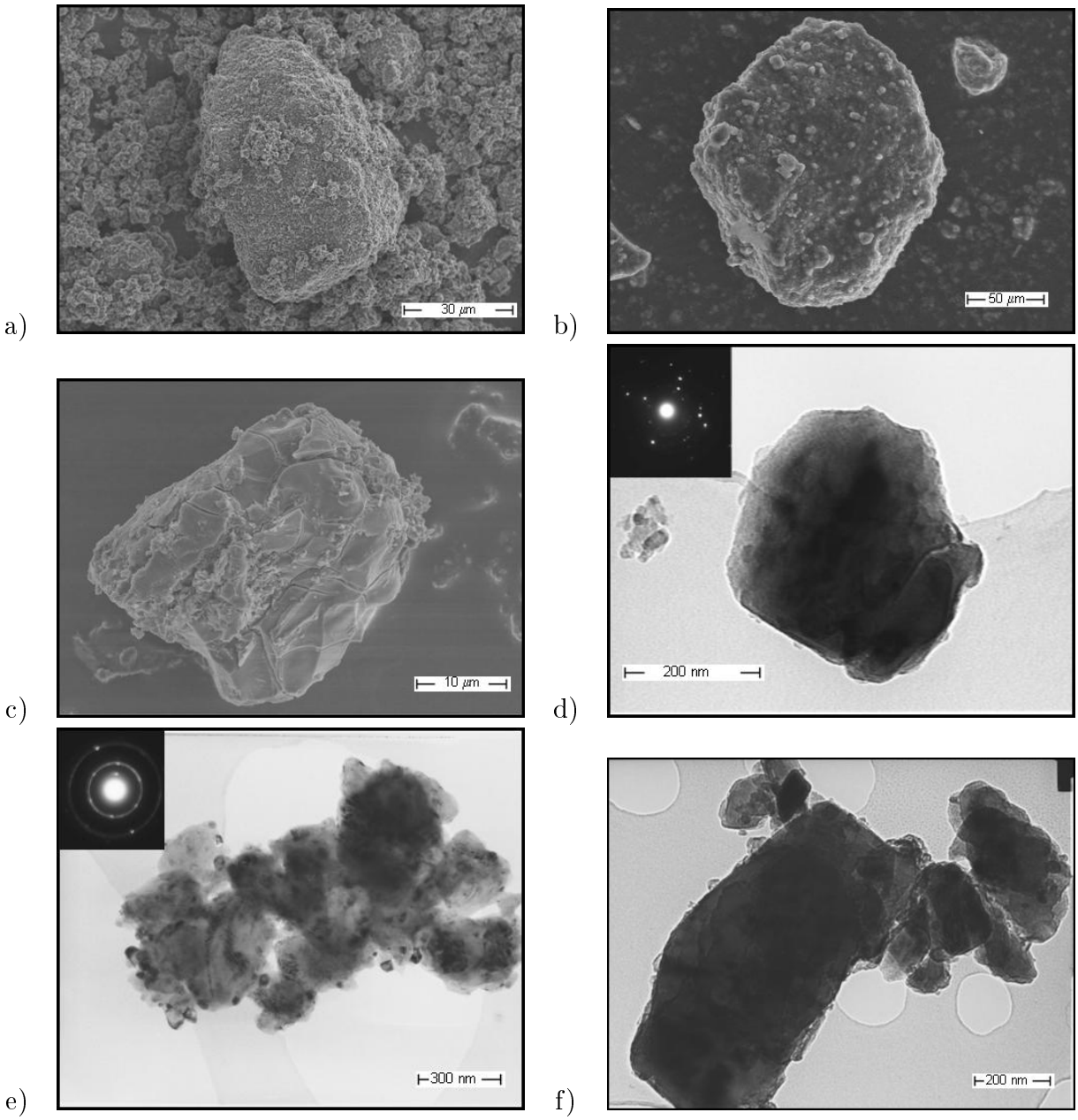


Figure 4.10: Variety of MgB_2 particles in as-purchased powder
a, b, c) SEM micrographs
d, e, f) TEM micrographs

within the Sedigraph (these include stainless steel and polyethylene).

The Reynolds number is calculated using Equation 4.1 where Re is the Reynolds number for a particle, d is the diameter of the particle, v is the equilibrium sedimentation velocity, and ρ_0 and η are the density and viscosity of the fluid respectively.

$$Re = \frac{dv\rho_0}{\eta} \tag{4.1}$$

v is calculated from Stokes's Law (Equation 4.2) for the diameter of a particle of density ρ settling at velocity v.

$$d = \sqrt{\frac{18\eta v}{g(\rho - \rho_0)}} \tag{4.2}$$

But as d is related to v, the actual equation used to calculate d_{max} is obtained by combining Equation 4.1 and Equation 4.2 to give Equation 4.3.

$$d_{max} = \sqrt[3]{\frac{18\eta^2 \cdot Re}{\rho_0(\rho - \rho_0) \cdot g}} \tag{4.3}$$

Hence using Re we can calculate d_{max} for a variety of available liquids. The results are shown in Table 4.1 calculated for both $Re = 0.3$ and $Re = 0.5$.

Table 4.3: d_{max} for various liquids calculated from the Reynolds number limit. Viscosity at 30 °C was calculated from the best-fit line obtained from a plot of viscosity against temperature using the data in the CRC Handbook of Chemistry and Physics [59]

Liquid	ρ **(g/cm³)**	η **at 30 °C (mPa s)**	d_{max} **[Re = 0.3]** (μm)	d_{max} **[Re = 0.5]** (μm)
Ethanol	0.7893	0.9630	70.6	83.7
Ethylene Glycol	1.1088	13.12	383.0	454.1
Hexane	0.6603	0.2852	32.5	38.6
Isopropanol	0.7855	2.774	143.0	169.5
Methanol	0.7914	0.5103	46.2	54.8
n-Butanol	0.8098	2.596	136.0	161.3

It is clear from Table 4.3 that the dispersing liquid has a significant impact on the measurable particle size range. Initial experiments were carried out in isopropanol which

has an appropriate upper particle size limit when compared to the literature [65], and a typical particle size distribution for MgB_2 in isopropanol is shown in Figure 4.11. In addition, isopropanol has good dispersant properties with MgB_2 powder and tests could be carried out successfully without flocculation or bubble formation (indicated by the constant X-ray intensity with cell position while the sample is still being pumped around the cell, and hence the mixture in the cell is homogenous, see Figure 4.12). However it became clear during SEM observations that the Alfa Aesar powder contained a few particles of $d > 200\,\mu$m. Discussion with technical staff at Micromeritics indicated that when this occurred it could lead to a serious error in the analysis. As a result, ethylene glycol with the largest d_{max} values in Table 4.3 was tested as a dispersant; this liquid permits a higher upper particle size limit compared to isopropanol, but its higher viscosity limits the measurable lower particle size limit.

The particle size distribution (Figure 4.13) indicates fewer large particles for the test carried out in ethylene glycol; this suggests that these agglomerates are larger than the maximum particle size. Unfortunately, for ethylene glycol fluctuations in X-ray intensity are seen at the top of the cell (Figure 4.14). The intensity is initially lower than the constant value (18 kilocounts/s) measured at higher points in the cell, and then higher. This is indicative of possible flocculation of particles during the test, and means the test in invalid. In addition, the non-continuous nature of the apparent particle size distribution is further evidence of flocculation in ethylene glycol (Figure 4.13). The test time is significantly increased when using ethylene glycol rather than isopropanol, making it extremely time-consuming to measure small particle diameters. Finally, the high viscosity of the ethylene glycol meant it was very difficult to clean the tubing of the Sedigraph after use, potentially increasing the possibility of contamination for future samples. For these reasons, I decided that ethylene glycol is not suitable for use as a dispersing liquid during X-ray sedimentation measurements. This meant that there were no readily available liquids for which accurate measurements could be obtained for this material using the Sedigraph, and so an alternative method for measuring the particle size distribution was

sought.

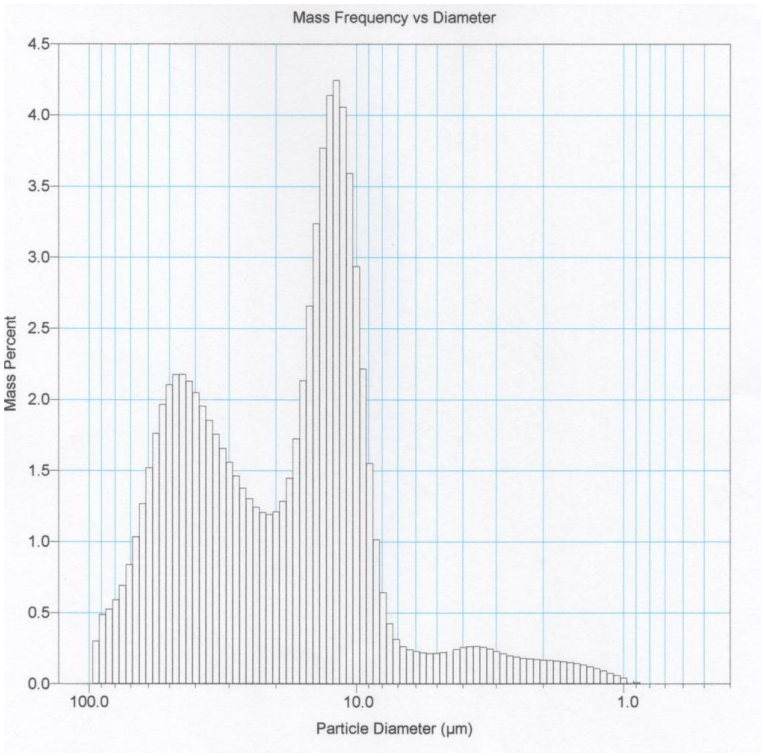


Figure 4.11: Particle size distribution of as-purchased MgB_2 powder measured by X-ray sedimentation using isopropanol as the dispersion medium

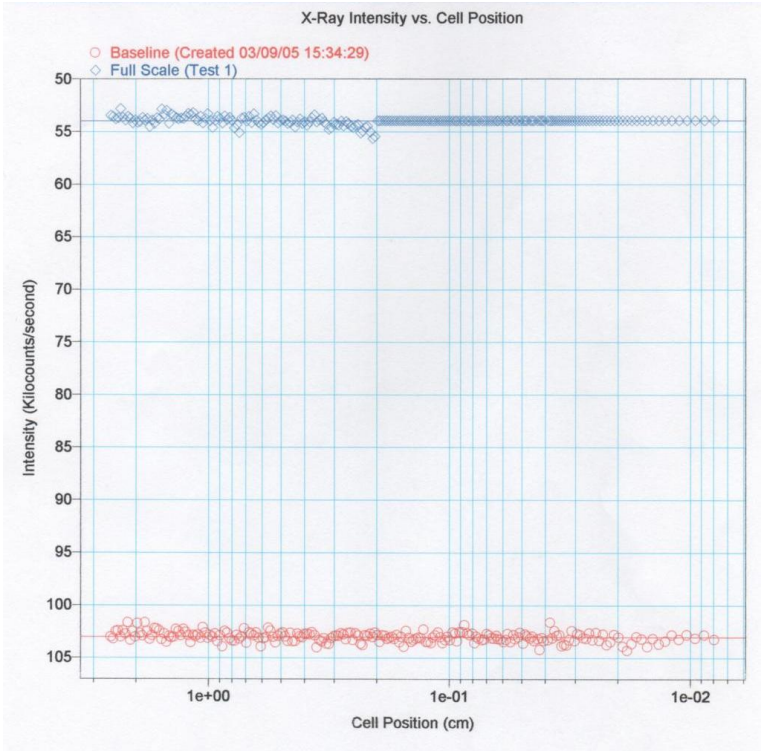


Figure 4.12: X-ray signal stability for Sedigraph run in isopropanol shown in Figure 4.11

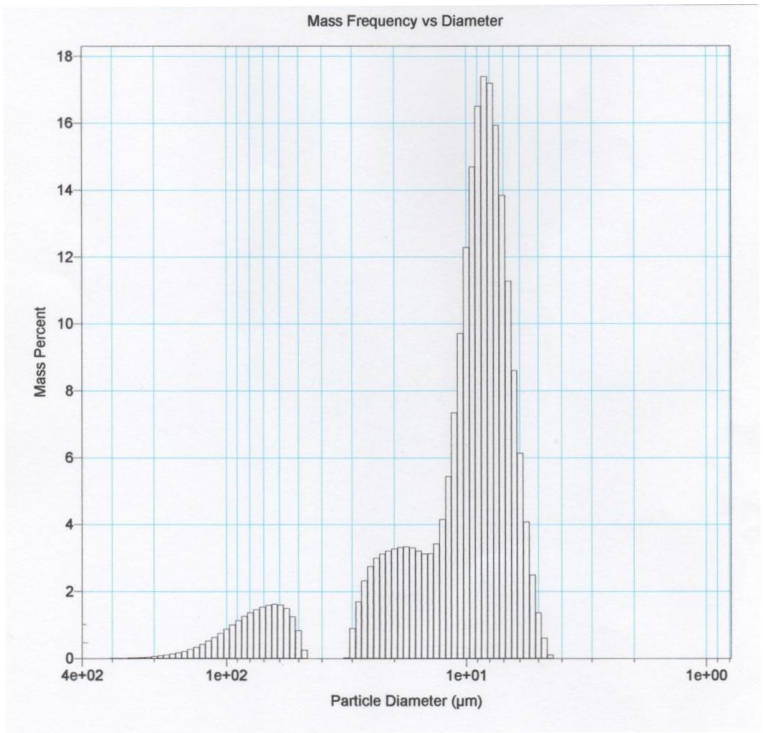


Figure 4.13: Particle size distribution of as-purchased MgB_2 powder measured by X-ray sedimentation using ethylene glycol as the dispersion medium

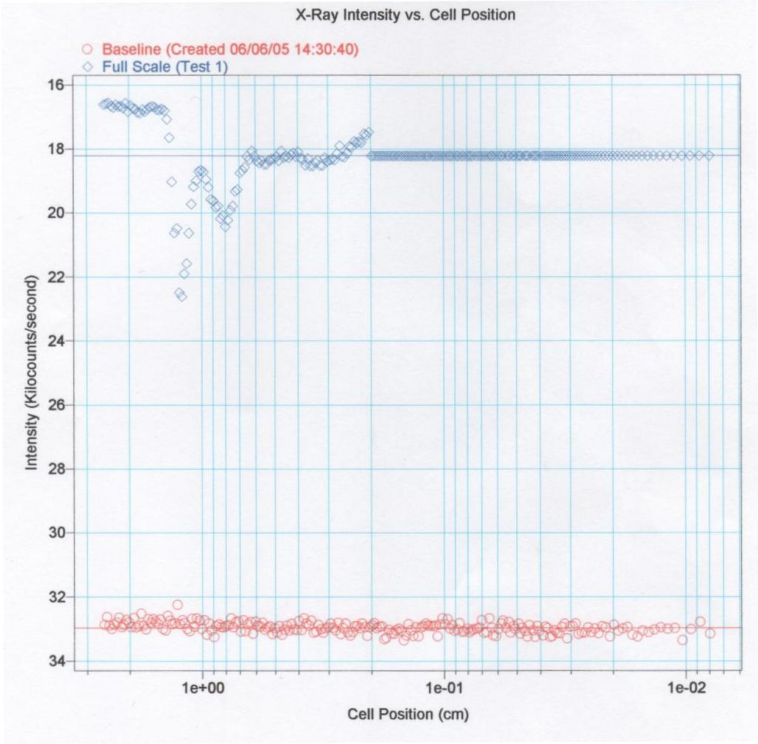


Figure 4.14: X-ray signal stability for Sedigraph run in ethylene glycol shown in Figure 4.13

4.1.2.3 Laser diffraction

After the difficulties experienced with using the Sedigraph, I borrowed a Malvern Mastersizer S from the EPSRC Engineering Loan Pool (operated by the Science & Technology Facilities Council). This instrument uses laser diffraction to measure particle size. A dispersion of solid particles in a liquid is pumped through a cell mounted in the path of a laser beam. The laser light scatters at characteristic angles dependent on the particle size. Detectors mounted at various angles to the laser beam detect this pattern and use the Fraunhofer or Mie theories to calculate the particle size distribution. The Fraunhofer theory takes no account of the adsorption of light by the particles (*i.e.* assumes they are opaque), and additionally assumes the particles are disc-shaped. The Mie theory used in this work is more accurate as it allows for the adsorption of light by considering the refractive index and transparency of the particles, and assumes particles are spherical as the measurements are based on scattering volume not on actual dimensions.

The Mastersizer S consists of a long bench-top unit enclosing the laser unit at one end

and with a mounting for the cell at the other. Lenses are mounted periodically along the laser path. The cell is linked to an external dispersion unit by polyethylene tubing. The cell can be completely removed and dismantled for cleaning, which was done whenever the background scan indicated contamination. The machine is linked to a computer with a dedicated interface program for recording measurements. The basic procedure is as follows. The dispersing liquid is added to the dispersion unit and pumped into the cell, then a background reading is taken. The solid is then added to the dispersion unit while the liquid is still being pumped through the cell. Once the predetermined obscuration level of the laser is reached, sufficient sample has been added. Measurements are then taken of the particle size distribution.

Extensive tests were carried out to determine the parameters which gave an accurate measurement of the particle size distribution in the MgB_2 powder. A number of variables could be adjusted; the dispersion concentration (proportional to the obscuration of the laser beam), the dispersing liquid, the speed at which the dispersion is stirred in the dispersing unit, and the dispersion method. The optimum value for each of these variables can be found by systematic variation of the variable plotted against the particles size for which 90 vol.% of the particles have diameters below the given spherical diameter ($d_{v,90}$), the median diameter ($d_{v,50}$), and the particle size for which 10 vol.% of the particles have diameters below the given spherical diameter ($d_{v,10}$). The process of determining the optimum value of each variable is described below.

The obscuration of the laser beam is controlled by the amount of solid material which is added to the Mastersizer S dispersion system following the initial measurement of the background (laser beam passes through the dispersing liquid only). At very low concentrations, insufficient numbers of particles will be measured. At very high concentrations, multiple scattering events can occur leading to inaccurate results. Figure 4.15 shows the effect on $d_{v,90}$, $d_{v,50}$ and $d_{v,10}$ of changing the obscuration by adding increasing amounts of MgB_2 to the dispersing unit. Little variation is seen in the measures of particle size for the various obscuration. Therefore I decided to use the manufacturers guideline and add

solid to an obscuration of approximately 25 %.

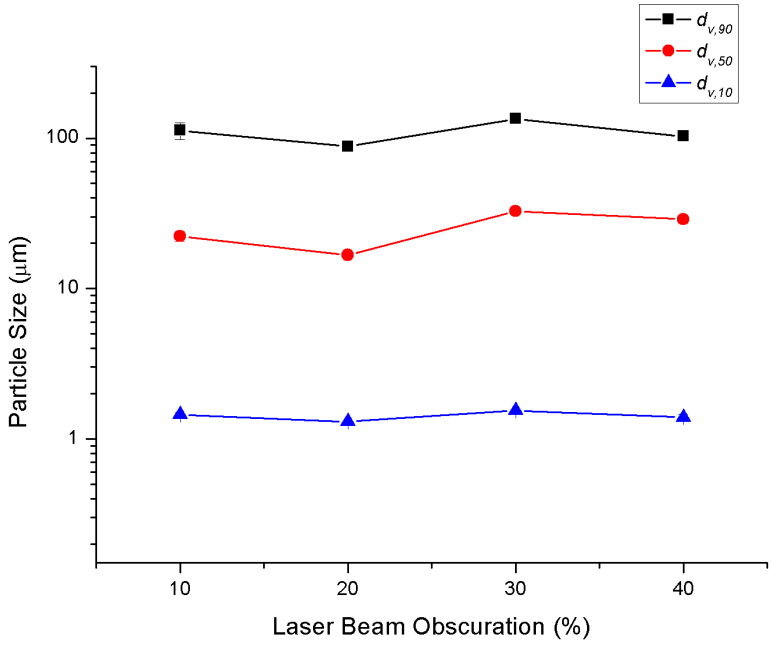


Figure 4.15: Effect of systematic variation of the obscuration of the laser beam on measured particle size distribution in the Mastersizer S. The obscuration of the laser beam is proportional to the concentration of solid in the dispersing liquid.

The stirring speed of the dispersion unit can be manually set at any point in the range $0 < v\,(\text{rpm}) < 3500$. According to the manufacturers instructions, if the speed is too slow, large particles are not propelled around the tubing and into the cell, and so $d_{v,90}$, $d_{v,50}$ and $d_{v,10}$ are underestimated. However at excessive speeds the particles are vigorously agitated which can lead to break-up of particles (depending on the strength of the material). For MgB_2 in isopropanol, the speed was optimised by measuring the $d_{v,90}$, $d_{v,50}$ and $d_{v,10}$ values obtained for the same sample when using different stirring speeds (Figure 4.16). Measurements were repeated five times and averaged. The most consistent results were obtained for $v > 1500$ rpm where the curves in Figure 4.16 begin to plateau so 2000 rpm was used as the stirring speed. The plateau indicated that the Mastersizer did not break up the MgB_2 particles, as this would have resulted in a bell-shaped curve.

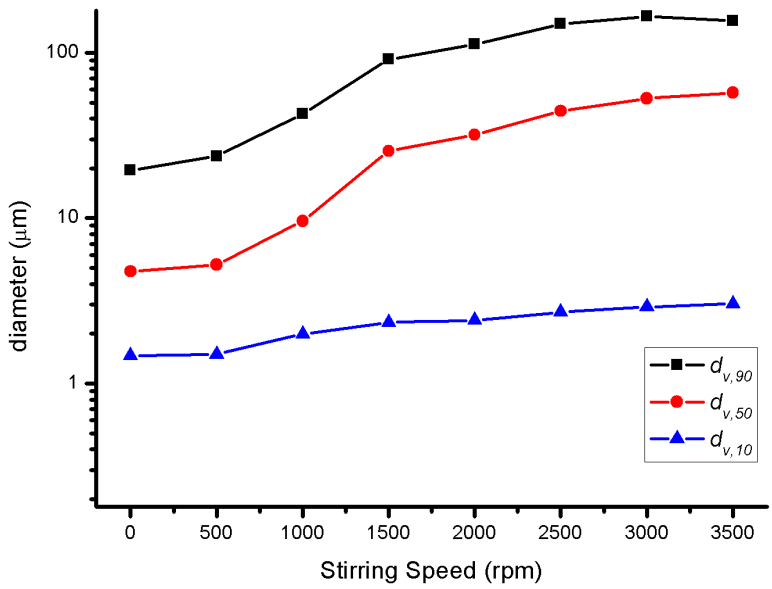


Figure 4.16: Determination of optimum rotation speed of the Mastersizer S Small Volume Dispersion Unit

The Mastersizer S can accept samples in a number of ways. Dry samples can be added directly to the Small Volume Dispersion Unit or dispersed samples can be added using a pipette. Pre-dispersing the samples in a small quantity of dispersing liquid allows the solid phase to be dispersed by a number of methods prior to adding to the sample; adding the samples dry means that the sample is dispersed only by the stirring of the dispersion unit.

Initially, dry powder was added to isopropanol directly in the dispersing unit and the measurement taken. Further tests using pre-dispersion methods were then carried out using 0.1 g MgB_2 powder added to 5 ml of isopropanol in a 14 ml vial. The vial was then subjected to one of the following dispersion methods:

- stirring (circulation using a pipette) for 30 s
- ultrasonication using an ultrasonic bath for 30-600 s
- ultrasonication using an ultrasonic probe for 30-300 s

As the dispersion methods are intended to break up the agglomerates in the powders, the quality of the dispersion can be assessed using the $d_{v,90}$, $d_{v,50}$ and $d_{v,10}$ values. In this case, the best dispersion (*i.e.* the dispersion method which produces the most broken-up agglomerates and hence the most accurate measure of the true particle size) is that with the *smallest* $d_{v,90}$, $d_{v,50}$ and $d_{v,10}$ values. Following dispersion by the methods above, particle size distributions were measured for all samples.

The smallest $d_{v,90}$, $d_{v,50}$ and $d_{v,10}$ values were obtained after 6 min in the ultrasonic bath (Figure 4.17). The ultrasonic probe requires a larger sample volume to be of use; the heating due to the action of the probe resulted in greater agglomeration than for the ultrasonic bath (Figure 4.18). The optimum ultrasonication time is a balance between having sufficient time to break up the agglomerates, and avoiding the temperature rise which occurs when small volumes of liquid are ultrasonicated for long times. The effect of heat was investigated by measuring the particle size distribution of dispersions at 4 °C (ice bath), 25 °C (room temperature) and 40 °C (warm bath). The effect of temperature on $d_{v,90}$, $d_{v,50}$ and $d_{v,10}$ is shown in Figure 4.19. From this graph, it is clear than agglomeration is more severe in samples at higher temperatures. For this reason, care was taken to prevent the samples heating up during ultrasonication by adding ice to the water in the ultrasonic bath.

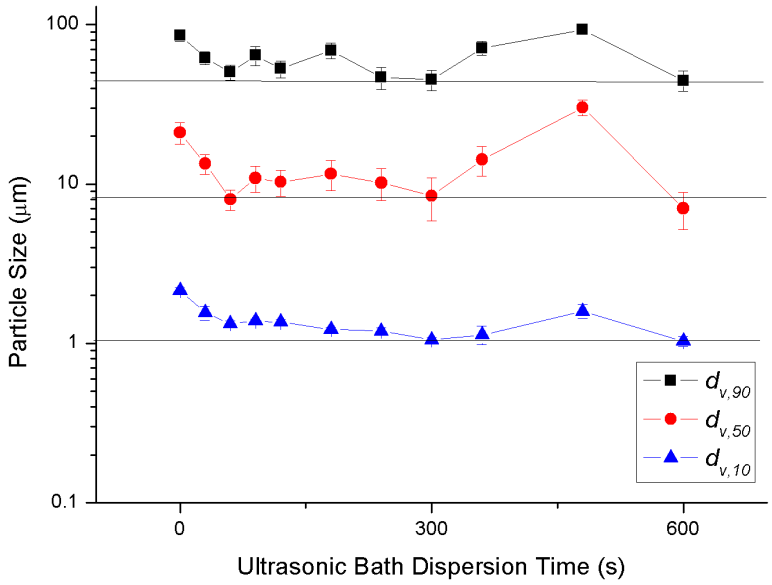


Figure 4.17: Effect of ultrasonication using ultrasonic bath on particle size distribution. The horizontal lines are a guide to the eye.

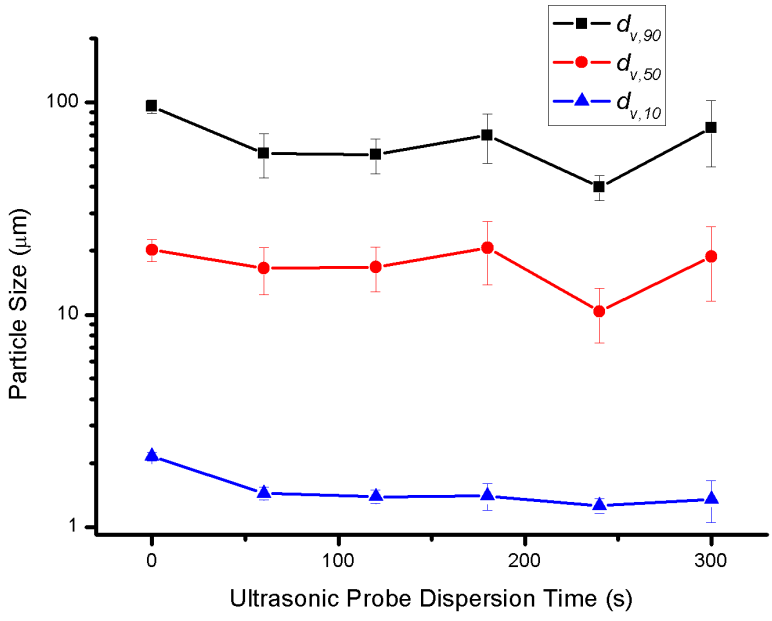


Figure 4.18: Effects of ultrasonication using ultrasonic probe on particle size distribution

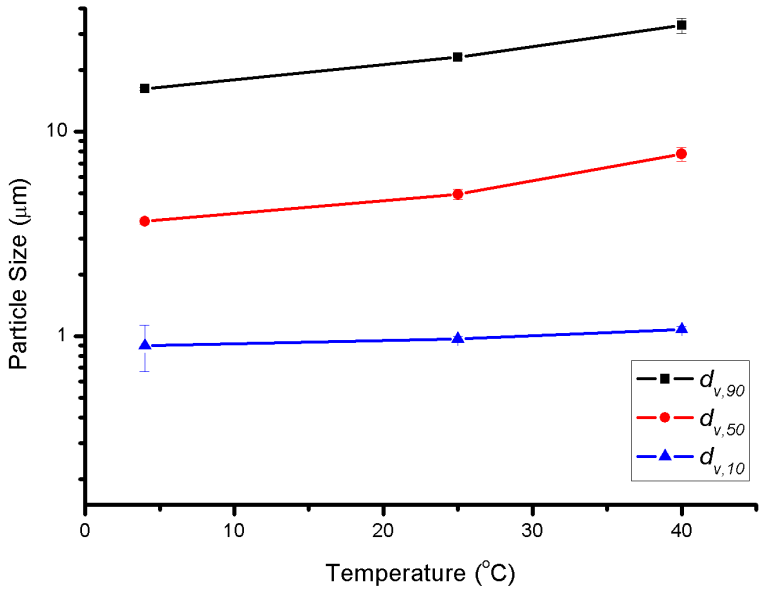


Figure 4.19: Effect of dispersed sample temperature on measured particle size distribution

This extensive calibration work reveals that the difference between the measured particle size distribution of powders which were added dry, stirred, and following ultrasonication is significant (Figure 4.20). After ultrasonication the volume of large particles is dramatically reduced, with $d_{v,90}$ falling to 24.8 μm (compared to $d_{v,90}$ = 114 μm for the dry powder) indicating that some of these large "particles" are in fact soft agglomerates of finer material. Even the limited agitation caused by briefly stirring the powder has some effect on the particle size, reducing $d_{v,90}$ from 114 μm for the dry powder to 95.7 μm for the stirred powder, indicating that the some of these agglomerates are very easy to break up, and so would be readily broken up during mechanical processing. However if any of them are well adhered (and therefore difficult to break up), the density of bulk samples produced from this powder will be affected as agglomerates contain internal porosity.

Comparison of the measurements of the Sedigraph 5100 and the Mastersizer S (Figure 4.21) indicate that the Sedigraph appears to underestimate the proportion of fine particles compared to the Mastersizer S. Subsequent measurements on modified powders were only carried out using the Mastersizer S (see Chapter 5).

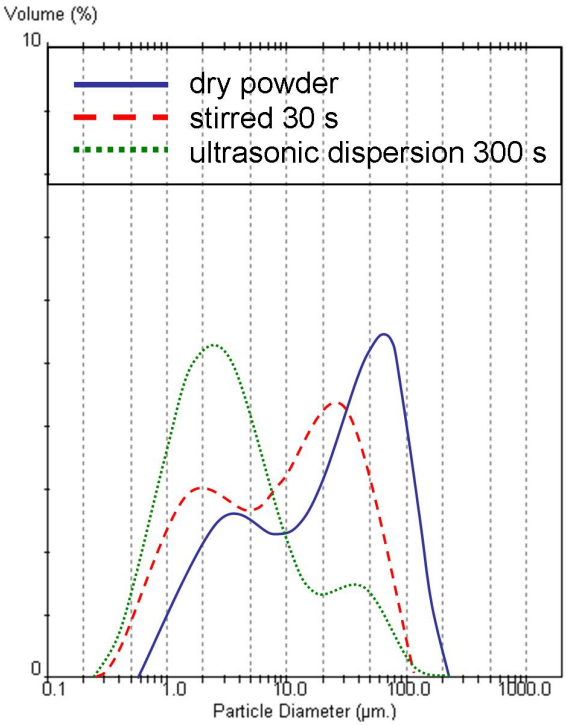


Figure 4.20: Particle size distributions of as-purchased MgB_2 powder measured by laser diffraction

The particle size distribution of a different batch of Alfa Aesar powder (#06051) was also measured. This powder was prepared in the same ways as the first batch (added dry, and dispersed by stirring and ultrasonication), and the results are shown in Figure 4.22 with traces of the distribution for the main batch (#20031) for comparison. The earlier batch (#06051) initially has a mono-modal distribution when added dry or stirred; however ultrasonication reveals a bi-modal distribution. Both batches contain a wide range of particle sizes from around $0.3\,\mu\text{m} < d_v < 100\,\mu\text{m}$ following ultrasonication, though batch #20031 contains a larger volume of fine material than batch #60501 when added as dry powder. While there is always some variation in the particle size distribution for different powder samples prepared in the same way from the same batch, the batch-to-batch variation seen here is more significant than that observed for various samples of #20031. Particle size distribution measurements were repeated using three different samples from batch #20031 with good agreement. These results indicate the importance of carrying out these measurements for each powder used.

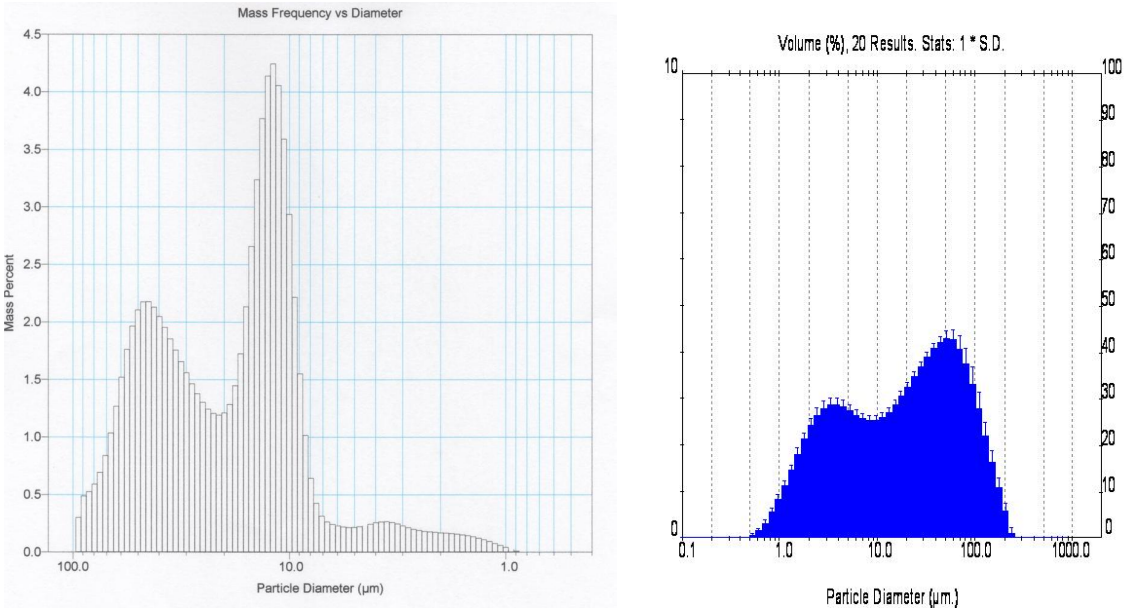


Figure 4.21: Comparison of Sedigraph (left) and Mastersizer (right) measurements of the same batch of as-purchased MgB_2 powder. Both powders were initially stirred in isopropanol prior to measurement.

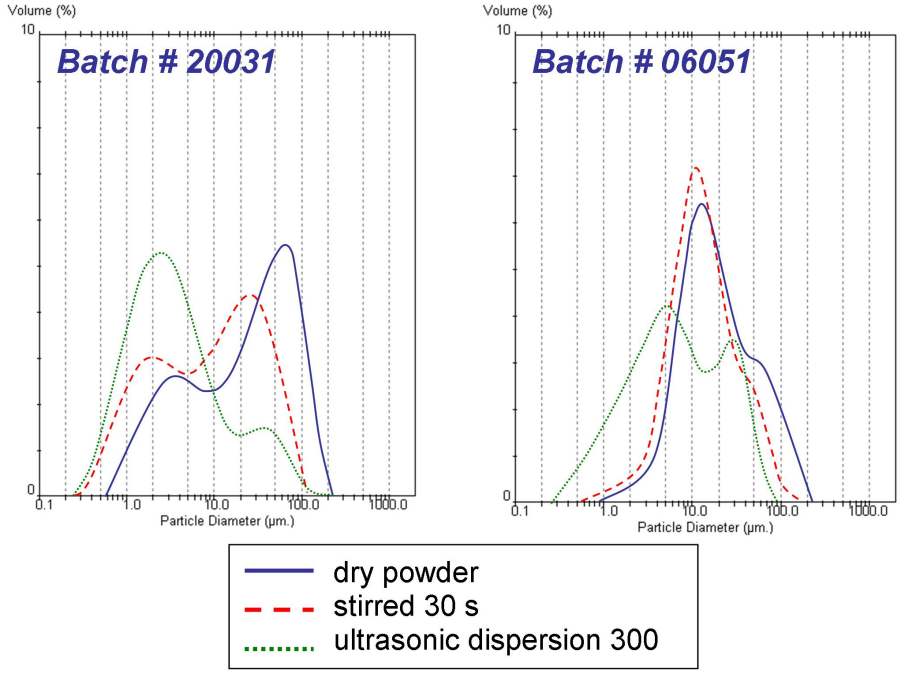


Figure 4.22: Comparison of particle size distributions obtained for samples of MgB_2 powder from two different batch numbers

This extensive calibration and examination of as-purchased MgB_2 powder indicates the importance of the choice of dispersion method in measuring the particle size. The few

reports of particle size distribution of MgB_2 powder in the literature (see, for example, [64; 65]) are most similar to those measured here for the dry powder, however this neglects the agglomeration, which may be reduced by mechanical processing, leading to a smaller effective particle size. This affects the packing density of the powder. In addition, the effect of ball milling may be overstated in the literature; in particular, very short milling processes are likely to be simply breaking up agglomerates, and to minimise contamination it may be better to do this using ultrasonication or mechanical processing. Finally, it has been demonstrated that the widely-used Alfa Aesar MgB_2 powder varies in particle size from batch-to-batch, particularly when dry, as the extent of agglomeration varies significantly.

4.1.3 Summary

Characterization of as-purchased MgB_2 powder indicates that is is relatively pure, though it contains some impurities detectable by XPS measurements, including carbon and oxygen and small amounts of silicon, nitrogen, fluorine and argon. However these impurities are likely to be confined to the surface. Observation of the particles using electron microscopy indicates that the powder is inhomogeneous, consisting variously of single-crystal particles and agglomerates with a wide size range. Accurate measurements using laser diffraction indicate that the particle size range of the dry powder is approximately $0.6 < d_v(\mu\text{m}) < 300$ with $d_{v,50} = 30\,\mu\text{m}$ and that it is extensively agglomerated. Ultrasonication reduces the particle size range to $0.3 < d_v(\mu\text{m}) < 80$ ($d_{v,50} = 8.4\,\mu\text{m}$) and changes the shape of the particle size distribution considerably.

4.2 Pressureless Heat-Treatment

4.2.1 Measurement of increase in MgO content using XRD

Many studies on the production of MgB_2 artefacts have cited the need to protect the material from air during heat-treatment to minimise the formation of impurity phases (see, for example, Agrestini *et al* [97] and Section 2.5.4.1). Tests were carried out using several methods of protection. The success of each protection method was assessed by measuring using XRD the amount of MgO formed on the surface of the bulk pellet following heat-treatment. In order to do this, a reliable method of measuring the MgO content had to be established. Standard powder samples containing known proportions of MgO (BDH Ltd) and MgB_2 (Alfa Aesar) were prepared. XRD spectra for the range $10^o < 2\theta < 85^o$ were recorded for each sample. Two pairs of peaks were selected for comparison as they lie within a few $^o2\theta$ of each other (this minimises systematic intensity variations due to different incident angles of the X-rays). Details of the peaks used are shown in Table 4.4.

Table 4.4: Details of the XRD peaks used for MgO content calibration

	MgB_2 Peak	2θ	MgO Peak	2θ
Pair 1 (B1 and O1)	(110)	59.884^o	(220)	62.302^o
Pair 2 (B2 and O2)	(201)	76.123^o	(311)	78.689^o

The strongest peak in the MgB_2 XRD spectrum is $(101)_{MgB_2}$ at $2\theta = 42.411^o$; for MgO the strongest peak is $(200)_{MgO}$ which lies at $2\theta = 42.916^o$. This pair of peaks was not used as they overlap severely, such that the MgO peak cannot be separated from the MgB_2 peak.

Peak areas were assessed using the Philips ProFit program, which uses a pseudo-Voigt function for peak fitting. The ratios of the peak areas were calculated for B1:O1 and B2:O2 and plotted against added MgO content. The errors in the added MgO content were estimated at ± 1 wt.%. The error in the ratio of the peak areas, due to the assumption of a pseudo-Voigt peak shape, was found to be negligible (< 0.05). There was significantly more scatter in the results for the ratio B2:O2 because of the low intensity of the O2 peak

(Figure 4.23), and the MgO peak could not be detected for MgO content below 6 % rather than 5 % for the B1:O1 ratio. For this reason, I decided that the peak area ratio B2:O2 is unsuitable for analysing MgO content. The resulting ratios of peak areas for B1:O1 have been plotted against the MgO content of the standards and a standard curve generated using an exponential decay relationship (Figure 4.24).

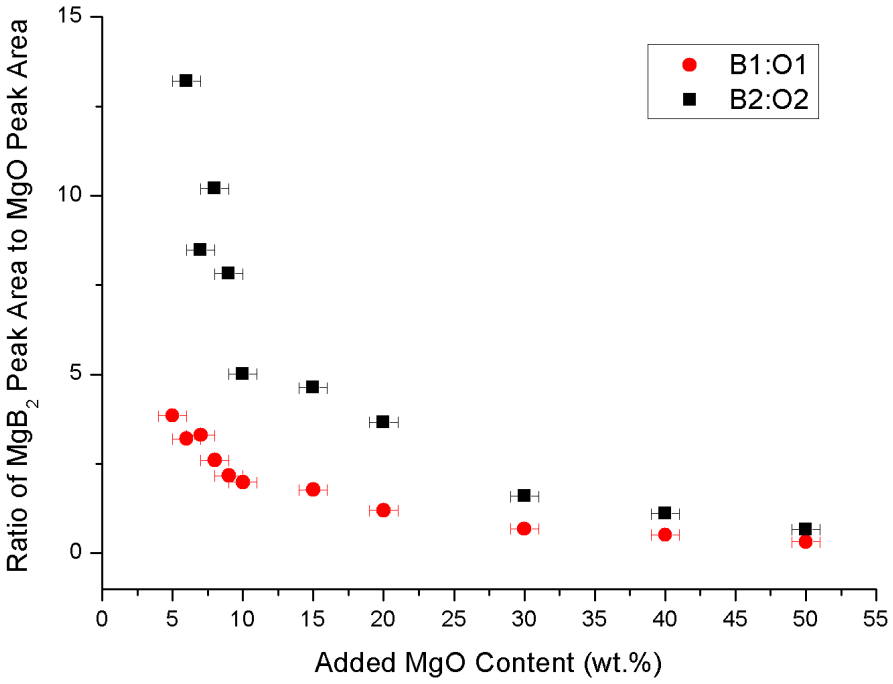


Figure 4.23: Comparison of MgO content calibration curves calculated from XRD scans using peak area ratios B1:O1 (red) and B2:O2 (black).

Below an MgO content of 5 wt.%, peak O1 is very weak. The calculated ratio flucuated with MgO content (for $0-5$ wt.%) rather than in a monotonic relationship. Therefore the MgO content of samples containing less than 5 wt.% MgO cannot be accurately measured using this diffractometer. This indicates the limitation of using XRD measurements to establish purity of MgB_2 samples. Previously this powder has been reported as containing less than 5 % MgO measured from XRD spectra [131] but this measurement is likely to have serious errors even when calculated using Rietveld refinement.

To calculate MgO content for samples with unknown composition, XRD scans were

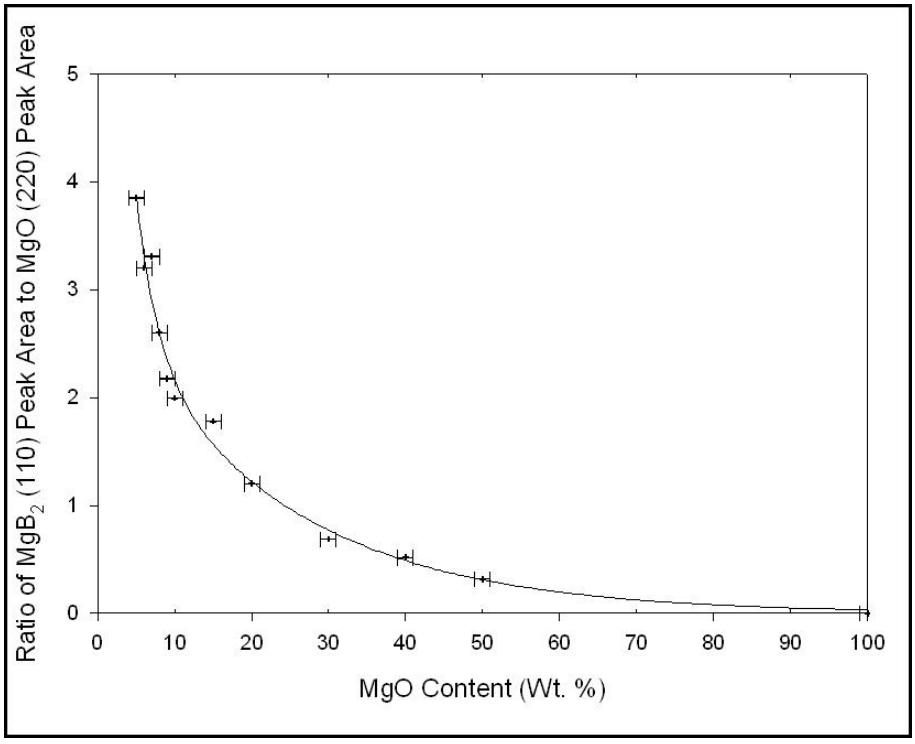


Figure 4.24: Calibration curve for MgO content in MgB_2 samples determined using XRD, peak area ratio B1:O1, and fitted to a exponential decay curve using Origin 8.0 software

taken in the same way and the areas of peaks B1 and O1 were measured using ProFit software. The ratio of the peak areas (y) was calculated and the MgO content (x) obtained using the exponential decay equation generated by the Origin software in Figure 4.24 (Equation 4.4).

$$y = 8.4908\, e^{-0.3507x} + 3.0208\, e^{-0.0456x} \tag{4.4}$$

4.2.2 Establishing the method for pressureless heat-treatment

The lack of consensus in the literature (see Section 2.5.1 on page 26) on the most effective heat-treatment meant it was important for me to establish a reliable method. The main priority was to minimise the increase in impurity content during heat-treatment so that any changes in density could be attributed to the densification by sintering, rather than to the formation of denser impurities such as MgB_4.

Heat-treatment was initially carried out in a tube furnace. The pressed pellet was

placed in an alumina boat at the centre of the hot zone. Heat-treatment at 950 °C for 30 min (heating rate 500 °C/h; cooling rate set as 650 °C/h then furnace cooling which is slower that the set rate) was carried out using high-purity Ar gas (BOC Pureshield 99.995 %) flushed through the furnace for 30 min prior to heat-treatment at 600 cm^3/min, and throughout the heat-treatment at 400 cm^3/min. The pellet produced was covered in white powder (shown using XRD to be MgO). Most MgO was found on the top side of the pellet. The underside of the pellet was not completely covered in MgO, being protected where it was in contact with the alumina boat. The experiment was repeated using highly reducing $Ar - 4\,\% H_2$ gas, but the MgO patches still formed, probably due to the equilibrium reaction $Mg + H_2O \rightleftharpoons MgO + H_2$ at 950 °C.

Alternative methods for protection during heat-treatment using shielding methods rather than gases were investigated. Welding samples into metal tubes was abandoned when it became clear that the pellet was heated significantly during the welding process, as shown by the results in Table 4.5. The best results were obtained by using a box furnace with an insert to allow heat-treatment in an inert gas environment. The volume of gas required is large, so $Ar - 4\,\% H_2$ could not be used for safety reasons. Instead high-purity argon gas was used. Significant oxidation still occurred (Table 4.5) when samples were unprotected, but because the furnace working volume is significantly larger than a tube furnace a powder bed could be used to prevent oxidation.

Graphite powder is often used (as in a graphite resistance furnace [218]), but as carbon is a strong source of pinning when used as an additive in MgB_2 powders, using a graphite powder bed could lead to misleading results. The rate of diffusion of carbon into the MgB_2 bulk would be temperature-dependent, and so it would be difficult to separate the effects of the heat-treatment and the graphite content. Instead, a powder bed of Alfa Aesar MgB_2 powder was used. This was placed in a closed alumina crucible with the pellet at the centre. Several samples could be heat-treated simultaneously.

At high temperatures MgB_2 can break down to Mg vapour and MgB_4 (see Section 2.5.4.1 on page 41). In the presence of oxygen, Mg vapour rapidly forms MgO, as appears to occur

here. Some magnesium oxide still formed in many samples even with the added protection of the MgB_2 powder bed; this is probably due to the adsorbed oxygen and water on the particle surfaces in the as-purchased powder before heat-treatment. Evidence for this comes from the fact that further protection of the MgB_2 pellet by enclosing the powder bed inside a second powder bed made no difference to the increase in MgO content, which was around 5 wt.% in both cases (see Figure 4.25 and Table 4.5). However the MgB_2 powder bed protection method avoids the white patches of oxide which presumably are caused by extensive reaction with oxygen from the Ar gas or from leaks allowing air into the furnace, and the increase in MgO content is significantly lower than for the other methods tested.

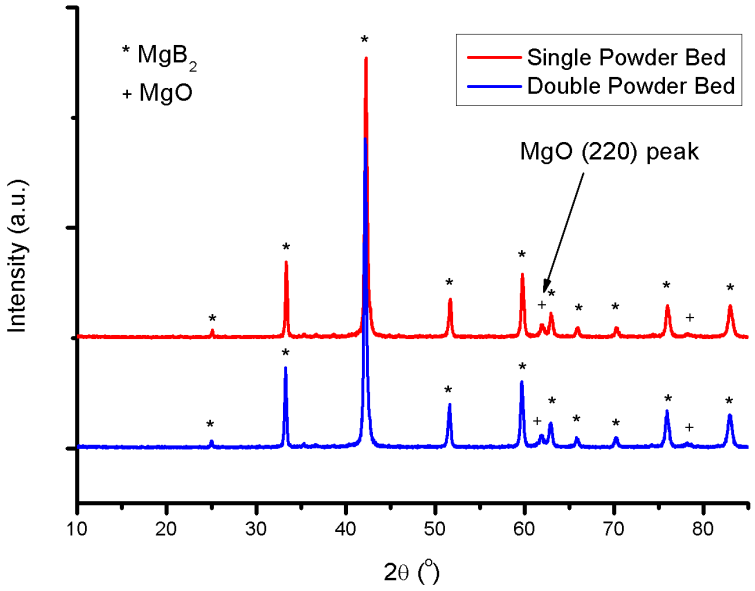


Figure 4.25: Comparison of XRD spectra taken from samples heat-treated to the same temperature but encapsulated in a (a) single and (b) double powder bed of MgB_2 powder during heat-treatment at 950 °C

The surface MgO compositions for representative samples prepared by each method are shown in Table 4.5. It is clear from the data in this table that to produce MgB_2 with MgO content of less than 10 wt.% at heat-treatment temperatures of 950 °C or above requires the extra protection of the closed Al_2O_3 crucible and MgB_2 powder bed. Heat-treatment

in air is particularly detrimental, with an increase in MgO content of nearly 17 wt.% for heat-treatment at the relatively low temperature of 650 °C. An MgO content of 10 % can be considered an upper limit for engineering applications of MgB_2 artefacts.

4.2.3 Standard method for pressureless heat-treatment

Bulk MgB_2 samples were produced by uniaxially pressing 0.5 g of MgB_2 powder in a stainless-steel die of diameter 9.1 mm. These samples were heat-treated in flowing argon using an adapted box furnace with an insert to allow the use of gases (Carbolite). The ramp rate was 10 °C/min and the sample was held at the chosen peak temperature for 1 h. This relatively short heat-treatment was chosen to mimic the heat-treatment typically used for annealing wires by our collaborators in Bratislava (950 °C for 30 min). A longer time ($\sim$ 1 h) was used to allow the bulk samples sufficient time to be sure that the entire body has reached the peak temperature (wires are typically 1-2 mm in diameter and are surrounded by a metal sheath, and so wires reach the peak temperature more rapidly than bulk samples). All samples were placed at the centre of an MgB_2 powder bed within a closed Al_2O_3 crucible because the previous experiments indicated that this method gave the lowest MgO content (see Section 4.2.2).

Samples were heat-treated at temperatures up to 1100 °C and then subjected to a series of characterization tests to measure the impurity content and density, and to assess the effect of heat-treatment on the microstructure.

4.2.4 Impurity Content post-Heat-Treatment

4.2.4.1 XRD

The surfaces of all pellets produced were examined using XRD; for clarity only four characteristic spectra are shown in 4.26. The spectrum of the non-heat-treated pellet is similar to that of the starting powder. The spectrum of the pellet heat-treated at 1100 °C contains significantly larger peaks due to impurity phases than those heat-treated at lower

Table 4.5: MgO content of the surface of MgB_2 pellets heat-treated using a number of methods

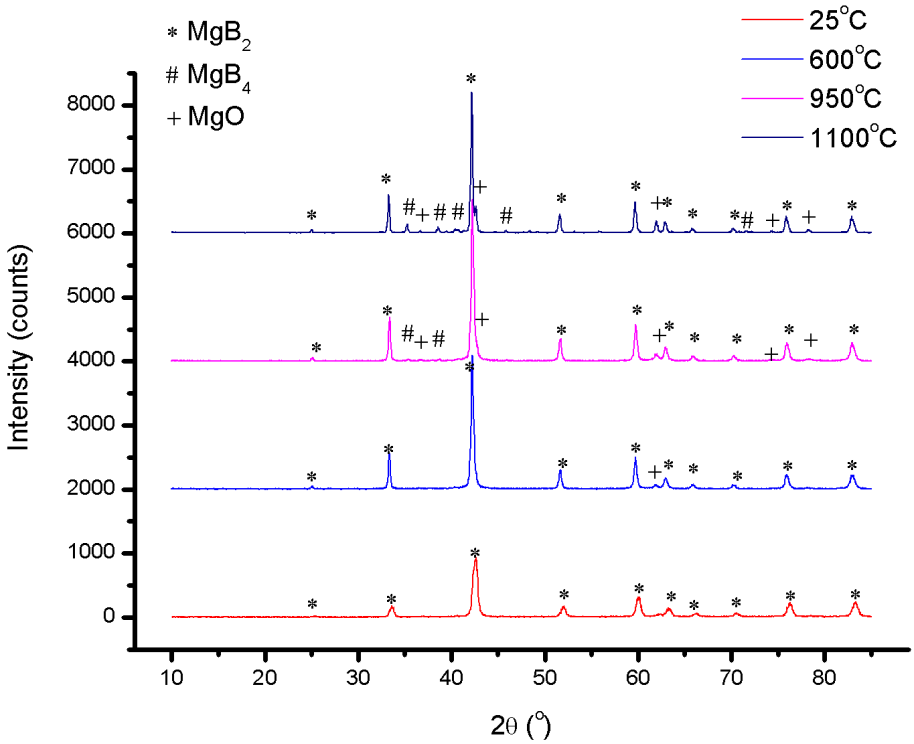
Heat-Treatment Method	**Heat-Treatment Temperature**	**Increase in MgO Content**
Tube Furnace, air, Al_2O_3 boat	650 °C	16.8 wt.%
Tube furnace, Ar-4 % − H_2 gas, Al_2O_3 boat	1000 °C	66.4 wt.%
Tube furnace, Ar-4 % − H_2 gas, welded into Fe tube	1000 °C	49.6 wt.%
Box Furnace with insert, Ar gas, Fe tube (sealed by pressing)	1000 °C	55.3 wt.%
Box furnace with insert, Ar gas, uncovered Al_2O_3 crucible	1000 °C	44.4 wt.%
Box furnace with insert, Ar gas, MgB_2 powder bed, closed Al_2O_3 crucible	1000 °C	8.3 wt.%
Box Furnace with insert, Ar gas, MgB_2 powder bed, single closed Al_2O_3 crucible	950 °C	5.2 wt.%
Box furnace with insert, Ar gas, double MgB_2 powder bed, two Al_2O_3 crucibles	950 °C	5.1 wt.%

temperature. These can be assigned to various planes in the patterns of MgB_2, MgO and MgB_4. Small peaks due to MgB_4 can be seen in the spectrum of the sample heat-treated at 950 °C but none can be readily distinguished from the background in the spectrum of the sample heat-treated at 600 °C. The size of the MgO (220) peak increases with heat-treatment temperature.

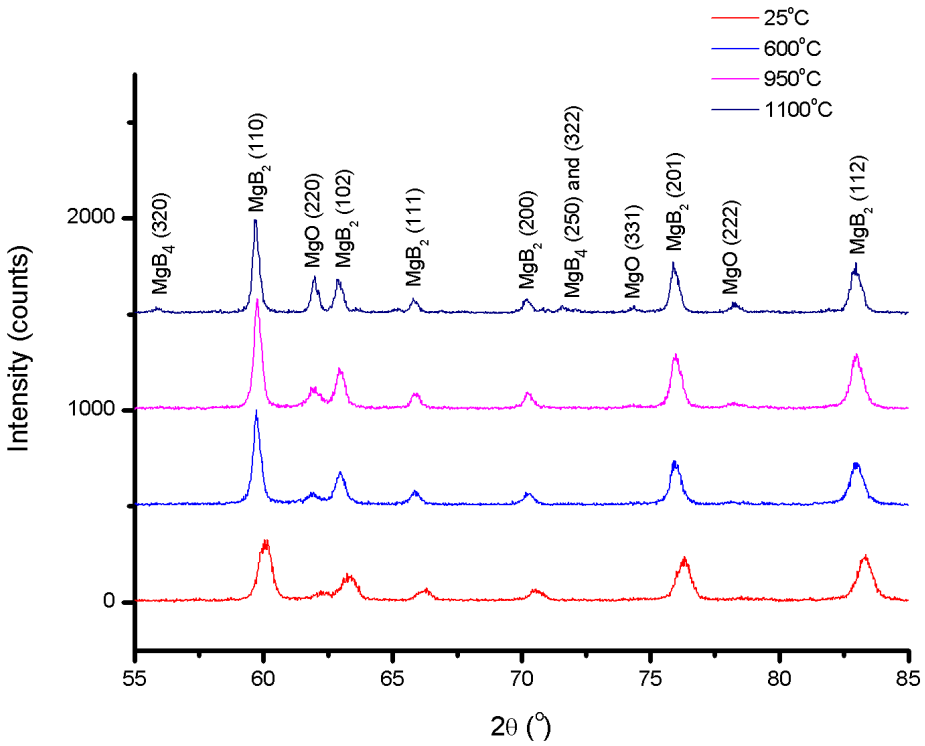
Peaks due to MgO are not discernible from the background for heat-treatment temperatures below 600 °C. Above this temperature MgB_2 begins to break down to Mg vapour and MgB_4 in the presence of oxygen gas [96]. The precise mechanism is unclear; however it seems likely that the O_2 originates either from the Ar gas (which would only need to contain ∼0.1 vol.% of O_2 to form 10 wt.% MgO during heat-treatment*) or from a leak in the gas inlet system, or from water vapour or gases adsorbed onto the surface of the MgB_2 powder. The Ar gas used in these tests was BOC Pureshield Argon, with a stated purity of 99.995 % so it seems likely that one or both of the latter explanations is the case. The remaining boron either forms MgB_4 (which is difficult to detect in small quantities using XRD as the spectrum does not contain many large peaks) or other boron-containing phases such as B_2O_3 which may be amorphous.

A clustering analysis using the Philips X'Pert Highscore Software was carried out on the XRD scans of all pellets produced from commercial MgB_2 powder. This analysis can be useful in detecting small differences in impurity content in XRD spectra. One scan from each sample (scans were collected using identical conditions in the XRD) is input into the clustering analysis program. This program then fits the data in each scan using a least-squares regression to obtain a mathematical representation of each scan. These are then compared, and the percentage difference between each pair of scans is charted. The degree of similarity between the scans is represented on a dendrogram. A larger separation between scans (on the x-axis) implies a greater dissimilarity between the two samples.

*Molar calculations using $Mg + \frac{1}{2}O_2 \rightarrow MgO$, and $p_{argon} = 0.25$ bar, argon gas flow-rate = 200cm^3/min during test, and assuming sample exposed to Ar gas for 5 h above MgO formation temperature (including heat-up and cool-down).



(a)



(b)

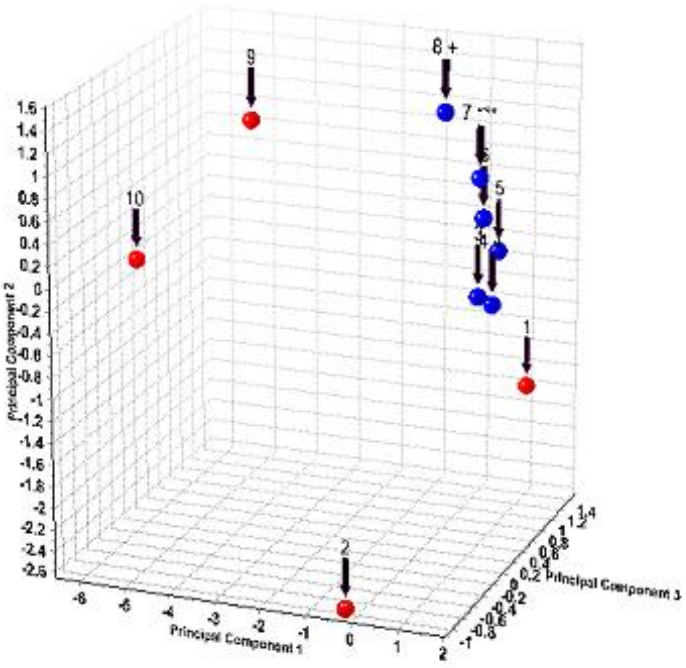
Figure 4.26: XRD spectra of MgB_2 pellets heat treated up to 1100 °C
a) Wide angular range
b) Expanded 2θ range containing peaks due to impurity phases

A principal components analysis was also carried out whereby the mathematical similarity between the scans is plotted graphically in three dimensions. The program uses the mathematical analysis to determine the degree of dissimilarity described above. The three components of the mathematical fitting which vary most significantly between scans (the three so-called "principal components") are established, and each scan is plotted on the diagram as a function of these values. In general the principal components analysis is most useful when the cluster analysis includes very different spectra (indicated by a large separation distance in the dendrogram), as otherwise the normalisation of the principal components leads to apparent large differences between scans where they are in reality very similar. All the MgB_2 powder samples produced very similar XRD scans, so clustering analysis was rather misleading, and therefore it was only used in this work for bulk samples.

Using this method for the XRD scans of the bulk MgB_2 samples produced the principal components analysis diagram and dendrogram shown in Figure 4.27 showing the relationship between the scans performed on the samples.

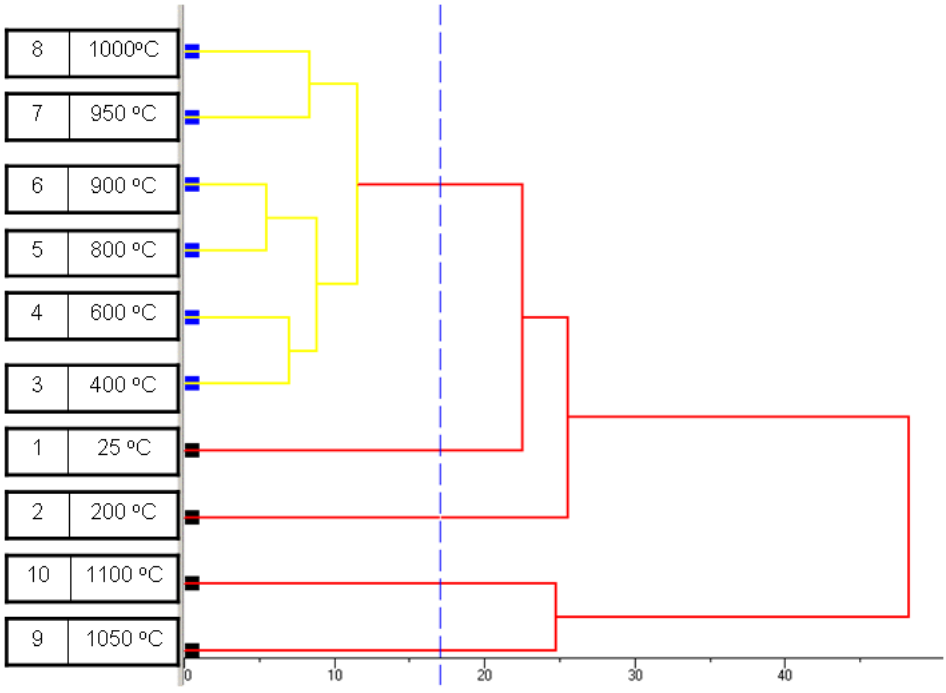
The dendrogram indicates that samples heat-treated between $400 - 1000\,^{\circ}C$ are more similar to each other than the other four samples (Figure 4.27b). This indicates that moderate temperature heat-treatment has some effect on the XRD scan (perhaps decreasing the amorphous content by evaporation or crystallisation). The remaining scans are grouped into low temperature ($25\,^{\circ}C$ and $200\,^{\circ}C$) and high temperature ($1050\,^{\circ}C$ and $1100\,^{\circ}C$) in the dendrogram (Figure 4.27b) The principal components analysis (Figure 4.27a) is in agreement with the dendrogram in grouping the scans into one large cluster for moderate heat-treatment temperatures (blue spots in Figure 4.27a).

MgO is an important impurity as its formation appears almost unavoidable during heat-treatment of MgB_2. When samples consist of a large fraction of impurity phases, other measurements of the material characteristics (*e.g.* density) must take account of this or else risk producing misleading results. For this reason, the calibration curve (Figure 4.24) developed to measure the MgO content of samples heat-treated in different environments



Number	Peak Temperature (°C)
1	25
2	200
3	400
4	600
5	800
6	900
7	950
8	1000
9	1050
10	1100

(a) Principal Components Analysis



(b) Dendrogram

Figure 4.27: Cluster Analysis for MgB_2 bulk heat-treated at $25 - 1100\,^oC$

was used to measure the quantity of MgO formed during heat-treatment. The increase in MgO content is shown in Table 4.6. For the sample heat-treated at high temperatures the MgO content as a percentage of the crystalline material in the sample is lower than that stated in Table 4.6, as the sample contains phases other than MgB_2 and MgO which are not taken into account.

Table 4.6: Impurity content of MgB_2 pellets from XRD analysis

Heat-Treatment Temperature (°C)	Increase in MgO Content as wt.% of MgB_2Content
25 (i.e. No Heat-Treatment)	0 (by definition)
200	$0-5\,\%$ (below detection limit)
400	$0-5\,\%$ (below detection limit)
600	$0-5\,\%$ (below detection limit)
800	$0-5\,\%$ (below detection limit)
900	5.0 %
950	5.0 %
1000	5.5 %
1050	6.0 %
1100	7.5 %

This calibration method was also used to establish whether the MgO content was particularly high at the surface. Depth profiling was carried out by obtaining a series of scans of the surface of a pellet heat-treated at 1100 °C with material removed between scans using SiC grinding paper, and the depth measured using a micrometer. The depth profile is shown in Figure 4.28. The MgO level at the surface is around 1 wt.% higher than that measured at a depth of 0.2 mm, and this level continues through the bulk of the material; this difference is within the error for these measurements. The MgO content increased appreciably throughout the sample during heat-treatment at high temperatures, not just on the surface. This means that either a large amount of O_2 gas or other oxygen-containing species are adsorbed onto the surface of particles in the green compact, or that the oxygen in the Ar gas or can easily penetrate the porous MgB_2 pellet during heat-treatment leading to reaction.

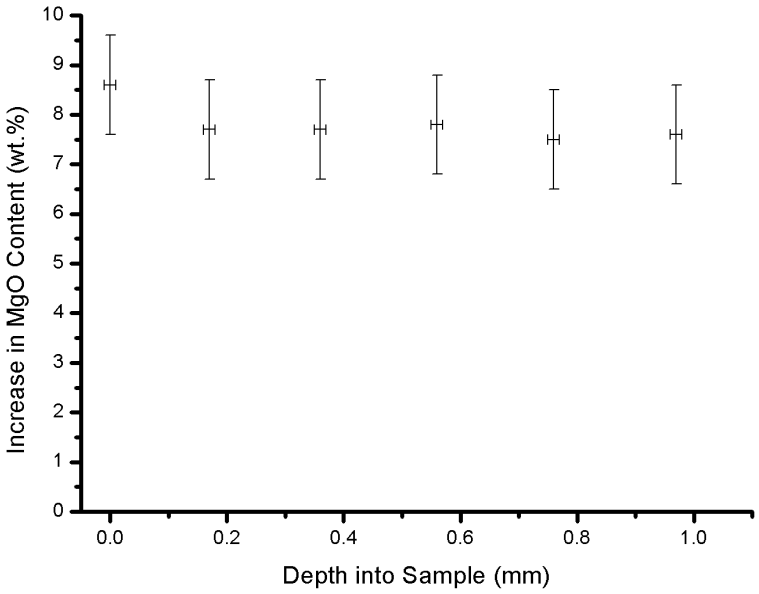


Figure 4.28: XRD depth profile for the increase in MgO content in MgB_2 bulk following heat-treatment at 1100 °C

4.2.4.2 EDX

EDX was not helpful for the examination of MgB_2 bulk samples because previous analysis of powder established that the only elements present in detectable quantities were Mg, B and O; and examination of the bulk samples confirmed that this remained the case after heat-treatment. As shown earlier, EDX cannot be used to establish whether areas consist solely of MgO or Mg-B phases because oxygen is present over most of the sample, and the errors in measuring the Mg:O peak ratio for MgB_2 and MgO regions are too great (see Section 4.2.4.2). This effect is exaggerated for rough porous samples (such as these) where it is difficult to know from which area the X-rays for a particular element originated. Finally, because the X-ray yield for boron is low, it is difficult to carry out quantitative EDX analysis, and so EDX cannot be used effectively to distinguish between areas of MgB_2 or higher borides such as MgB_4.

4.2.5 Density and Connectivity

The density of MgB_2 samples was measured before and after heat-treatment using Archimedes' method, and compared to that of pure MgB_2 calculated from the lattice parameters ($2.63\,g/cm^3$). Overall, the density following heat-treatment was similar to the density prior to heat-treatment at around 65 % of the theoretical density (see Figure 4.29), with variations largely falling within the estimated experimental error. Interestingly, there is no clear trend in the density change at high temperature, indicating that the density change is probably due to random fluctuations and experimental error rather than to any phase change or loss of material (for example by magnesium vaporization). To check the repeatability of these observations, three samples were made and heat-treated at each of the temperatures 600 °C, 950 °C and 1100 °C, with similar changes in density resulting for all of the samples.

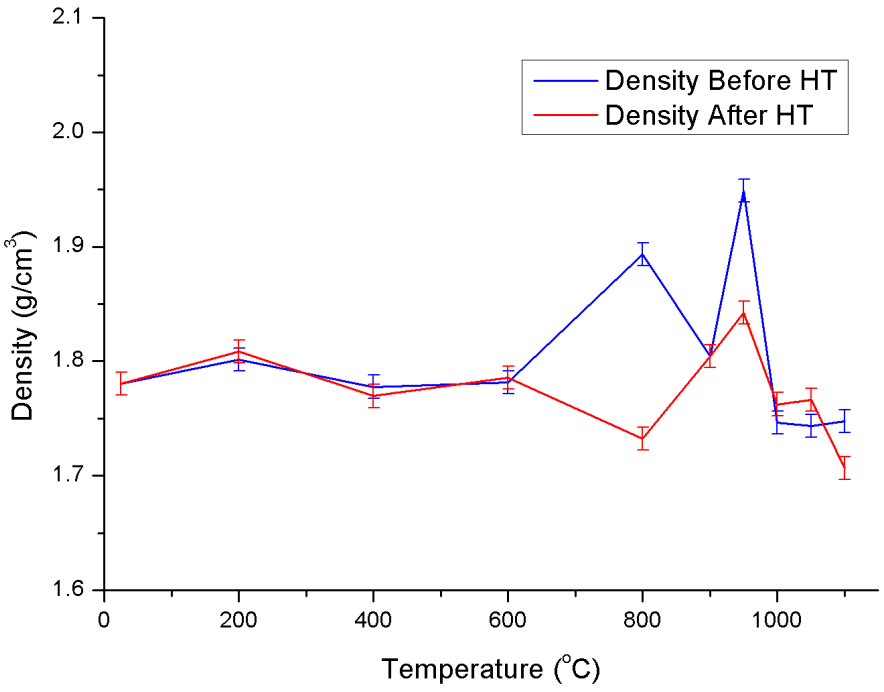


Figure 4.29: Change in relative density of bulk MgB_2 samples heat treated at temperatures up to 1100 °C in Ar gas

The evidence from the density measurements indicates that no true sintering behaviour

(leading to a large increase in density) has occurred. However initial sintering stages, such as adhesion between particles in contact and diffusion from the surface of particles, can occur without leading to densification [47], and so further tests were carried out in order to establish whether any of the characteristic signs of early stage sintering could be found.

Hardness testing can be used to measure the connectivity and density of ceramic compacts because, as the connectivity between particles increases, the resistance to permanent indentation increases. To measure the hardness, large pyramidal indentations were made using a Vickers hardness indenter with a fairly large load of 2 kg such that the indentations covered a large area (to avoid merely testing the hardness of individual particles of magnesium diboride). The diagonal lengths of the indents were measured using an optical microscope, and converted to Vickers hardness values. These were then plotted against the heat-treatment temperature for the pellet (Figure 4.30).

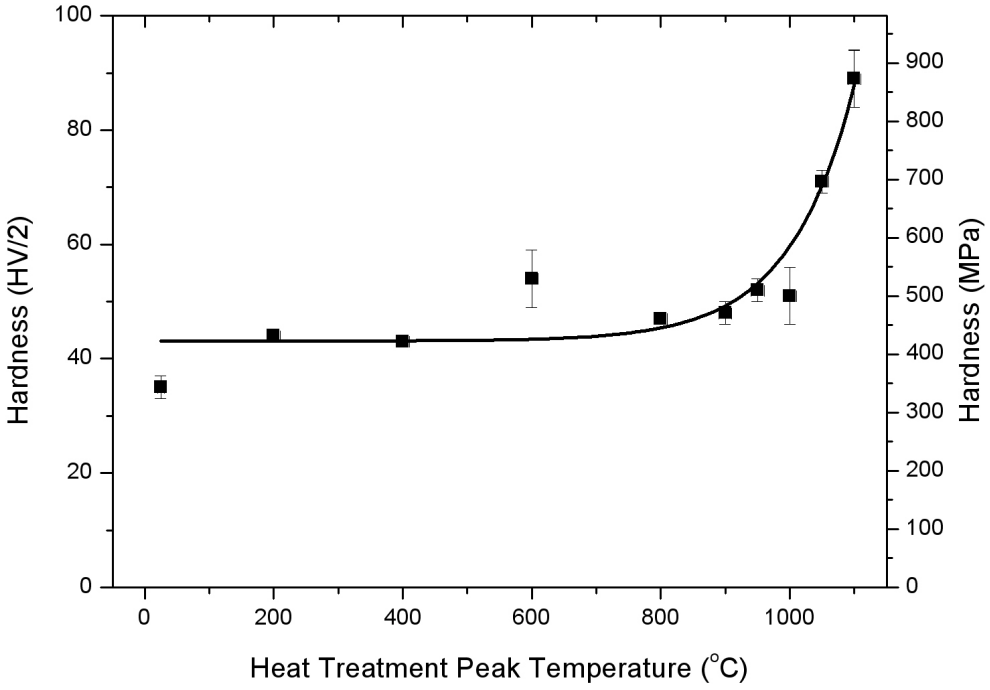


Figure 4.30: Variation in hardness with heat-treatment temperature

The hardness† is around 40 HV/2 for heat-treatment temperatures up to about 1000 °C

†Conversion: 1 HV/2 ≃ 9.807 MPa; HV/2 denotes the hardness in units of Vickers Hardness Number

(1 h in Ar gas). Above this temperature, the hardness rises rapidly, reaching about 90 HV/2 for heat-treatment at 1100 °C. The data has been fitted to the exponential relationship shown in Figure 4.30.

This hardness is significantly lower than that reported for dense MgB_2 produced by HIPing by Takano *et al* (1700 − 2300 MPa) [60]. Additionally, the hardest sample contains the largest amount of MgO (see Table 4.6), and has been shown from XRD scans to contain the additional impurity phase MgB_4. The formation of these impurity phases may be the true reason for the increase in hardness seen at high temperatures. Two scenarios can be envisaged for the mechanism. The formation of impurity phases may act as a binder between particles, leading to increased resistance to indentation. Alternatively, areas consisting largely of impurity phases may form at high temperatures. If these areas are harder than the surrounding matrix, the overall hardness would be increased in these areas. However in this case we would expect significantly more scatter in the data at high temperatures; the standard deviation of hardness measurements for pellets heat-treated across the entire temperature range is approximately constant at around 5 % of the mean hardness value for the sample.

Scanning electron microscopy was carried out on fracture surfaces of all samples to observe any changes in microstructure following heat-treatment. Micrographs of representative samples across the temperature range are shown in 4.31. There is little visual difference between the fracture surface of the sample which has not been heat-treated, and those which have undergone heat-treatment up to 1100 °C. Certainly for samples heat-treated up to 1100 °C no real difference is observed compared to the green compact. The sample heat-treated at 1100 °C appears to have experienced some grain growth with grains appearing smoother and larger (Figure 4.31d). This may be indicative of the formation of impurity phases or the effect of heat-treatment. As there are no signs of occluded porosity, clearly any sintering which has occurred is not very extensive, which is why it is not reflected in the density values. However this may explain the increase in hardness

measured with a 2 kg applied load

for the samples heat-treated above 1000 °C (see Figure 4.30).

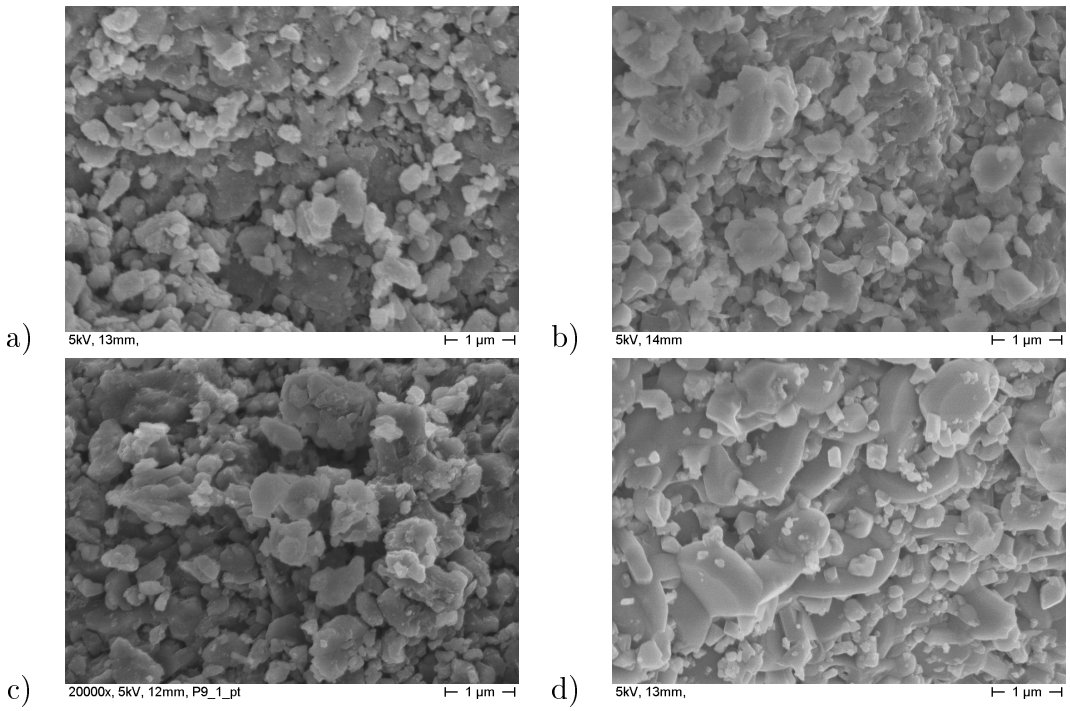


Figure 4.31: SEM images of fracture surfaces of bulk MgB_2 heat-treated up to 1100 °C
a) no heat-treatment (as pressed)
b) 600 °C for 1 h in Ar
c) 950 °C for 1 h in Ar
d) 1100 °C for 1 h in Ar

4.2.6 Magnetic Measurements

Magnetic measurements on selected samples were made using the Quantum Design Magnetic Property Measurement System (MPMS) by Dr D. Prabhakaran of the Department of Physics at the University of Oxford. Measurements were made at the commonly-used temperatures of 4 K and 20 K to aid comparison with the work of other research groups. The results of these measurements are shown in Figures 4.32 and 4.33. For ease of comparison, Tables 4.7 and 4.8 show the change in magnetization for the samples at 0 T, 1 T and 3 T, and H_{c2} (the applied magnetic field at which $\Delta M = 0$).

The heat-treatment strongly affects the magnetization in the sample. Connectivity increases with heat-treatment (as indicated by the rate of decrease in M with applied field; the more rapid the decrease the poorer the connectivity).

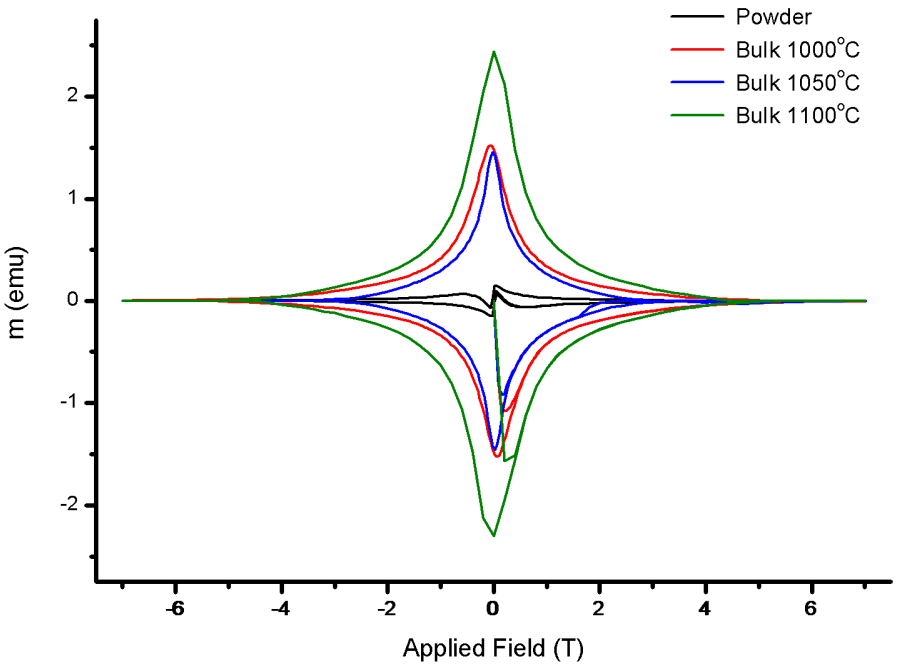


Figure 4.32: SQUID measurements at 4 K of magnetic moment in bulk MgB_2 samples

Table 4.7: Magnetization of MgB_2 samples at 4 K

Sample	ΔM at 0 T (emu)	ΔM at 1 T (emu)	ΔM at 3 T (emu)	H_{c2} ($\Delta M = 0$) (T)
Powder	0.122	0.08	0	4.8
1000 °C	3.03	0.75	0.16	5.6
1050 °C	2.91	0.56	0.02	5.6
1100 °C	4.72	1.30	0.25	5.4

Table 4.8: Magnetization of MgB_2 samples at 20 K.

Sample	ΔM at 0 T (emu)	ΔM at 1 T (emu)	ΔM at 3 T (emu)	H_{c2} ($\Delta M = 0$) (T)
Powder	0.12	0.08	0.02	2.7
1000 °C	1.61	0.32	0.01	3.4
1050 °C	2.90	0.56	0.01	3.2
1100 °C	2.77	0.55	0.00	3.0

Values of $J_{c,mag}$ were calculated for the bulk samples from the magnetization loops by using the Bean model (Equation 4.5).

$$J_{c,mag} = 2\frac{\Delta M}{d} \tag{4.5}$$

To obtain $J_{c,mag}$ in the standard units of A/cm^2, ΔM must be calculated in units of emu/m^3. To convert from emu/m^3 to A/m^2 ΔM must be multiplied by 10^{-3}. The characteristic length d was taken to be the thickness of the sample (*i.e.* the dimension perpendicular to the applied magnetic field). The $J_{c,mag}$ versus applied magnetic field curves are shown in Figure 4.34 for 4 K and 20 K.

At 0 T, 20 K the highest $J_{c,mag}$ achieved was a respectable value of 5×10^4A/cm^2 for the pellet heat-treated at 1100 °C. In comparison, dense hot-pressed MgB_2 samples achieved 10^5A/cm^2 under the same conditions [15]. This indicates that samples prepared by pressureless heat-treatment can achieve high $J_{c,mag}$ despite their low density. However, the hot-pressed sample has superior flux pinning, retaining $J_{c,mag} \geq 10^3$A/cm^2 to 4.3 T, while the pressureless heat-treated sample could only sustain this up to 2.3 T. This is presumably due to the improved microstructure of the hot-pressed sample, consisting of well-connected grains with a relatively small grain size due to rapid heat-treatment.

4.2.7 Summary

Bulk magnesium diboride is difficult to fabricate without the formation of impurity phases during heat-treatment, in particular MgO. A robust method was established using a MgB_2 powder bed which reduced the MgO formation to a minimum. The increase in MgO content was measured by comparing the XRD scans of heat-treated samples to those of specially prepared known standards. An increase of around 7.5 wt.% should be expected throughout the sample following heat-treatment at 1100 °C.

Density, hardness and magnetization measurements and SEM observations were made to assess the connectivity. Little change in density is observed for heat-treatment up to

1100 °C. Otherwise, the results of all tests indicate some increase in connectivity for heat-treatment above 1000 °C. The hardness remains more or less constant for heat-treatments up to 1000 °C, then increases significantly in comparison to the initial hardness, but insignificantly compared to the increase in hardness observed following pressure-assisted heat-treatment which is known to produce dense material. SEM images corroborate these observations, and indicate no signs of true sintering behaviour such as neck formation and occluded porosity, though some grain growth was observed following heat-treatment at 1100 °C. Magnetization measurements indicate that a significant increase in connectivity occurs for bulk samples compared to powders, and an increase in the diameter of the magnetization loop is observed for increasing heat-treatment temperature. The optimum magnetization behaviour is observed following heat-treatment at 1100 °C.

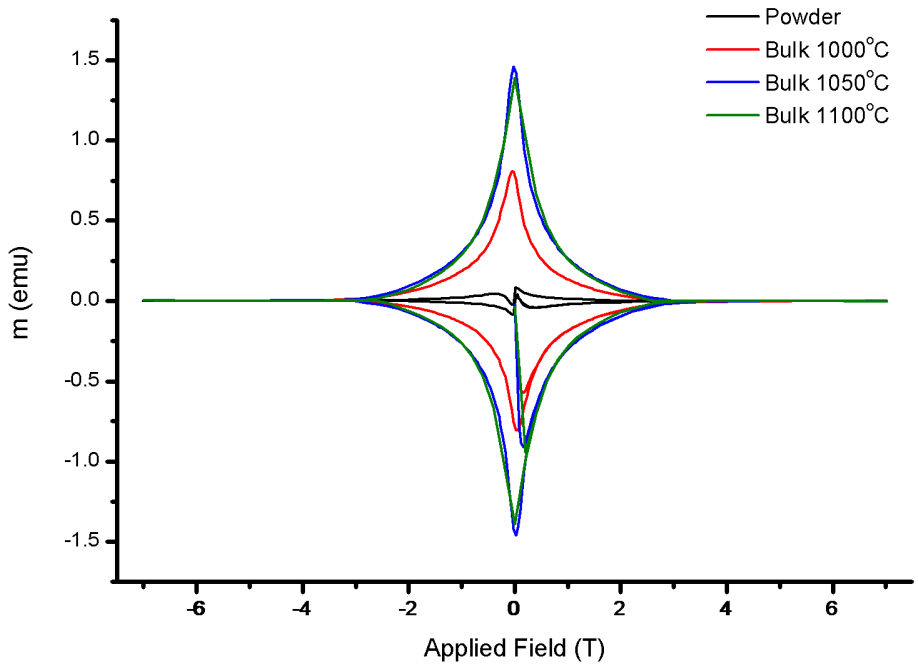
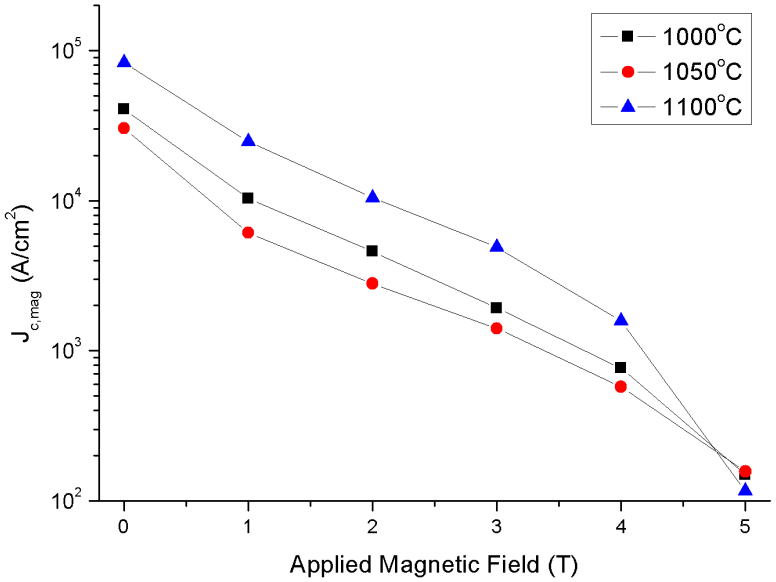
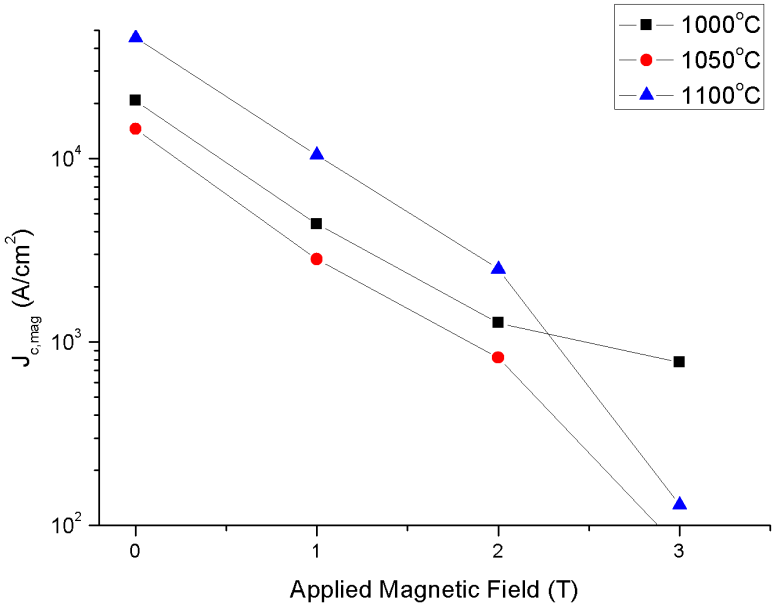


Figure 4.33: SQUID measurements at 20 K of magnetic moment in bulk MgB_2 samples



(a)



(b)

Figure 4.34: Calculated $J_{c,mag}$ curves for bulk samples produced from as-purchased MgB_2 powder
a) 4 K
b) 20 K

5 Modification of Magnesium Diboride Powder

The limited sintering behaviour observed in the previous chapter led me to explore methods to encourage connectivity by modifying the starting powder. The particle size distribution of ceramic powders is an important factor in determining the sintering rate [50]. Separation (sieving and sedimentation) and milling processes (ball milling and attrition milling) were used to alter the particle size distribution of the as-purchased Alfa Aesar MgB_2 powder. Milling can produce particles with a smaller particle size than any particle found in the starting powder. Separation processes can only produce fractions with sizes within the original starting range. The break-up of particles during milling exposes fresh surfaces, which can lead to an increase in the impurity content if the freshly exposed MgB_2 reacts with the milling fluid or atmosphere.

This chapter describes the effects of these processes on the particle size distribution and impurity content of the MgB_2 powder. The results of using these powders to produce bulk MgB_2 will be discussed in Chapter 6.

5.1 Sieving

As described in Section 3.1.1 on page 50, Alfa Aesar MgB_2 powder was sieved into four fractions based on their sieve diameter d_{sieve} (see Section 3.4.1 on page 64 for descriptions of the various measures of particle size). The fractions produced will be referred to as

follows:

- $d_{sieve}\,(\mu\mathrm{m}) > 106$ as $d_{>106}$
- $80 < d_{sieve}\,(\mu\mathrm{m}) < 106$ as d_{106}
- $50 < d_{sieve}\,(\mu\mathrm{m}) < 80$ as d_{80}
- $d_{sieve}\,(\mu\mathrm{m}) < 50$ as d_{50}

5.1.1 Impurity Content

As sieving divides the powder into fractions based on particle size, no significant change in the distribution of impurities from the as-purchased MgB_2 powder was expected. Impurity content measurements were still carried out, however, because it was conceivable that a greater proportion of impurities may be contained within, for example, the smallest particle size fraction (this would occur if for example the impurities were contained within a surface layer of similar thickness for all particle sizes, hence a greater volume of the smallest particles would be made up of impurity phases). The XRD scans of the powders are shown in Figure 5.1. The MgO (220) peak around $2\theta = 60\,^{\circ}$ is detectable in the scans for $d_{>106}$ and d_{106}, suggesting that a greater proportion of these samples consists of MgO compared to the finer powders. However the peak area ratio for these scans lay in the region where the MgO content could not be calculated accurately (see Section 4.2.1 on page 109), indicating that the MgO content was between $0 - 5\,\mathrm{wt.\%}$.

As XRD scans indicated that no significant proportion of *new* impurity phases were introduced from the sieving procedure, further impurity analysis was not carried out on these samples.

5.1.2 Particle Sizing

Particle size distribution measurements were carried out using the Malvern Mastersizer S laser diffraction system. Particle size distributions were measured using samples which

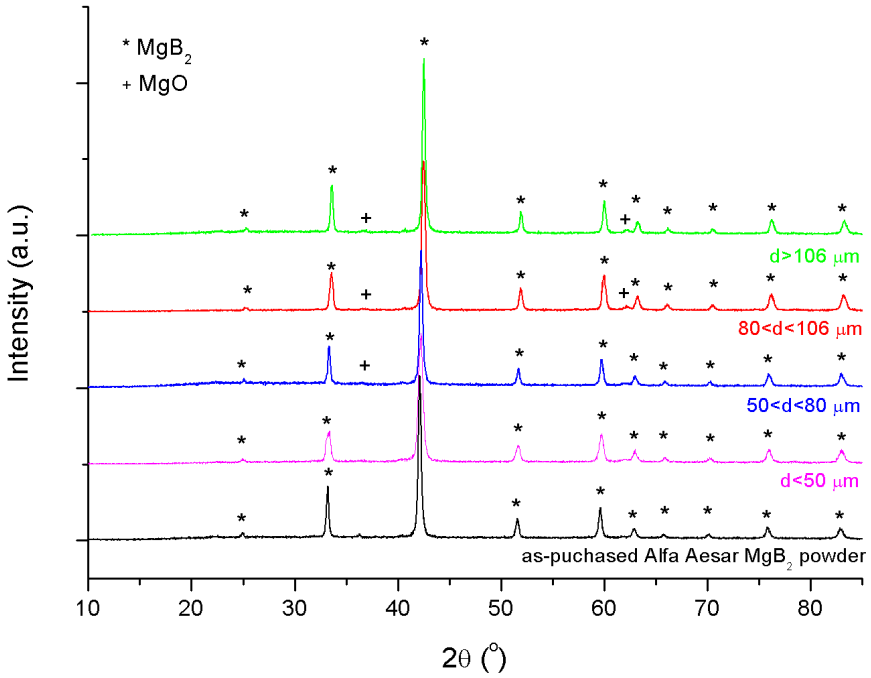
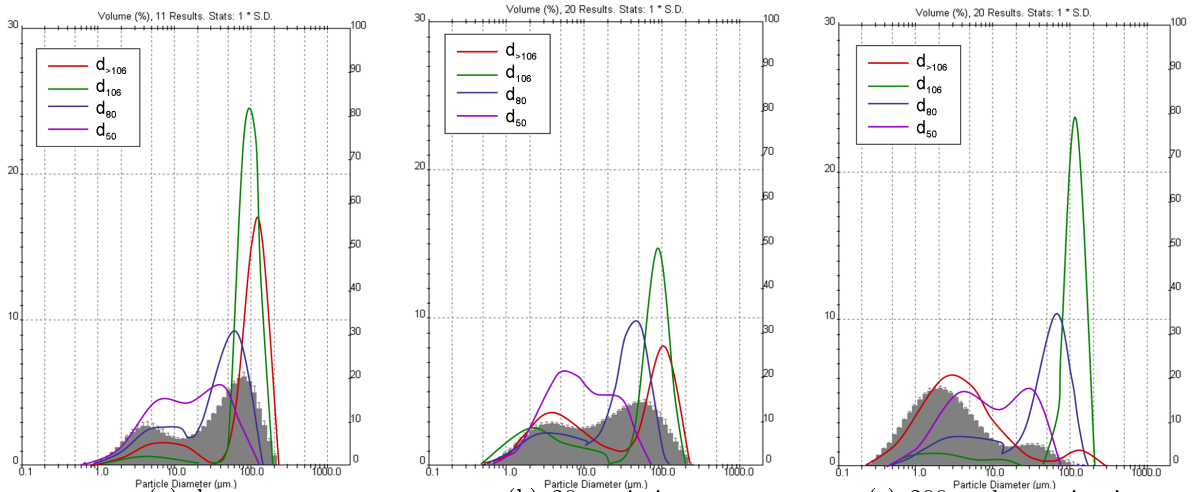


Figure 5.1: XRD spectra of sieved powders in comparison to starting powder

were added as dry powder, dispersed by mechanical stirring in isopropanol, and dispersed in isopropanol using an ultrasonic bath for 300 s. These particle size distributions for each fraction are shown in Figure 5.2, with those for the sieved fractions shown using lines overlaid on the equivalent particle size distributions for as-purchased powder (displayed as histograms). As shown previously for the as-purchased powder, the measured particle size distributions are highly dependent on the process used for dispersion of the powder prior to insertion into the laser diffraction system.

The approximate particle size range contained within each sieved fraction is indicated in Table 5.1 for dry, stirred and ultrasonicated samples. The spherical equivalent diameters measured from the volume of the particles by laser diffraction do not match exactly with the sieve size diameter. Even though the two diameters measure different physical characteristics of the particles, the particle size range is too broad to be merely due to the different measures used. In particular, in order to observe the smallest particles within the coarse fraction without this being due to some problem with the sieving, the particles



(a) dry (b) 30 s stirring (c) 300 s ultrasonication

Figure 5.2: Particle size distribution of sieved powders measured by laser diffraction

would be have to be disc or rod shaped with a large aspect ratio. SEM observations (see Figures 5.3-5.6) indicate that this is not the case.

It is clear from the changes indicated from the dry powder to the ultrasonicated powder in Figure 5.2 that the coarsest fraction $d_{>106}$ is in fact mostly made up of rather loosely bound agglomerates of much smaller particles as the position of the largest peak shifts from around 150 μm for the dry powder to 30 μm for the ultrasonicated powder. In contrast, ultrasonication makes little difference to the d_{106} fraction, indicating that this fraction is mostly made up of either non-agglomerated particles or hard agglomerates which cannot be broken up with ultrasound. It is evident that some smaller particles must have become attached to the larger particles temporarily during sieving, as the fraction consists of one large peak with approximate peak position around 100 μm, with a smaller peak at lower sizes. This is also true for the coarsest fraction $d_{>106}$. The fraction d_{80} has a very broad size range from $0.6 \lesssim d_v\,(\mu\text{m}) \lesssim 150$ with, again, little change following ultrasonication. The smallest fraction d_{50} similarly changes little during the different dispersion methods, though there is a shift from $0.9 \lesssim dv\,(\mu\text{m}) \lesssim 150$ in dry powder to $0.4 \lesssim dv\,(\mu\text{m}) \lesssim 70$ after ultrasonication. It is evident from these data that the agglomerates which are readily broken up by ultrasonication are mainly contained within the coarsest fraction $d_{>106}$.

Table 5.1: Particle size ranges measured by laser diffraction for sieved powder fractions

sieve diameter	diameter measured by laser diffraction (μm)		
(μm)	dry	stirred 30 s	ultrasonicated 300 s
$d_{sieve} > 106$	$0.8 \lesssim d_{vol} \lesssim 200$	$0.6 \lesssim d_{vol} \lesssim 300$	$0.2 \lesssim d_{vol} \lesssim 270$
$80 < d_{sieve} < 106$	$1 \lesssim d_{vol} \lesssim 200$	$0.6 \lesssim d_{vol} \lesssim 250$	$0.4 \lesssim d_{vol} \lesssim 200$
$50 < d_{sieve} < 80$	$0.8 \lesssim d_{vol} \lesssim 150$	$0.7 \lesssim d_{vol} \lesssim 150$	$0.4 \lesssim d_{vol} \lesssim 150$
$d_{sieve} < 50$	$0.6 \lesssim d_{vol} \lesssim 150$	$0.8 \lesssim d_{vol} \lesssim 90$	$0.4 \lesssim d_{vol} \lesssim 70$

The shape of the particles in each size fraction was also examined by SEM using the JEOL 840F. A selection of images indicating the variety of shapes in each particle size fraction is shown in Figures 5.3-5.6. An immediate observation is that none of the fractions contain disc or rod-shaped particles with sufficiently large aspect ratio in order for d_{sieve} and d_v to vary enough to allow the inclusion of fine particles in the coarse fraction. This indicates that the presence of small particles in the coarse fraction is in fact due to sieving errors such as the inclusion of weakly bound agglomeration due, for example, to static charges, van-der-Waals forces, or capillary forces from moisture adsorption. These processes, occuring following sieving, may also be responsible for the presence of particles up to 150 μm diameter in the finest fraction (nominally $d_{sieve} < 50\,\mu$m).

SEM observations indicate that the coarsest fraction $d_{>106}$ consists mainly of large agglomerated particles (Figure 5.3a). Figure 5.3c shows a large particle of diameter $50 - 100\,\mu$m (depending on the dimension examined) and Figure 5.3d shows the surface of this agglomerate at higher magnification. These images show that the large particles are made up of agglomerates of smaller particles, in agreement with the particle size distributions measured by laser diffraction. Some smaller particles were observed on the carbon tab in addition to the large coarse particles (Figure 5.3b). These have probably been temporarily attached to the particles during sieving and removed during the SEM sample preparation, which involves dispersion in methanol.

Observations on d_{106} revealed a greater proportion of smaller particles than in $d_{>106}$ (Figure 5.4a). In addition to coarse agglomerates of around 100 μm as seen in $d_{>106}$,

clearly agglomerated particles of around $5 - 10\,\mu$m such as that shown in Figure 5.4b were observed.

d_{80} mostly consists of the finer particles as observed in d_{106}. Some coarser particles were also observed (Figure 5.5c), but in general these were smaller than $100\,\mu$m. The surface of the larger particles (Figure 5.5d) appeared different to the coarse particles in $d_{>106}$ and d_{106}, consisting of well-connected larger particles with just a few small particles scattered about the surface, in contrast to the larger fractions which appeared to be made up of individual particles.

d_{50} appears to be mostly made up of fine agglomerated particles such as that in Figure 5.6b. The largest particles were around $25\,\mu$m in diameter, and the surface of the particles (Figure 5.6d) is covered in smaller particles.

Overall the SEM observations of the particles revealed that there are generally coarse agglomerates and finer particles in each sample. No sieved fraction contained a noticeably larger proportion of elongated particles. Laser diffraction measurements detected particles which do not match the sieve size, which is likely to be due to the agglomeration of particles whilst the powder is dry.

5.2 Sedimentation

Sedimentation was carried out in order to produce samples with a significantly smaller particle size than that possible by sieving. In addition, fractions consisting of very large particles were produced to indicate the suitability of this technique for removing the largest particles which can distort wire cross-sections, especially in multifilament structures where the filament width is similar to the size of the largest particles (see example microstructures in Pachla *et al* [219]). Powders with Stokes's diameters (d_{St}) of $100\,\mu$m and $1\,\mu$m powders were produced using the method described in Chapter 3 (Section 3.1.2 on page 51). These will be referred to as $d_{>100}$ and $d_{<1}$ respectively.

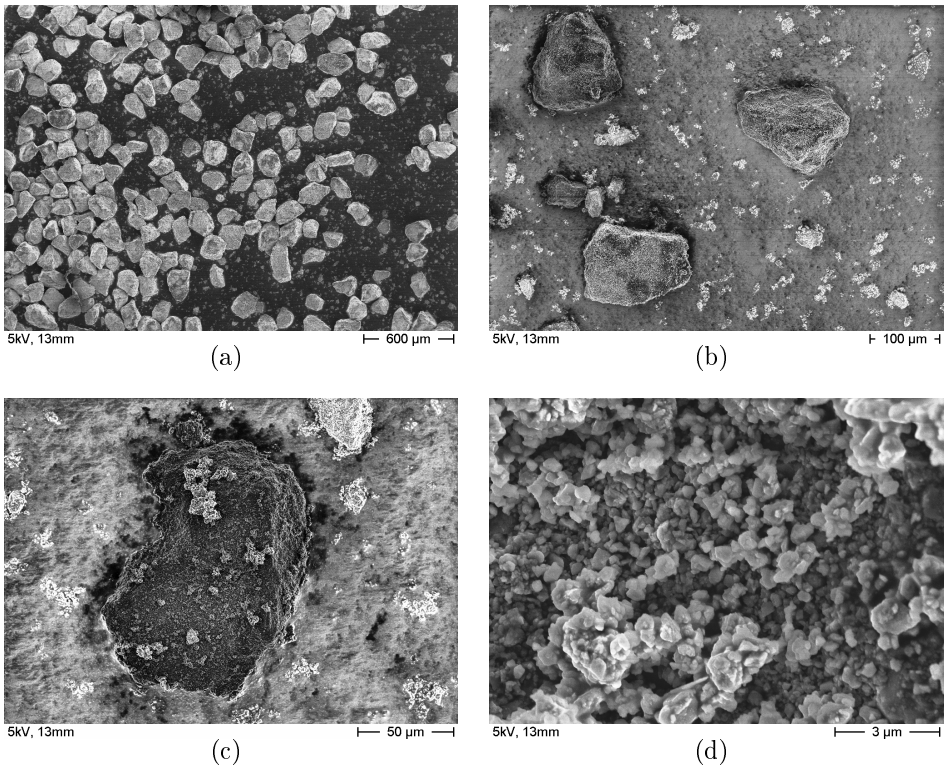


Figure 5.3: SEM images of sieved powder particles in the $d_{>106}$ fraction

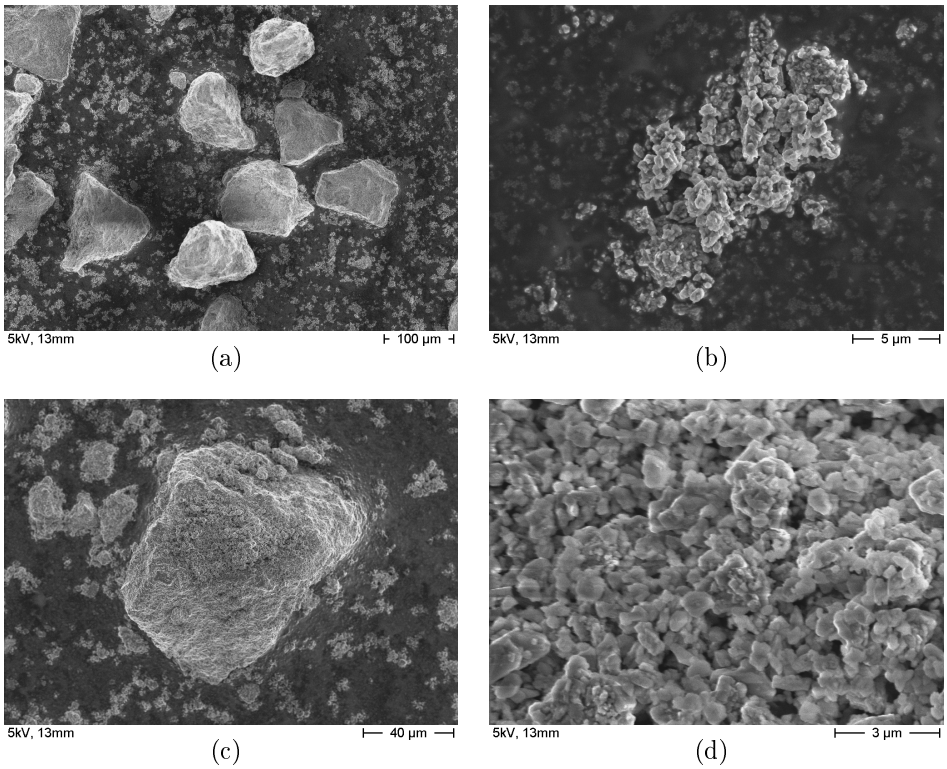


Figure 5.4: SEM images of sieved powder particles in the d_{106} fraction

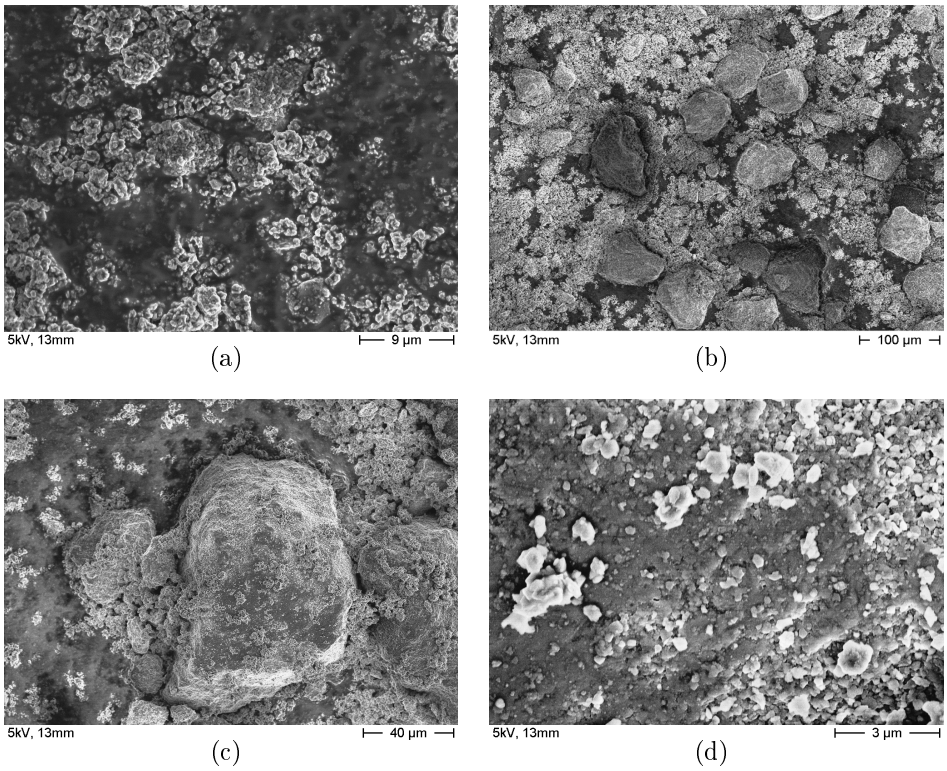


Figure 5.5: SEM images of sieved powder particles in the d_{80} fraction

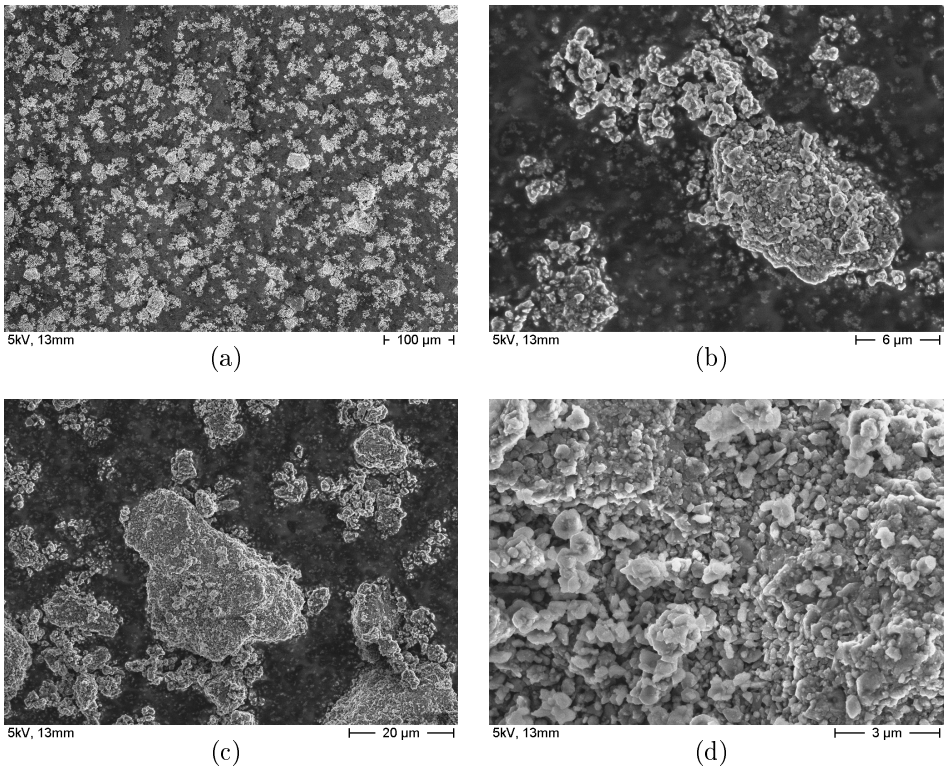


Figure 5.6: SEM images of sieved powder particles in the d_{50} fraction

5.2.1 Impurity Content

The impurity content of the sedimented materials was determined using XRD. The spectra are shown in Figure 5.7. The samples are both mostly MgB_2 within the detection limits of the likely impurity phases; a small peak due to MgO was observed in the sedimented powder $d_{>100}$, but this lay in the region where the MgO content could not be accurately measured (see Section 4.2.1 on page 109). There may be a greater proportion of MgO contained in the coarser material than in the finer material in the as-purchased powder, in agreement with the observations on sieved material (Section 5.1.1). No other phases are observed. In the case of the sedimented powder $d_{<1}$, the powder was in contact with the isopropanol for around 24 h but this did not introduce large quantities of crystalline impurity phases to the powder.

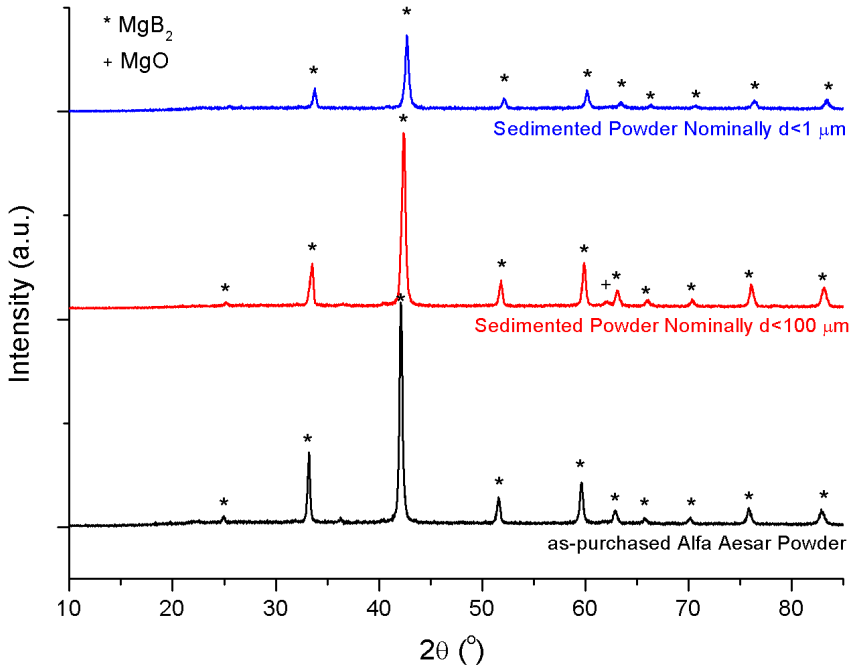


Figure 5.7: XRD spectra of sedimented powders

5.2.2 Particle Sizing

The larger fraction $d_{>100}$ is primarily made up of coarse agglomerates as shown in Figures 5.8a and 5.8b. The coarse agglomerates appear similar to those observed in SEM micrographs in the sieved powder fraction $d_{>106}$. The surface of the particles is made up of smaller particles (Figure 5.8c). The finer fraction $d_{<1}$ consists mainly of very fine material dispersed evenly across the tab (Figure 5.8d). Occasional larger clusters were observed but it is difficult to establish whether these are due to the method of dispersion on the tab or if they are truly agglomerated. In addition, several large coarse agglomerates were observed (Figure 5.8e). The surface of one of these agglomerates in shown in Figure 5.8f. In general all the particles are fairly rounded and not noticeably elongated.

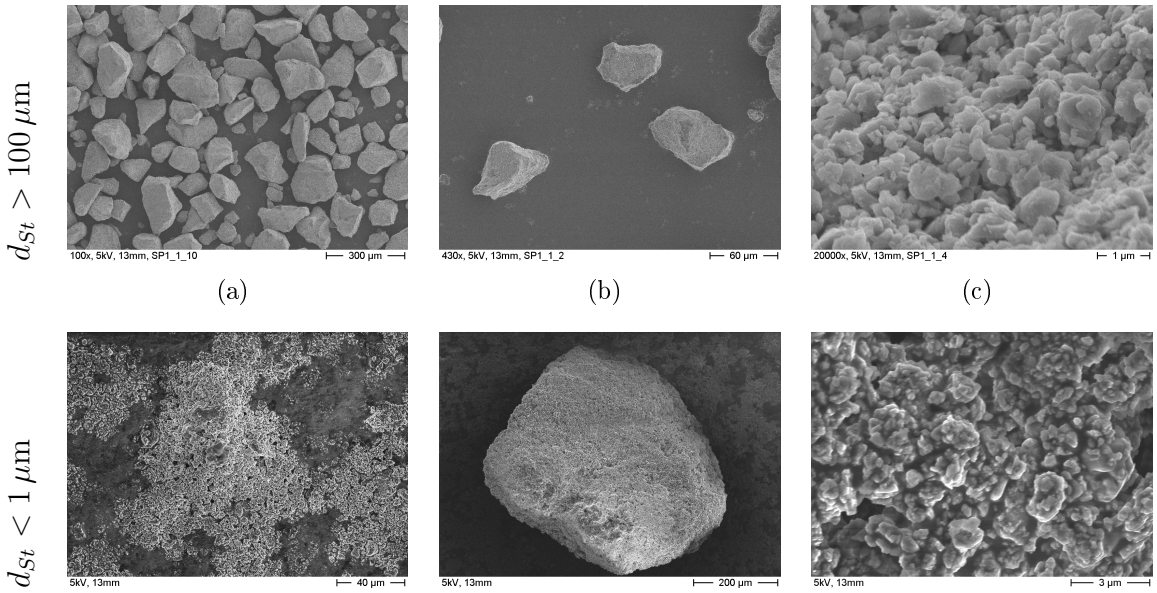


Figure 5.8: SEM images of particles in MgB_2 powder fractionated by sedimentation

Particle size analysis was carried out by laser diffraction using the Malvern Mastersizer S. In order to investigate the effect of the drying procedure, samples were measured which had been dried and not dried, *i.e.* the sample was retained as a slurry of MgB_2 powder and isopropanol. The dried powders were added to the Mastersizer S as dry powders, after re-dispersion by 30 s stirring in isopropanol, and following 300 s ultrasonication. No significant changes in particle size distribution were observed with increased degree

of dispersion for the coarse fraction $d_{>100}$. Most of the particles had diameters above $100\,\mu$m, but a few smaller particles were observed. Comparing the dried and non-dried powders, the stirred powder has a similar particle size distribution when dried or not dried. The ultrasonication of the powder indicates a remarkable change from the dried powder to the non-dried powder. The non-dried powder readily breaks up, similarly to the as-purchased powder (see Section 4.1.2.3 on page 99). The ultrasonicated dried powder has a similar particle size distribution to the non-ultrasonicated sample. This indicated that the drying procedure causes the formation of hard agglomerates which cannot be broken up by ultrasonication, as suggested earlier (see above).

The results are more difficult to interpret for the smaller fraction, as the particle size ranges are similar for dried and non-dried samples. It is immediately apparent that the attempt to produce the $d_{<1}$ sample has not been very successful; while the sample largely consists of particles with $d < 100\,\mu$m, there is a very large volume of material which has $d > 1\,\mu$m. In addition, comparison of the stirred particle size distributions indicates that the drying procedure introduces more coarse agglomeration into the material. While the non-dried powder mostly consists of particles of $d < 10\,\mu$m, the dried powder contain particles/agglomerates with $d > 100\,\mu$m.

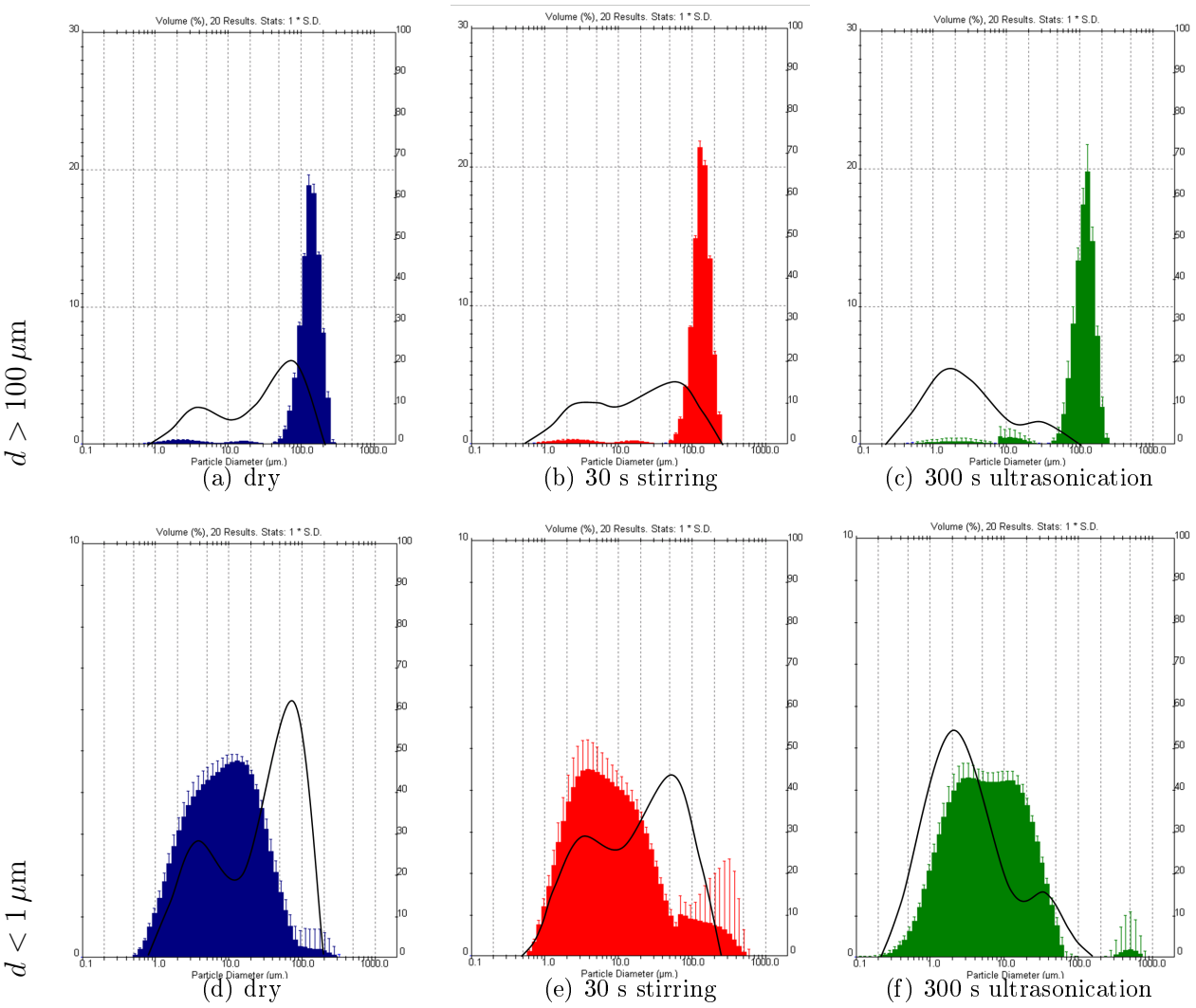


Figure 5.9: Particle size distributions of sedimented powders which were dried after sedimentation. The black line on each plot is a trace of the equivalent plot for as-purchased Alfa Aesar MgB_2 powder

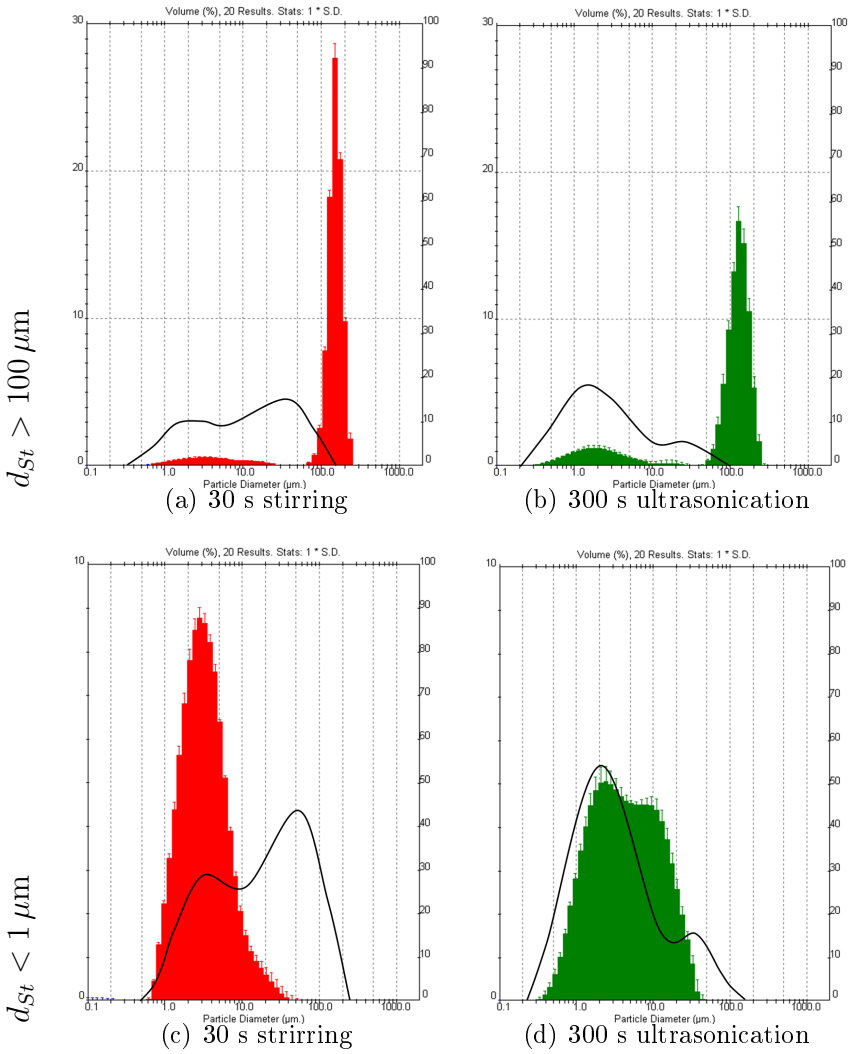


Figure 5.10: Particle size distributions of sedimented powders not dried

5.3 Ball Milling

Ball milling was carried out at two times during my project. Initially, powders which had been exposed to air were ball milled for 8 h and 20 h respectively. These powders are referred to as the "initial" powders. These powders were entirely dried by evaporating the isopropanol with the assistance of a hot plate. When it became apparent that the impurity content may be dependent on air exposure of the powder prior to milling, and that the measured particle size may depend on the drying method, a further series of ball milled powders were prepared ("second series"). Equivalent ball milling containers packed

in air or in the nitrogen glove box were prepared. Powders were ball milled for 1 h, 8 h and 20 h. From these the sample was split with half retained as a MgB_2/isopropanol slurry while the other part was dried using a hot-plate as described in Section 3.1.3 on page 54.

5.3.1 Impurity Content

XRD spectra for the powders produced in all the ball milling runs indicated no measurable increase in crystalline impurity content (Figures 5.11 and 5.12). The MgO peak at around $2\theta = 60^{\circ}$ is labelled in both scans but the peak ratio in each case indicated that the MgO content lay in the region where it could not be measured accurately ($0-5$wt.%). No evidence of contamination by zirconia from the ball milling media was found in the XRD spectra.

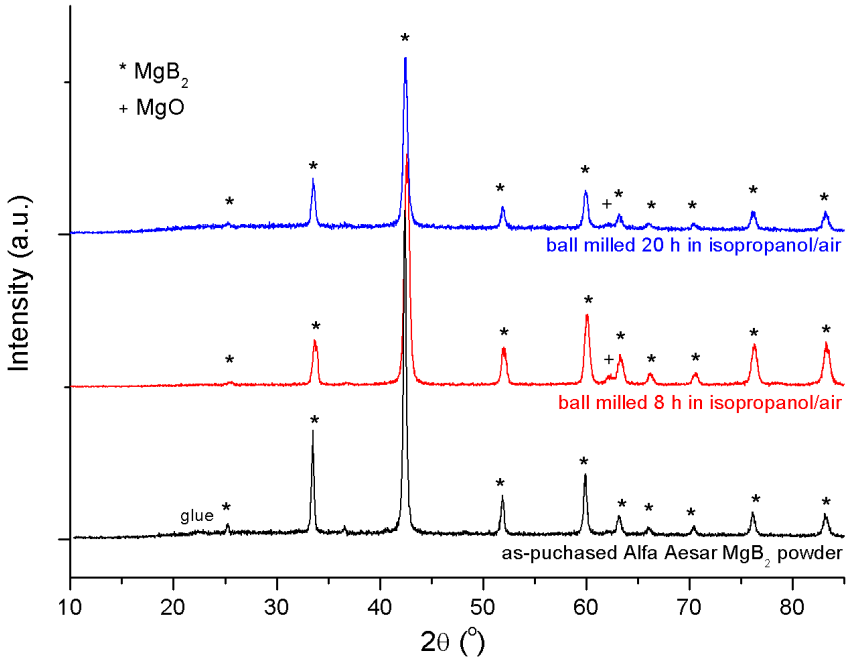


Figure 5.11: XRD spectra of powders ball milled in air for 8 h and 20 h. The spectrum for the pre-ball milled powder (as-purchased Alfa Aesar MgB_2) is included for comparison.

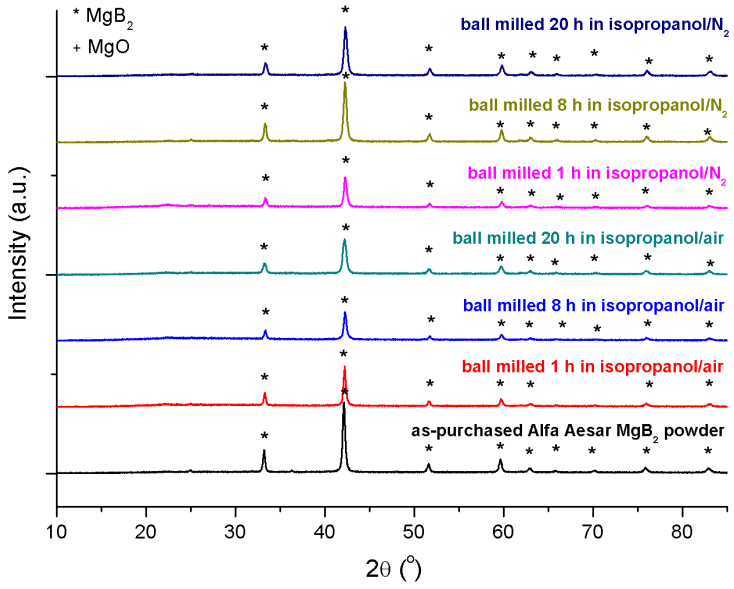


Figure 5.12: XRD spectra of the second series of ball milled powders packed in air and in nitrogen.

It is apparent from the XRD data that there is little variation in the crystalline impurity content of the ball milled powders. However it is likely that prolonged exposure to isopropanol, and in some cases air will change the impurity content as carbon and oxygen-containing species will be adsorbed onto the surface of the particles, and this may only be indicated by impurity formation after heat-treatment. The results from these powders will be compared with those from the heat treated pellets produced from these powders in Chapter 6.

XPS measurements were carried out with the assistance of Dr Alison Crossley on the two initially produced powders, and the wide-angle scans are shown in Figure 5.13. A small quantity of zirconia was detected on the surface of the powder ball milled for 8 h, but none in that ball milled for 20 h, indicating that there is little wear of the milling media during ball milling. Fluorine, nitrogen, silicon and argon were detected in one or other of the samples as they had been previously in the as-purchased powder. The carbon content increased significantly from 8 h to 20 h ball milling. The magnesium and boron content decreased as a proportion of the total. This indicates that the increased exposure

to isopropanol increases carbon contamination on the particle surfaces significantly. This may lead to the formation of impurity phases following heat-treatment. However, in the case of MgB_2, exposure to carbon can improve the superconducting properties, as carbon doping has been shown to improve flux pinning and hence increase J_c at high magnetic fields for MgB_2 [220].

Table 5.2: Elemental composition of the surface of initially produced ball milled powders measured by XPS. All elemental contents are in at.%.

	Mg	B	O	C	F	N	Zr	Si	Ar
8 hours	11.3	10.3	30.4	43.1	2.8	1.8	0.1	1.3	0.0
20 hours	5.1	7.1	25.5	59.1	1.0	0.6	0.0	1.4	0.2

In addition to containing the lowest proportion of Mg and B on the surface, the powder ball milled for 20 h in isopropanol/air contained the least MgB_2 of any powder measured by XPS (Figure 5.14a). Much of the boron in this sample is in the form of B_2O_3, and the intensity of the Mg 2p peak is reduced (Figure 5.14b). The powder ball milled for 8 h contained more MgB_2, and was also relatively free of the boron peaks at around 183 eV as seen for the attrition milled powder (Figure 5.14a).

EDX analysis was carried out on both initially produced ball milled powders. A typical scan and SE image for each powder are shown in Figures 5.15 and 5.16. In this case, zirconium (originating from the ball milling media, and therefore in the form of ZrO_2) was detected in the case of the 20 h powder and not in the case of the 8 h powder, the reverse to the result of the XPS. This indicates that the zirconium content is dispersed inhomogeneously through the samples and at low levels (measured as 0.4 at.% of the Mg content by EDX; in contrast, for the 8 h ball milled powder the XPS measured the Zr content as 0.9 at.% of the Mg content).

5.3.2 Particle Sizing

SEM images of typical particles observed in the initial series of powders ball milled for 8 h and 20 h are shown in Figure 5.17. Because the particles were dispersed for analysis

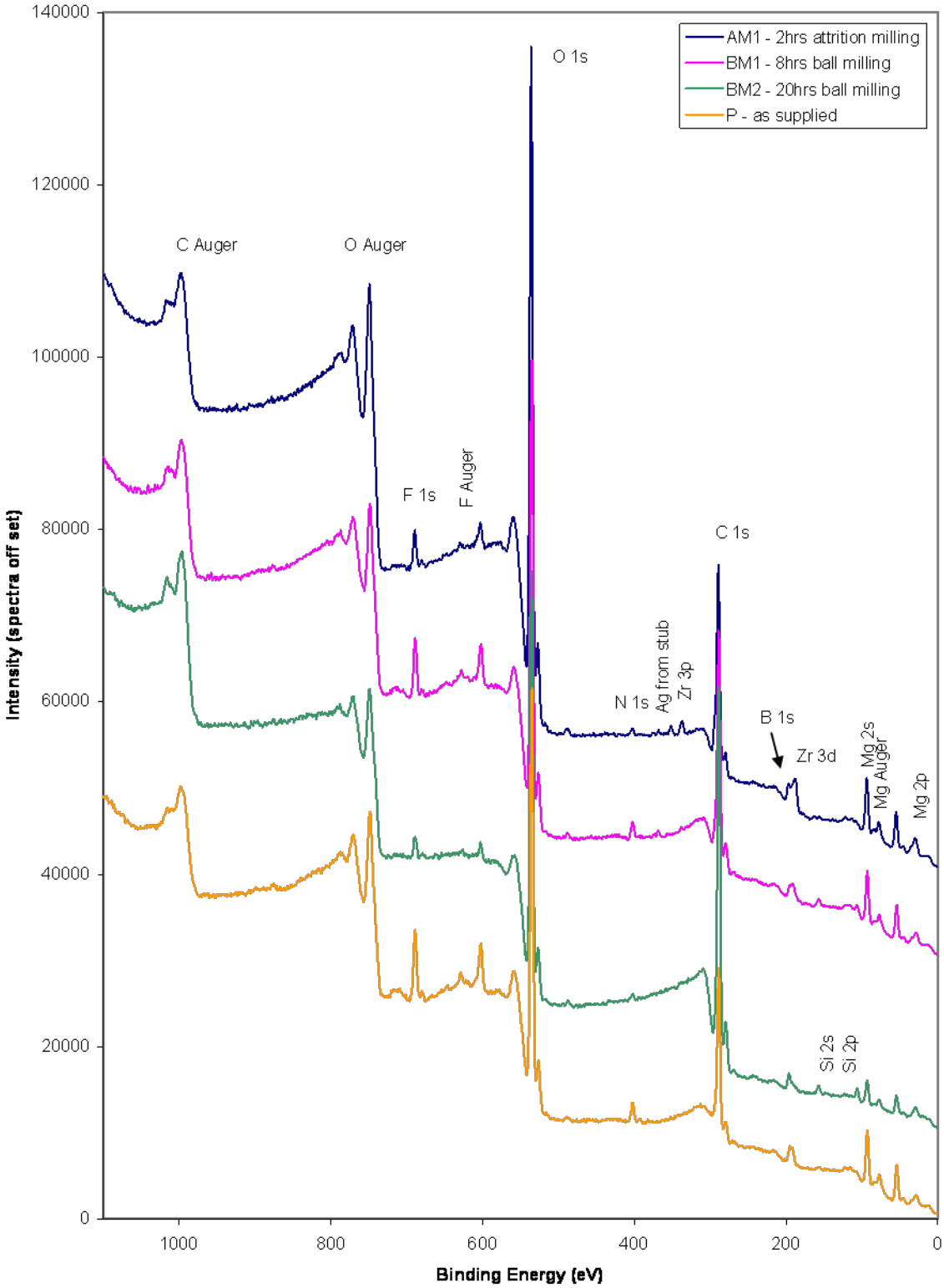
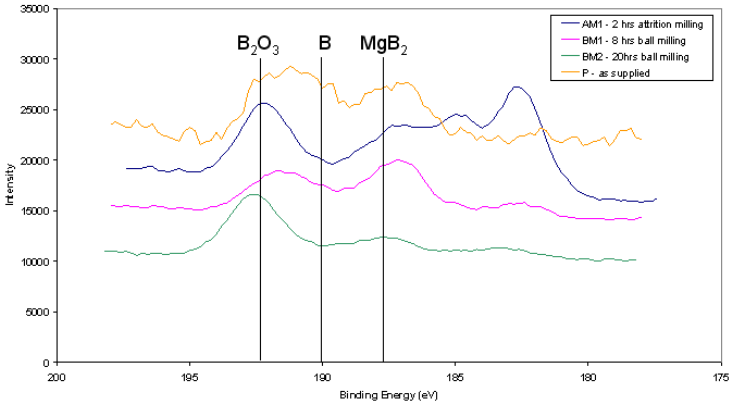
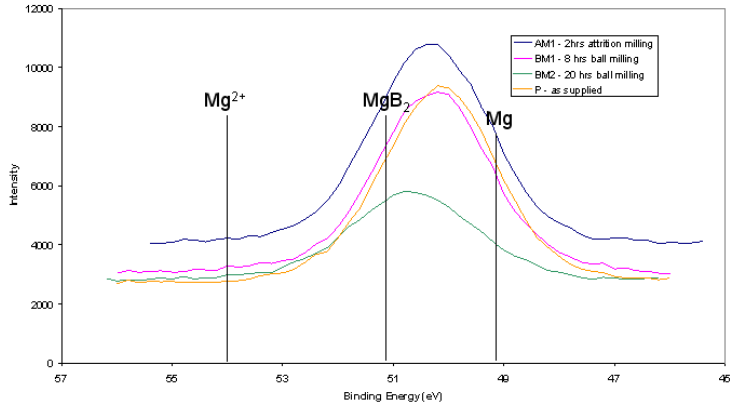


Figure 5.13: Wide-energy-range XPS scans



(a)



(b)

Figure 5.14: Narrow-energy-range XPS scans fora) Boron 1s peakb) Magnesium 2p peak

as described in Section 3.4.4 on page 70, the background to these images is typically the carbon tab, not other particles. For each powder, Figure 5.17a and 5.17d show agglomerates of finer particles, Figures 5.17b and 5.17e show large harder agglomerates, and Figure 5.17c and 5.17f show the surfaces of those agglomerates. While some large agglomerated particles were observed in both powders (Figure 5.17b and 5.17e), in general the particle size is smaller for the sample ball milled for 20 h. However it is difficult to establish from these images whether the large agglomerates are artefacts of the drying process or if they remain after ball milling. For this reason, the second series where the milled powder was partly dried and partly retained as a slurry was also examined.

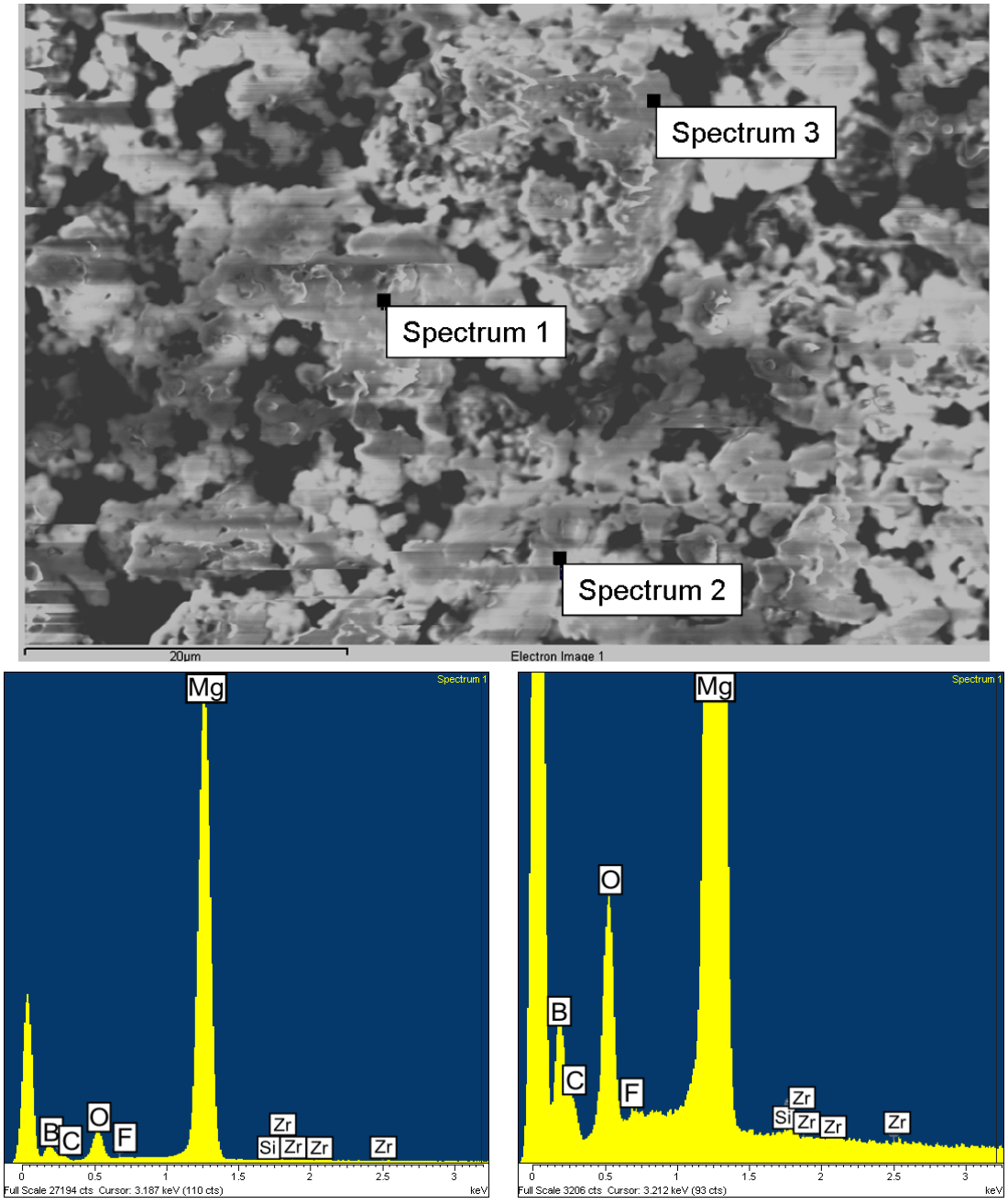


Figure 5.15: EDX spectra of ball milled powder, initial run, 8 h milling in isopropanol/air. The streaking in the image is due to charging of the powder, which was not coated as this would affect the EDX analysis.

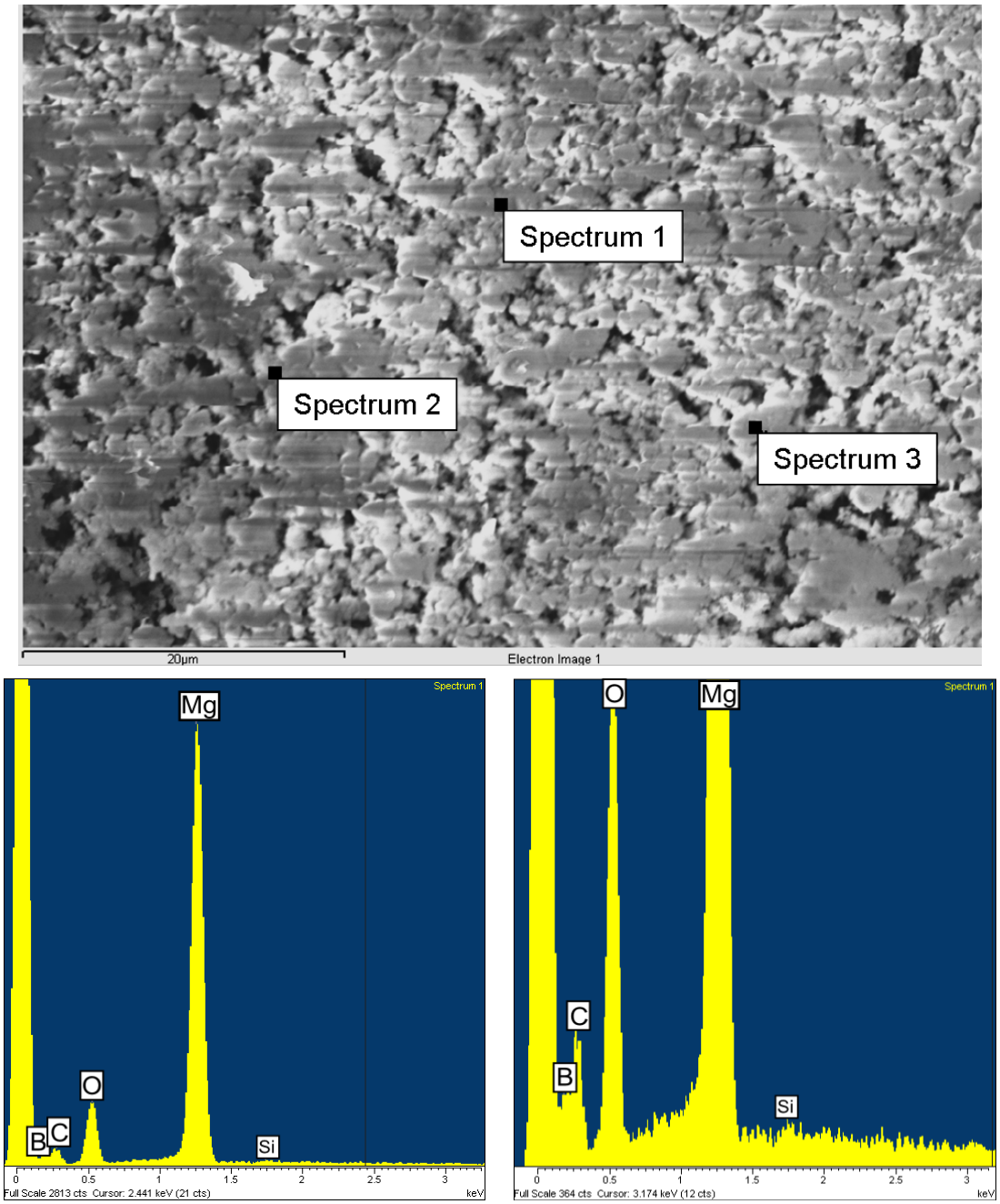


Figure 5.16: EDX spectra of ball milled powder, initial run, 20 h milling in isopropanol/N_2. The streaking in the image is due to charging of the powder, which was not coated as this would affect the EDX analysis.

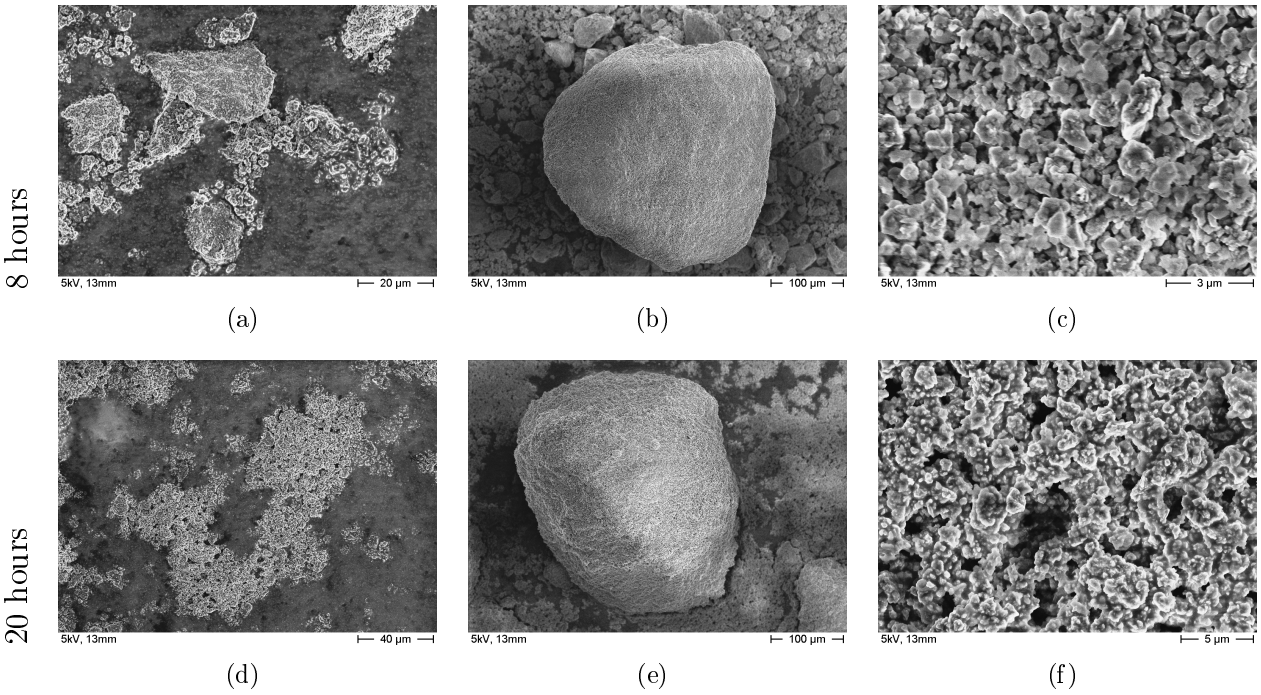


Figure 5.17: SEM images of initially produced ball milled powders

Figure 5.18 shows various dried and non-dried particles from the second series of ball milled powders. There is little variation between the powders ball milled in air (Figure 5.18) and in nitrogen (Figure 5.19). It was difficult to establish the average particle size or to make generalised observations of morphology from SEM images, but it appeared that most samples contained a range of particle sizes. Most particles were well-rounded and not angular (*e.g.* Figure 5.18a), due to the milling process, but a large number of highly agglomerated particles were seen (*e.g.* Figure 5.18b, c, d, f and Figure 5.19b, c, d, e, f). Agglomeration was more extensive in the powders which had been dried, in agreement with the particle size distributions determined by laser diffraction (see below). In general it was possible to observe both coarse and fine particles/agglomerates, but in the case of the powder ball milled in isopropanol/air (Figure 5.18a) only coarse particles could be found in the sample.

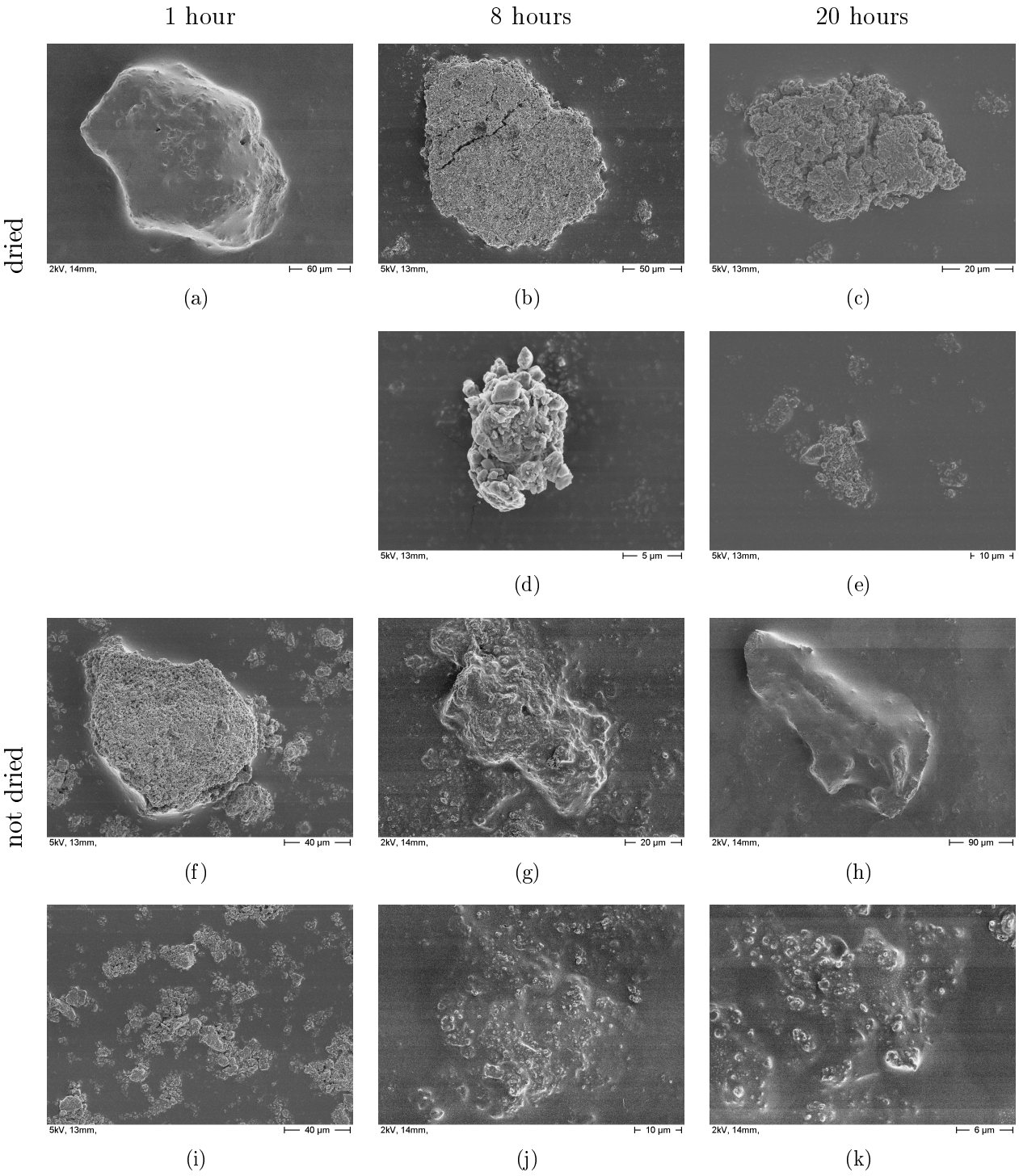


Figure 5.18: SEM images of second series of ball milled powders, milled in isopropanol/air

As the particle size range was too great to assess accurately from limited SEM observations, laser diffraction measurements were carried out using the Mastersizer S to obtain measurements using a greater number of measured particles. The results for the

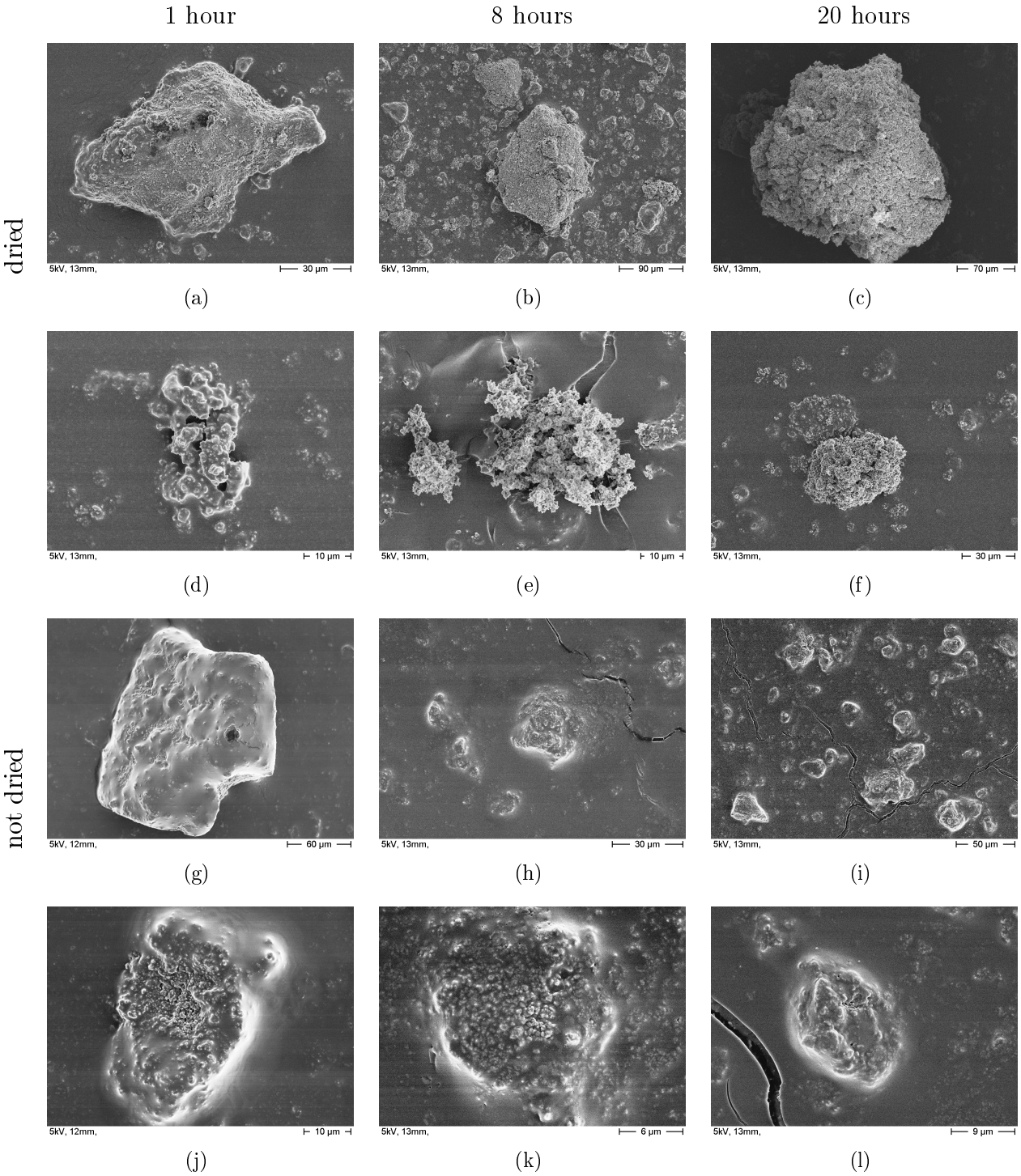
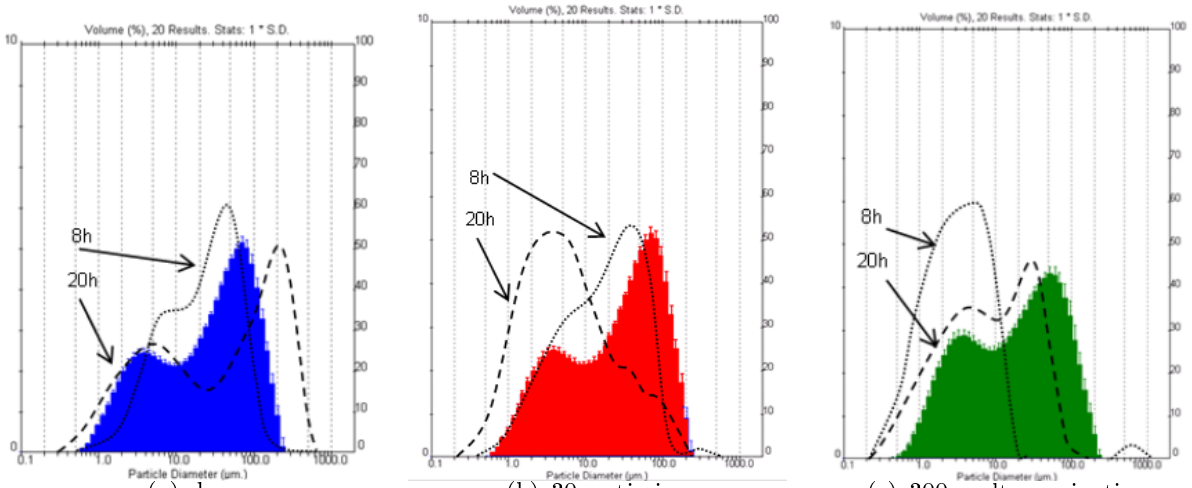


Figure 5.19: SEM images of second series of ball milled powders, milled in isopropanol/N_2

initial run of ball milled powders are shown in Figure 5.20. In each case, the histogram indicates the scan for the as-purchased powder, while the lines represent the trace of the histogram for the ball milled powder dispersed in the same way. As shown previously for as-purchased, sieved and sedimented powders, the method of dispersion has a huge influence on the measured particle size distribution. For the initially produced 8 h ball milled powder, the increased degree of dispersion leads to a steady decrease in the median particle size. The initially produced 20 h ball milled powder had better dispersion for the stirred sample than for the ultrasonicated sample. This implies that either ultrasonication causes agglomeration in this sample, or that the sample is highly inhomogeneous. This makes it difficult to draw any reasonable conclusions about this sample.

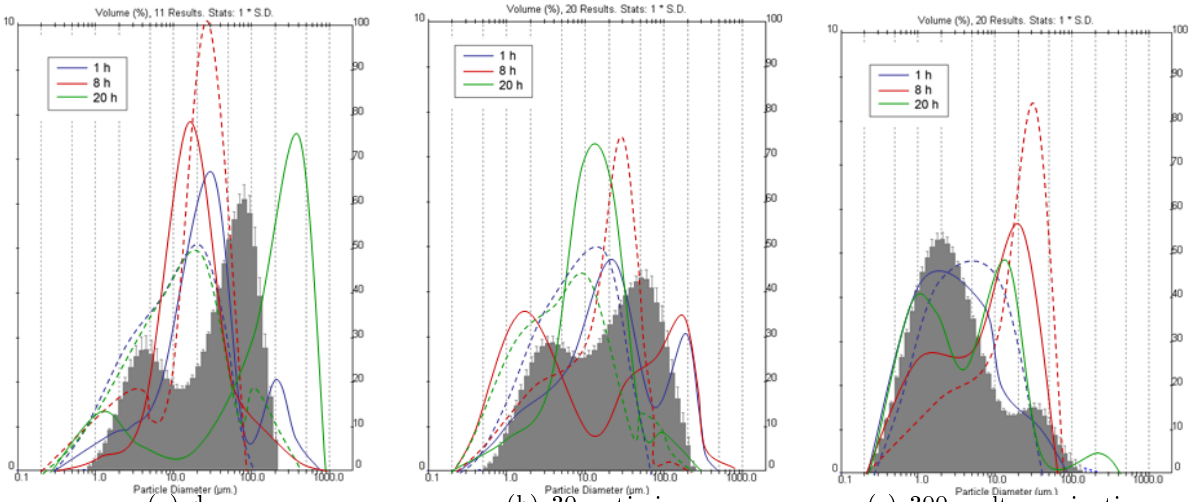


(a) dry (b) 30 s stirring (c) 300 s ultrasonication

Figure 5.20: Laser diffraction particle size distributions of initial series of ball milled powders, milled for 8 h or 20 h in isopropanol/air

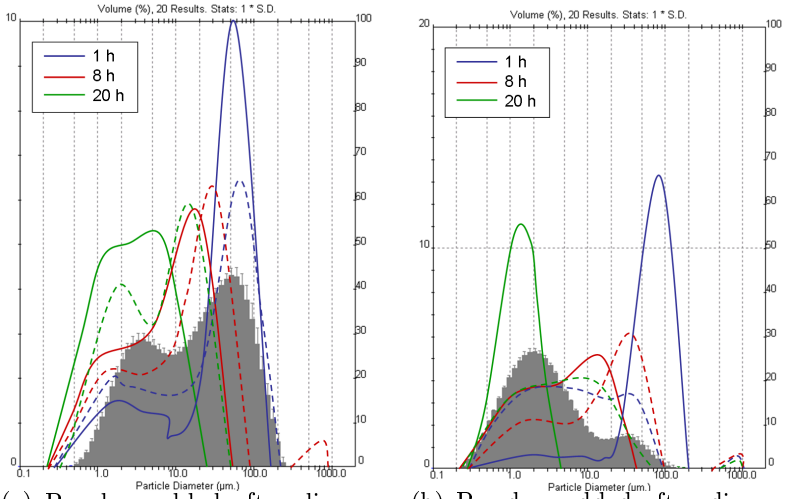
For the second series of ball milled powders, particle size distributions were measured for both dried powders and for slurries which had not been dried and were added directly as a slurry. These are shown in Figures 5.21 and 5.22. While for the dry powders the particle size distributions appear to be extremely varied for the different samples, after ultrasonication the particle size distributions are fairly similar. The samples ball milled for 8 h did not appear to respond well to ultrasonication, still consisting of a large volume of particles with $d_v > 10\,\mu$m after 300 s of ultrasonication. In comparison to the as-

purchased powder, for the dried powder the lower limit is decreased significantly, but following ultrasonication the as-purchased powder has a similar total size range. This is also illustrated by Figure 5.23 which records $d_{v,90}$, $d_{v,50}$ and $d_{v,10}$. For the powders added to the Mastersizer S while still dry, these values increase for ball milling for 1 h to 8 h then decrease again for 20 h milling. There is clearly an anomaly associated with the 8 h ball milling time, similar to that seen for the impurity analysis.



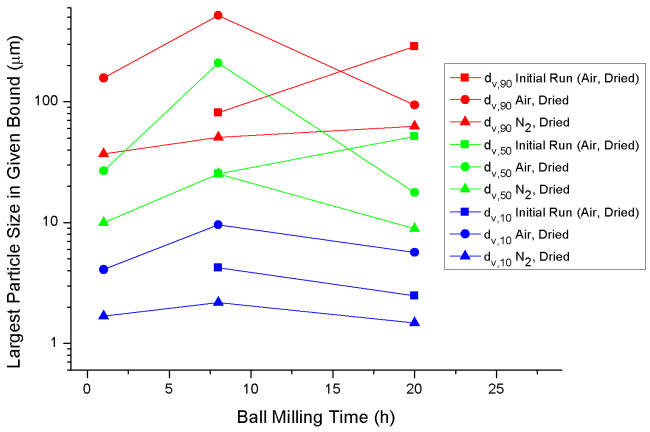
(a) dry (b) 30 s stirring (c) 300 s ultrasonication

Figure 5.21: Comparison of particle size distributions of powders ball milled in air (solid lines) and in nitrogen (dashed lines).

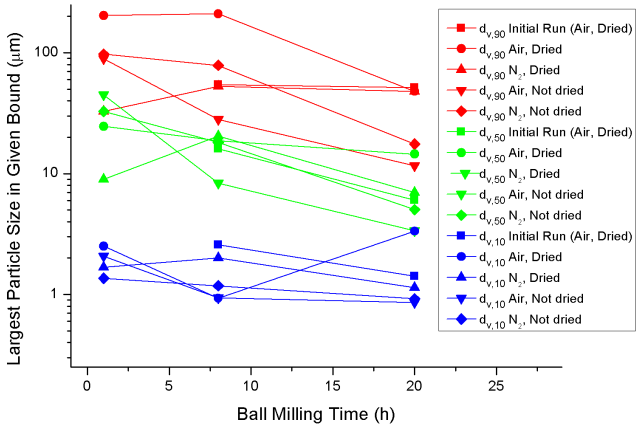


(a) Powders added after dispersion by 30 s stirring (b) Powders added after dispersion by 300 s ultrasonication

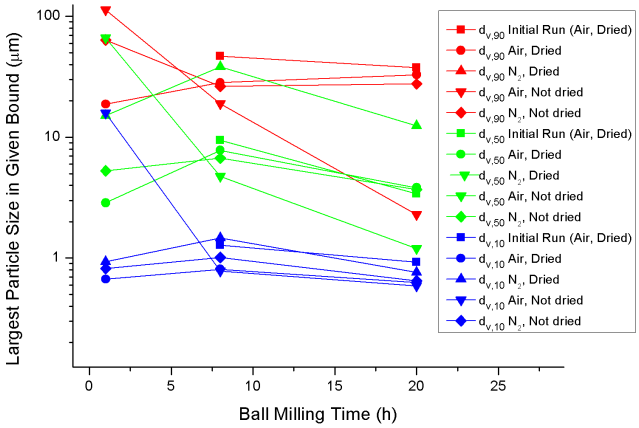
Figure 5.22: Comparison of particle size distributions of powders ball milled in air (solid lines) and in nitrogen (dashed lines), without drying



(a) dry powders



(b) stirred for 30 s



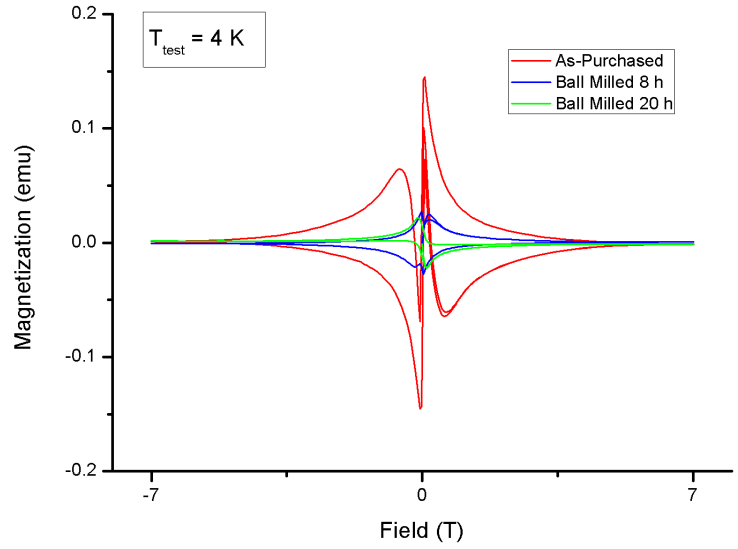
(c) 300 s ultrasonic dispersion

Figure 5.23: Graphs indicating the variation of $d_{v,90}$, $d_{v,50}$ and $d_{v,10}$ with ball milling time for samples ball milled in air and N_2, and with the powders dried or not dried prior to analysis

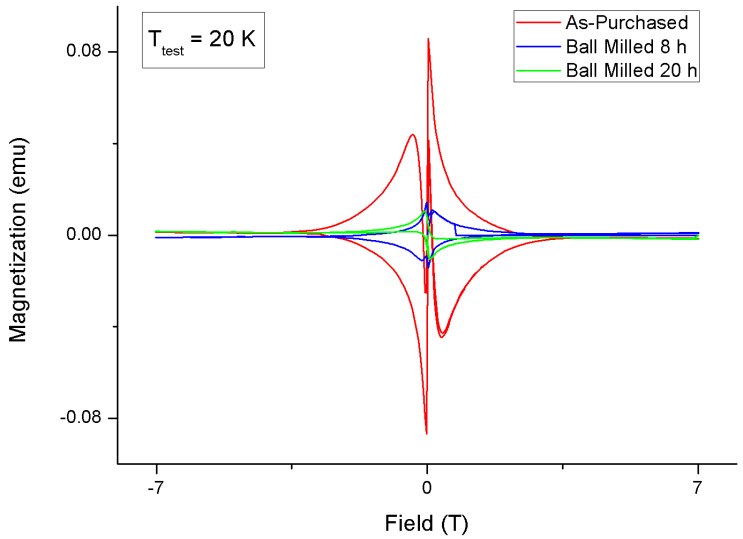
The particle size distributions for the powders which were not dried are shown in Figure 5.22. Again, for the stirred powder the particle size distributions are similar for the two series milled in nitrogen and air for each milling time. The particle size distributions of powders post-ultrasonication are significantly different due to the break-up of agglomerates. The smallest median particle size is for the sample ball milled for 20 h and packed in air ($d_{v,50} = 1.2\,\mu$m). With a few exceptions, $d_{v,90}$, $d_{v,50}$ and $d_{v,10}$ decrease with increased milling time for the stirred powders.

5.3.3 Magnetization Measurements

Magnetization curves were measured at 4 K and 20 K for the initially produced ball milled powders with a total applied magnetic field range of ± 7 T, and are plotted in Figure 5.24 along with the data for the as-purchased MgB_2 powder. While the size of the magnetization loops is extremely small (as might be expected for a powder with little to no connectivity), it is noticeable that the magnetization loops for the ball milled powders are severely decreased, with both H_{irr} and the value of the magnetization at 0 T being significantly smaller than for the as-purchased powder at 4 K and 20 K. The values of the magnetization at 0 T of the ball milled powders at 20 K are approximately half that measured at 4 K. The decrease is as expected by the relationship between induced current, magnetic field and temperature in superconductors (see Section 1.3.1 on page 5).



(a)



(b)

Figure 5.24: SQUID magnetization measurements on initially produced ball milled MgB_2 powders with comparison to as-purchased MgB_2

5.4 Attrition Milling

Powder was prepared by attrition milling for 2 h at 500 rpm as described in Section 3.1.4 on page 57.

5.4.1 Impurity Content

The impurity content measured using XRD of the MgB_2 powder did not increase following attrition milling for 2 h (see Figure 5.25). A small broad peak appeared at the correct position for the MgO peak at around $2\theta = 60^{o}$ but as with the earlier powders concentration of MgO was too low to be accurately measured, therefore it lies between $0 - 5$ wt.%. The formation of MgO during milling is not completely impossible; the attrition process is highly erosive and produces a significant increase in temperature which is not readily conducted away by the ceramic tank lining. This may lead to the breakdown of isopropanol to water (which is highly reactive with MgB_2) and alkane gases. The highly erosive environment of the attrition mill might also be expected to cause contamination by wear of the milling media and tank material, but peaks due to the relevant materials (Al_2O_3 and ZrO_2) were not observed in the XRD spectra.

XPS analysis was used to examine the surface of the attrition milled powder, and the wide angle scan is shown in Figure 5.26. Approximate at.% values for the proportion of elements contained on the powder surface are shown in Table 5.3. It is evident from this analysis that in the surface layers the magnesium content is severely depleted, while that of oxygen and carbon is significantly increased. This suggests that the isopropanol has permanently contaminated the surfaces of the powder particles. As XPS is carried out in an ultra-high vacuum system the C signal cannot be from volatile impurities.

Extra peaks were observed in the B 1s XPS spectrum for the attrition milled powder compared to the as-purchased powder (Figure 5.27a). These could not be identified, but may result from higher magnesium-borides which have not been extensively studied by XPS. The magnesium peaks 2s and 2p contained only one peak; in the Mg 2p spectrum

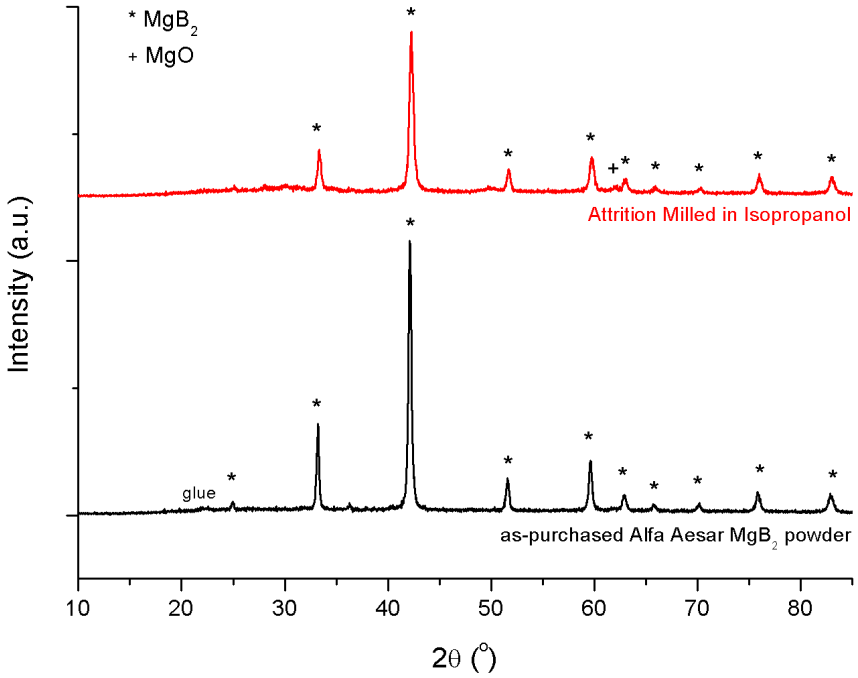


Figure 5.25: XRD spectrum of the attrition milled MgB_2 powder compared to as-purchased starting powder

at around 51 eV, corresponding to MgB_2 (Figure 5.27b).

In addition to the hydrocarbon impurities, small amounts of fluorine, silicon, argon and nitrogen were detected: these elements were also observed in the as-purchased powder (see Section 4.1.1.4 on page 88). Unlike the as-purchased MgB_2 powder, 0.6 at.% of zirconium was detected in this sample, the largest proportion in all the measured milled powders. The origin of this impurity is the attrition milling media (yttria-stabilised-zirconia).

Table 5.3: Quantified elemental analysis of attrition milled powder from XPS data. All elemental contents are given in at.%.

Mg	B	O	C	F	N	Zr	Si	Ar
11.4	10.3	39.8	35.5	1.7	0.7	0.6	0.1	0.1

EDX analysis was also carried out on a sample produced by attaching a thick layer of attrition milled powder to a carbon tab. EDX collects X-rays from significantly deeper into the sample than XPS. Averaged across 3 sampled sites (see Figure 5.28) the Zr content

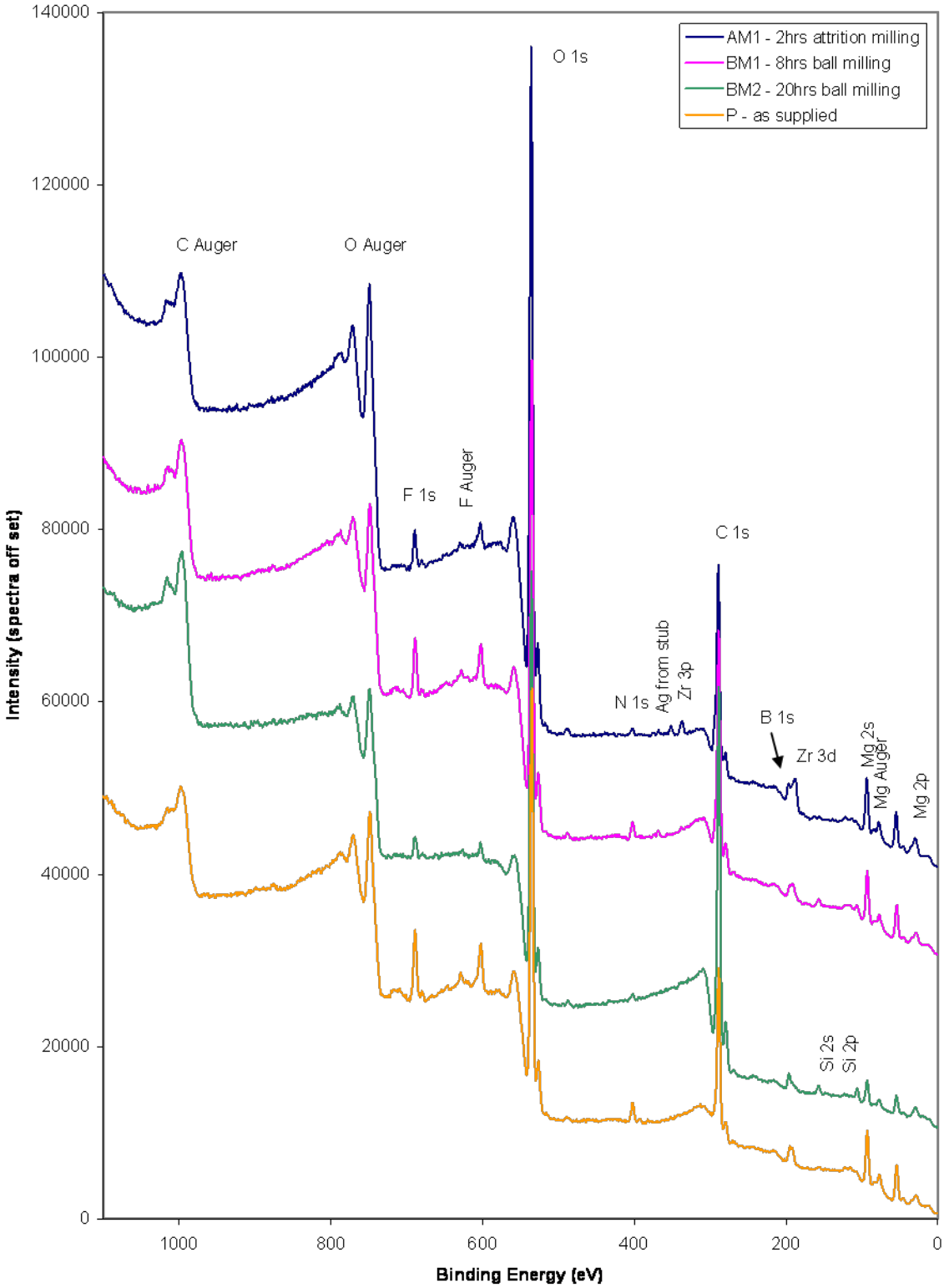
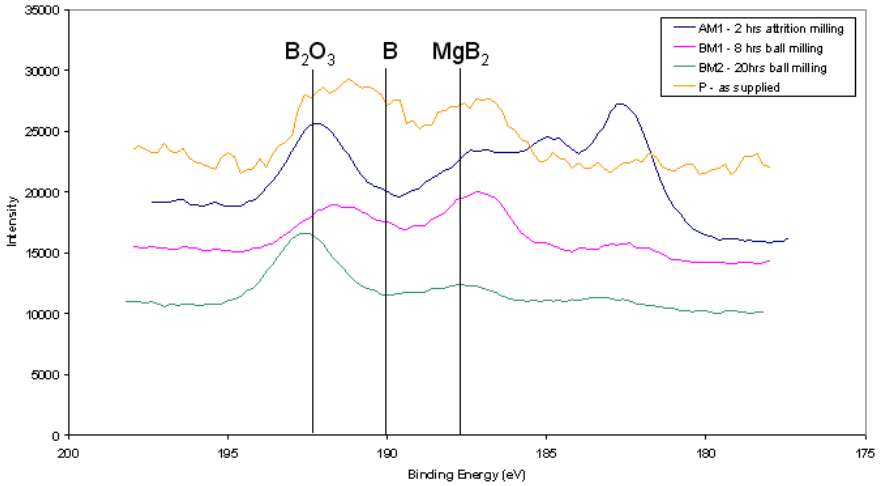
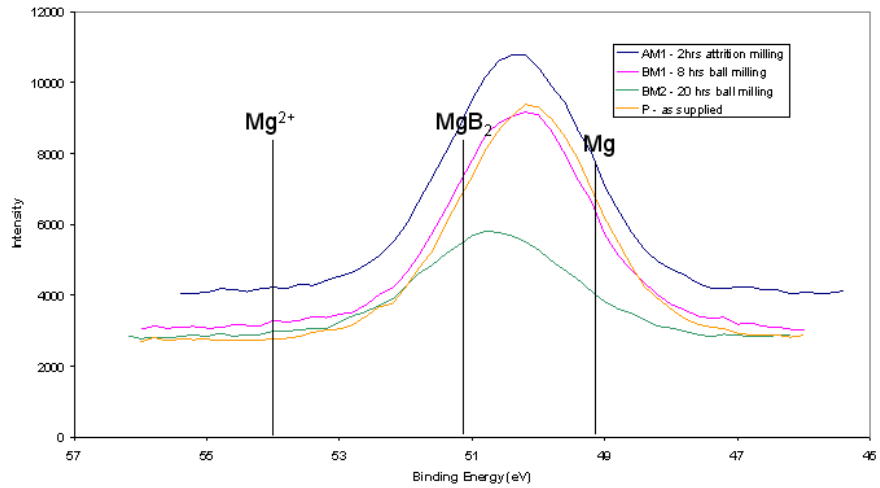


Figure 5.26: Wide-energy-range XPS scan



(a)



(b)

Figure 5.27: Narrow-energy-range XPS scans fora) Boron 1s peakb) Magnesium 2p peak

was measured as 0.95 at.% of the magnesium content; in contrast, XPS measurements indicated that the zirconium content was 5 at.% of the magnesium content. This difference indicates Zr contamination is mainly confined to the surface layers of the particles.

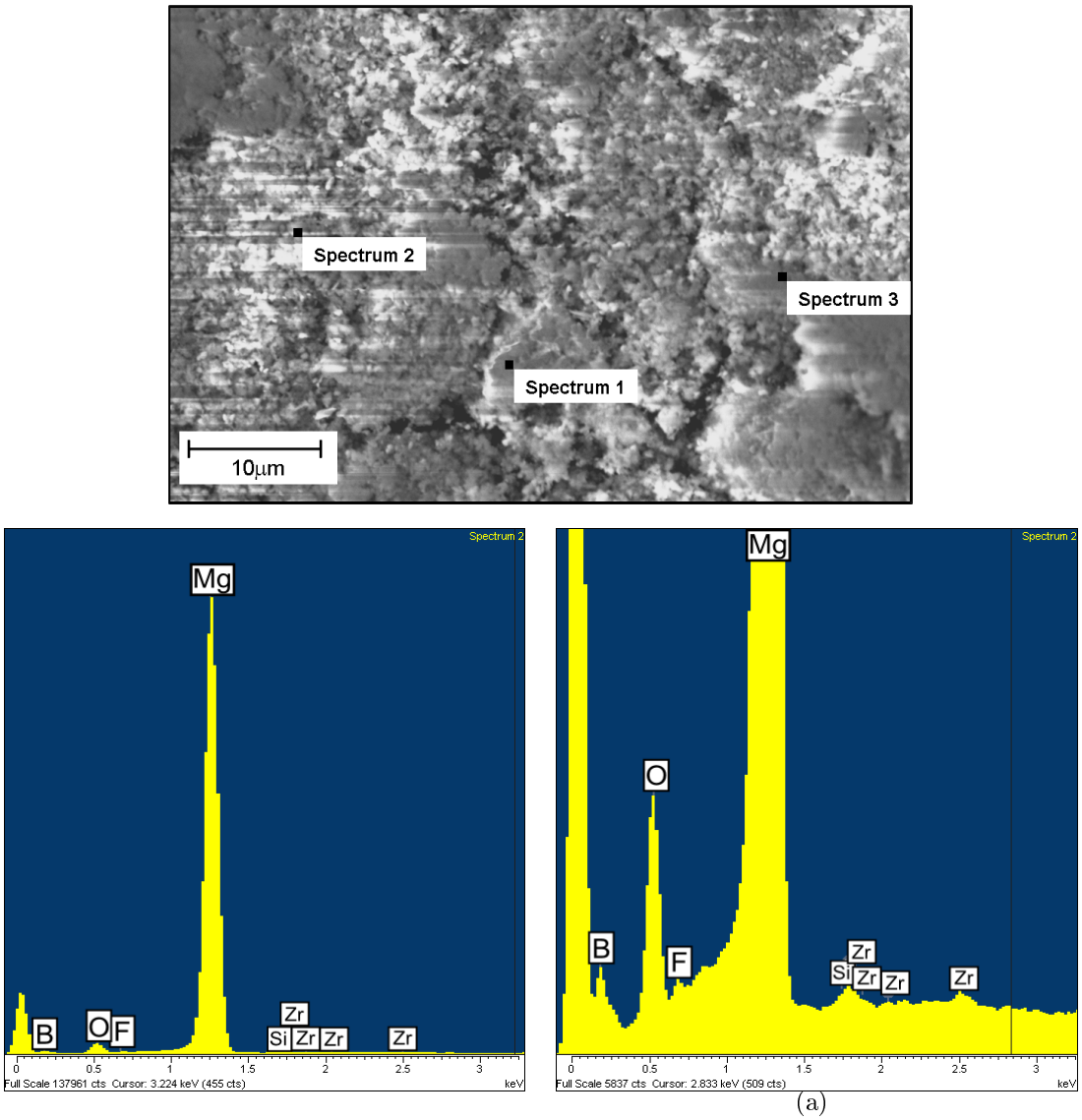


Figure 5.28: EDX spectra of attrition milled MgB_2 powder. The streaking in the image is due to charging, because this sample was not coated in order to avoid altering the chemical analysis.

5.4.2 Particle Sizing

SEM images of typical powder particles are shown in Figure 5.29. The smallest particles were difficult to image as they were very small and so the observations are mainly confined

to the larger particles. Later tests using laser diffraction (see below) confirmed that the volume fraction of small particles in the equivalent powder (SEM samples are most similar to the Mastersizer samples which were prepared by stirring in isopropanol) is very small (Figure 5.30b), though enormously larger after ultrasonication. Figure 5.29c shows the surface of the agglomerated particle in Figure 5.29b, it is made up of a cluster of much smaller particles, some of the individual features having $d < 1\,\mu$m. However as these features significantly overlap it is difficult to determine whether they are truly individual particles or are actually simply rough regions of larger particles.

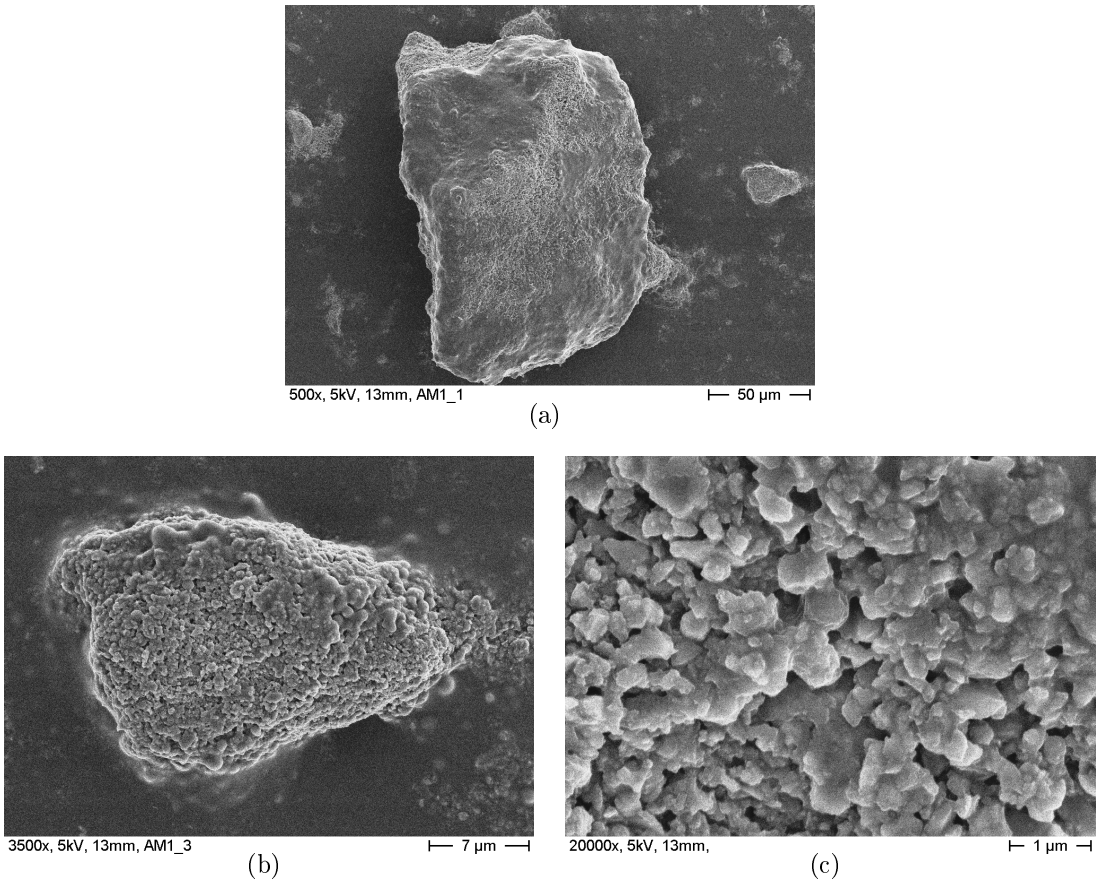
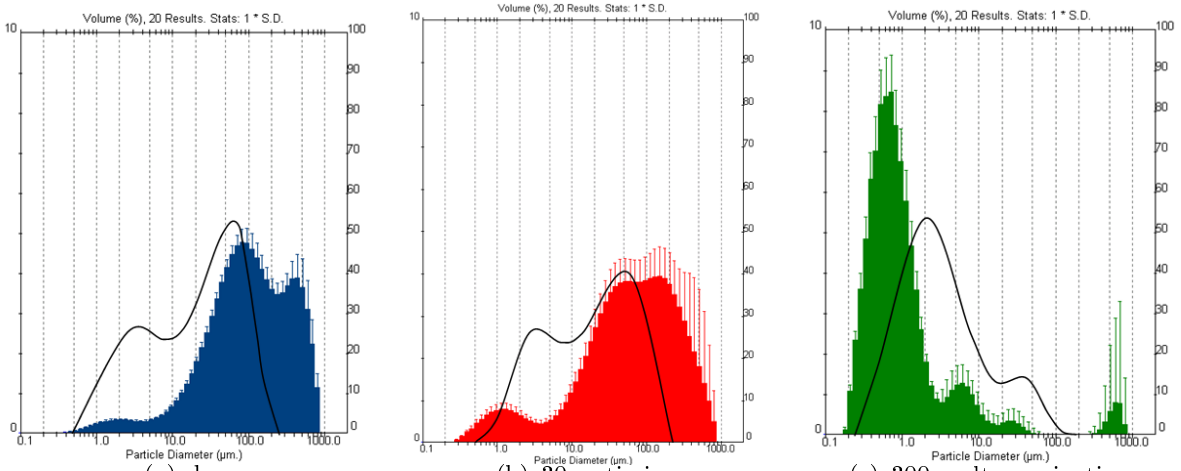


Figure 5.29: SEM images of attrition milled powder particles

The particle size distribution of the attrition milled powder was determined using laser diffraction using the Mastersizer S. Again the powder was prepared for the Mastersizer by dispersing it using different methods as discussed for the as-purchased powder (see Section 4.1.2.3 on page 99). For this powder stirring in isopropanol for 30 s increased

the volume fraction of smaller particles (the peak centred on $d_v = 1\,\mu$m in Figure 5.30b) compared to the sample added dry (Figure 5.30a). When the ultrasonicated sample was measured the majority of the volume of the powder consisted of very small particles of $d_v < 2\,\mu$m (Figure 5.30c), which is in agreement with the observation of agglomerates in the SEM (Figure 5.29). A few large agglomerates remained; this is either due to the ultrasonic treatment not being completely optimised for this sample, or because some agglomerates were more strongly bonded than the others.

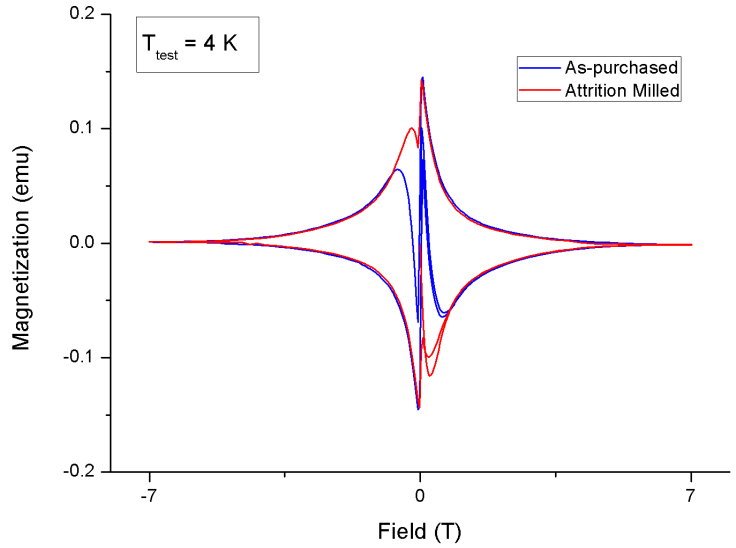


(a) dry (b) 30 s stirring (c) 300 s ultrasonication

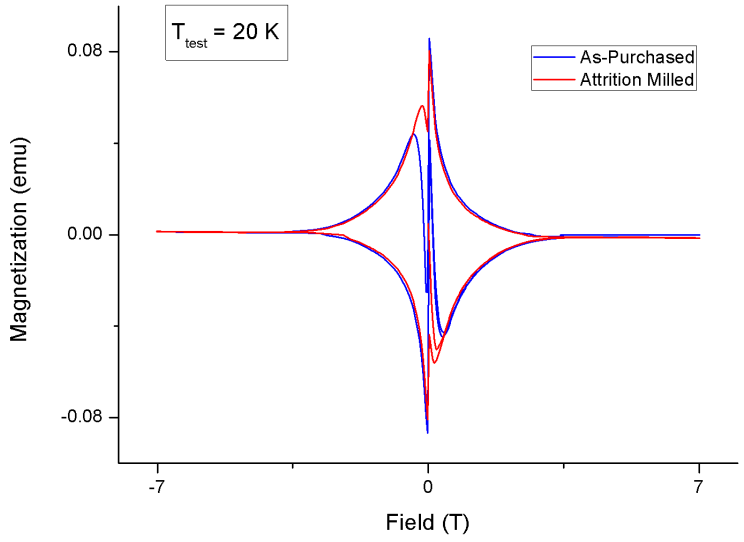
Figure 5.30: Laser diffraction particle size distributions for attrition milled MgB_2 powder

5.4.3 Magnetization Measurements

No real changes were observed in magnetization measurements for these powders compared to the as-purchased powder, indicating that the zirconium contamination has not significantly affected the superconducting properties. The loops are both extremely small at 20 K indicating almost complete loss of superconductivity in the powder. However given the inherent lack of conductivity in a powder compared to a pellet or similar bulk sample this is not especially surprising.



(a) At T = 4 K



(b) At T = 20 K

Figure 5.31: SQUID magnetization measurements for attrition milled MgB_2 powder and as-purchased MgB_2 powder.

5.5 Summary

Powders with a wide range of particle size distributions were produced by separation and milling processes. In general the separation procedures were unsuccessful at producing the expected particle size distributions. This was particularly apparent for the sedimented powder $d_{<1}$ which had a very similar particle size distribution to the starting powder when dried (see Figure 5.9). This is due to agglomeration during drying (see Figures 5.9 and 5.10), agglomeration during separation due to local charging, and the differences in the particle size criterion for the separation process (d_{sieve} or d_{St}) and the measured particle size criterion (d_v).

The milling procedures produced finer powders than the separation procedures. The median particle size decreased with increased ball milling time (Figure 5.23) with the smallest being $d_{v,50} = 1.2\,\mu$m for the non-dried powder ball milled for 20 h in air (second run), measured following ultrasonication. In comparison, the as-purchased powder measured under the same conditions had $d_{v,50} = 8.3\,\mu$m.

Like the as-purchased powder (see Section 4.1.2.3 on page 99), the measured particle size distributions vary according to the sample preparation method due to agglomeration in the samples. The post-milling drying process results in greater and harder agglomeration than seen in the original powder. For the powder ball milled for 20 h not dried before analysis, and dispersed using ultrasonication, $d_{v,50} = 1.2\,\mu$m. When the same powder was dried and re-dispersed under the same conditions, it had $d_{v,50} = 3.8\,\mu$m. There was a much larger difference in $d_{v,90}$ for the two powders, with $d_{v,90} = 2.3\,\mu$m for the non-dried powder and $d_{v,90} = 34.1\,\mu$m for the dried powder when dispersed by ultrasonication (Figure 5.21 and Figure 5.22). This latter value is still significantly lower than that for the same powder added dry with no dispersion ($d_{v,90} = 94.4\,\mu$m). The agglomerates can be broken up by ultrasonication indicating that they are fairly soft. Examination of the density of green compacts produced from these powders will establish whether uniaxial pressing provides sufficient mechanical pressure to allow an increase in packing density to occur. This will be discussed in Chapter 6.

6 Pressureless Heat-Treatment of Modified Powders

The separation and milling processes carried out on the as-purchased Alfa Aesar powder in Chapter 5 produced powders with a range of particle size distributions and impurity content. This chapter discusses the effectiveness of these powders in changing the properties of the green compact and the post-heat-treatment MgB_2 bulks by analysing their density, hardness, microstructure and impurity content, and comparing these to the properties of samples produced from the unmodified as-purchased MgB_2 powder.

6.1 Pellets Produced from Sieved Powders

6.1.1 Density

Pellets were produced from sieved powders by uniaxial pressing of 0.5 g of each sieved powder. The pellets were heat-treated at 1100 °C, as previous work had established that densification of MgB_2 requires heat-treatment at high temperature, and any densification which occurred should be evident by heat-treating at this temperature. The density of the pellets was measured before and after heat-treatment using Archimedes' method (Figure 6.1). As for the pellets pressed from as-purchased powder, the absolute density after heat-treatment varies little from that of the green compact. Such small changes in density are probably due to an increase in impurity content following heat-treatment and indicate that real densification has not occurred. Further tests of hardness and impurity content

and microscopic observations were made to establish whether any of the samples show initiation of sintering mechanisms which have not led to significant densification but have increased the connectivity.

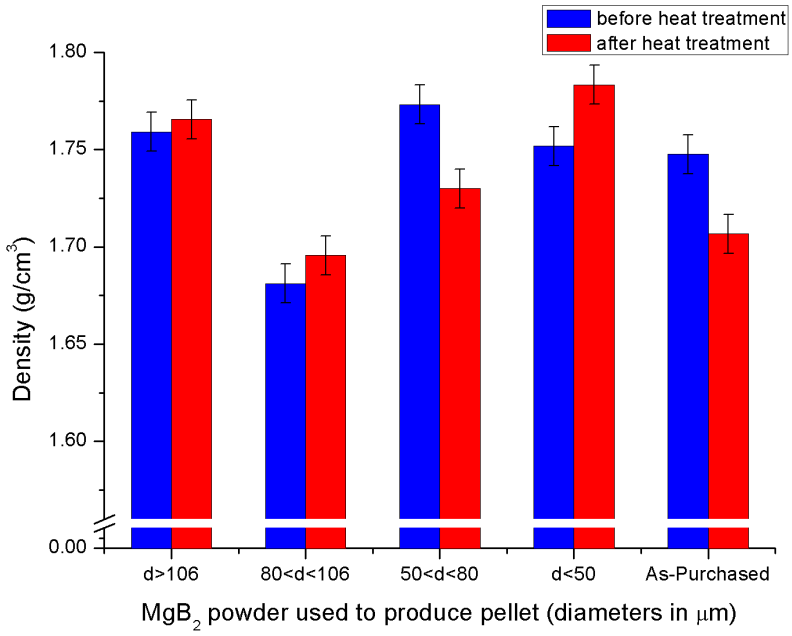


Figure 6.1: Density of bulk pellets produced from sieved powders before and after pressureless heat-treatment at 1100 °C in Ar gas

6.1.2 Hardness

The hardness data for these sieved samples is similar to the previous pressureless heat-treated pellets produced from as-purchased MgB_2 powder (see Figure 6.2). However, the mean hardness values of the pellets produced from the coarser fractions (79 ± 1 HV/2) for $d_{>106}$ and 61 ± 1 HV/2 for d_{106}) are lower than that of the pellet produced from as-purchased MgB_2 (89 ± 5 HV/2), while those of the two finer fractions are higher (101 ± 5 HV/2 d_{80} and 121 ± 2 HV/2 for d_{50}). This is probably because the finer particles give more contacts per unit volume, increasing the resistance to indentation.

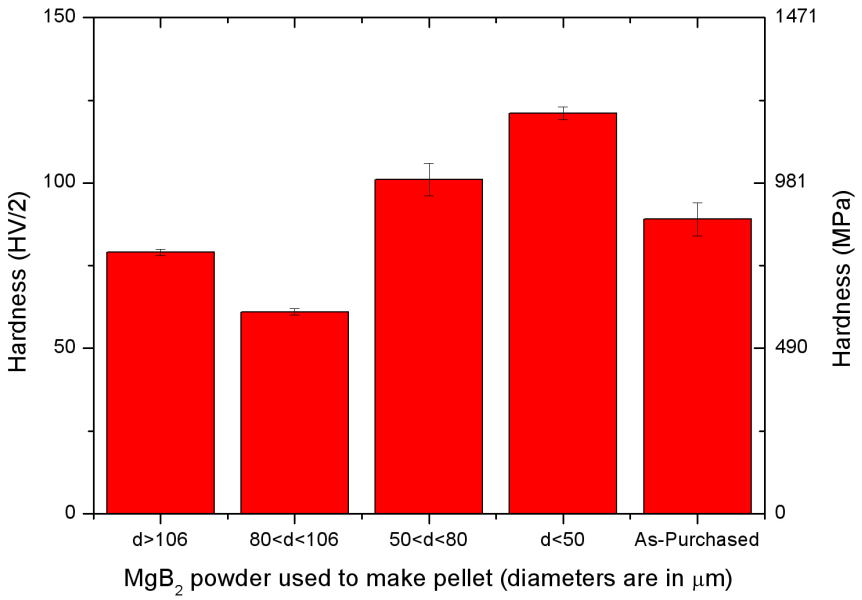
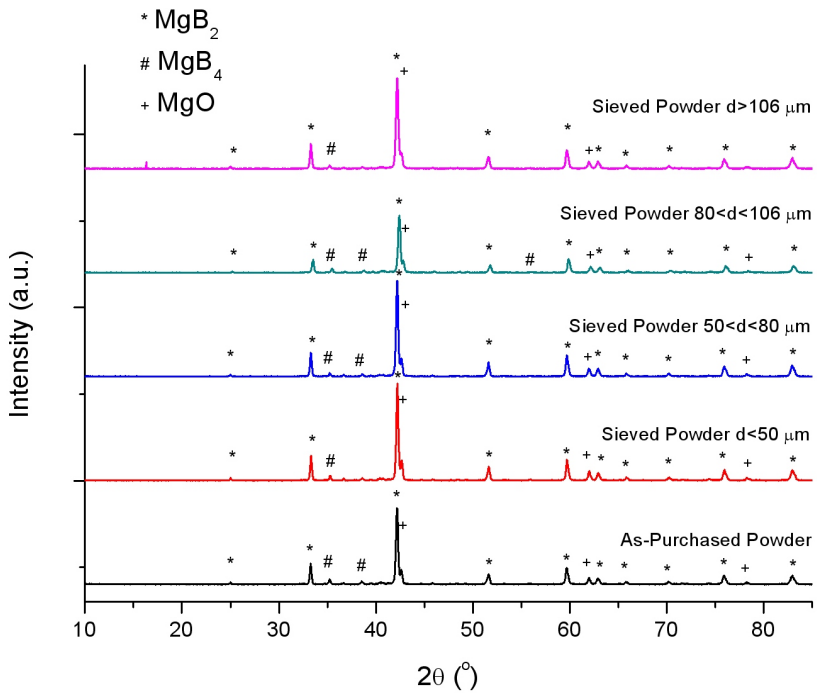


Figure 6.2: Vickers hardness of pellets produced from sieved powders, after heat-treatment at 1100 °C in Ar gas

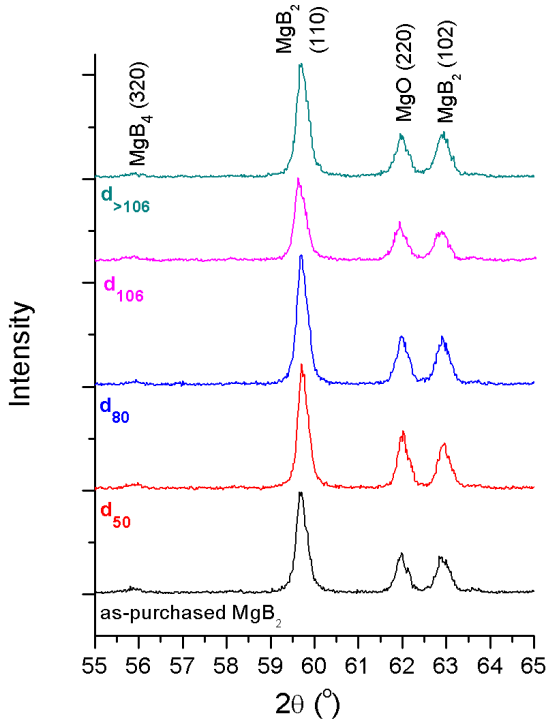
6.1.3 Impurity Content by XRD

The impurity contents of the pellets produced from sieved powders were assessed using X-ray diffraction. All peaks detected could be assigned to one of the phases MgB_2, MgB_4 and MgO. This is the same as for the as-purchased powder heat-treated at the same temperature, which indicates that the sieving process does not introduce additional sources of impurity phases. The exposure to air during the sieving process has no effect on the MgO concentration after heat-treatment.

The MgO content of the pellets increased to similar levels as for the as-purchased powder heat-treated at the same temperature (Table 6.1). The total MgO level was measured as 1.3 wt.% more for the pellet produced from the d_{50} sieved powder fraction than for the equivalent pellet produced from as-purchased powder.The cluster analysis did not indicate any variation between the pellets produced from the various sieved powder fractions. In the dendrogram, the very low distance to unification of the XRD scans of the pellets (Figure 6.4b) indicates that the sieved powder pellets are more similar to each other than



(a)



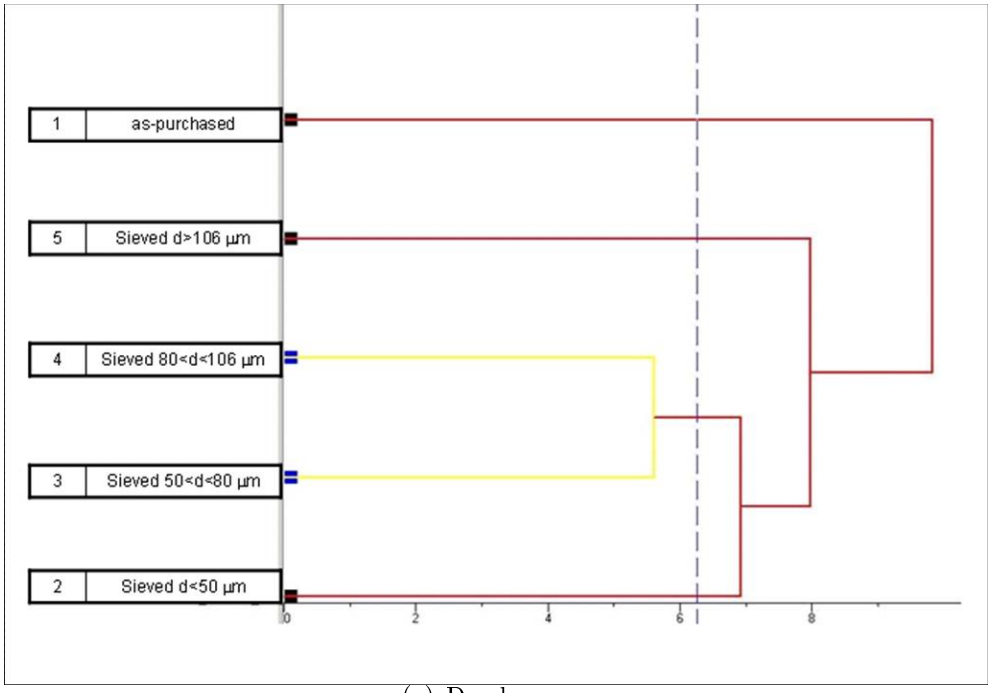
(b)

Figure 6.3: XRD spectra for pellets produced from sieved powders and heat-treated at 1100 °C in Ar gas
a) Wide angular range
b) Expanded 2θ range, containing discernible peaks due to MgO impurity phase

to the as-purchased powder.

Table 6.1: MgO content of the sieved powder pellets after heat-treatment at $1100\,^oC$

Sieve Size Distribution of Starting Powder (μm)	MgO Content (as % of MgB_2 Content)
$d_{sieve} > 106$	8.0 %
$80 < d_{sieve} < 106$	8.2 %
$50 < d_{sieve} < 80$	7.4 %
$d_{sieve} < 50$	8.6 %
as-purchased	7.3 %



(a) Dendrogram

Figure 6.4: Cluster analysis of XRD spectra of pellets produced from sieved powders and heat-treated at $1100\,^oC$

The impurity content affects the theoretical maximum density of the material. For a single phase material this is calculated from the lattice parameters, as measured by X-ray diffraction. The density of a composite material can be calculated using a rule of mixtures with the theoretical maximum density for each phase weighted by the measured volume fraction. The calculated densities of the sieved powder compacts are given in Table 6.2. These calculations assume that the material is a composite of MgO and MgB_2 only. For several samples studied in this work, MgB_4 is also present but this has not been

measured due to lack of suitable standards. MgO has a maximum density of 1.94 g/cm^3, MgB_2 2.63 g/cm^3, and MgB_4 2.78 g/cm^3, so the MgO content has a greater effect on the calculated density of an MgO/MgB_2 composite than MgB_4 does on a MgB_4/MgB_2 mixture, as the densities of MgO and MgB_2 are more different. Even at a level of 1 % MgO in MgB_2 the maximum density is altered outside the error (0.4 %). The MgB_4 content must reach 11 % before it has a similar effect on the density of an MgB_4/MgB_2 composite. Even on this basis, the density of the samples is still low compared to the maximum achievable density. But this shows that the lowering of the overall density discussed in Section 6.1.1 is misleading as the actual maximum density of the material is also reduced. Using these more accurate calculations, all the measured sample relative densities increase after heat-treatment.

Table 6.2: Calculated composite relative densities of pellets produced using sieved powders pre- and post-heat-treatment at 1100 °C. The relative density prior to heat-treatment is calculated assuming the pellet is 100 % MgB_2.

Powder Used to Produce Pellet	Relative Density Pre-Heat-Treatment	Relative Density Post-Heat-Treatment
$d_{>106}$	67 %	69 %
d_{106}	64 %	66 %
d_{80}	67 %	68 %
d_{50}	67 %	70 %

6.1.4 SEM Microscopy

Scanning electron microscopy was carried out on fracture surfaces of the pellets. Characteristic images shown in Figure 6.5 reveal an inhomogeneous microstructure. In some areas the fracture surface is clearly made up of individual particles (*e.g.* Figure 6.5b). In others increased connectivity is observed, with a smoother microstructure containing closed pores (*e.g.* Figure 6.5f). This is similar to the sample produced from as-purchased MgB_2 powder heat-treated at 1100 °C (Figure 4.31 on page 125).

As little grain growth, sintering or densification occurs during the processing of the material, the hardness and density of the heat-treated pellets is similar to those of the as-pressed pellets (see Figure 4.29 on page 122 and Figure 4.30 on page 123). I concluded that

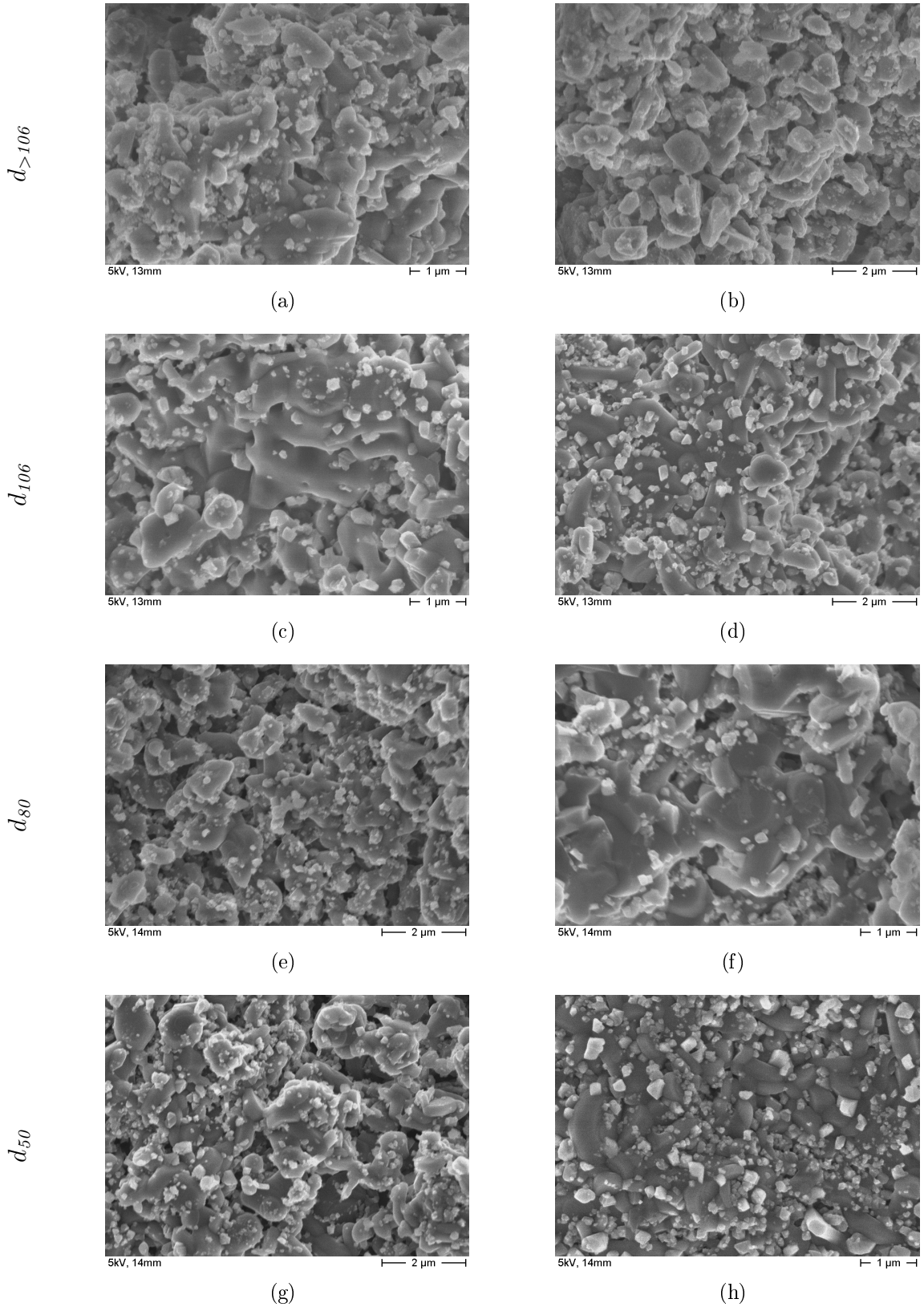


Figure 6.5: SEM images of the fracture surfaces of pellets produced from sieved MgB_2 powders heat-treated at 1100 °C

use of sieved powder does not give significant differences in the properties of heat-treated MgB_2. The hardness increases a little at 1100 °C but not significantly in comparison to that of the hardness of samples which have truly sintered, indicating that no significant sintering has taken place. None of the sieved powders are fine enough to lower the sintering temperature to encourage substantial densification. The compaction of the initial green compact of the sieved powders is slightly higher than for as-purchased powders, apart from for d_{106} which is lower due to porous agglomerates in this fraction (see Figure 5.2 on page 134). The largest difference in density from the as-purchased powder pellet is around $0.06\,g/cm^3$ for the pellet produced from d_{50} powder, which is insignificant compared to that required for full densification. This indicates that the particle size distributions of the sieved powders are not suitable for significantly increasing the packing density. I therefore discontinued work on sieved material.

6.2 Pellets Produced from Sedimented Powders

Pellets were produced by uniaxial pressing from the sedimented MgB_2 powders described as $d_{>100}$ and $d_{<1}$ in Chapter 5. The pellets were heat-treated at 950 °C or 1100 °C, and characterised as before. The results are compared to MgB_2 bulks prepared from as-purchased powder.

The intention of preparing sedimented powders was twofold. First, to modify the particle size distribution of the powder so as to increase the packing density and the likelihood of sintering. Secondly, to increase the packing density by mixing together particles of different sizes in order that the gaps between larger particles were filled by the smaller fractions. This requires a mixture of at least two particle size fractions with a large size difference [50]. A basic calculation was carried out to establish the sizes required. Assuming a particle size for the coarse fraction of $d_{St} = 100\,\mu m$, the maximum size of a spherical particle which will fit into the interstice between the coarse particles was calculated as $15.4\,\mu m$ (see Figure 6.6). Sedimented fractions were therefore prepared with nominal

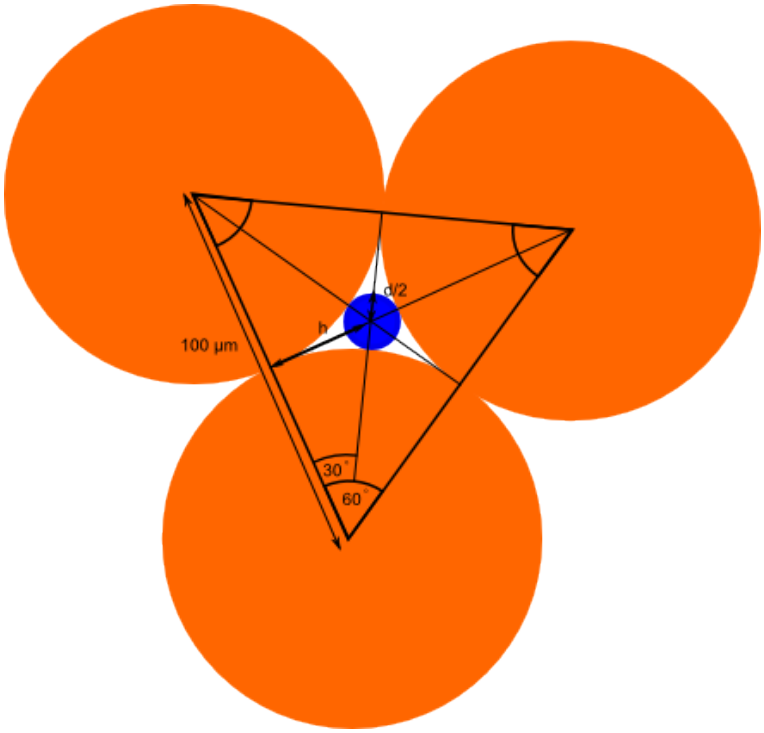


Figure 6.6: Calculating the size of interstices between particles with $d = 100\,\mu m$

$d_{St} > 100\,\mu$m and $d_{St} < 1\,\mu$m. Then, assuming that the coarse fraction of particles had perfect tetragonal packing (PF_c) (see Reed [50] for description), and that the packing of the small particles in the interstices was also tetragonal (PF_f), the maximum achievable packing fraction was calculated using Equation 6.1 [50] to be approximately 93 %. For random packing of both fractions (for mono-size coarse particles this is around 65 %), the approximate maximum achievable packing density using the same particle size fractions is around 88 % [50], which is still higher than that of the green compacts produced from as-purchased MgB_2 powder (approximately 65 %).

$$PF_{max} = PF_c + (1 - PF_c)PF_f \tag{6.1}$$

"Mixed pellets" were produced by thoroughly mixing $d_{>100}$ and $d_{<1}$ powders in a mass ratio of 74 wt.% $d_{>100}$ powder to 26 wt.% $d_{<1}$ powder. This was calculated to give a sample of 88% of the theoretical density, assuming random packing of each powder and thorough dispersion of the fine particles in the interstices between the larger particles.

6.2.1 Density

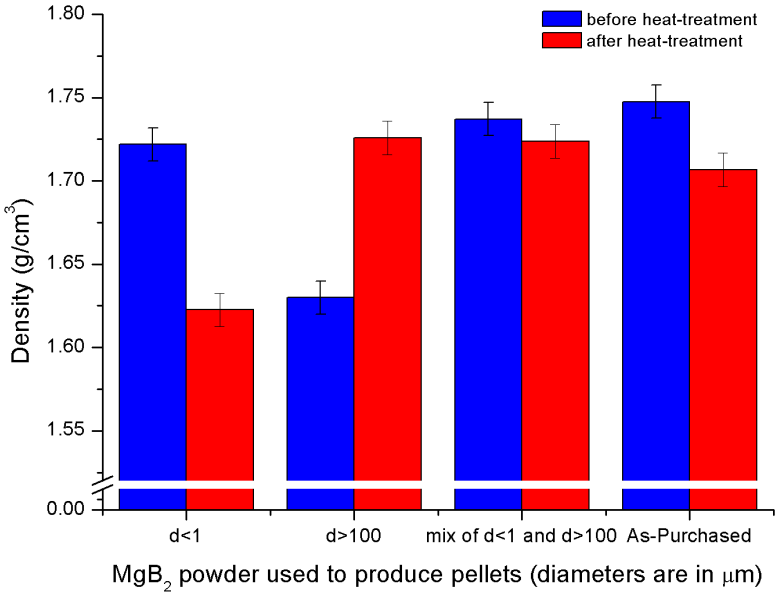
The densities of the pellets were measured before and after heat-treatment (Figure 6.7). The density following heat-treatment at 950 °C decreases for the $d_{<1}$ pellet, whereas it increases for the $d_{>100}$ pellet. Densities for the mixed pellets and the as-purchased powder vary little within the experimental error. The densities of pellets heat-treated at 1100 °C decrease on heat-treatment. No pellet was produced from $d_{<1}$ powder for heat-treatment at 1100 °C as between heat-treatments particle size distribution data was obtained indicating that the $d_{<1}$ powder had a significantly broader particle size distribution than expected. Due to the difficulties of obtaining sufficient $d_{<1}$ powder to produce a bulk pellet this preparation route was abandoned.

None of the pellets heat-treated at either temperature increase dramatically in density (Figure 6.8). For significant densification to have occurred the numerical value of the density would be closer to the theoretical maximum density 2.63 g/cm^3. On the scale of this figure the density variations appear as random fluctuations.

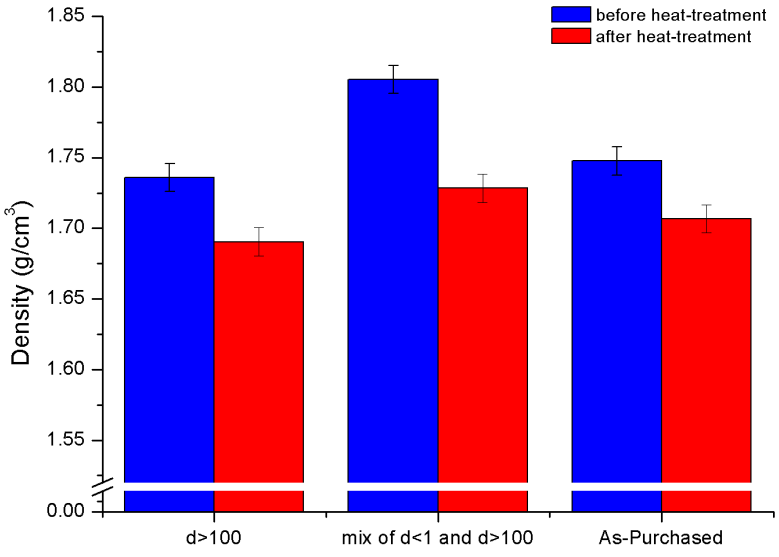
It is clear from these density measurements that attempts to increase the packing density of the green compact have not been successful. While the density of the green compact at 69 % is among the highest measured for any of the MgB_2 samples in this work, it is far from the potential maximum calculated above (93 % for tetragonal packing; 87 % for random packing)

6.2.2 Hardness

The Vickers hardness values of the sedimented pellets are shown in Figure 6.9. That of the pellet produced from $d_{>100}$ powder is initially similar to that of the as-purchased powder, but decreases significantly for the pellet heat-treated at the higher temperature of 1100 °C. The reason is that the coarse fraction consists predominantly of loosely bound agglomerates which are crushed by the indenter, offering decreased resistance to indentation despite similar overall density and MgO impurity level to pellets produced from the as-purchased powder. Similar behaviour was seen in the sieved pellets (see Section

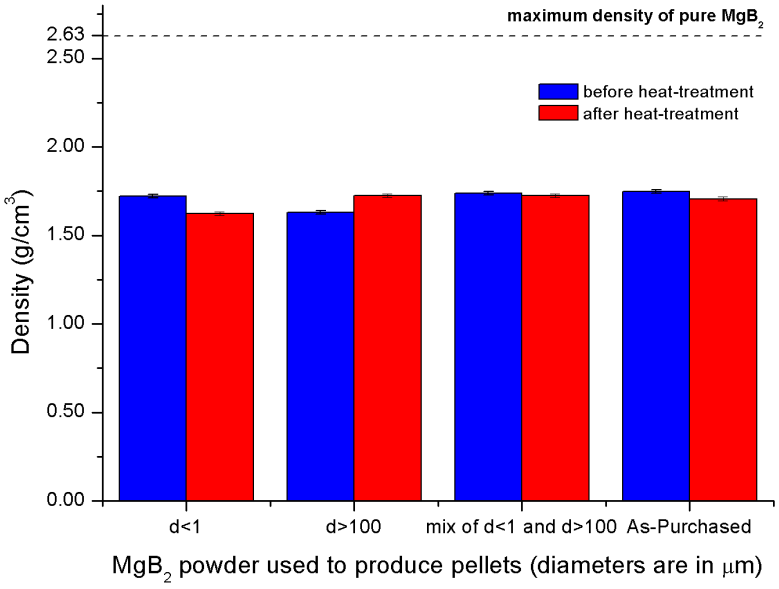


(a)

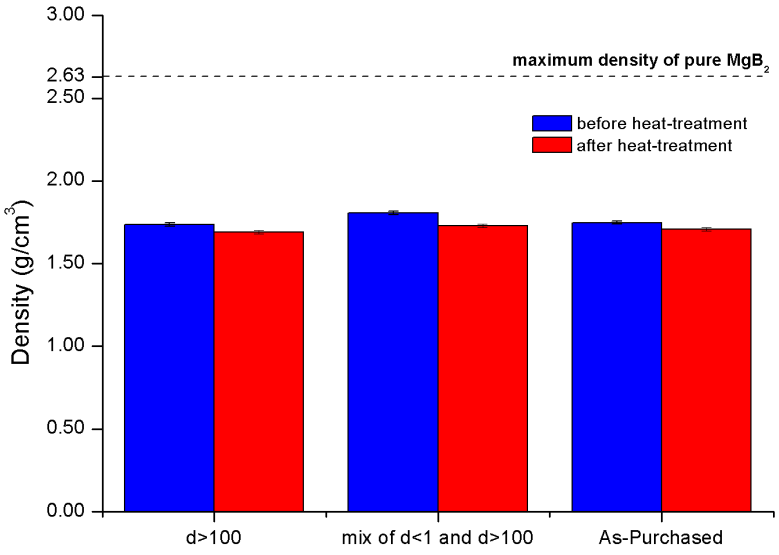


(b)

Figure 6.7: Density of pellets produced from sedimented powders before and after heat-treatment
a) heat-treated at 950 °C
b) heat-treated at 1100 °C



(a)



(b)

Figure 6.8: Density of pellets produced from sedimented powders before and after heat-treatment on scale indicating extent of densification required to achieve the theoretical density of MgB_2.
a) heat-treated at 950 °C
b) heat-treated at 1100 °C

6.1.2 and Figure 6.2 above) The $d_{<1}$ pellet heat-treated at 950 °C has a very low hardness similar to that of as-purchased powder heat-treated at low temperatures. The mixed powder shows the most improvement from 950 °C to 1100 °C, with the hardness at 950 °C being below the equivalent for the as-purchased powder and that for 1100 °C being above. However in line with the density measurements, none of the pellets has the significantly elevated hardness indicative of densified MgB_2.

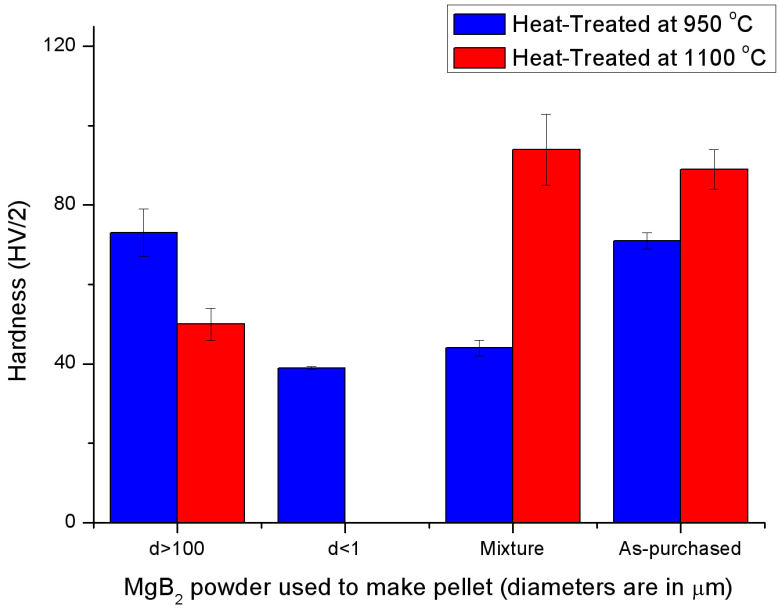
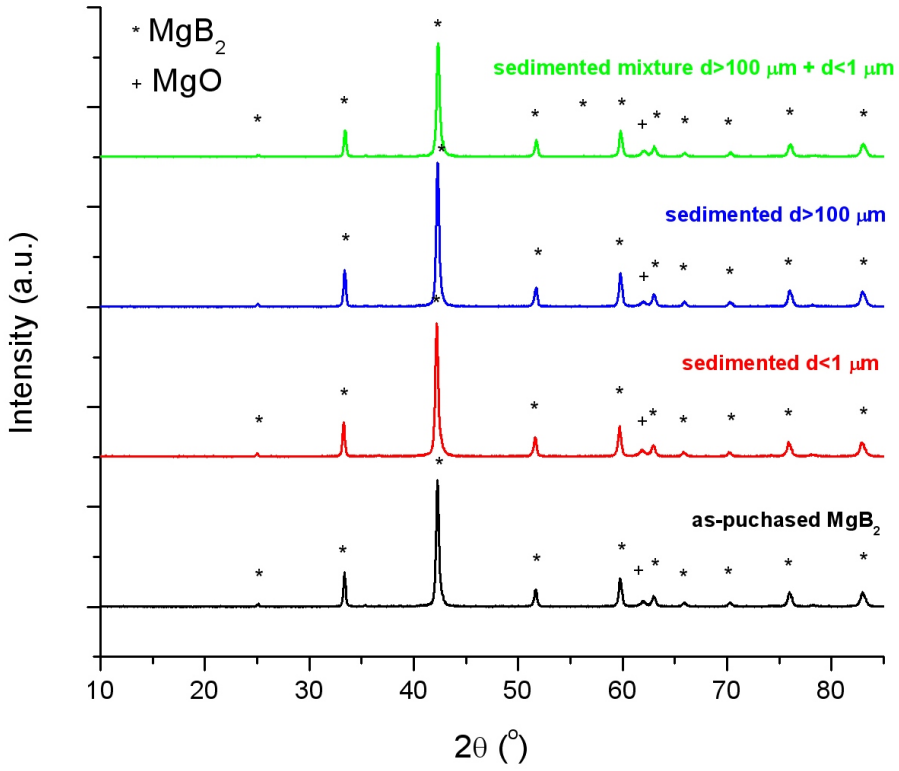


Figure 6.9: Hardness of pellets produced from sedimented MgB_2 powders

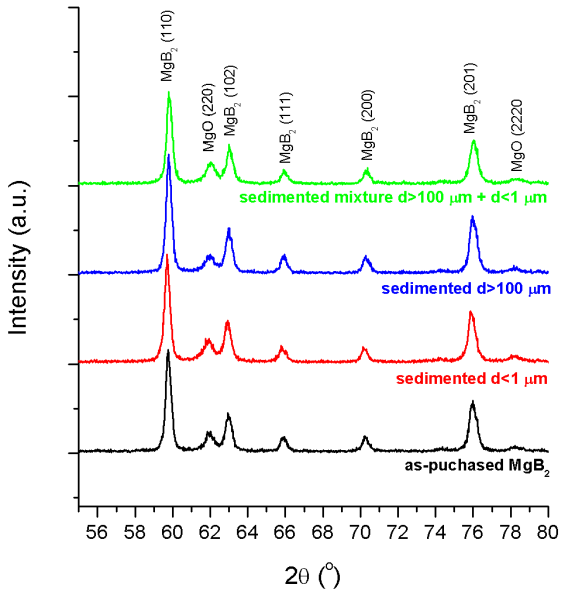
6.2.3 Impurity Content

The crystalline impurity content of the sedimented pellets was determined using X-ray diffraction. The spectra measured for pellets heat-treated at 1100 °C contain peaks attributable to MgB_2, MgO and MgB_4 while those for the pellets heat-treated at 950 °C contain only peaks due to MgB_2 and MgO.

A cluster analysis was carried out on the XRD spectra taken from pellets produced from sedimented powder (Figure 6.12). The sample produced from $d_{<1}$ powder and heat-treated at 1100 °C clusters with the others heat-treated at 950 °C; other than this the

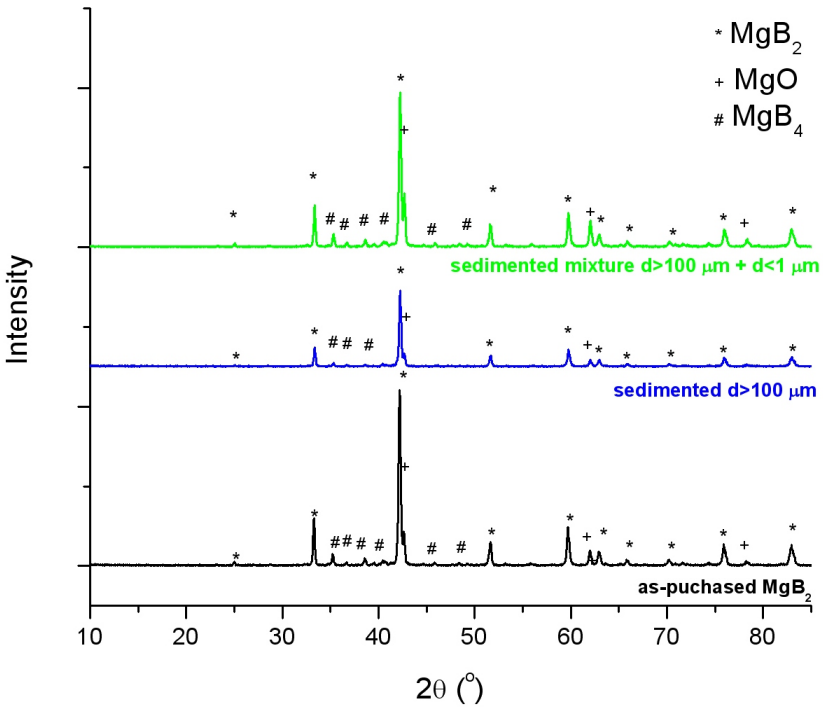


(a) Wide angular range

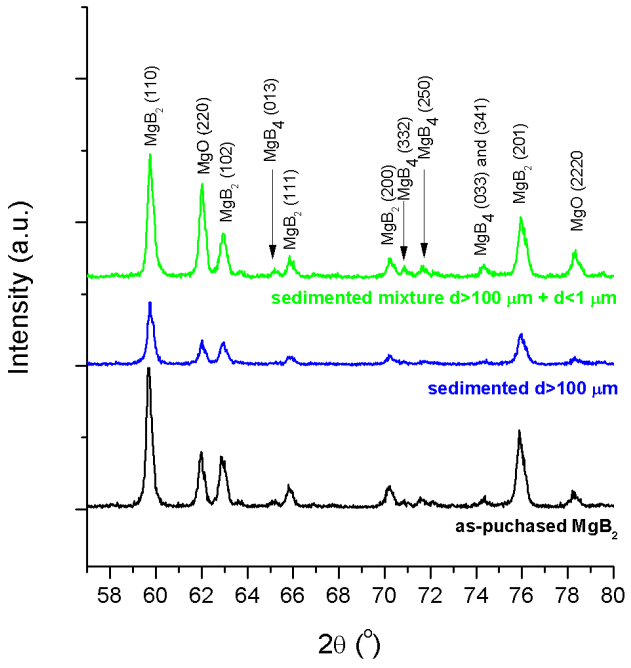


(b) Region containing peaks used for calibration of MgO content

Figure 6.10: XRD spectra of pellets produced from sedimented powders heat-treated at 950 °C



(a)



(b)

Figure 6.11: XRD spectra of pellets produced from sedimented powders heat-treated at 1100 °C
a) Wide $\theta - 2\theta$ angular range
b) Expanded $\theta - 2\theta$ range containing peaks used for calibration of MgO content

pellets are grouped based on heat-treatment temperature.

The MgO contents measured from XRD scans of the pellets after heat-treatment are given in Table 6.3. The high value for the pellet produced from mixed sedimented powders and heat-treated at 1100 °C may be due to the prolonged exposure to isopropanol during sedimentation to obtain the $d_{<1}$ fraction. The measured MgO contents of the pellets produced from the mixed powders and the $d_{<1}$ powder and heat-treated at 950 °C are similar.

Table 6.3: MgO content of pellets produced from sedimented powders and heat-treated at 950 °C and 1100 °C

Starting Powder	MgO Content (as % of MgB_2 content)	
	950 °C	1100 °C
$d_{>100}$	0- 5 % (out of range)	7.2 %
$d_{<1}$	7.2 %	-
Mix of $d_{<1}$ + $d_{>100}$	7.3 %	17.2 %
as-purchased MgB_2	5.1 %	7.3 %

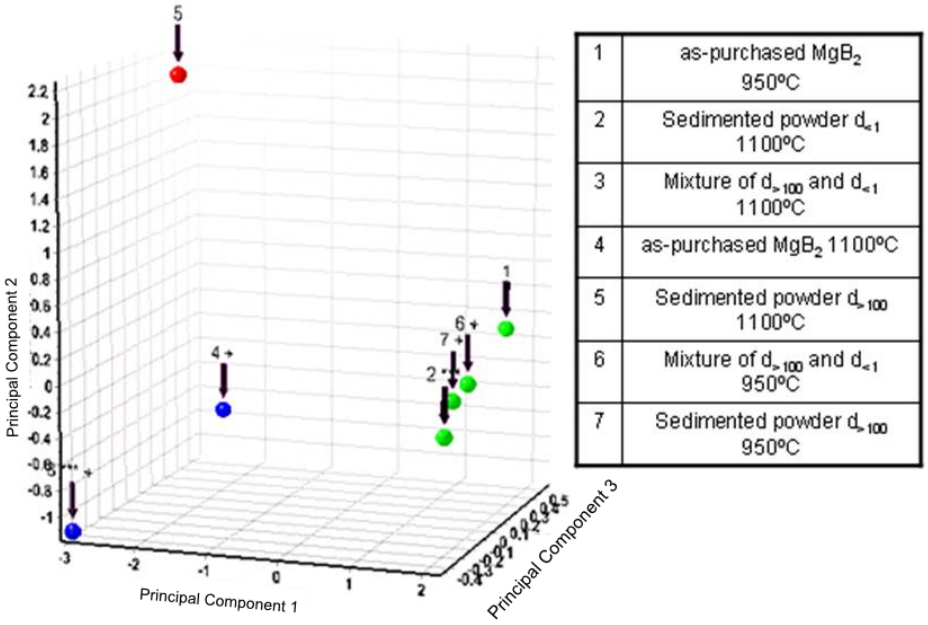
The increase in impurity content affects the maximum density which can be achieved, as discussed above for sieved powders. Treating the pellet prior to heat-treatment as pure MgB_2 and that after heat-treatment as a composite of MgB_2 and MgO only, the corrected relative densities are as shown in Table 6.4.

Table 6.4: Calculated composite relative densities of sedimented powder pellets pre and post-heat-treatment at 950 °C and 1100 °C. The relative density prior to heat-treatment is calculated assuming the pellet is 100 % MgB_2.

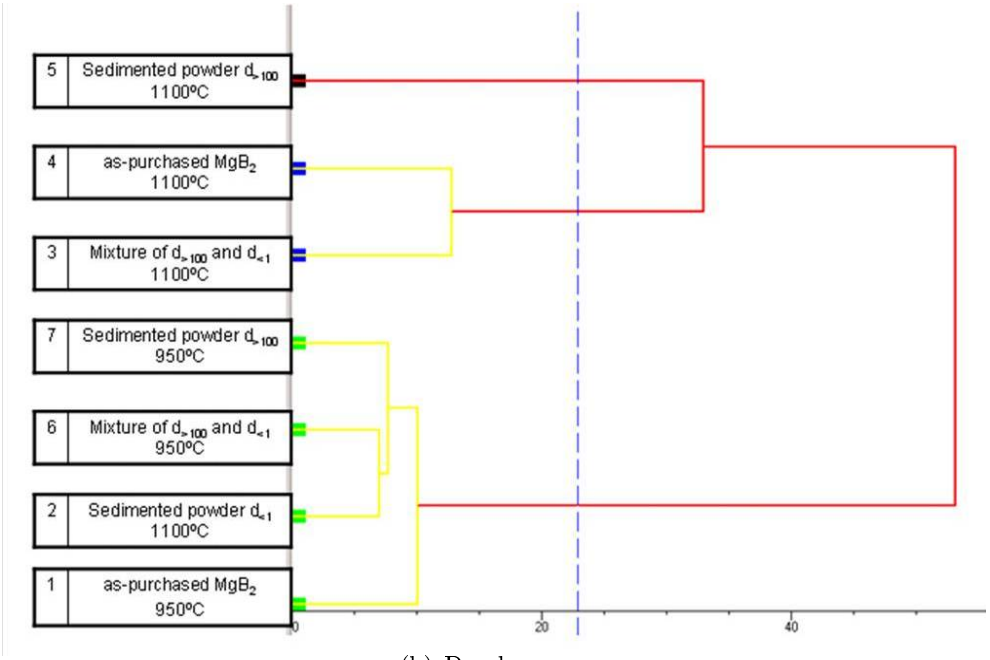
Starting Powder	Relative Density of Pellets			
	pre-HT at 950 °C	post-HT at 950 °C	pre-HT at 1100 °C	post-HT at 1100 °C
$d_{>100}$	62 %	67 %	66 %	66 %
$d_{<1}$	65 %	63 %	-	-
Mix	66 %	67 %	69 %	70 %

6.2.4 Microscopy

SEM images were taken of fracture surfaces of the pellets produced from $d_{>100}$ and $d_{<1}$ (Figure 6.13). The sample produced from $d_{<1}$ and heat-treated at 950 °C appears



(a) Principal Components Analysis



(b) Dendrogram

Figure 6.12: Cluster analysis of XRD spectra of pellets produced from sedimented powders and heat-treated at 950 ºC and 1100 ºC

powder-like (Figures 6.13a and b), similar to that for the as-purchased powder (see Figure 4.31c), which is not unexpected as the particle size distributions were found after these pellets were made to be very similar (see Section 5.2.2 on page 140). The pellets produced from $d_{>100}$ powder are more interesting. The pellet heat-treated at 1100 °C consists of connected particles with a smoother appearance (Figure 6.13d) similar to the observations for the as-purchased powder heat-treated at the same temperature (see Figure 4.31d). The sample produced from $d_{>100}$ and heat-treated at 950 °C (Figure 6.13f) resembles the pellet produced from as-purchased powder heat-treated at 1100 °C, rather that heat-treated at 950 °C, the particles are again more amalgamated. This may be due to the agglomerates in the coarse powder which are composed of much smaller particles (see Section 5.2.2 on page 140). The finer powder is initially more consolidated, and this means that the densification is more pronounced. This indicates that if the right conditions are established to balance length of heat-treatment with loss of material through magnesium evaporation, the MgB_2 may be induced to sinter at lower temperatures by restricting the particle size to very small particles, even if those particles are initially agglomerated. However as the agglomerates are inherently porous, the packing would be improved if agglomeration were minimised.

Particle size distributions were also measured for powder mixtures. These are shown in Figure 6.14 for powders which had been dried and in Figure 6.15 for powder which had not been dried. The drying process again causes hard agglomeration which cannot be reversed by ultrasonication, while the non-dried powders following ultrasonication consist mainly of particles of $d \leq 20\,\mu$m. The agglomeration is not necessarily a problem, as the packing density could be increased using powder containing agglomerates, but agglomerates contain significant internal porosity and hence lower the packing density below that calculated for the ideal pellet. In addition, the lower size fraction was nowhere near the particle size intended, and the actual particle size distribution is very wide. This is unlikely to aid the ordered hexagonal packing assumed in the model, and a much more likely model is that of random packing of the particles, which for a log-normal distribution

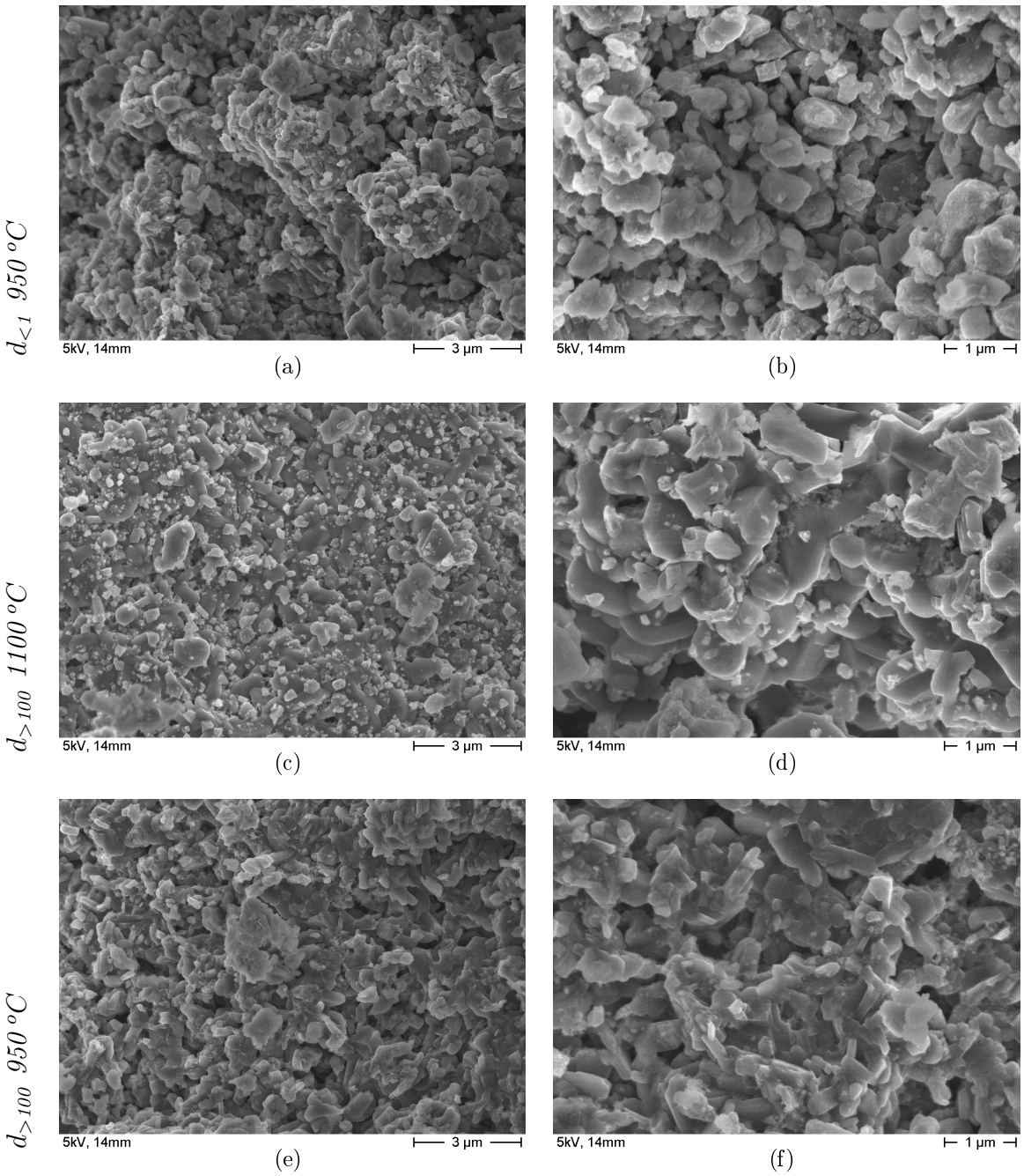
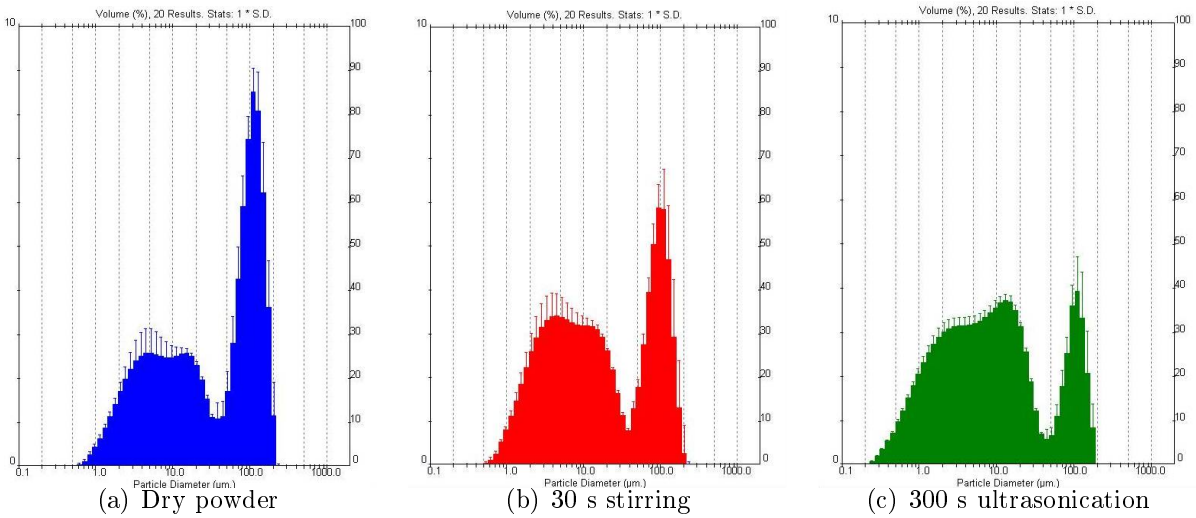


Figure 6.13: SEM images of pellets produced from sedimented powders and heat-treated at the temperatures indicated

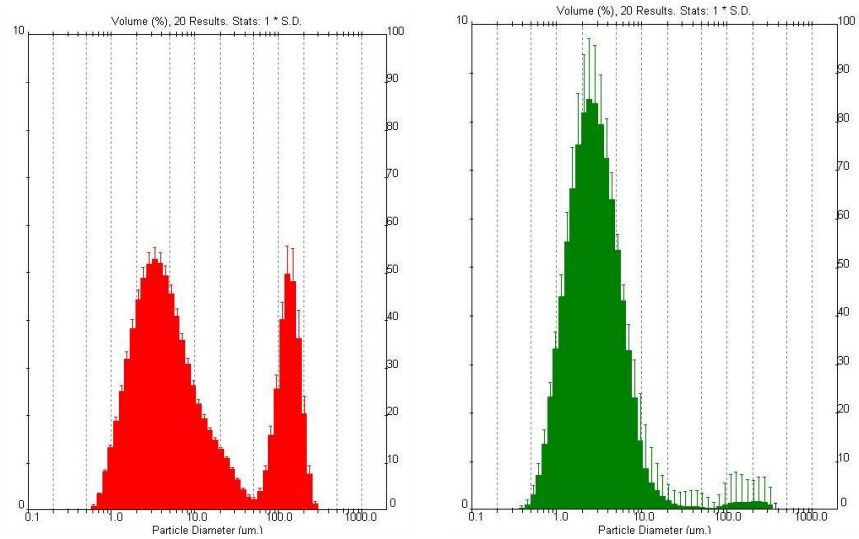
gives a maximum packing density of 65-69 % depending on the standard distribution to the particle sizes [50]. These values are approximately those obtained for these MgB_2 pellets.



(a) Dry powder (b) 30 s stirring (c) 300 s ultrasonication

Figure 6.14: Particle size distributions measured by laser diffraction of mixtures of sedimented MgB_2 powders $d_{>100}$ (dried) and $d_{<1}$ (dried) (50:50 ratio) in isopropanol

The effect of particle size on packing density is well-studied in systems such as glass spheres [221], and models have been established such as the Andreasen distribution [222] which can pack to a density $> 80\,\%$ [50]. The difficulties encountered in this work are due to hindered motion of particles during pressing, with the main cause being the extensive agglomeration established from particle size distribution measurements.



(a) 30 s stirring (b) 300 s ultrasonication

Figure 6.15: Particle size distributions measured by laser diffraction of mixtures of sedimented MgB_2 powders $d_{>100}$ (slurry) and $d_{<1}$ (slurry) (50:50 ratio) in isopropanol

The reason why the mixture of $d_{<1}$ and $d_{>100}$ powders was unsuccessful in increasing the packing density is because producing by sedimentation starting powder of a narrow mono-disperse particle size distribution is difficult, and many apparently "large" particles were in fact loose agglomerates of smaller particles that could have been broken up by ultrasonication. The results in Section 6.1 indicate that the sieving technique was also not suitable to produce these finer powders. The particle size data in Chapter 5 was only obtained later in the project due to the limited availability of the loaned Mastersizer equipment, so this fact could not be established until then.

6.3 Pellets Produced from Ball Milled Powders

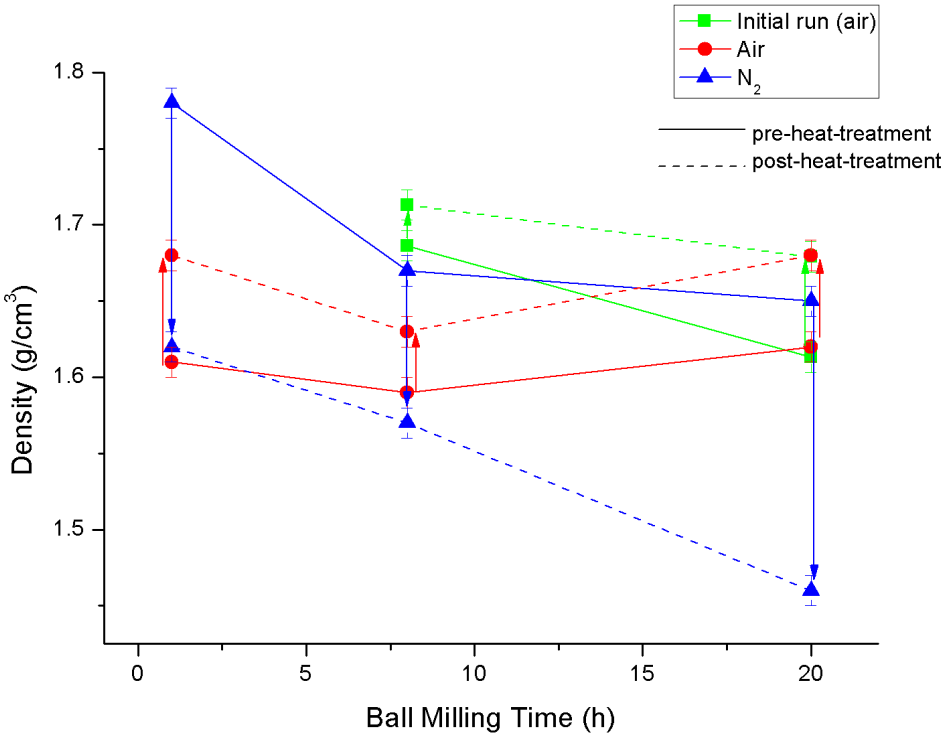
Ball milled powders were produced as described in Chapter 5. Pellets were produced from all the dried powders by uniaxial pressing, and then heat-treated between 950 °C and 1100 °C in flowing Ar gas for 1 h at the peak temperature, and characterized by density and hardness measurements, SEM observations, and XRD scans.

6.3.1 Density

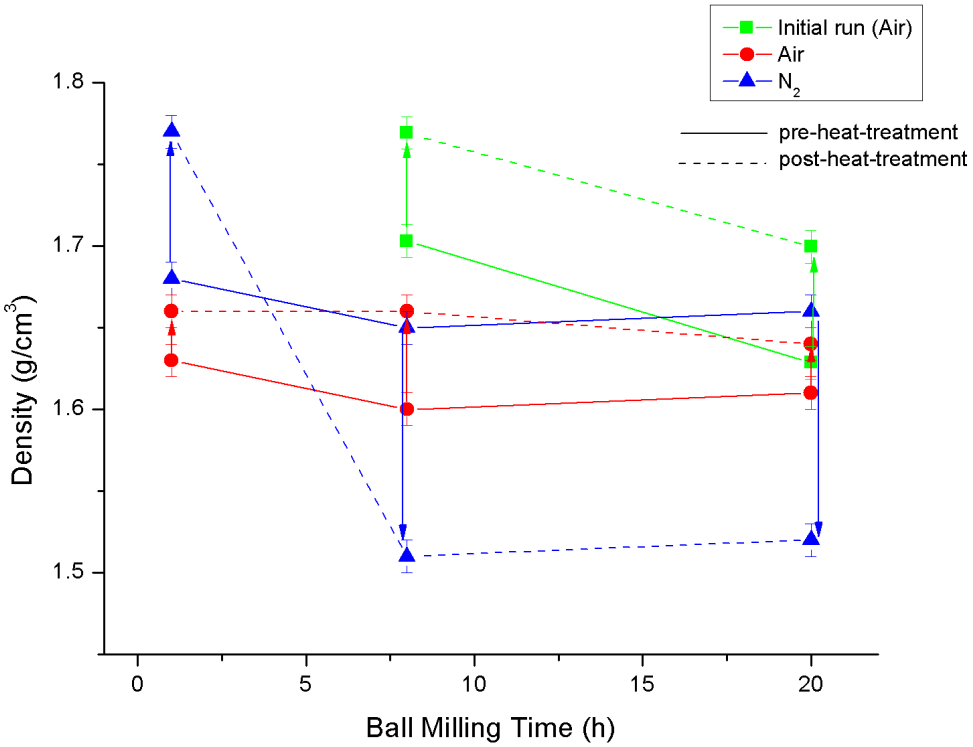
The density of the samples was measured before and after heat-treatment at 950 °C and 1100 °C (Figure 6.16). The density does not change by more than 0.3 g/cm^3 for any sample. The error in the density measurement is estimated at 0.01 g/cm^3. In the case of all the samples prepared in air (initial and second sets of samples), the density increases slightly after heat-treatment for all samples. The density of samples prepared in nitrogen decreases following heat-treatment other than for the sample prepared in nitrogen, ball milled for 1 h and heat-treated at 1100 °C. It is possible that nitrogen gas has been adsorbed onto particle surfaces during preparation, and that this has been released during heat-treatment, decreasing the density of the final sample.

6.3.2 Impurity Content

XRD scans were carried out on the pellets produced from ball milled powders to determine variations in impurity content. Figure 6.17 shows the XRD scans on the pellets produced from the powder ball milled for 8 h in the initial run. These contain MgB_2 and MgO peaks, and those heat-treated at 1050 °C and 1100 °C also contain significant fractions of MgB_4. Figure 6.18 is the equivalent for the pellets produced from the powder ball milled for 20 h in the initial run. The major difference between the two sets of samples is that the pellets from the 20 h powder gave discernible peaks due to MgB_4 for all heat-treatment temperatures shown. The MgO peaks are also larger in the powder milled for 20 h. This indicates that the 20 h ball milled powder contains more impurities (*e.g.* amorphous impurities, or compounds such as $Mg(OH)_2$) prior to heat-treatment which form MgB_4 and MgO during heat-treatment than the 8 h ball milled powder. As these cannot be detected in the XRD scan of the powder (a characteristic broad "hump" would be visible for $10^o < 2\theta < 30^o$, see Figure 5.11 on page 144), these are likely to be amorphous impurities. However it is not surprising that the powder ball milled for a long period should have an increased impurity content; the surface area increases due to break-up of particles during milling, and so a greater surface area is available for adsorbed



(a)



(b)

Figure 6.16: Density of pellets produced from all ball milled MgB_2 powders heat-treated at
a) 950 °C
b) 1100 °C

impurities.

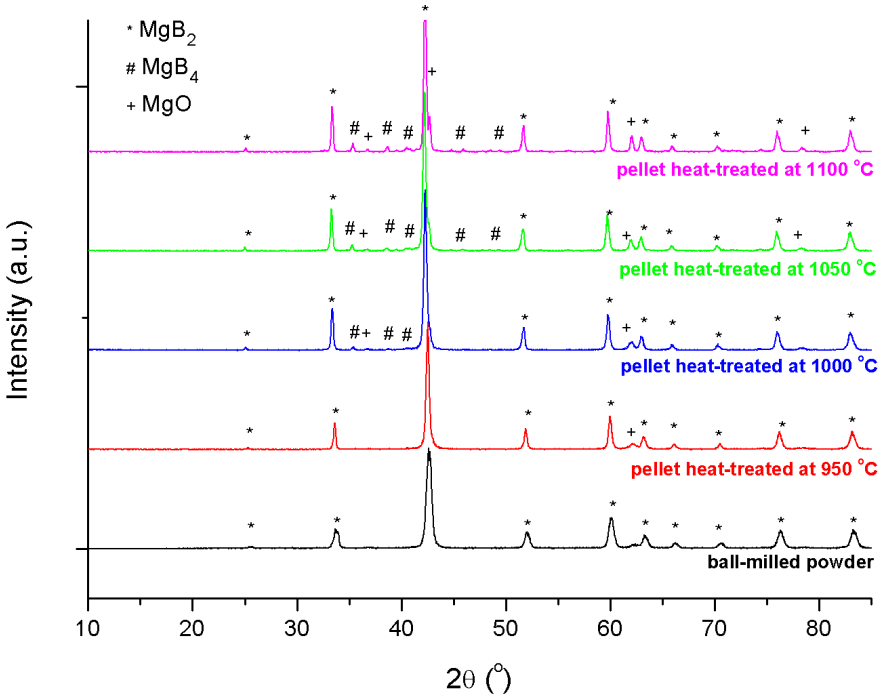


Figure 6.17: XRD spectra of pellets produced from initially-produced 8 h ball milled powder

The MgO content was measured for all samples (Table 6.5). The trend for the powder ball milled for 8 h is very similar to that for the pellets produced from as-purchased powder. The pellets produced from powder ball milled for 20 h have significantly higher MgO levels and these are more or less constant with respect to the heat-treatment temperature at around 36 % of the MgB_2 content.

Table 6.5: MgO content of pellets produced from initially produced ball milled powders

Heat-Treatment Temperature (°C)	MgO Content as % of MgB_2 Content		
	Powder Ball Milled 8 h in Air	Powder Ball Milled 20 h in Air	As-Purchased MgB_2
950	5.3	37.6	5.1
1000	6.4	35	5.6
1050	6.2	36.2	6.0
1100	7.3	39.1	7.3

XRD spectra for the pellets produced from the second series of ball milled powders

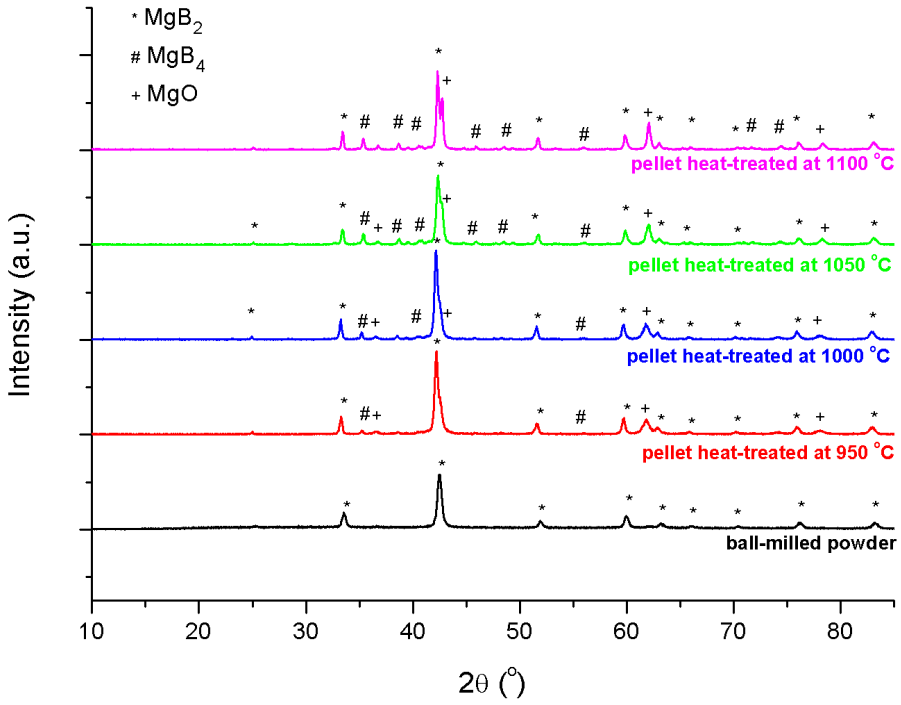


Figure 6.18: XRD spectra of pellets produced from initially-produced 20 h ball milled powder

(Figures 6.19, 6.20 and 6.21) indicate that packing in nitrogen or air makes little difference to the impurity content of the pellets, with the same MgO, MgB_4 and MgB_2 peaks visible for samples milled for the same time and heat-treated at the same temperature. Peaks due to MgB_4 appear at lower temperatures for the samples ball milled for 20 h, indicating that there are increased impurities in these powders (see earlier discussion for initial ball milling run).

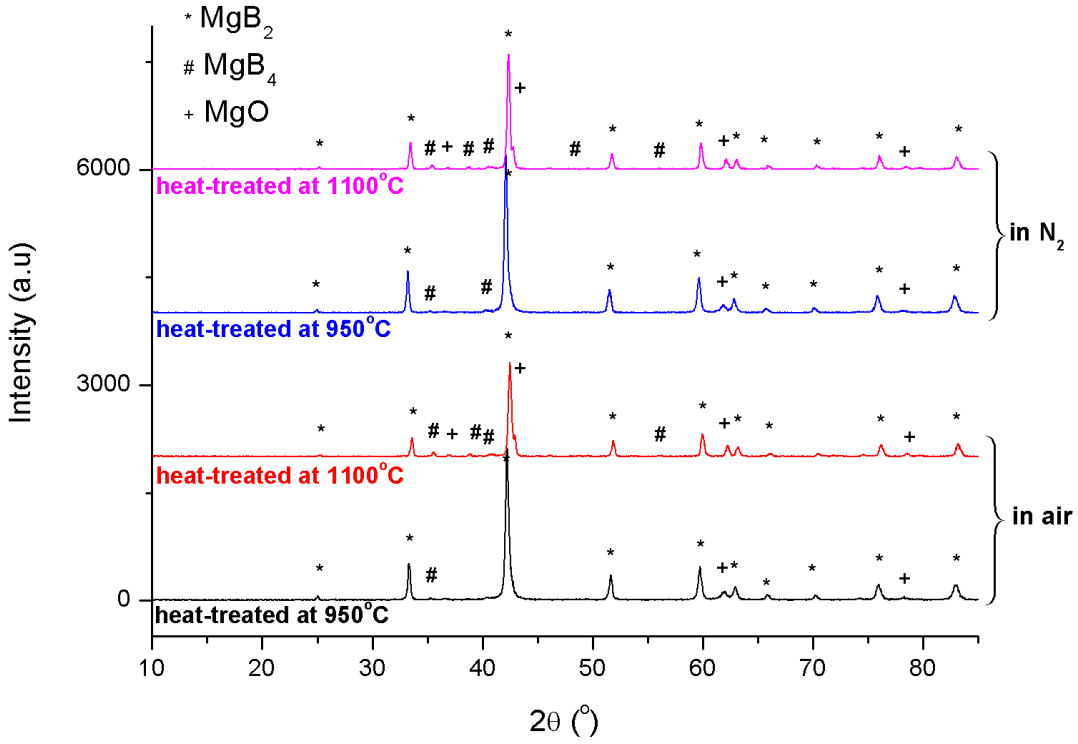


Figure 6.19: XRD spectra for second series of ball milled powders heat-treated between 950 − 1100 °C and milled for 1 h

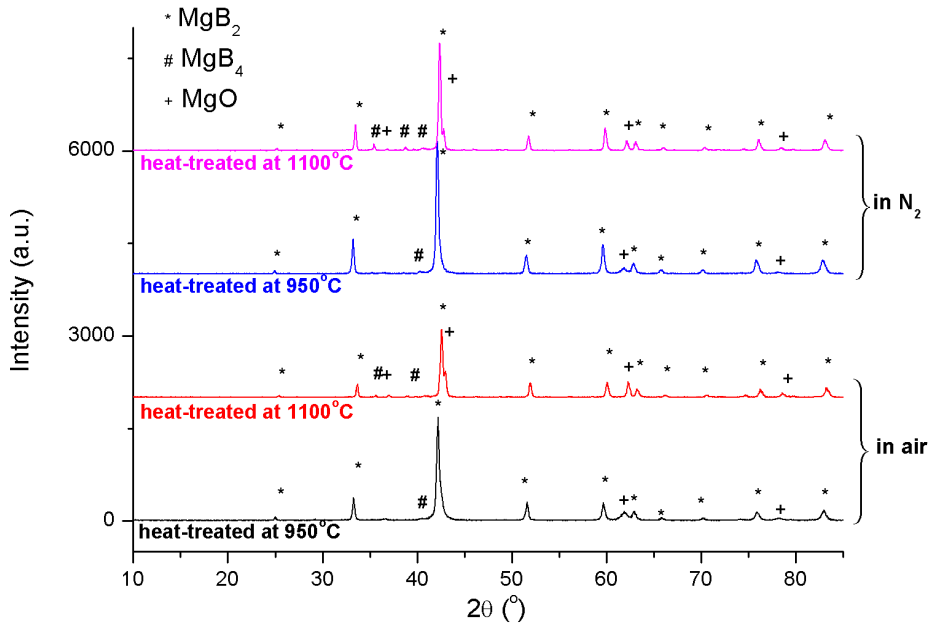


Figure 6.20: XRD spectra for second series of ball milled powders milled for 8 h heat-treated between 950 − 1100 °C

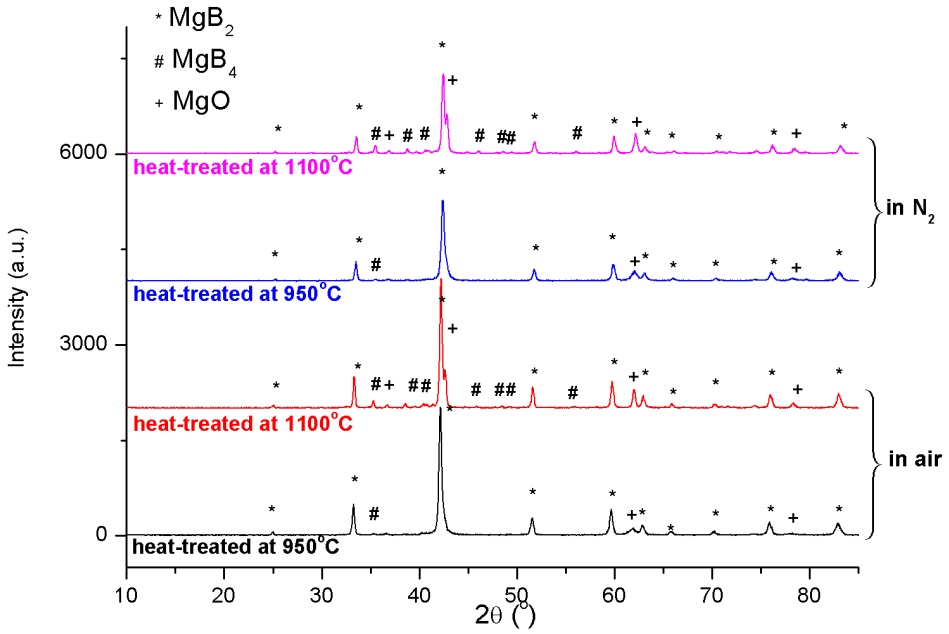
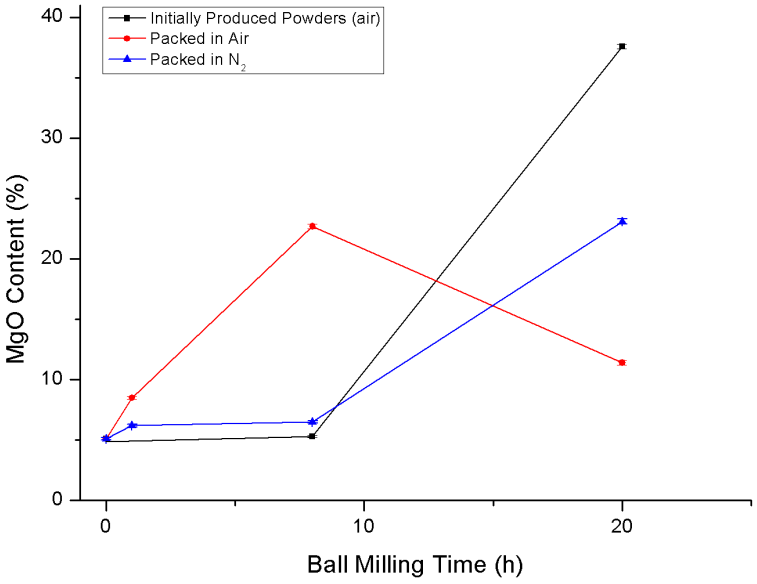


Figure 6.21: XRD spectra for second series of ball milled powders milled for 20 h heat-treated between 950 − 1100 °C

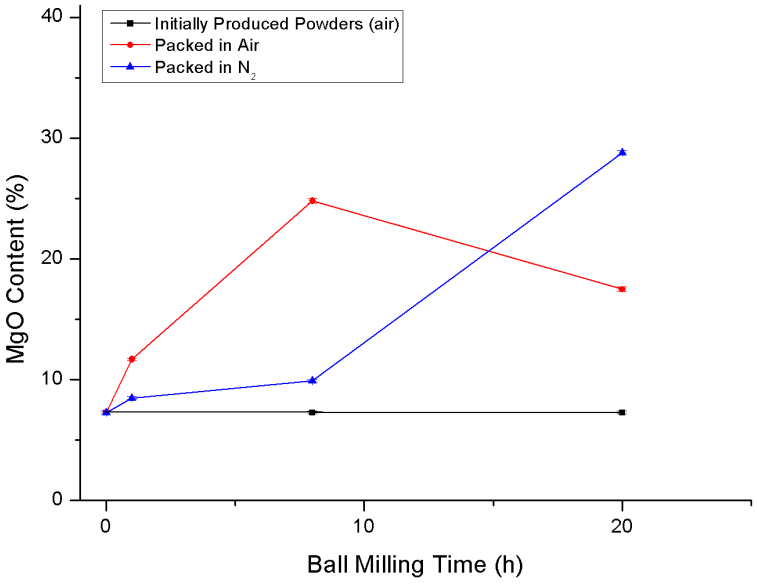
The MgO contents increase with heat-treatment temperature (Table 6.6) for pellets of the same powder heat-treated at 950 °C and 1100 °C. For the milled powders prepared under nitrogen the MgO content also increases with increasing milling time for each temperature, but no trend could be identified for the milled powders prepared in air. The trends in MgO content are shown graphically in Figure 6.22. Packing in nitrogen does not prevent MgO formation, suggesting that the origin of the MgO is the Ar gas used during heat-treatment, as discussed earlier, and/or impurities adsorbed to the surface of the MgB_2 powder.

Table 6.6: MgO content of pellets produced from the second series of ball milled powders

Heat-Treatment Temperature (°C)	MgO Content as % of MgB_2 Content						
	Powder Ball Milled in Air			Powder Ball Milled in N_2			As-Purchased MgB_2
	1 h	8 h	20 h	1 h	8 h	20 h	
950	8.5	22.7	11.4	6.2	6.5	23.1	5.1
1100	11.7	24.8	17.5	8.5	9.9	28.8	7.3



(a)



(b)

Figure 6.22: Variation in MgO content with ball milling duration for all pellets produced from all ball milled powders, heat-treated at
a) 950 °C
b) 1100 °C

The MgO content affects the maximum possible density of the material, and so more accurate relative densities were calculated using the MgO content measured for each sample (Table 6.7). These mostly lie between 60 % and 70 %, apart from those produced from powder ball milled in the initial run for 20 h and heat-treated at 950 °C (72 % post-heat-treatment) and 1100 °C (74 % post-heat-treatment). For all pellets produced from powders packed in air the relative density increased after heat-treatment. For pellets produced from powders packed in nitrogen the density decreases apart from for the sample produced from powder ball milled for 1 h and heat-treated at 1100 °C, whose relative density increased by 5 %.

Table 6.7: Calculated composite relative densities of ball milled powder pellets pre and post-heat-treatment at 950 °C and 1100 °C. The relative density prior to heat-treatment is calculated assuming the pellet is 100 % MgB_2.

a) Pellets heat-treated at 950 °C

Ball-Milling Time (h)	Relative Density					
	Initial Run		Second Run			
	(air)		(air)		(nitrogen)	
	pre-HT	post-HT	pre-HT	post-HT	pre-HT	post-HT
1	-	-	61 %	66 %	68 %	63 %
8	64 %	66 %	60 %	67 %	63 %	61 %
20	61 %	72 %	62 %	66 %	63 %	60 %

b) Pellets heat-treated at 1100 °C

Ball-Milling Time (h)	Relative Density					
	Initial Run		Second Run			
	(air)		(air)		(nitrogen)	
	pre-HT	post-HT	pre-HT	post-HT	pre-HT	post-HT
1	-	-	62 %	66 %	64 %	69 %
8	65 %	69 %	61 %	69 %	63 %	59 %
20	62 %	74 %	61 %	66 %	63 %	64 %

A depth analysis of the MgO content of pellets prepared from ball milled powder and heat-treated at 1100 °C was carried out by taking XRD spectra at several points through the depth of the sample up to approximately half the original height (Figure 6.23 - 8 h milled powder; Figure 6.24 - 20 h milled powder). The MgO content of the 8 h milled

powder pellet increases slightly with depth, while that for the 20 h milled powder is approximately constant (as for the pellet produced from as-purchased powder) but very high at approximately 50 %. The small increase for the former powder is partially due to the different scale of the graph and larger absolute errors in the MgO measurements. The worst fit line would be approximately flat, and the maximum variation between any pair of datum points is 5 % MgO.

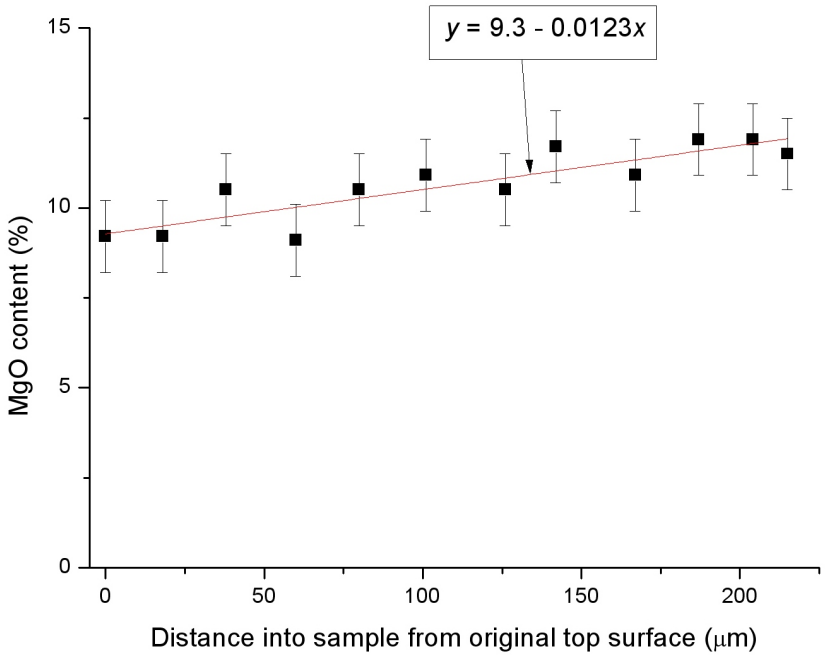


Figure 6.23: XRD depth analysis of MgO content for pellet produced from initially-produced powder ball milled for 8 h and heat-treated at 1100 °C

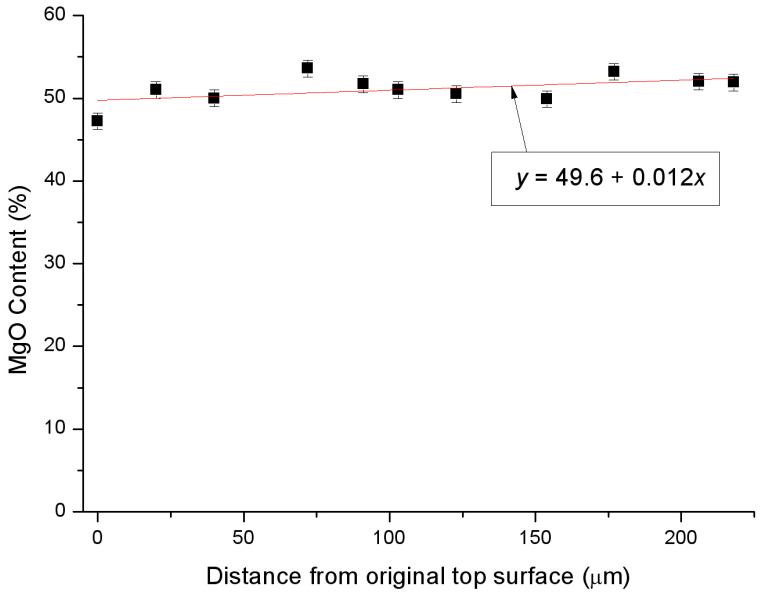
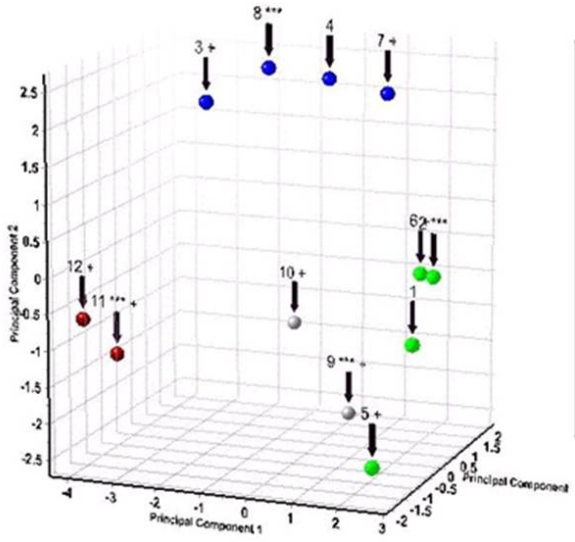


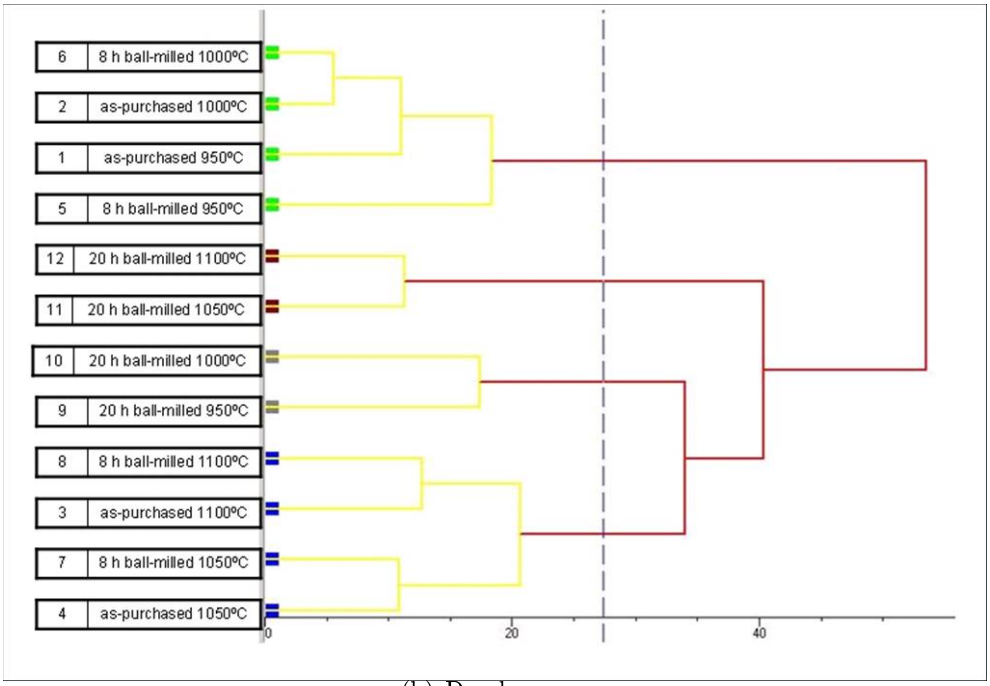
Figure 6.24: XRD depth analysis of MgO content for pellet produced from initially-produced powder ball milled for 20 h, and heat-treated at 1100 °C

Cluster analyses were carried out on the XRD spectra (Figures 6.25, 6.26 and 6.27). Figure 6.25 shows how the pellets produced from as-purchased MgB_2 and the initially produced powder ball milled for 8 h cluster for the 950 °C and 1000 °C heat-treatment temperatures. The pellets produced from powder ball milled for 20 h and heat-treated at the same temperatures are very close to this cluster. At higher temperatures, pellets produced from 8 h ball milled and as-purchased powder heat-treated at 1050 °C and 1100 °C are clustered and distant from those heat-treated at lower temperatures, while the pellets produced from powder ball milled for 20 h and heat-treated at 1050 °C and 1100 °C are separated from all the other scans described.



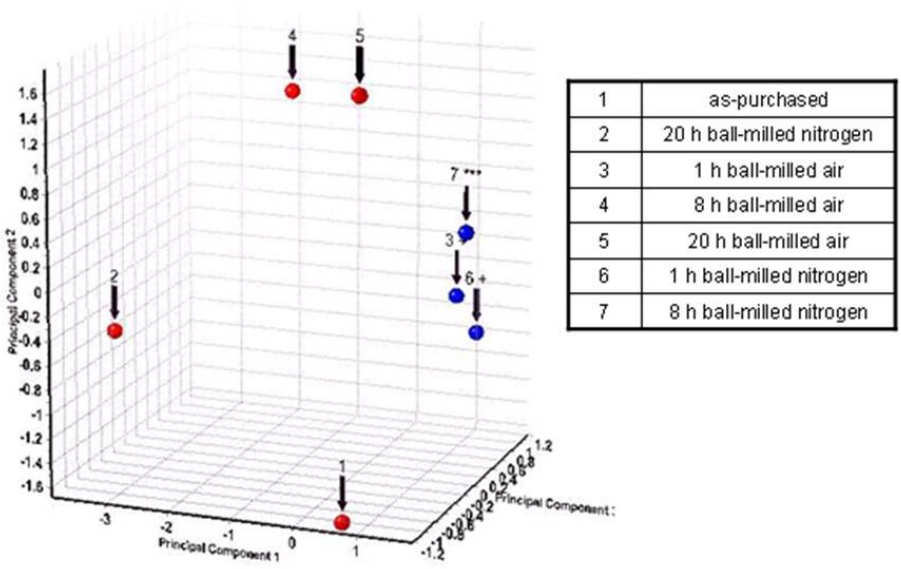
1	as-purchased 950ºC
2	as-purchased 1000ºC
3	as-purchased 1050ºC
4	as-purchased 1100ºC
5	8 h ball-milled 950ºC
6	8 h ball-milled 1000ºC
7	8 h ball-milled 1050ºC
8	8 h ball-milled 1100ºC
9	20 h ball-milled 950ºC
10	20 h ball-milled 1000ºC
11	20 h ball-milled 1050ºC
12	20 h ball-milled 1100ºC

(a) Principal Components Analysis



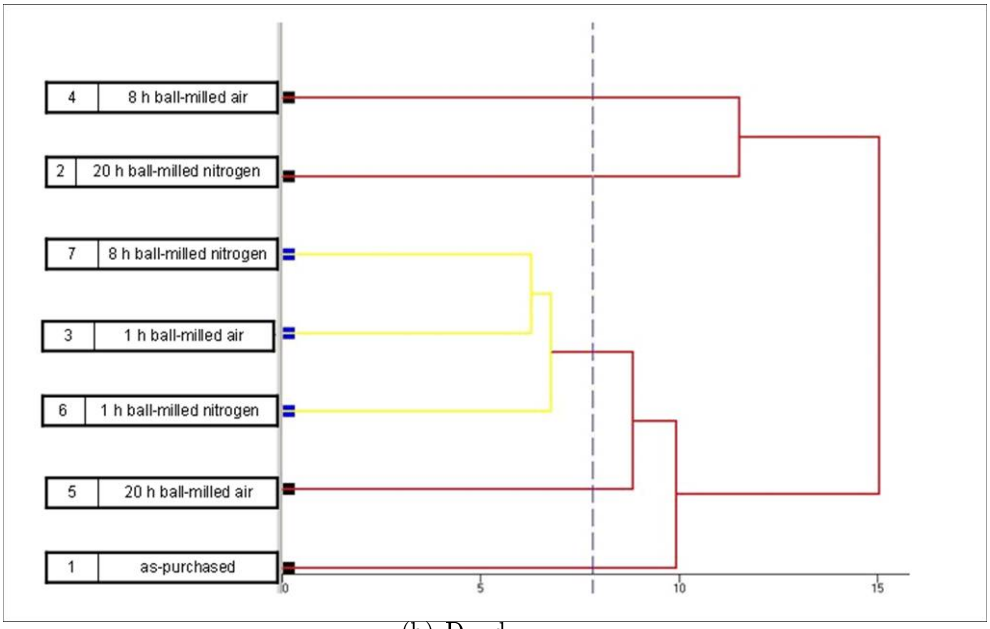
(b) Dendrogram

Figure 6.25: Cluster analysis of XRD spectra of pellets produced from initially produced ball milled powders heat-treated between 950 ºC and 1100 ºC



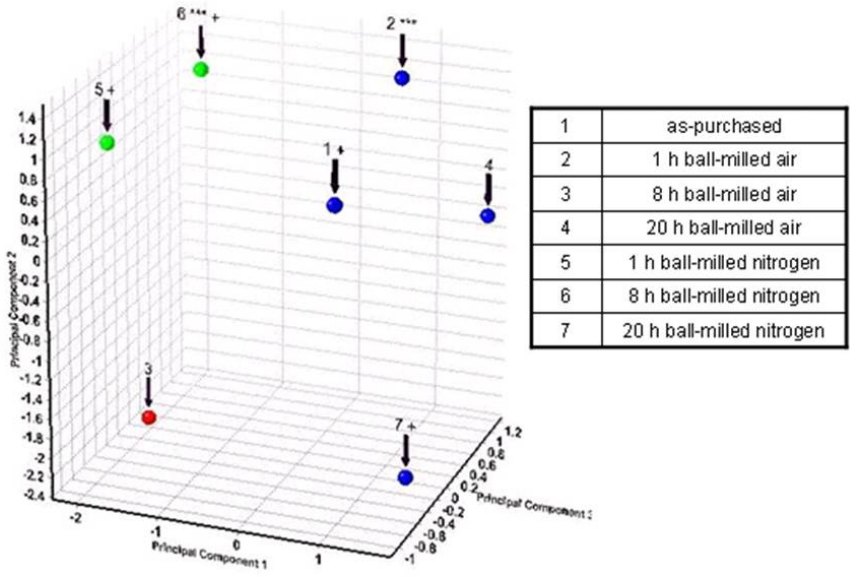
1	as-purchased
2	20 h ball-milled nitrogen
3	1 h ball-milled air
4	8 h ball-milled air
5	20 h ball-milled air
6	1 h ball-milled nitrogen
7	8 h ball-milled nitrogen

(a) Principal Components Analysis



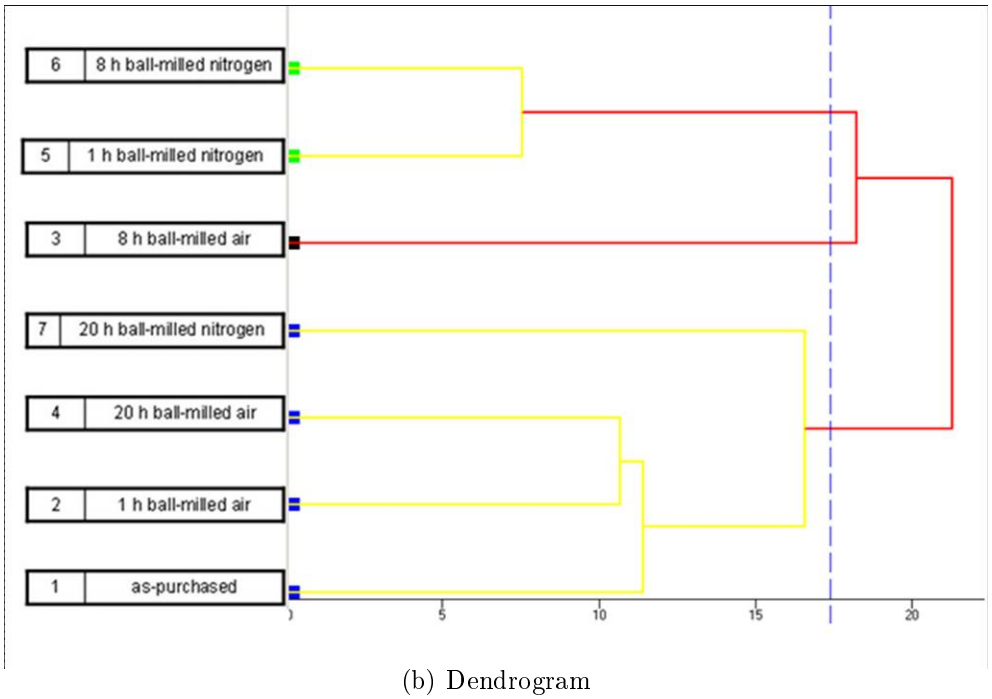
(b) Dendrogram

Figure 6.26: Cluster analysis of XRD spectra of pellets produced from second series of ball milled powders and heat-treated at 950 °C



1	as-purchased
2	1 h ball-milled air
3	8 h ball-milled air
4	20 h ball-milled air
5	1 h ball-milled nitrogen
6	8 h ball-milled nitrogen
7	20 h ball-milled nitrogen

(a) Principal Components Analysis



(b) Dendrogram

Figure 6.27: Cluster analysis of XRD spectra of pellets produced from second series of ball milled powders and heat-treated at 1100 °C

For the samples produced in the second run (Figure 6.26), the pellets heat-treated at 950 °C seem illogically clustered. Only one cluster is clearly identified, consisting of both the pellets produced from powders ball milled for 1 h, and the powder ball milled for

8 h after packing in nitrogen. The impurity content is lower for the sample packed in nitrogen, in agreement with the calculated MgO content (Table 6.6). Otherwise the XRD spectra are fairly disparate. For the samples heat-treated at 1100 °C no obvious clustering is evident for any of the samples (Figure 6.27).

6.3.3 Hardness

The Vickers hardness was plotted against the ball milling time for all samples heat-treated at 950 °C or 1100 °C (Figure 6.28). The hardness increased with heat-treatment temperature for all samples except the samples produced from powder ball milled in the initial run for 20 h (packed in air). No consistent trend can be identified in the hardness versus ball milling time. This may be due to fluctuations in the impurity content, though there is also no convincing correlation between hardness and MgO content for these samples (Figure 6.29). The highest hardness measured was around 175 HV/2 for the samples produced from the two powders packed in air, ball milled for 8 h, and heat-treated at 1100 °C. The hardness of the pellet made from initially produced powder has a larger spread ($\pm$14) of hardness values compared to that from the second run ($\pm$2), indicating an inhomogenous microstructure, verified by SEM observations (see Section 6.3.4 on page 204).

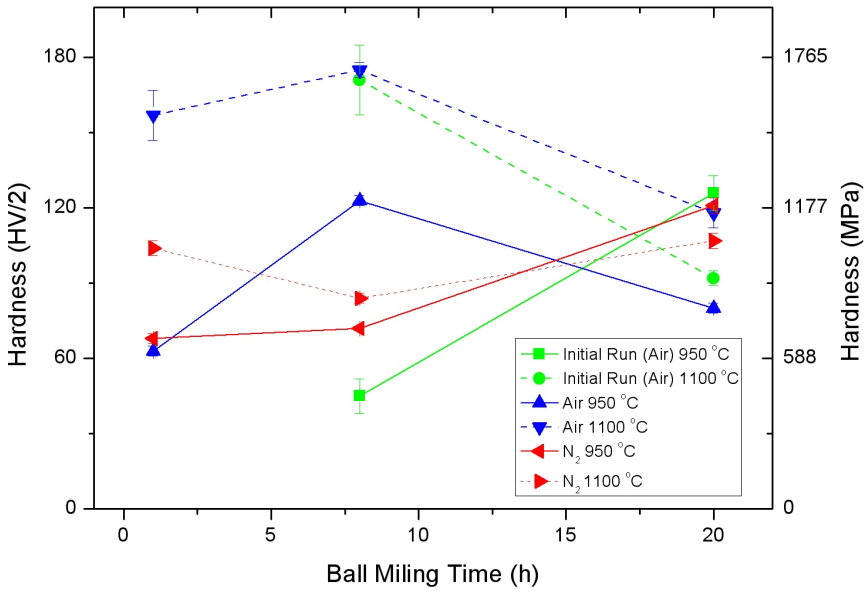


Figure 6.28: Hardness of pellets produced from all ball milled powders and heat-treated at 950 °C or 1100 °C

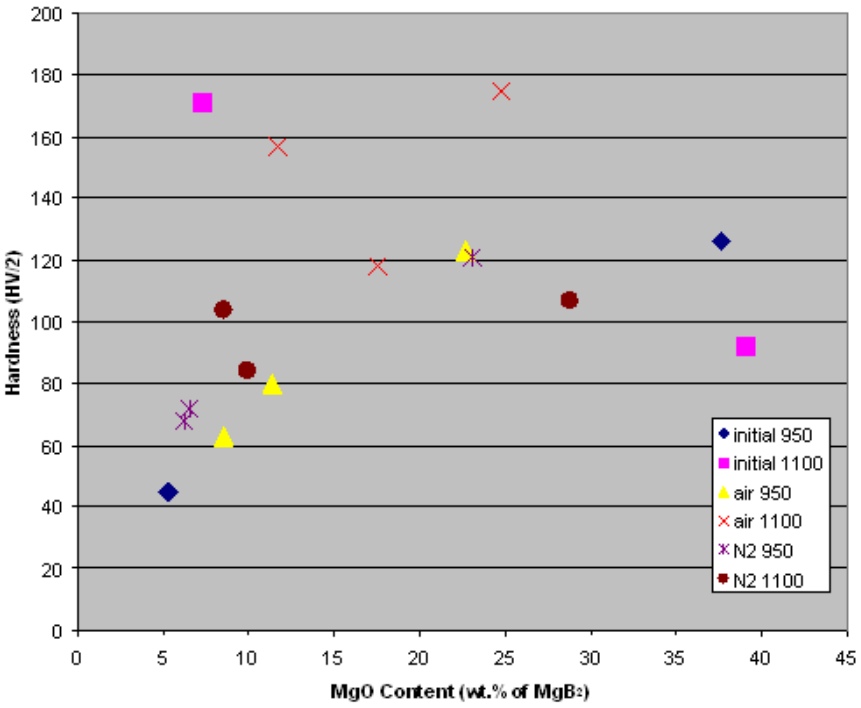


Figure 6.29: Hardness versus MgO content for all MgB_2 bulks produced from ball milled powders

6.3.4 SEM the presence of

Fracture surfaces of the pellets were examined by SEM. For the samples produced from initially-produced powders with 8 h milling, the pellet heat-treated at 1100 °C (Figure 6.30d-f) is significantly denser than that heat-treated at 950 °C (Figure 6.30a-c), and the equivalent bulks produced from as-purchased powder (Figure 4.31). Occluded porosity (isolated pores surrounded by densified material), neck formation and a smoother appearance is observed (Figure 6.30e). In comparison, the pellets produced from powders ball milled for 20 h remain powdery and not densified even for high temperature heat-treatment (Figure 6.31).

Despite extensive observations, densified regions were not observed in the samples produced from powders made in the second run and heat-treated at 950 °C (Figure 6.32). The pellets prepared from powders packed and dried in air or nitrogen are similar in appearance. The fracture surfaces are particulate and powder-like, with no signs of occluded porosity or neck formation observed. For samples heat-treated at 1100 °C the pellets contained a few small areas of material which appears denser and less powder-like (particularly Figure 6.33b,c and d) , indicating early-stage sintering. No regions of occluded porosity were observed.

6.3.5 Magnetization Measurements

Magnetization measurements were carried out at 4 K and 20 K on the samples produced from the initially produced ball milled samples heat-treated at 1100 °C (Figures 6.34 and 6.35) and are compared to those on pellets produced from as-purchased MgB_2 heat-treated at the same temperature and the as-milled powder.

The heat-treated sample produced from powder ball milled for 8 h has a larger magnetization loop than the sample produced from as-purchased MgB_2 when measured at both 4 K and 20 K, indicating an increase in connectivity. Those for the as-milled powder are vanishingly small by comparison indicating that pressing and heat-treatment increases the magnetic susceptibility over the entire range of applied magnetic field. Both the

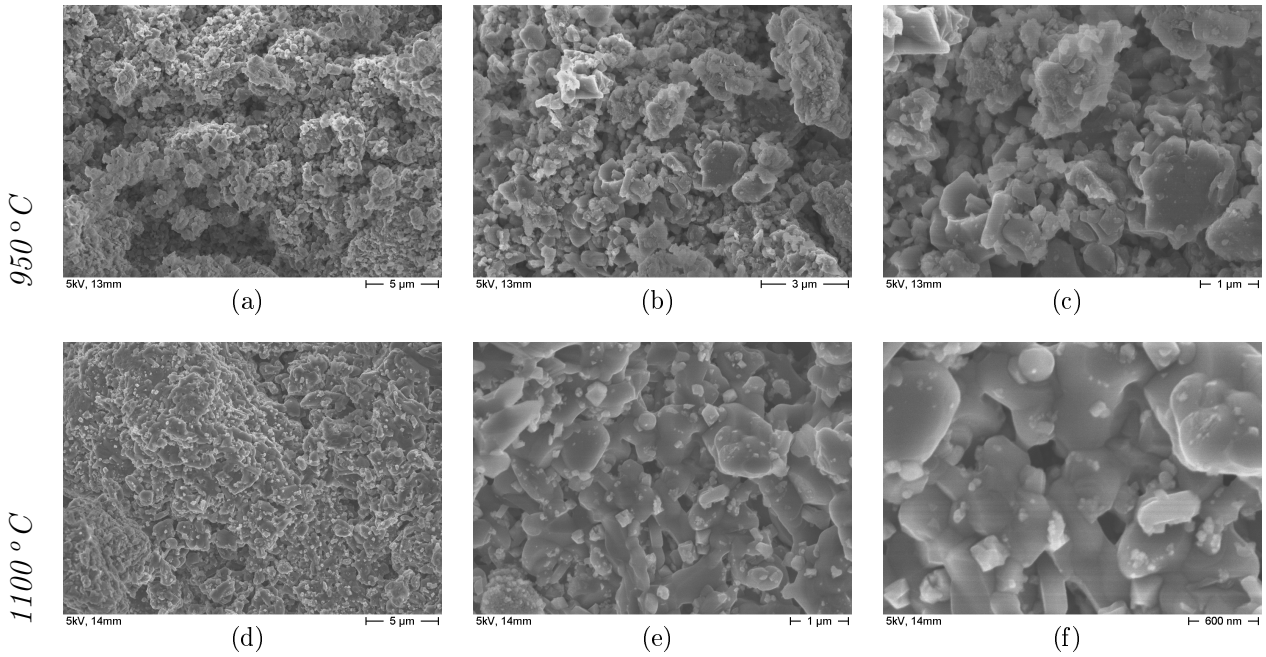


Figure 6.30: SEM images of the fracture surfaces of pellets produced from initially-produced 8 h ball milled powder heat-treated at the indicated temperatures

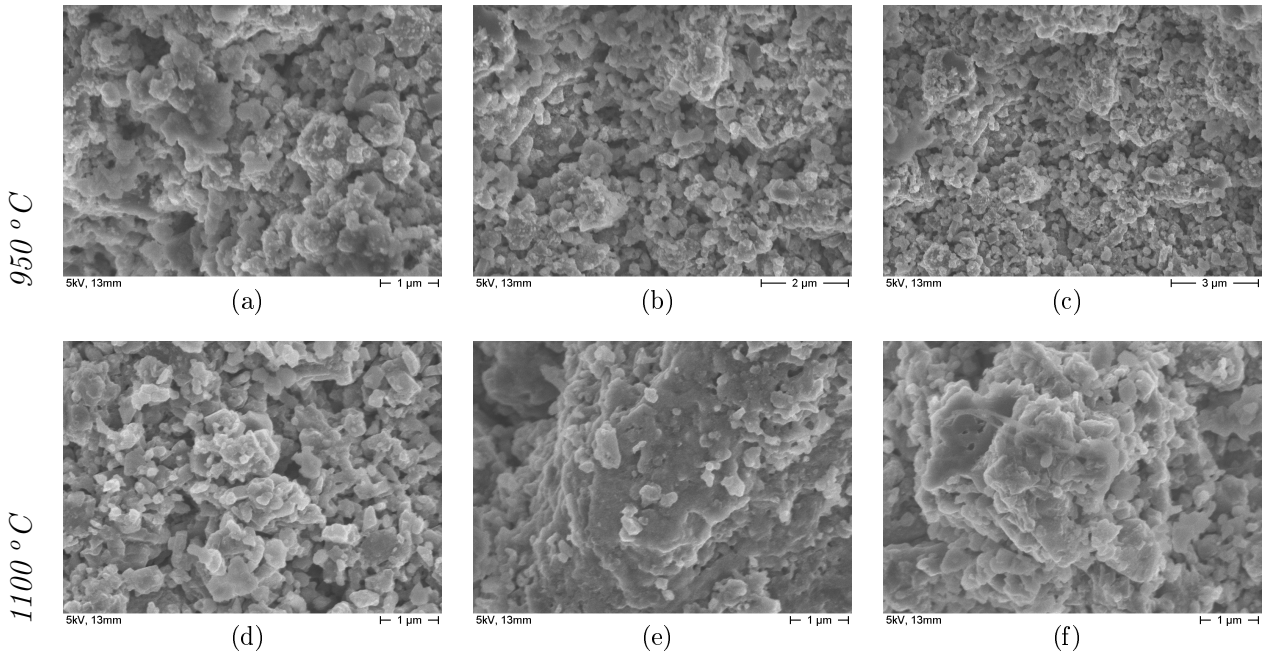


Figure 6.31: SEM images of the fracture surfaces of pellets produced from initially-produced 20 h ball milled powder heat-treated at the temperatures indicated

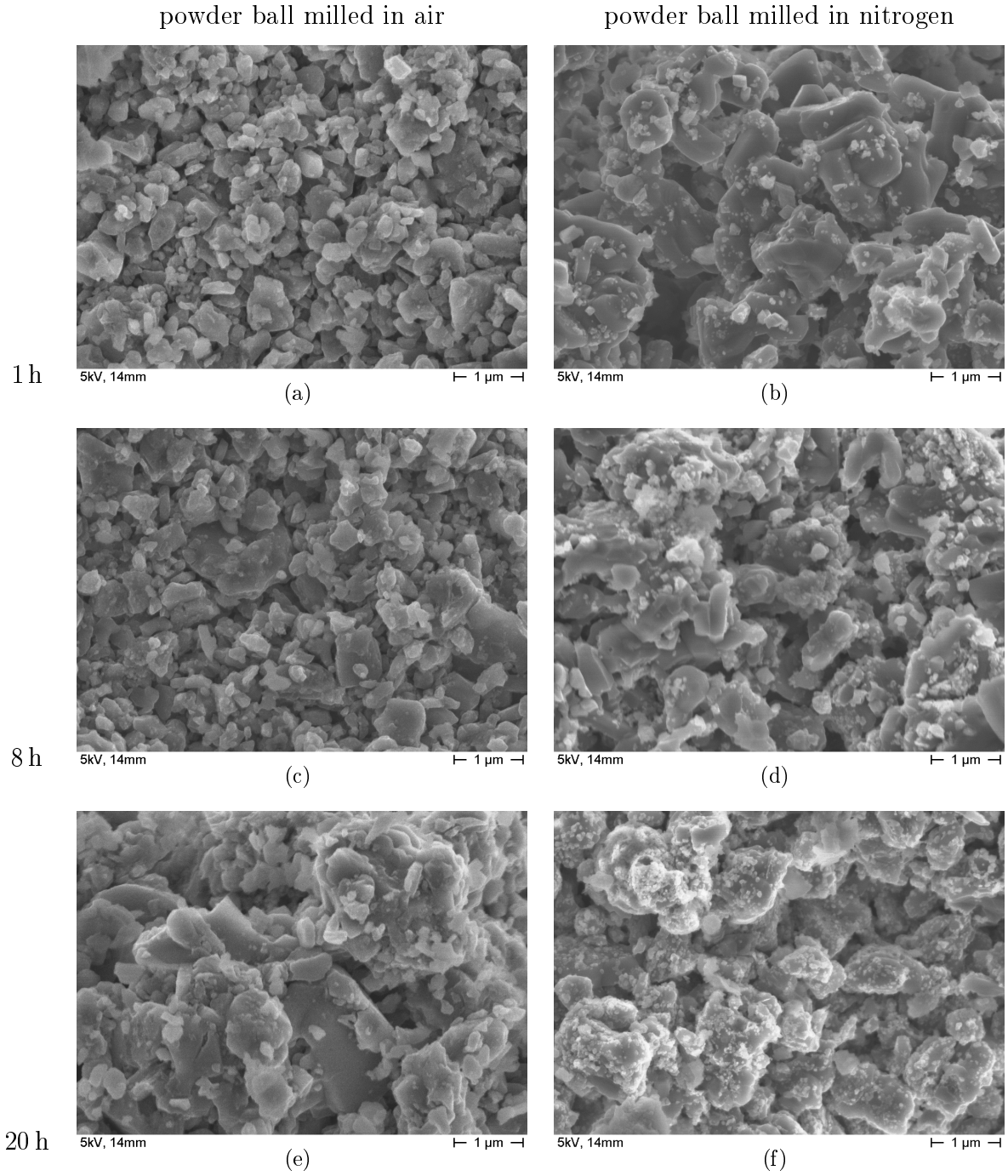


Figure 6.32: SEM images of the fracture surfaces of pellets produced from second series of ball milled powders heat-treated at 950 ^oC

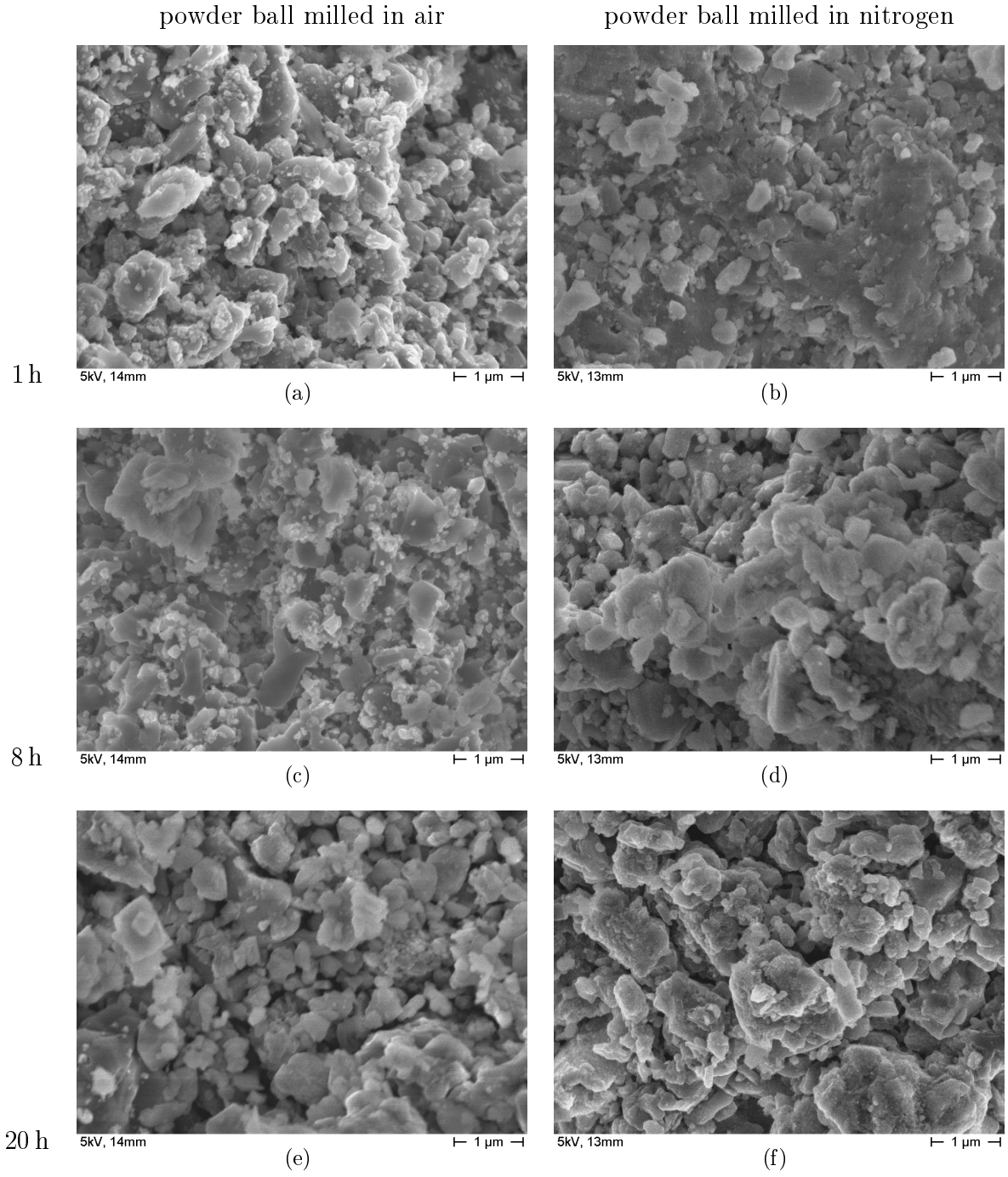
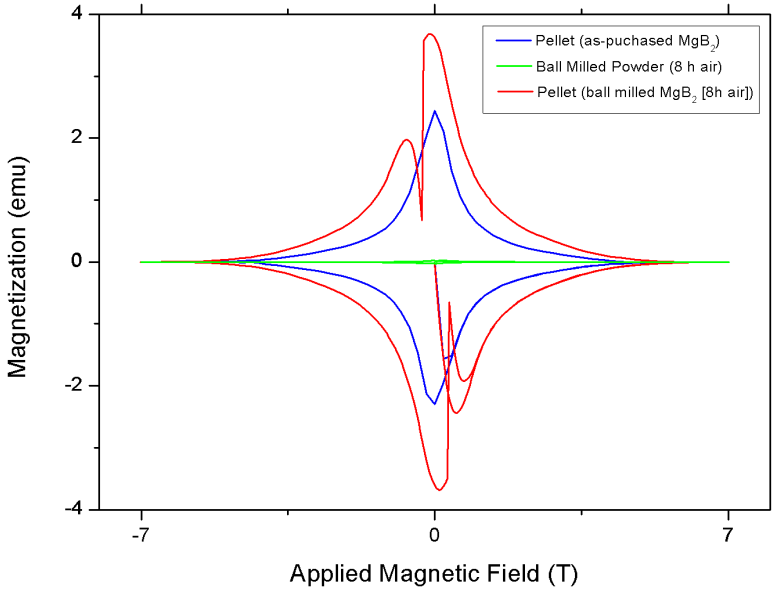


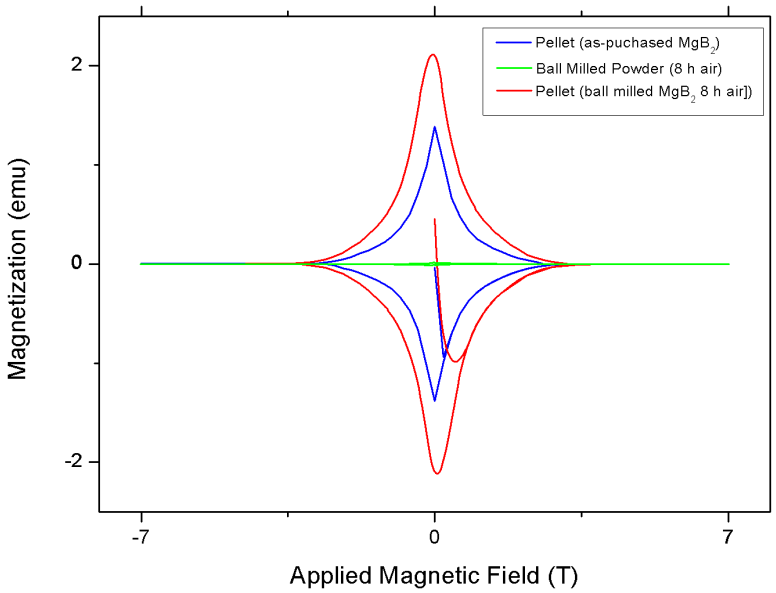
Figure 6.33: SEM images of fracture surfaces of pellets produced from second series of ball milled powders heat-treated at 1100 °C

compression during pressing and at least some initial sintering processes during the heat-treatment increase the connectivity between the particles. At 4 K, H_{c2} for the 8 h ball milled pellet is around 6.0 T while values for the ball milled powder and the as-purchased powder pellet are 3.0 T and 4.2 T respectively. At 20 K, H_{c2} for the 8 h ball milled pellet falls to around 3.4 T while values for the ball milled powder and the as-purchased powder pellet are 1.7 T and 3.0 T respectively.

By comparison, the magnetization signal for the pellet produced from powder ball milled for 20 h is significantly smaller than that measured from as-purchased MgB_2, and is only a little larger than from the as-milled powder at 20 K (Figure 6.35), indicating that the connectivity between particles has not been enhanced by the heat-treatment for these samples. This is probably due to the increased impurity content in these samples (see Figure 6.21 and Table 6.5) which reduces the fraction of superconducting MgB_2 phase in the sample, so separating the MgB_2 grains and reducing connectivity. At 4 K, H_{c2} for the 20 h ball milled pellet is around 3.4 T while those for the ball milled powder and the as-purchased powder pellet are 2.4 T and 4.2 T respectively. At 20 K, the H_{c2} values fall to 1.6 T, 1.3 T and 3.0 T respectively. This indicates that longer term ball milling degrades the superconductivity dramatically, in agreement with the findings of Chen *et al* [99] for milling using the *in situ* processing route. Their ball milling set-up was different from mine, and their precursor materials were Mg and B rather than MgB_2, and hence effect of milling even for the times indicated would not be expected to correspond to my results. In contrast to their findings, very little ZrO_2 could be detected by XRD or XPS in my ball milled samples. However, they suggest that the source of the degradation in their samples is actually amorphization of the MgB_2 powder during milling rather than the presence of ZrO_2. This is indicated by the fact that ZrO_2 added to MgB_2 without ball milling did not affect T_c; however no magnetization measurements are given for these samples so it is difficult to compare them to my measurements. No amorphization (indicated by a rise in the background between $10^o \lesssim 2\theta \lesssim 20^o$) was observed in the XRD spectra for my samples, so this explanation seems unlikely to be the case for my samples. The problem

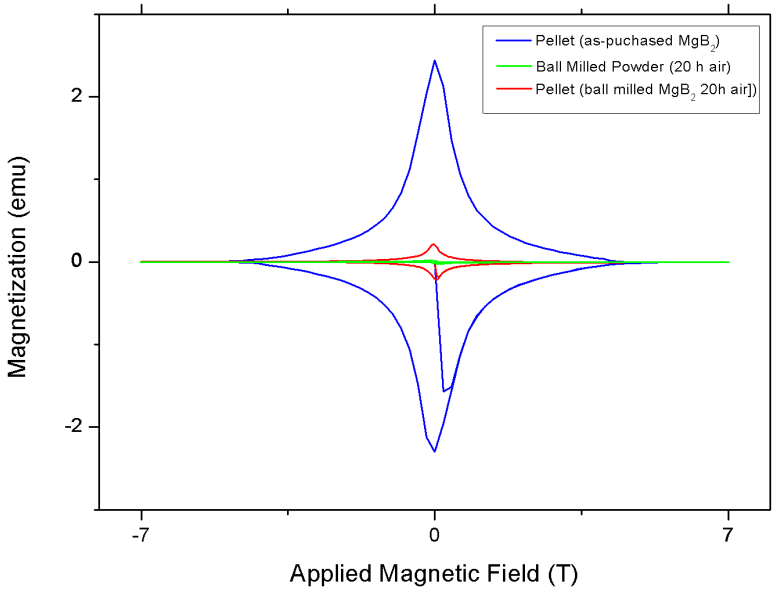


(a) T = 4 K

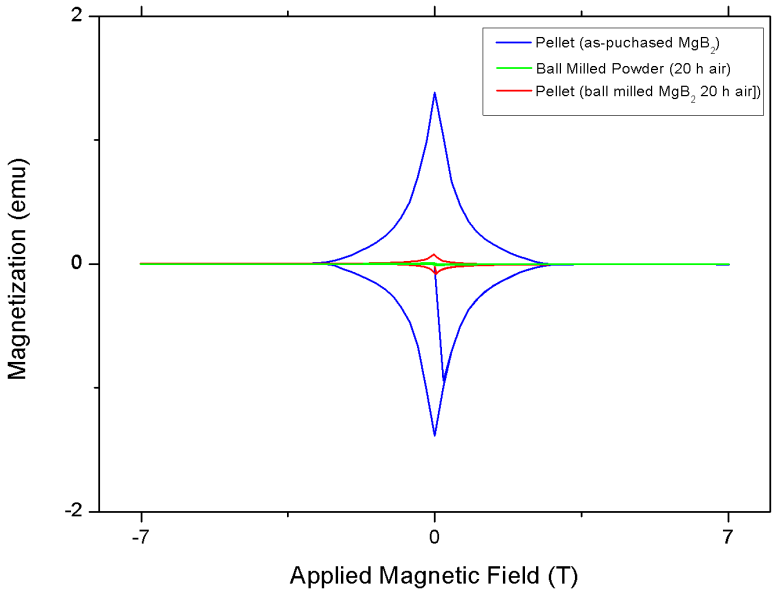


(b) T = 20 K

Figure 6.34: SQUID magnetization measurements on pellet produced from initially produced 8 h ball milled MgB_2 powder heat-treated at 1100 ^oC. The magnetization loops for the pellet produced from as-purchased powder and heat-treated at the same temperature, and for the as-ball milled powder are included for comparison.

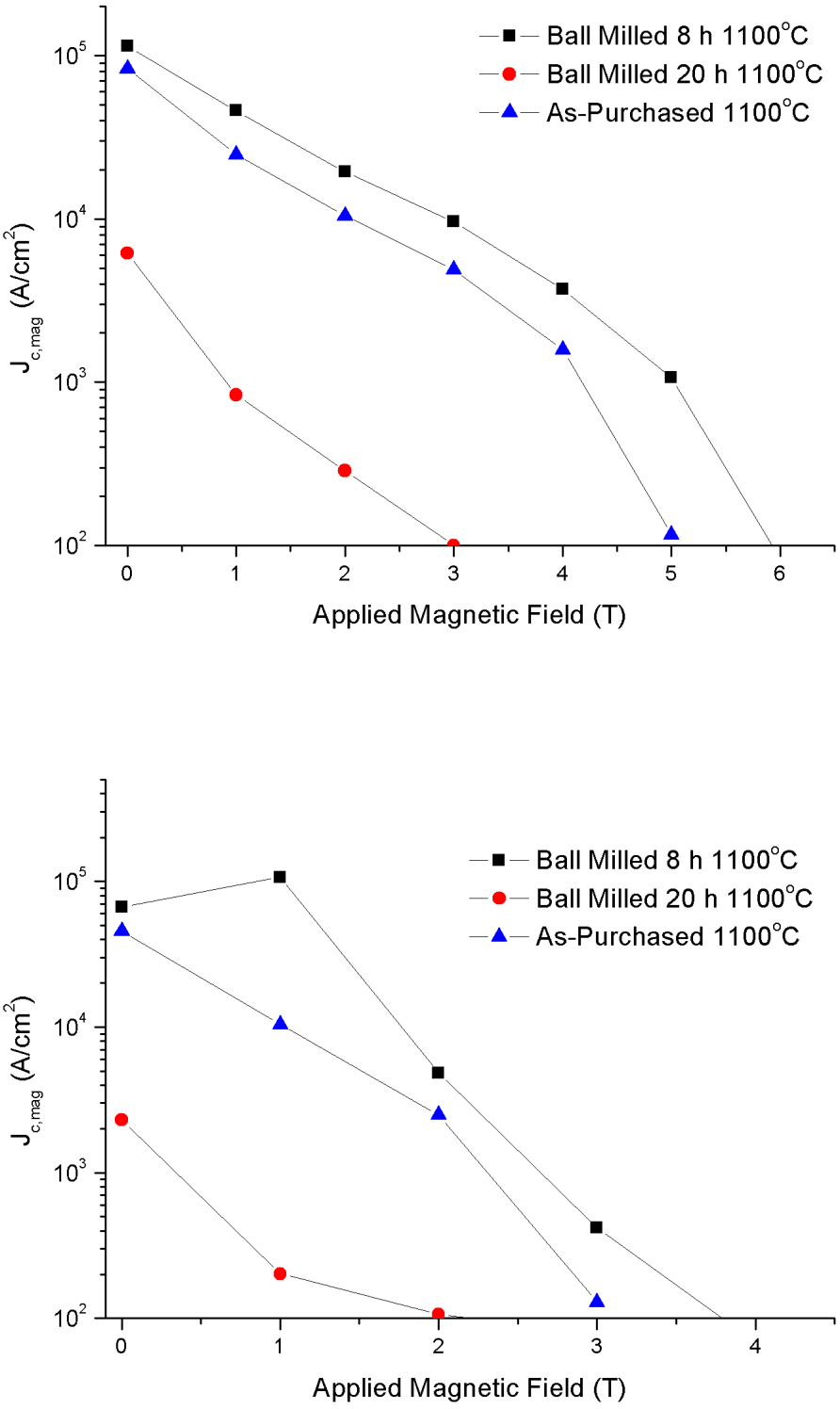


(a) T = 4 K



(b) T = 20 K

Figure 6.35: SQUID magnetization measurements on pellet produced from initially produced 20 h ball milled MgB_2 powder heat-treated at 1100 ^oC. The magnetization loops for the pellet produced from as-purchased powder and heat-treated at the same temperature, and for the as-ball milled powder are included for comparison.



(a)

Figure 6.36: Calculated $J_{c,mag}$ curves for bulk samples produced from ball milled and as-purchased MgB_2 powders
a) 4 K
b) 20 K

is more likely to be due to the large increase in impurity content following heat-treatment.

$J_{c,mag}$ versus magnetic field curves were calculated using the Bean Model as previously (see Section 4.2.6 on page 125). They are shown in Figure 6.36 for both ball milled powders and the as-purchased powder, and indicate, as discussed above, that the sample produced from powder ball milled for 20 h has poorer superconducting performance to that from as-purchased powder. The sample produced from powder ball milled for 8 h has higher $J_{c,mag}$ for given applied magnetic field compared to the as-purchased pellet at 4 K and 20 K. This pellet had similar density, higher hardness, and similar impurity content to the as-purchased pellet heat-treated at the same temperature. This suggests that the hardness indicates a slight increase in connectivity which is not reflected in the density measurement, but which nonetheless improves the $J_{c,mag}$.

6.4 Pellets Produced from Attrition Milled Powder

MgB_2 bulks were produced from dried attrition milled powder as described in Chapter 3. The bulks were then characterized by density and hardness measurements, XRD and SEM. In addition, SQUID magnetization measurements were carried out on selected samples.

6.4.1 Density

The absolute value of the density of the attrition milled powder pellets consistently increases following heat-treatment (Figure 6.37). In comparison to these pellets from attrition milled powders, the densities of pellets produced from the as-purchased powder are relatively constant. However there is no correlation between heat-treatment temperature and density change for the attrition milled pellets, indicating the behaviour may in fact be more complicated than the simple onset of sintering. The obvious complicating factor in this case is the impurity content.

The green density of the attrition milled pellets is consistently lower than that of the pellets produced from as-purchased powder. As the attrition milled powder is highly

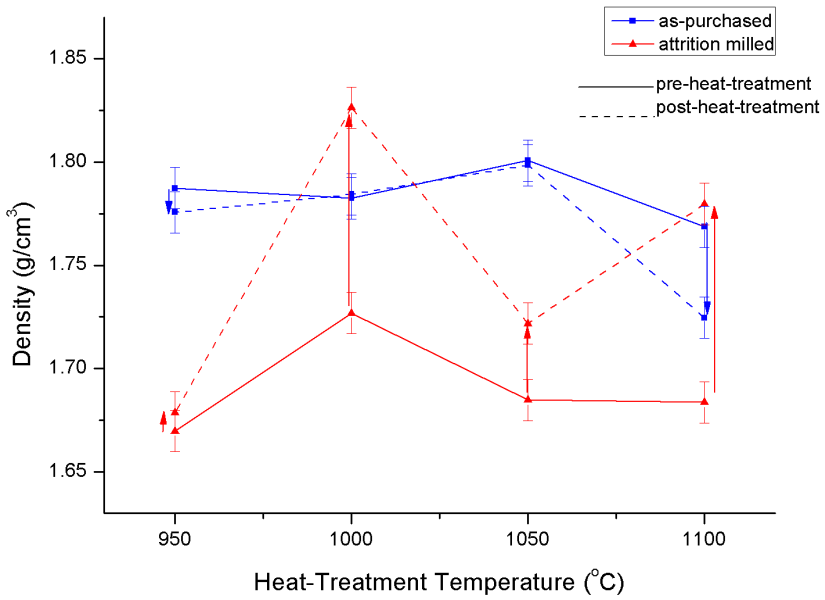


Figure 6.37: Density of pellets produced from attrition milled powder before and after heat-treatment between 950 – 1100 °C

agglomerated (see Section 5.4.2 on page 163), the most likely explanation for this is that the agglomerates are inherently porous and hence the total packing density is lower for the same mass of MgB_2. The pre-heat-treatment densities are not identical for each pellet due to variations in the particle size distribution of the small amount of powder used to produce each pellet, which leads to slight variations in the packing density of the initial green compact.

6.4.2 Impurity Content

Wide angle XRD scans on the attrition milled powder pellets are shown in Figure 6.38 for all heat-treatment temperatures. In comparison to the as-purchased powder, peaks indicating the presence of MgB_4 appear at a lower temperature (1000 °C for attrition milled pellets versus 1050 °C for the as-purchased MgB_2 pellets).

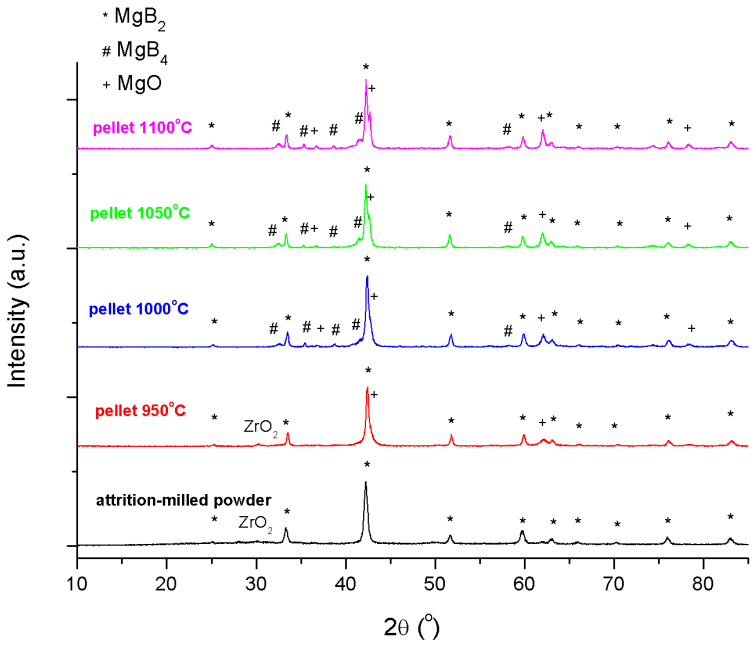


Figure 6.38: XRD spectra of pellets produced from attrition milled powder before and after heat-treatment between 950 °C and 1100 °C

The MgO content measured from XRD spectra is very high, and varied little with heat-treatment temperature (Table 6.8). After heat-treatment at 1050 °C or 1100 °C the MgO content was around 37 % while for 950 °C and 1000 °C it was lower at 30.5 % and 31.6 % respectively. This difference is consistent with the appearance of peaks due to MgB_4 in the XRD spectra after heat-treatment at higher temperature (Figure 6.38).

Table 6.8: MgO content of pellets produced from attrition milled powder after heat-treatment

Heat-Treatment Temperature (°C)	MgO Content (%)
950	30.5
1000	31.6
1050	37.0
1100	36.9

An MgO depth profile was carried out on a specially produced pellet made from attrition milled powder and heat-treated at 1100 °C for 1 h in Ar gas. This sample had a higher MgO content on the surface at 40 % and is approximately constant throughout the depth. One possible reason for the measured difference in surface MgO content is that the calibration

curve (Figure 4.24 on page 111) flattens significantly for MgO contents above about 30 %, increasing the error in the measurements.

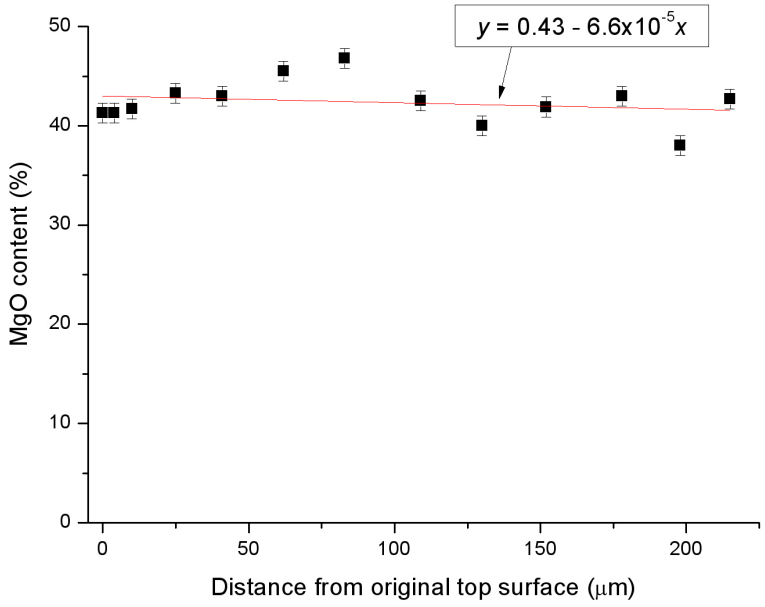


Figure 6.39: Depth analysis of the MgO content of a pellet produced from attrition milled powder heat-treated at 1100 °C

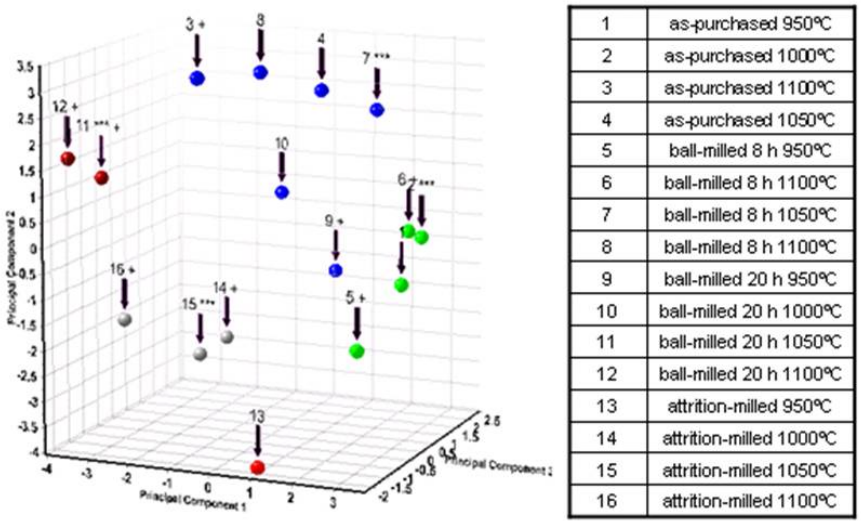
The composite density of the material was calculated taking into account the measured MgO content. The values from Table 6.8 were used as the MgO content for the samples along with their measured pre- and post-heat-treatment densities shown in Figure 6.37. A clear increase in density following heat-treatment was observed for all pellets (Table 6.9) . It is particularly noticeable that the pellet heat-treated at 1100 °C increases in density by 13 %, by far the largest increase in density seen in any samples prepared by pressureless heat-treatment. However, the large increase in density is accompanied by a very high impurity level, which may adversely affect the superconducting properties.

Table 6.9: Calculated composite relative densities of attrition milled powder pellets pre- and post-heat-treatment at the indicated temperatures. The relative density prior to heat-treatment is calculated assuming the pellet is 100 % MgB_2.

Heat-Treatment Temperature (°C)	Density Pre-Heat-Treatment	Density Post-Heat-Treatment
950	63 %	71 %
1000	66 %	71 %
1050	64 %	70 %
1100	64 %	77 %

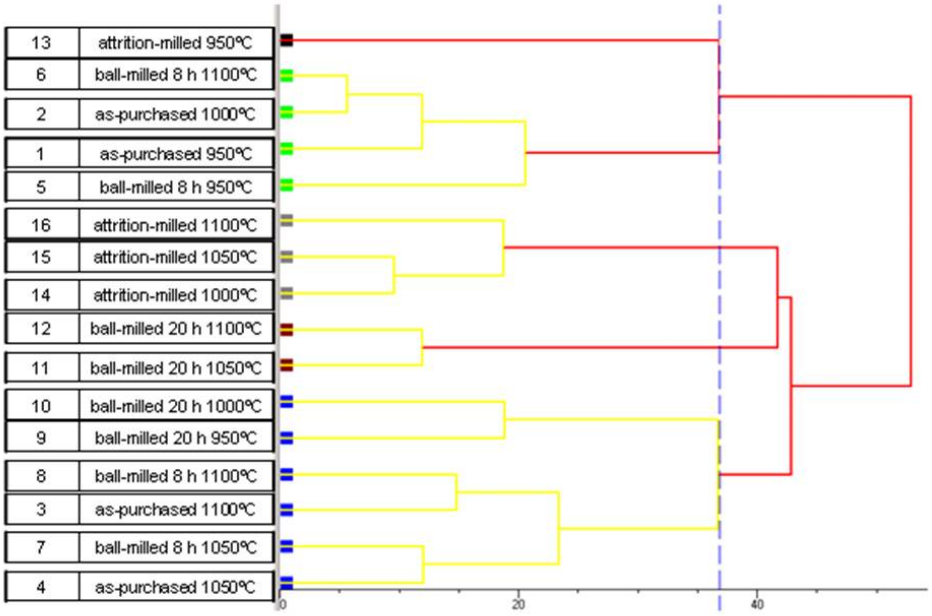
To gauge the similarity between the pellets produced from attrition milled, ball milled and as-purchased MgB_2 powders, a cluster analysis was carried out using the X'Pert HighScore software (Figure 6.40). The software grouped the scans into 5 clusters. Within these clusters, the attrition-milled pellets heat-treated between 1000 °C and 1100 °C are grouped together (grey spheres) and not with any other samples. The attrition-milled pellet heat-treated at 950 °C (red circle, 13) is not clustered with any other samples. This indicates that the attrition milled samples, while containing a similar amount of MgO to the ball milled samples are not actually all that similar. The cluster analysis can establish similarities between samples which are difficult to establish through comparison by eye. The dendrogram indicates that the pellets heat-treated at 1000 °C and 1050 °C are more similar to each other than to pellets heat-treated at 1100 °C.

Zirconium was detected in the attrition-milled powder by XPS prior to heat-treatment (see Section 6.4.2 on page 213), originating from wear of the milling media. Zirconia could not be detected in the XRD scans in Figure 6.38. The sample was also examined using EDX. A series of EDX spectra were obtained from the sample over a 3 by 4 grid, and the mean values of the elemental content calculated.The SEM image is shown in Figure 6.41a and the average spectrum in Figure 6.41b. The zirconium content was measured 2 ± 0.3 at.% of the total material present, or around 3 at.% of the total Mg content. This is slightly lower than the level measured using EDX for the attrition-milled powder (see Figure 5.28 on page 163).



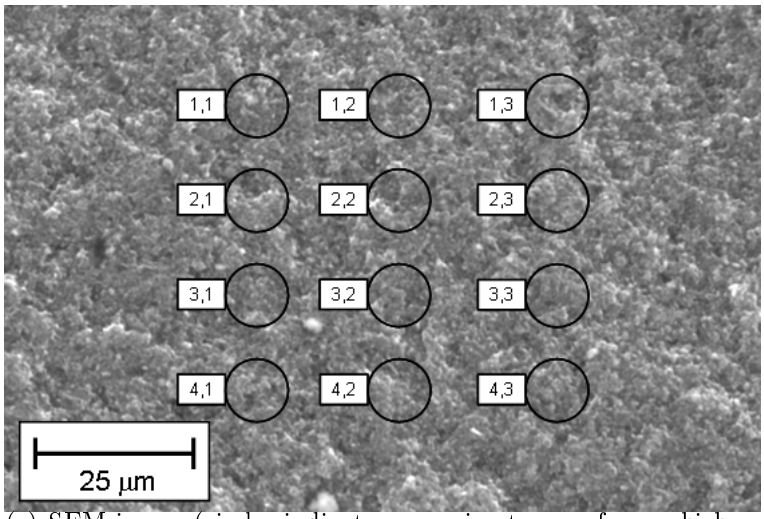
1	as-purchased 950°C
2	as-purchased 1000°C
3	as-purchased 1100°C
4	as-purchased 1050°C
5	ball-milled 8 h 950°C
6	ball-milled 8 h 1100°C
7	ball-milled 8 h 1050°C
8	ball-milled 8 h 1100°C
9	ball-milled 20 h 950°C
10	ball-milled 20 h 1000°C
11	ball-milled 20 h 1050°C
12	ball-milled 20 h 1100°C
13	attrition-milled 950°C
14	attrition-milled 1000°C
15	attrition-milled 1050°C
16	attrition-milled 1100°C

(a) Principal Components Analysis

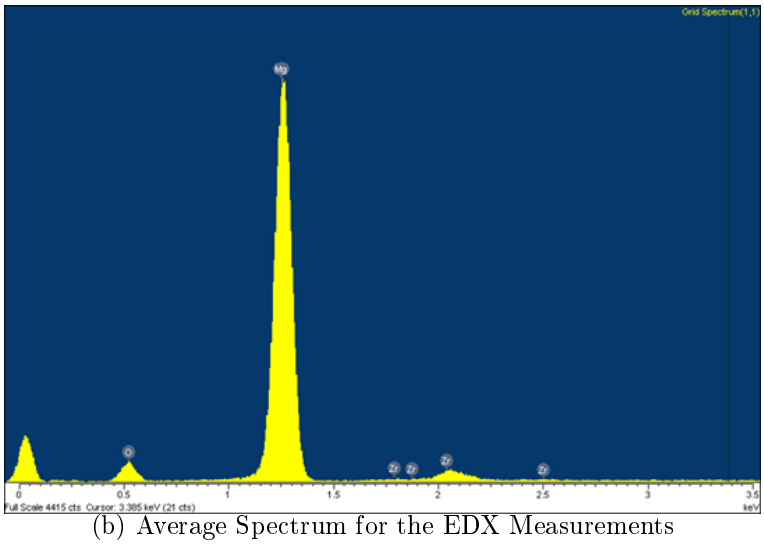


(b) Dendrogram

Figure 6.40: Cluster analysis of XRD spectra of pellets produced from initially-produced ball milled powders, attrition milled powder and as-purchased powder, and heat-treated between 950 °C and 1100 °C



(a) SEM image (circles indicate approximate area from which x-rays are generated)



(b) Average Spectrum for the EDX Measurements

Figure 6.41: EDX analysis of a pellet produced from attrition milled powder heat-treated at 1100 °C

6.4.3 Hardness

The Vickers hardness for the hardness of the pellets heat-treated between 950 °C and 1100 °C is shown in Figure 6.42. The hardness decreases with increasing heat-treatment temperature, opposite to the density. The decrease in hardness is due either to the rise in impurity content, or to the large degree of agglomeration in the attrition milled powder (see Figure 5.30). The agglomerates are relatively soft, as previously demonstrated by how easy it is to break them up with ultrasound, so it is not inconceivable that they

break apart during hardness testing leading to a decrease in the measured hardness. However this does not entirely explain why the hardness values for the pellets heat-treated at 950 °C and 1000 °C are significantly higher than that for the pellets heat-treated at 1050 °C and 1100 °C, as all pellets should on average contain a similar proportion of coarse agglomerates, nor why the pellets heat-treated at lower temperatures have significantly higher hardness than the equivalent pellets produced from as-purchased MgB_2 powder.

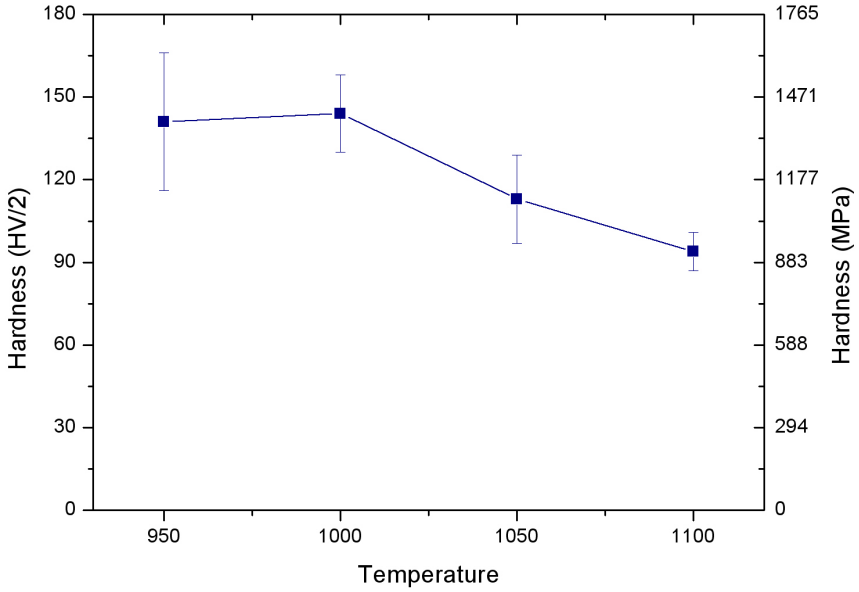


Figure 6.42: Hardness of pellets produced from attrition milled powder before and after heat-treatment between 950 – 1100 °C

6.4.4 SEM

Characteristic SEM images of fracture surfaces of pellets heat-treated at 950 °C and 1100 °C are shown in Figure 6.43. While the surface of the pellet heat-treated at 950 °C is particulate in nature (particularly noticeable in Figure 6.43c), the pellet heat-treated at 1100 °C contains a number of areas (Figure 6.43e and f) where the densification is significant. Regions of occluded porosity (*i.e.* closed rounded pores) are clearly visible. The sample is rather inhomogeneous however, and these regions are scattered throughout the sample and are only $1 - 2\,\mu$m in diameter. As the impurity content in this sample

is high, the question arose of whether these regions were actually impurity regions rather than regions of sintered MgB_2. Attempts to investigate this using back-scattered SEM were inconclusive as the resolution of the microscope was insufficient to detect these small regions given the small back-scattered contrast between MgB_2, MgO and MgB_4. The sample is too inherently porous to be suitable for techniques such as wavelength dispersive spectroscopy, which would be capable of detecting the light elements more accurately, so the answer to this question could not be conclusively determined.

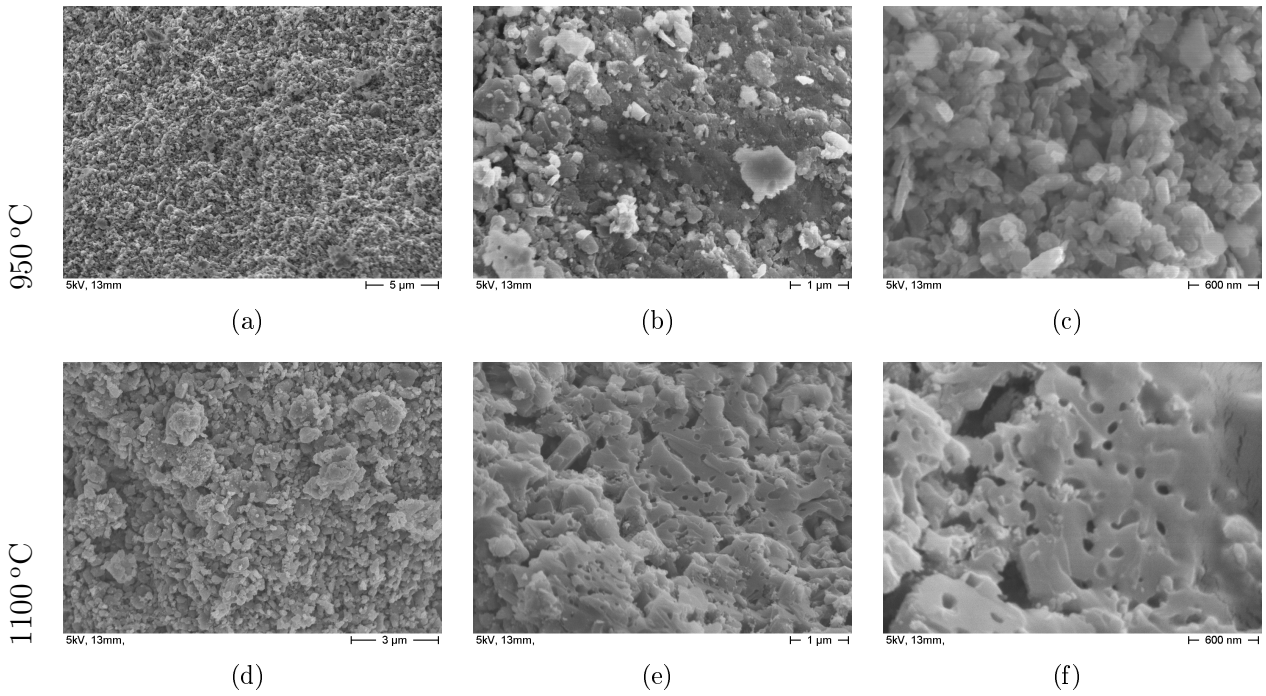


Figure 6.43: SEM images of fracture surfaces of pellets produced from attrition milled powder

6.4.5 Magnetization Measurements

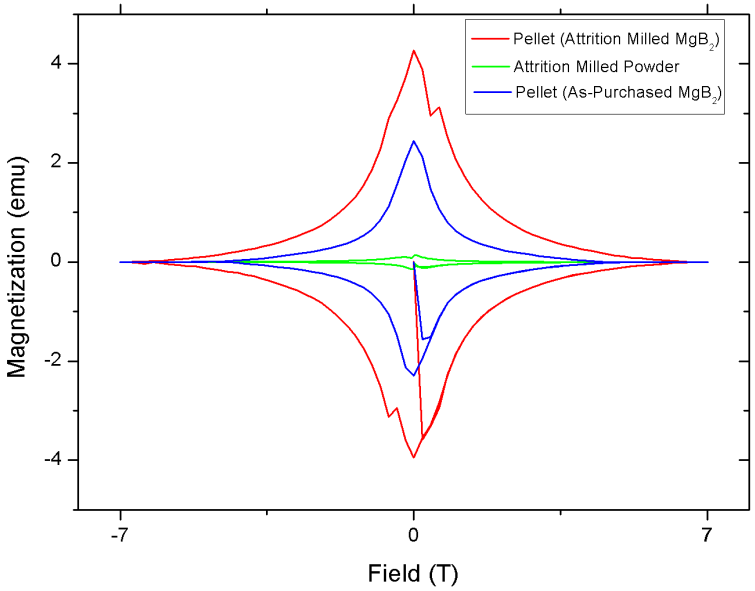
Magnetization was measured at 4 K and 20 K (Figure 6.44) for the attrition milled pellet heat-treated at 1100 °C, the attrition milled powder and the pellet made from as-purchased MgB_2 powder heat-treated at 1100 °C. At both temperatures the diameter of the loop for the attrition milled powder is significantly smaller than that for the pellets.

The larger magnetic dipole moments measured for the pellet produced from attrition milled powder indicate that its connectivity has increased compared to that of both the

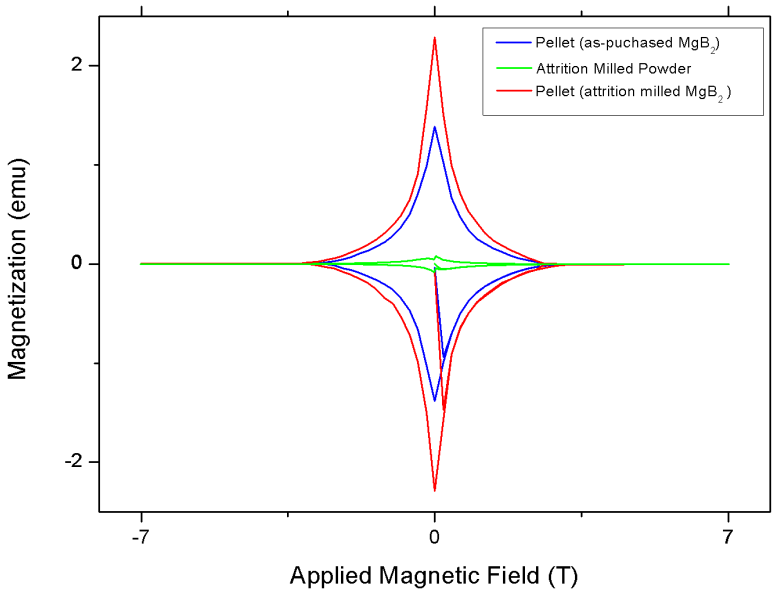
powder (in which connectivity is negligible) and the pellet produced from as-purchased MgB_2 powder. This observation suggests that the attrition milled powder pellet heat-treated at 1100 °C may be particularly suitable for fabrication of high density MgB_2 artefacts. In addition, H_{c2} (the value of the applied field at which the magnetization reaches zero) is largest for the attrition milled pellet at 4 K, having a value of approximately 6.6 T. The as-purchased powder pellet and the attrition milled powder have H_{c2} values of 4.2 T and 5.2 T respectively at the same temperature, though the magnetization ΔM is significantly lower at all magnetic fields for the powder. At 20 K the H_{c2} values are similar for all samples at around 3.0 T. As H_{c2} is a measure of the point at which the sample loses its superconducting properties, this indicates that at low temperatures the attrition milled pellet retains superconductivity in higher magnetic fields than the as-purchased powder pellet.

$J_{c,mag} - H$ curves were calculated using the Bean Model as described earlier (Section 4.2.6 on page 125), and shown in Figure 6.44. The $J_{c,mag}$ performance of the pellet produced from attrition milled powder was similar to that produced from as-purchased MgB_2 powder, though significantly higher (by one order of magnitude) at 5 T, 4 K. At 20 K the $J_{c,mag}$ of the attrition milled pellet rapidly falls below 10^2 A/cm^2.

Overall pellets produced by pressureless heat-treatment at 1100 °C of attrition milled powder have good superconducting characteristics, particularly at 4 K above 4 T. Densification was observed in this sample, increasing the relative composite density to 77 %, which is likely to contribute to this improvement. However the high impurity content of these pellets (MgO level of 36.9 % due to the formation of precursor impurities during milling) must cause a deterioration in superconducting properties. If attrition milled powder with fewer impurity precursors could be produced, it would be expected to have excellent superconducting properties.

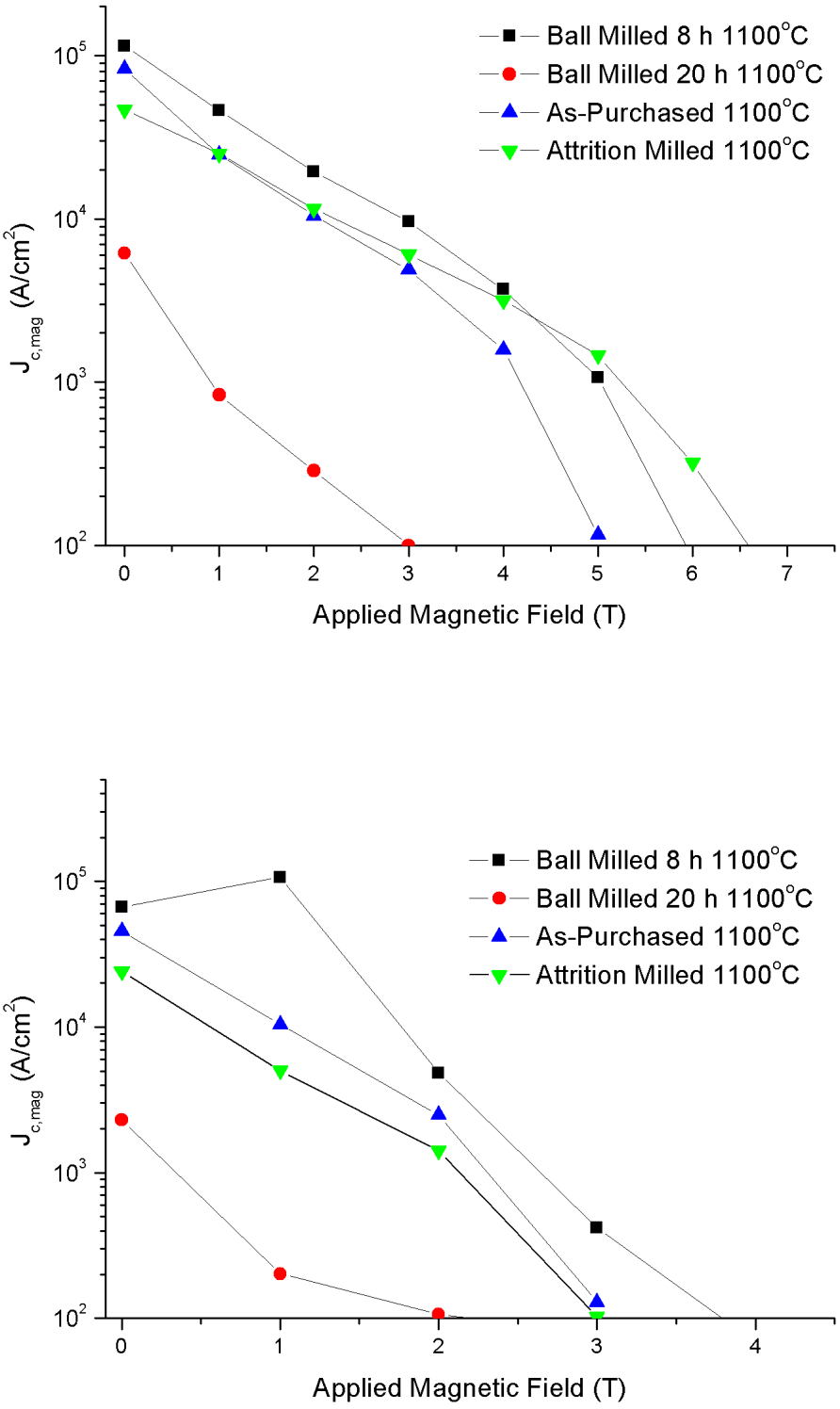


(a) T = 4 K



(b) T = 20 K

Figure 6.44: SQUID magnetization measurements on a pellet produced from attrition milled MgB_2 powder heat-treated at 1100 °C. The magnetization loops for the pellet produced from as-purchased powder and heat-treated at the same temperature, and for the as-milled powder are included for comparison.



(a)

Figure 6.45: Calculated $J_{c,mag}$ curves for bulk samples produced from attrition milled, ball milled and as-purchased MgB_2 powders
a) 4 K
b) 20 K

6.5 Summary

Using powders produced by separation (sieving and sediementation) to produce MgB_2 bulks by pressureless heat-treatment up to 1100 °C did not improve the density and connectivity. This is because of the difficulties of obtaining powders with small particle size without extensive agglomeration, which causes porosity in the green compact which is sustained in the final fired product.

Pellets fabricated from powders produced by short-duration ball milling (8 h) had improved superconducting properties compared to as-purchased powder heat-treated at the same temperature (1100 °C). The pellets had similar density and impurity content, but the pellet produced from ball milled powder had significantly higher hardness than that from as-purchased powder. This indicates that some increase in connectivity has occured, leading to the improved superconducting properties.

Long-duration ball milling (20 h) causes the formation of large volumes of impurity phases in heat-treated bulks at lower heat-treatment temperatures than for unmodified powder. A similar trend was observed for pellets produced from attrition milled powder, indicating that the milling is responsible for the formation of amorphous impurity phases which form MgO during heat-treatment. MgO contents (which were constant through the depth of the sample) were measured as up to 40 wt.% (for attrition milled powder heat-treated at 1100 °C). Some evidence of densification was observed in bulk produced from attrition milled MgB_2 heat-treated at 1100 °C, with the calculated relative composite density increasing to 77 %. This sample also had improved $J_{c,mag}$ at magnetic fields above 5 T compared to the as-purchased powder pellet and the other samples studied in this work.

While some signs of densification have been observed in some samples heat-treated at 1100 °C, full densification has not occured for any of the pressureless heat-treated MgB_2 bulks, and a significant increase in the green compact density has not been achieved. To determine the key parameters required for the densification of MgB_2, pressure-assisted heat-treatment techniques were used to produce dense MgB_2 (Chapter 7).

7 Pressure-Assisted Heat-Treatment

Studies by other research groups have established that pressure-assisted heat-treatment techniques such as HIPing [60; 149–153], hot pressing [15; 60; 144] and spark plasma sintering [145; 146; 194] can produce denser bulk MgB_2 than pressureless heat-treatment (see also Section 2.5.3 on page 35). However, no attempt has been made to establish the relative importance of the parameters which can be varied in these processes on the final density of the MgB_2 bulk. These parameters are the environment (*e.g.* Ar or vacuum), temperature, heating/cooling rate, and the applied pressure. In this chapter, I discuss the processing and characterization of bulk MgB_2 samples, and the effect on density of three pressure-assisted heat-treatment processes; resistive sintering, spark plasma sintering, and hot pressing.

7.1 Resistive Sintering

Resistive sintering was carried out as described in Section 3.2.2 on page 59 at the University of Birmingham. During the test, the temperature, ram pressure and ram displacement were monitored. Sintering was taken to commence at the point at which the displacement of the ram changed rapidly from its initial position, at around 3 min (see Figure 7.1). The temperature was held constant when sintering had begun for a period of 5 min. A complete run took around $15 - 30$ min, plus approximately 2 h to obtain a high vacuum, and approximately 1 h to cool down the die. Once the die was cooled to room temperature, it was removed from the chamber and the pellet was removed using

a uniaxial press. Resistively sintered pellets were produced from the following powders; as-purchased, attrition milled, ball milled for 8 h in air/isopropanol, ball milled for 20 h in air/isopropanol, sedimented powder nominally $d_{St} > 100\,\mu$m, and sedimented powder nominally $d_{St} < 1\,\mu$m (see Chapter 5 for details of the production of these powders).

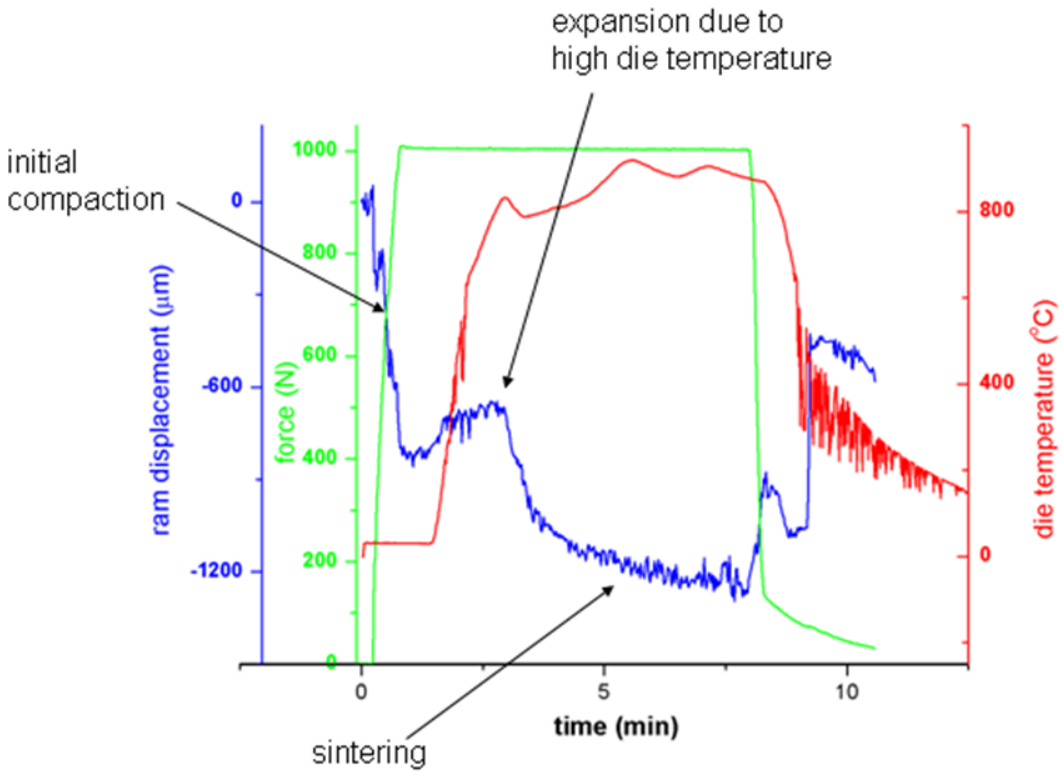


Figure 7.1: Variation in pressure, ram displacement and die temperature logged during resistive sintering of as-purchased MgB_2 powder. The time starts at the point at which the current was switched on.

7.1.1 Density

The densities of the resistive sintered samples were in the range $1.3 - 2.6\,\mathrm{g/cm^3}$ (Figure 7.2). The densest was that made from attrition milled powder, closely followed by that made from as-purchased powder. Compared to the density of pure dense MgB_2 (as calculated from the lattice parameters) these samples have relative densities of 91 % and 87 % respectively, while that of the lowest density samples (made from powder ball milled for 8 h in air, and from powder sedimented to give $d_{St} > 100\,\mu$m) are 55 % and 49 % re-

spectively, *i.e.* lower than that of the samples produced by pressureless sintering from the same powders (around 65 % of the MgB_2 maximum density, see Chapter 6). The sample produced from powder ball milled in air for 20 h has a density of 1.63 g/cm^3, or 62 % of the maximum for pure MgB_2, and that produced from sedimented powder nominally $d_{St} < 1\,\mu$m had a density of 2.01 g/cm^3 or 76 % of the theoretical maximum. The samples can be divided into those which have undergone significant densification above the values characteristic of samples prepared by pressureless heat treatment, and those which have not. Resistive sintering improved the density of samples produced from as-purchased, attrition milled and $d_{St} < 1\,\mu$m powders.

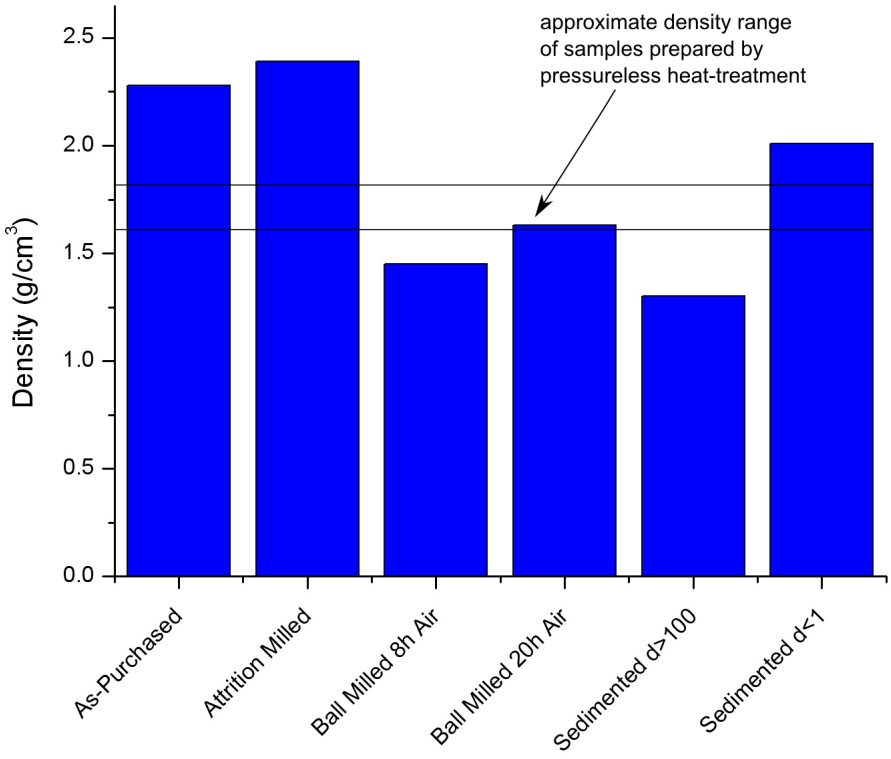


Figure 7.2: Density measured using Archimedes' method for all resistively sintered MgB_2 bulks

7.1.2 Hardness

The trend in the Vickers hardness of the samples mirrors that of the density, with the densest samples having the highest hardness values (Figure 7.3). The sample produced from powder ball milled in air/isopropanol for 8 h broke repeatedly on indentation, even

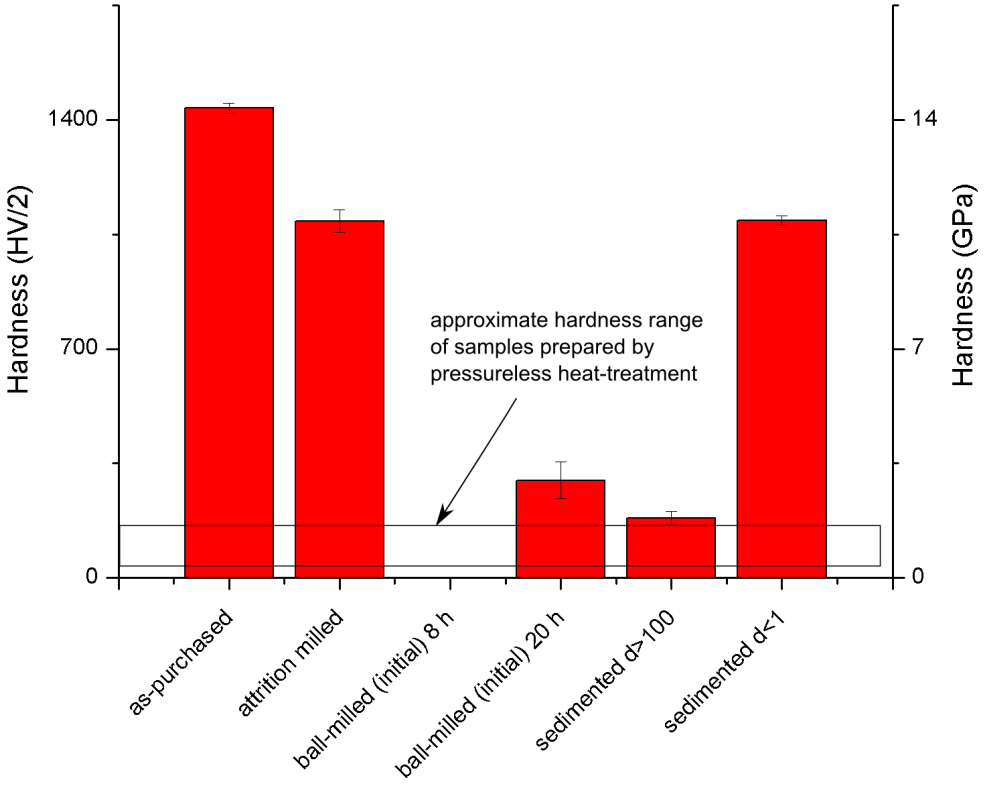


Figure 7.3: Hardness of all resistively sintered MgB_2 bulks. As the sample produced from MgB_2 powder ball milled for 8 h broke repeatedly on indentation, its hardness is recorded as zero.

when the minimum load was used, so its hardness is recorded as zero in Figure 7.3. Other than this result, the density and the hardness are well correlated for all the resistively sintered samples. For the powders ball milled for 20 h and sedimented with nominal $d_{St} > 100\,\mu$m the hardness of the resistive sintered sample is higher than that of the samples produced by pressureless heat-treatment at all temperatures. For the ball milled powder the resistively sintered pellet had hardness of 298 HV/2 versus 73 HV/2 for the pressureless heat-treatment; for the sedimented powder the equivalent values were 183 HV/2 versus 118 HV/2. Possible explanations for this (apart from enhanced sintering) are a size effect, as the resistively sintered samples are significantly smaller in both diameter and height compared to the pressureless heat-treated samples, or an overall increase in hardness due to the effect of carbon diffusion into the MgB_2 powder, forming a harder zone in the surface and edges of the pellet.

7.1.3 Impurity Content

The impurity content of the resistively sintered samples was assessed using XRD $\theta - 2\theta$ analysis. The spectra for each of the resistively sintered samples are shown in Figures 7.4-7.9, along with the scans for the starting powder and for the equivalent samples produced from the same powder by pressureless heat-treatment at 950 °C and 1100 °C. The MgO content of the resistively sintered samples was measured from the MgB_2 (110) and MgO (220) peak area ratios from the XRD spectra (as described in Section 4.2.1 on page 109), and the resulting MgO contents are given in Table 7.1.

Table 7.1: MgO content of resistive sintered pellets

Starting Powder	MgO content (% of MgB_2 content)	Density (g/cm^3)
as-purchased MgB_2	7.8	2.28
attrition milled	57.3	2.39
ball milled 8 h in air	not measurable: $0 - 5.0$	1.45
ball milled 20 h in air	45.8	1.63
sedimented $d_{>100}$	57.9	1.30
sedimented $d_{<1}$	21.9	2.01

Figure 7.4 shows the XRD spectra for the sample produced by resistive sintering of the as-purchased Alfa Aesar MgB_2 powder. The spectrum for the resistively sintered sample is most like the sample pressureless heat-treated at 1100 °C. Both spectra contain a number of peaks due to MgB_4 and MgO, as well as the MgB_2 peaks. The MgO content of these samples are almost identical, with the difference lying within the error of the calibration. The MgO content was calculated as 7.3 wt.% for the resistive sintered sample and 7.8 wt.% for the samples pressureless heat-treated at 1100 °C. This indicates that it is possible that the resistively sintered sample actually reached a higher temperature locally than indicated by the measurement of the die temperature. MgB_4 peaks were not observed for pressureless heat-treatment of this powder below 950 °C (Section 4.2.4.1 on page 114), and even then were significantly smaller than the MgB_4 peaks in the resistively sintered sample's XRD spectrum. As this reading is taken from a thermocouple placed within the die wall during heat-treatment, the sample temperature is not measured directly.

However, regardless of the true sample temperature, it is very promising that a sample with a substantially increased density (2.55 g/cm^3 for the resistive sintered sample versus 1.71 g/cm^3 for the pressureless heat-treated at 1100 °C sample) can be obtained without a corresponding increase in MgO content, and indicates that the density change for the resistively sintered sample is not merely due to a change in the composition of the samples.

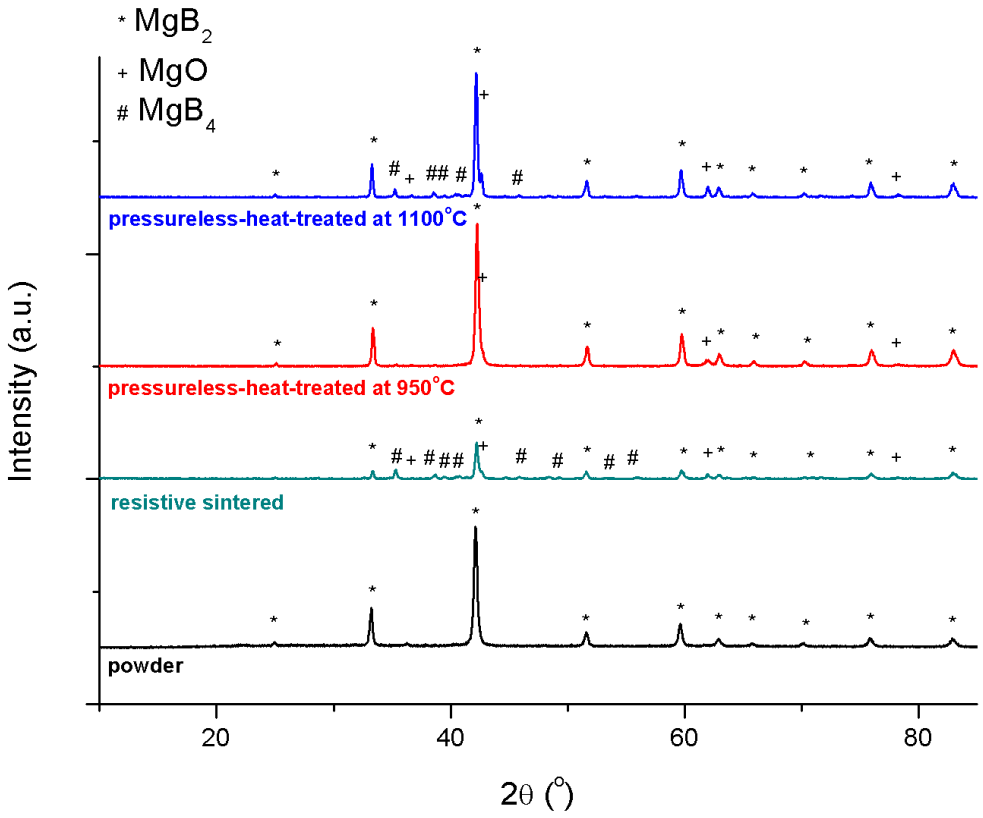


Figure 7.4: XRD spectrum for the resistively sintered pellet produced from as-purchased MgB_2 powder. The spectra for the starting powder, and pressureless sintered pellets heat-treated at 950 °C and 1100 °C are included for comparison.

Figure 7.5 shows the spectra for the samples produced from resistive sintering of powder ball milled for 8 h in isopropanol after having been packed in air. This sample shows no sign of increasing density and the anomalous low hardness values (see above). The spectrum for the resistively sintered sample contains one large peak which could not be identified. In addition, there are a few peaks attributable to MgB_4 which suggest that the powder has been heated to a temperature above 1000 °C by comparison with the XRD

spectra of pressureless heat-treated samples produced from the same powder (Figure 6.17 on page 191). Otherwise the spectrum mainly consists of peaks due to MgB_2. No peaks due to MgO were detected, so no MgO content could be measured for this sample. This suggests that the sample did not reach a high temperature, as a measurable quantity of MgO has formed in every other sample examined in this work heat-treated above 800 °C, and even for an unprotected sample heat-treated at 650 °C (see Table on page 115). It is possible that the peaks attributable to MgB_4 are due either to some other species, or originate from contamination of the die during earlier heat-treatment, and that the sample did not in fact reach the temperature required for either breakdown of the MgB_2, or for densification to occur, due to unknown problems with the heating. Therefore this sample was excluded from future analyses.

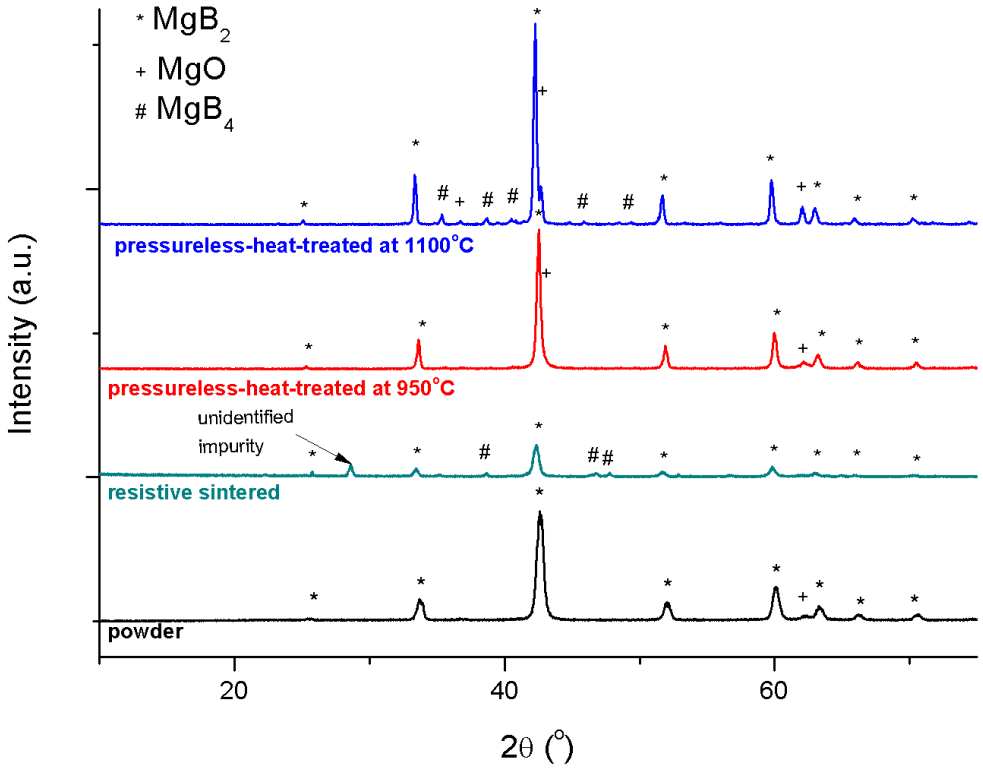


Figure 7.5: XRD spectrum for the resistively sintered pellet produced from MgB_2 powder which was ball milled for 8 h in air/isopropanol. The spectra for the starting powder, and pressureless sintered pellets heat-treated at 950 °C and 1100 °C are included for comparison.

Figure 7.6 shows the spectra for the samples produced from powder ball milled in isopropanol for 20 h following packing in air. The resistively sintered pellet contains a large concentration of MgO, similar to both pressureless heat-treated samples. In addition peaks are seen due to MgB_4. The MgO content of the resistively sintered sample was calculated as 45.8 % versus 37.6 % and 39.1 % for the samples pressureless heat-treated at 950 °C and 1100 °C respectively.

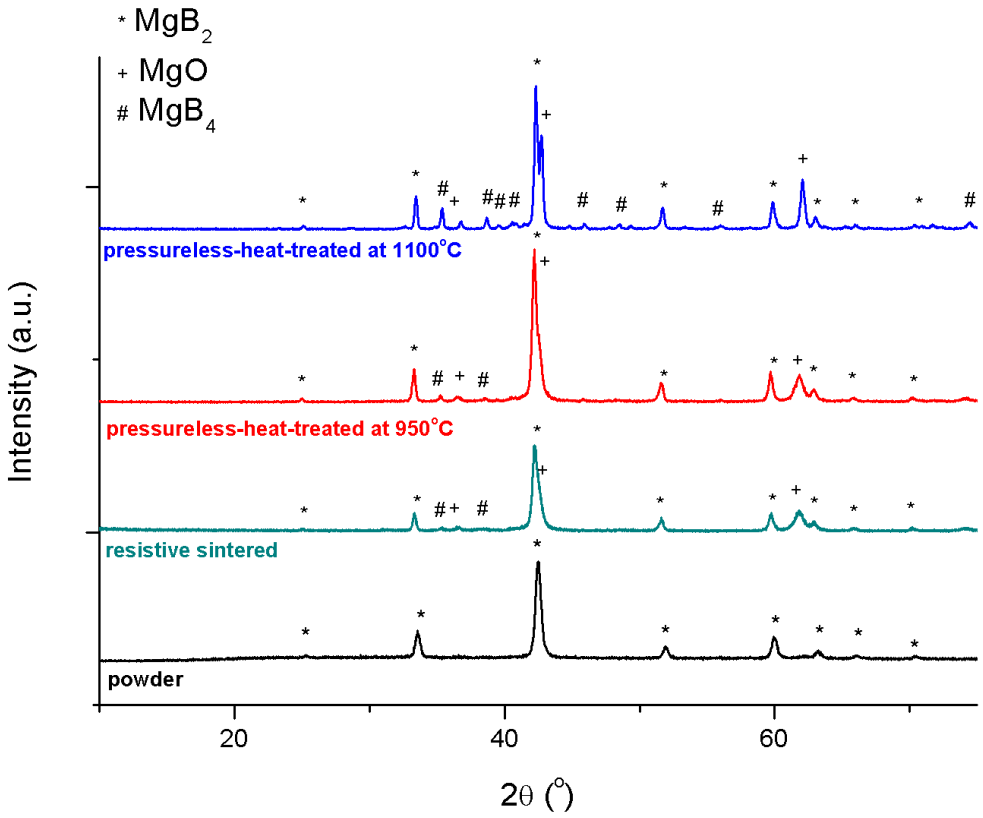


Figure 7.6: XRD spectrum for the resistively sintered pellet produced from MgB_2 powder which was ball milled for 20 h in air/isopropanol. The spectra for the starting powder, and pressureless sintered pellets heat-treated at 950 °C and 1100 °C are included for comparison.

Figure 7.7 shows the XRD spectra for the samples produced from attrition milled MgB_2 powder. The resistively sintered sample is again heavily contaminated with MgO and MgB_4. In addition, a peak due to zirconia (ZrO_2 plane (120) at $2\theta \simeq 32°$) is seen in both the resistively sintered sample and that pressureless heat-treated at 1100 °C. The

zirconia originates from the milling media, and was also seen in the as-milled powder using XPS (see Section on page 213). The MgO content of the attrition milled sample is extremely high (57.3 wt.%). This sample consists mainly of MgB_4 and MgO. This is rather different to the case for the samples prepared by pressureless heat-treatment which show a significant but not dominant MgO fraction (30.5 wt.% for pressureless heat-treatment at 950 °C; 36.9 wt.% for 1100 °C).

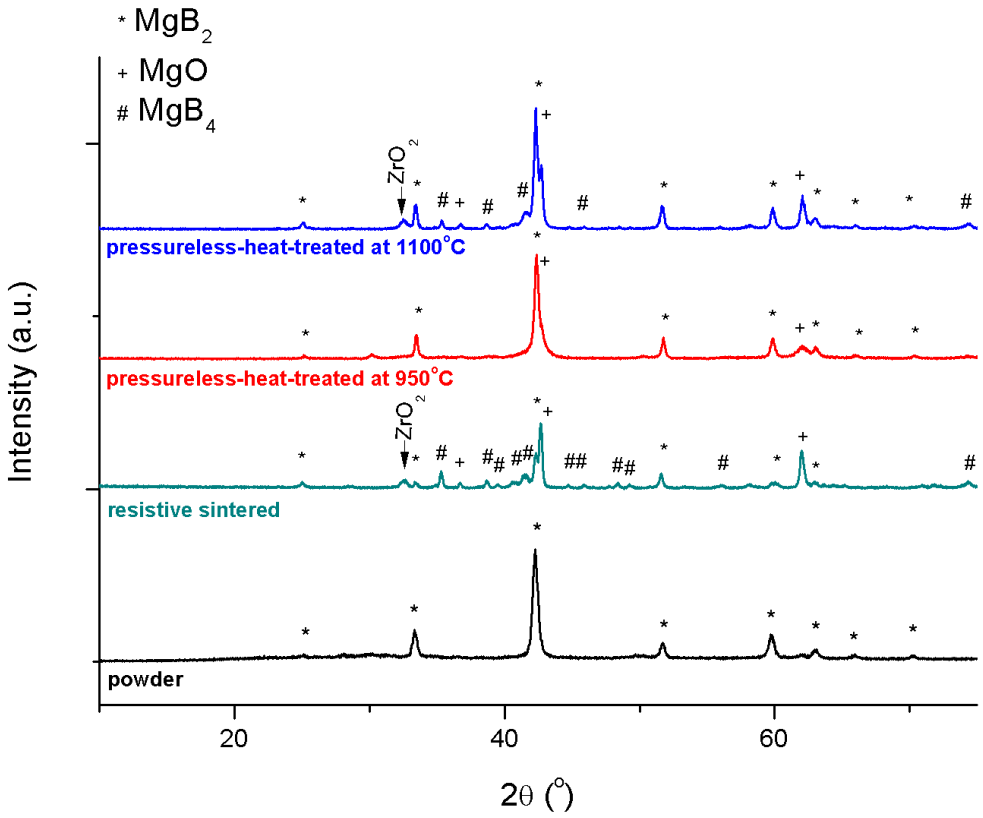


Figure 7.7: XRD spectrum for the resistively sintered pellet produced from MgB_2 powder which was attrition milled for 2 h in air/isopropanol. The spectra for the starting powder, and pressureless sintered pellets heat-treated at 950 °C and 1100 °C are included for comparison.

Figure 7.8 shows the XRD spectra for the samples prepared from the sedimented powder with nominal $d_{St} > 100\,\mu$m. The resistive sintered sample consisting mainly of MgO and MgB_4 (as indicated by the MgB_2 (110) peak at around 59° which is extremely small compared to the adjacent MgO (220) peak). No other phases were detected. The spectrum

is rather different from that of the pressureless heat-treated samples, which contain clear sharp peaks attributable to the MgB_2 phase, and a few small peaks due to MgO and MgB_4, but is similar to the resistively sintered sample prepared from attrition milled powder. However, while the latter sample densified dramatically compared to its pressureless heat-treated equivalents, that of the coarse sedimented powder did not. This indicates that impurity formation is not necessarily linked to the densification, and that it depends on amorphous impurities present prior to heat-treatment, which in turn depends on the method used to produce the starting powders.

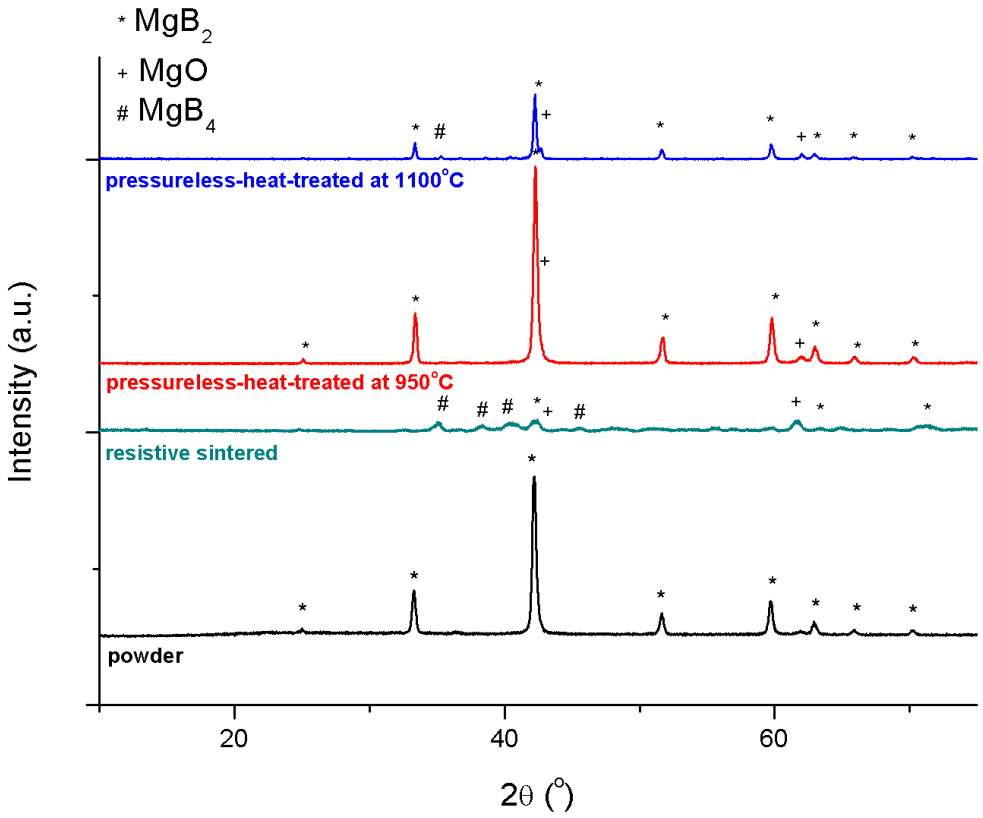


Figure 7.8: XRD spectrum for the resistively sintered pellet produced from MgB_2 powder which was sedimented in isopropanol to produce powder had nominal $d_{St} > 100\,\mu m$. The spectra for the starting powder, and pressureless sintered pellets heat-treated at 950 °C and 1100 °C are included for comparison.

In Figure 7.9, the XRD spectrum for the pellet resistively sintered from sedimented powder nominally $d_{St} < 1\,\mu$m is compared to the spectra for the starting powder and to the

pellet pressureless heat-treated at 950 °C only. No sample was produced by pressureless heat-treatment at a higher temperature (see Chapter 6). The resistively sintered sample has an increased impurity content (MgO content 21.9 wt%) compared with the sample pressureless sintered at 950 °C (MgO content 7.2 wt.%, see Section 6.2.3 on page 180), where only one peak due to MgO is discernible, with the other peaks all attributable to MgB_2.

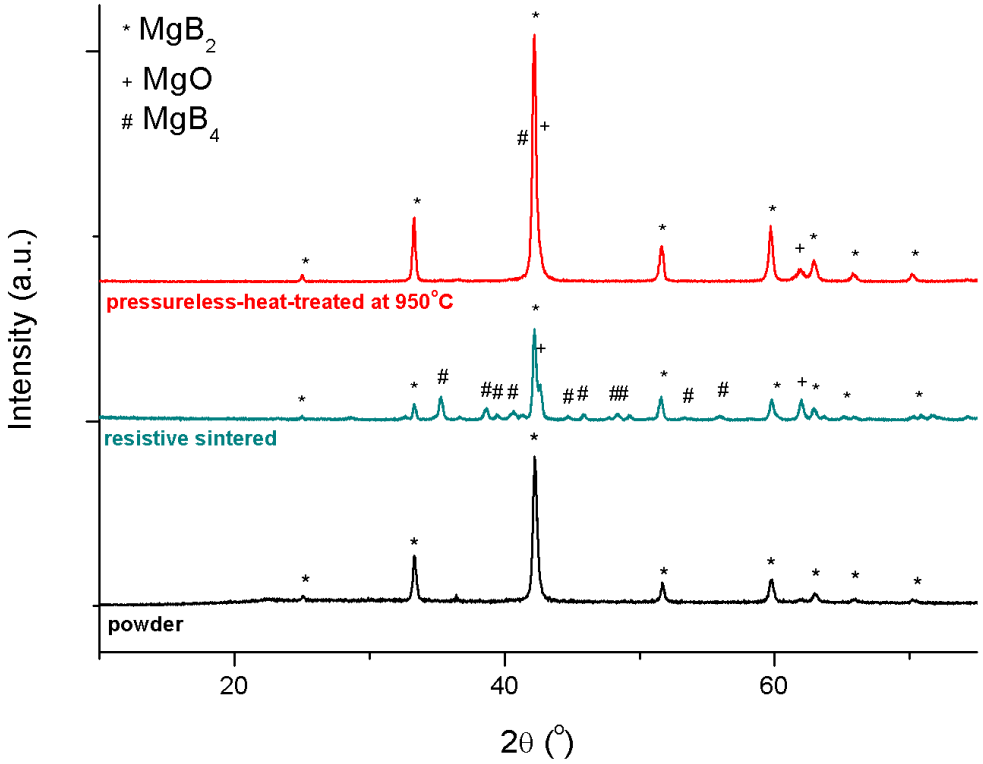


Figure 7.9: XRD spectrum for the resistively sintered pellet produced from MgB_2 powder which was sedimented in isopropanol to produce powder had nominal $d_{St} < 1\,\mu m$. The spectra for the starting powder, and pressureless sintered pellets heat-treated at 950 °C are included for comparison.

Table 7.1 on page 229 compares the MgO content of all the samples produced by resistive sintering in this work. It is immediately apparent that the MgO content is not correlated with the density; of the two densest samples, the pellet produced from as-purchased MgB_2 powder has an MgO content of 7.8 wt% of the MgB_2 content, while that produced from

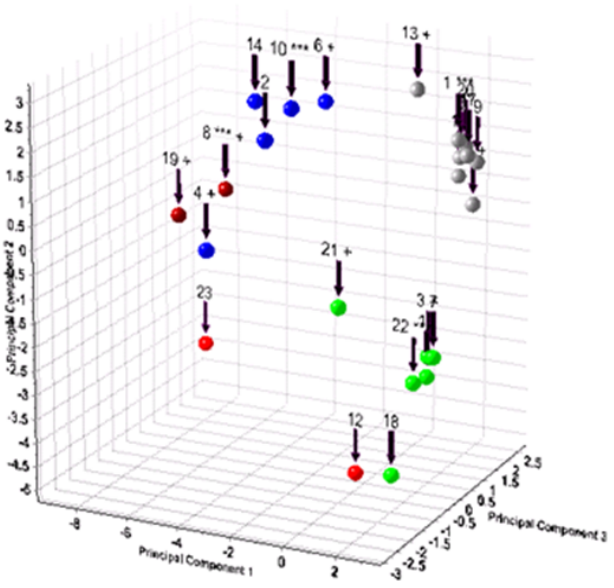
Table 7.2: Relative density of resistive sintered samples. The composite densities are calculated assuming that the samples consist of MgB_2 and MgO only.

Sample	Relative Density (%)
As-Purchased MgB_2	84
Attrition Milled MgB_2	74
8 h Ball Milled MgB_2	54*
20 h Ball Milled MgB_2	52
Sedimented $d_{>100}$ MgB_2	40
Sedimented $d_{<1}$ MgB_2	70

attrition milled powder has an MgO content of 57.3 wt%. Of the remaining samples, other than that produced from the powder ball milled for 8 h for which the MgO content fell below the measurable level, the MgO content is high ($22 - 58$ wt.%).

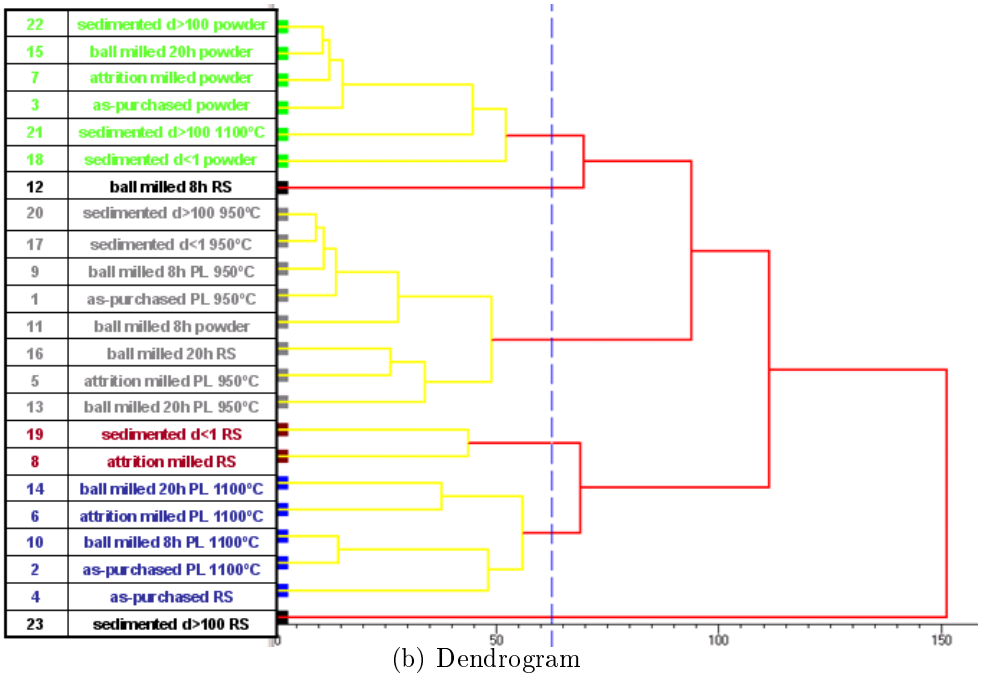
The high MgO content found in most of these samples means that the maximum density of the samples is dramatically altered from the theoretical maximum for pure MgB_2 ($2.63\,g/cm^3$). In Table 7.2 relative densities were calculated for each sample by comparing the actual measured density to the maximum density of a MgB_2/MgO composite containing only those two phases in the ratio given in Table 7.1.

The calculation of the density of the attrition milled resistively sintered pellet as above 100 % is because the calculation does not take into account the MgB_4 impurity phase. The exclusion of this phase (which has a theoretical density of $2.78\,g/cm^3$) leads to overcompensation in the calculated theoretical maximum densities. Calibration of the MgB_4 content in MgB_2 is required in order to accurately assess the relative densities of these samples. However it is still important to take into account the fact that maximum density of these MgB_2 bulks is lower than that of the MgB_2 phase, and may lead to misleading calculations of density. For example, the calculations indicate that despite the high MgO level, the relative density of the sample produced from sedimented powder nominally $d_{St} > 100\,\mu m$ is comparable to that of samples produced by pressureless sintering, and therefore showing that this sample did not sinter during resistive sintering. Without compensating for the high MgO content, the relative density would be calculated as 50 %, significantly lower than that of pressureless heat-treated samples.



1	as-purchased PL 950°C
2	as-purchased PL 1100°C
3	as-purchased powder
4	as-purchased RS
5	attrition milled PL 950°C
6	attrition milled PL 1100°C
7	attrition milled powder
8	attrition milled RS
9	ball milled 8h PL 950°C
10	ball milled 8h PL 1100°C
11	ball milled 8h powder
12	ball milled 8h RS
13	ball milled 20h PL 950°C
14	ball milled 20h PL 1100°C
15	ball milled 20h powder
16	ball milled 20h RS
17	sedimented d<1 950°C
18	sedimented d<1 powder
19	sedimented d<1 RS
20	sedimented d>100 950°C
21	sedimented d>100 1100°C
22	sedimented d>100 powder
23	sedimented d>100 RS

(a) Principal Components Analysis



(b) Dendrogram

Figure 7.10: Cluster analysis of XRD spectra of resistive sintered MgB_2 samples, with samples produced by pressureless heat-treatment included for comparison.

The cluster analysis of the XRD spectra for the resistively sintered pellets is shown in Figure 7.10. The resistively sintered samples produced from the powders ball milled for 8 h and sedimented with nominal $d_{St} > 100\,\mu$m are most similar to the starting powders. Most of the other resistive sintered samples are clustered near the equivalent sample pressureless heat-treated at 1100 °C, apart from that produced from powder ball milled for 20 h. This is contained in the largest cluster (silver/grey points) which contains mainly samples pressureless heat-treated at 950 °C. The sample which is least similar to all the others is the resistively sintered MgB_2 samples produced from powder sedimented with nominal $d_{St} > 100\,\mu$m. It is noticeable that the least dense samples have XRD spectra which are least similar to those of the other resistively sintered samples.

7.1.4 Microscopy

Optical micrographs were taken of the resistively sintered sample produced from as-purchased Alfa Aesar MgB_2 powder. Both the top surface and a cross-section through the pellet were polished using diamond paste and examined (Figures 7.11 and 7.12). Two distinctive regions were identified in the top surface of the sample; the centre (Figure 7.12a) and the edge (the annular region approximately 1mm from the edge of the sample, Figure 7.12b). For both sections, the centre of the pellet was significantly less porous than the edge, which appeared darker and more contaminated. This may be due to a reaction layer (either a layer of oxidised material, or a region contaminated with graphite diffusing from the graphite die), to inhomogeneous heating through the pellet during heat-treatment, or to the loss of magnesium from the surface resulting in porosity.

Scanning electron microscopy images were taken of fracture surfaces of all the resistively sintered samples. SEM images for the sample produced from as-purchased MgB_2 powder are shown in Figure 7.13. The sample is rather inhomogeneous: densified regions around 6 μm in diameter containing occluded porosity are seen (Figure 7.13a) alongside similarly sized regions of powdery non-densified material (Figure 7.13c). These resemble samples prepared from the same powder by pressureless heat-treatment (see Figure 4.31).

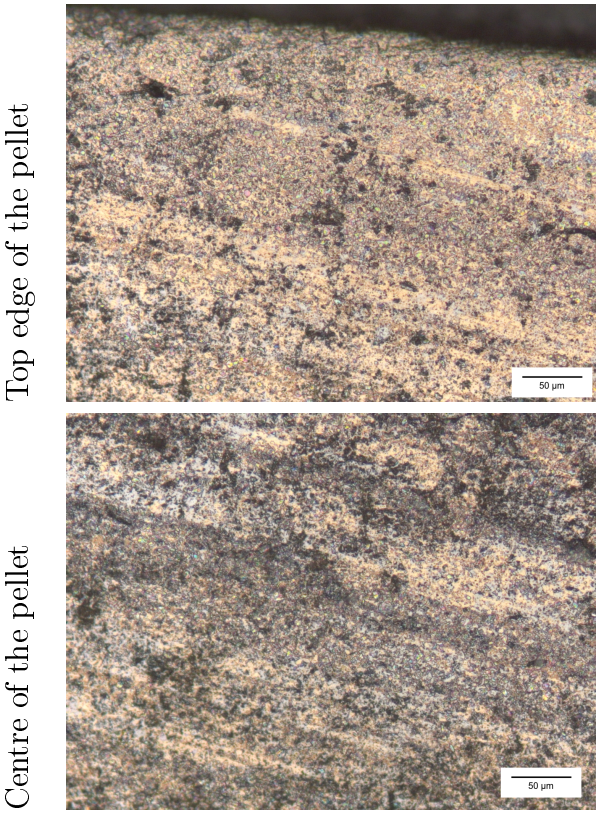


Figure 7.11: Optical micrographs for resistive sintered sample produced from as-purchased MgB_2. Images are of a polished cross-section through the centre of the sample.

SEM images of samples produced by resistive sintering of the ball and attrition milled powders are shown in Figure 7.14. The densified regions seen in the resistively sintered sample produced from the as-purchased powder were not found in these samples. The attrition milled sample contains several very rounded particles of around 300 nm diameter which are probably an impurity phase which has formed from the vapour phase during heat-treatment, given the high impurity content in this sample and the very rounded, almost spherical nature of some of the particles. The sample produced from ball milled powders still appear very particulate in nature, though more connectivity is seen in the sample produced from powder ball milled for 20 h with smoothed regions where particles have amalgamated (Figure 7.14h). These observations are consistent with the earlier observations of density and impurity content. The measured density increases are either due to an increase in impurity content, or to early-stage sintering behaviour.

SEM images of the samples produced by resistive sintering of sedimented powders

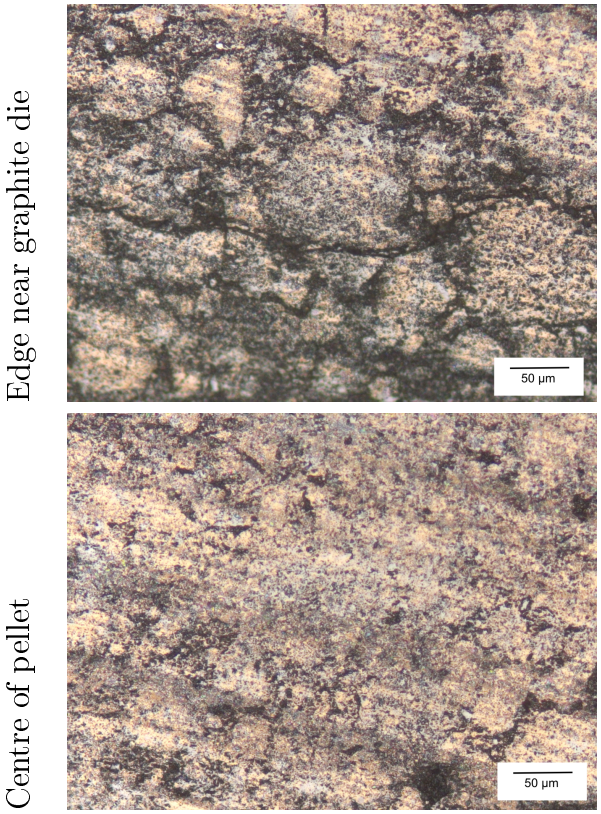
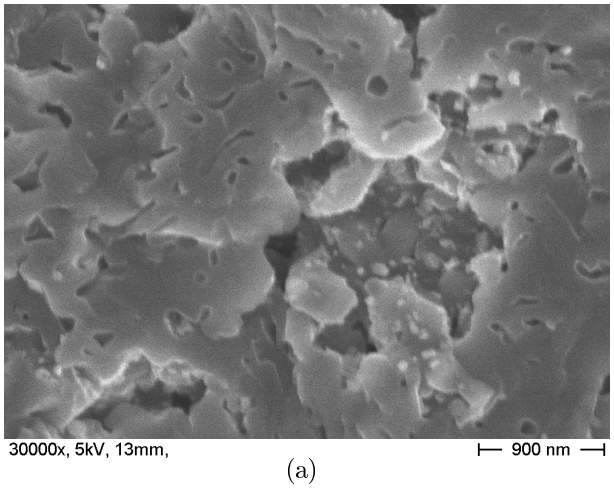
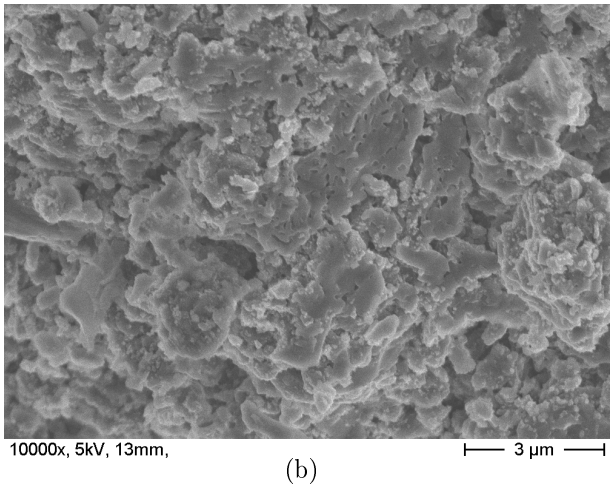


Figure 7.12: Optical micrographs for resistively sintered sample produced from as-purchased MgB_2. Images are of the polished top surface of the sample.

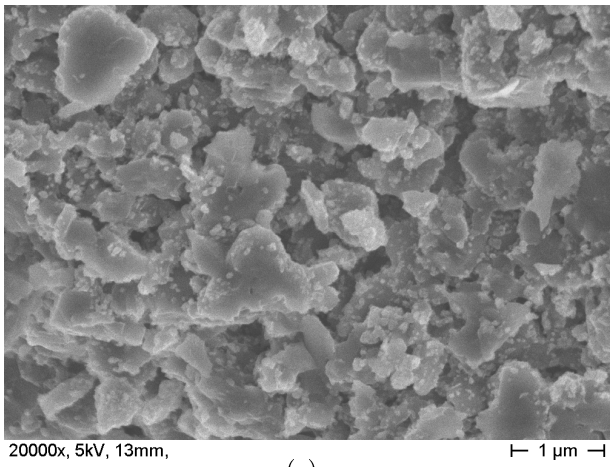
(Figure 7.15) indicate a similar microstructure to the sample produced from as-purchased powder (Figure 7.13). The samples both contain large semi-densified regions with occluded porosity (Figure 7.15a and d), along with similarly sized powdery regions (Figure 7.15 b and f). In addition, the sample produced from the finer material ($d_{St} < 1\,\mu$m) contains some highly densified regions with no observed occluded porosity. One of these areas can be seen in Figure 7.15e (on the right-hand side of the picture). The charging on the left of this image is due to the powdery region which is not well connected to the rest of the sample. The densified regions are larger in the sample produced from the finer material, which accounts for its higher hardness.



(a)



(b)



(c)

Figure 7.13: SEM images of a fracture surface of the resistively sintered sample produced from as-purchased MgB_2 powder

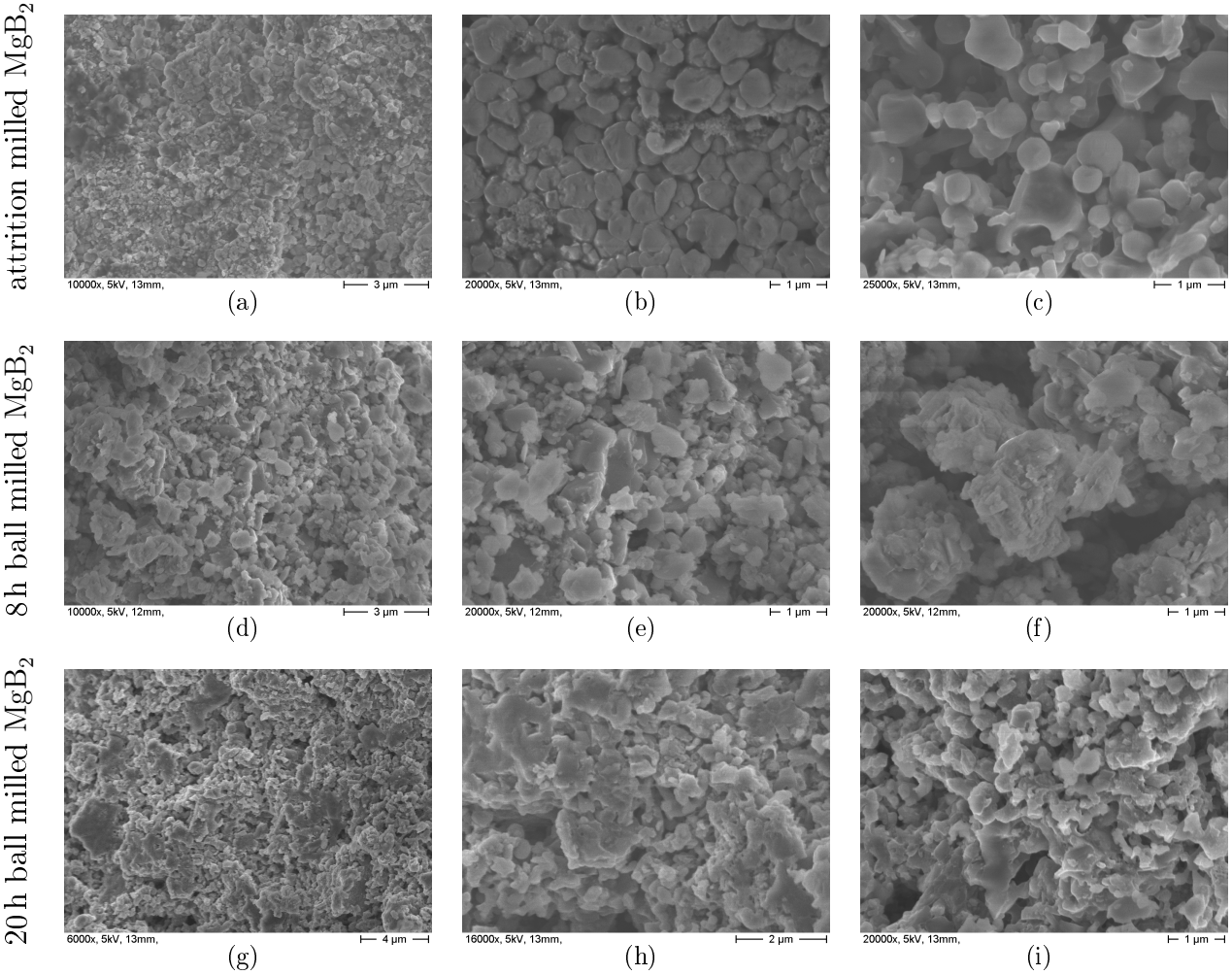


Figure 7.14: SEM images of fracture surfaces of resistive sintered samples produced from milled MgB_2 powders

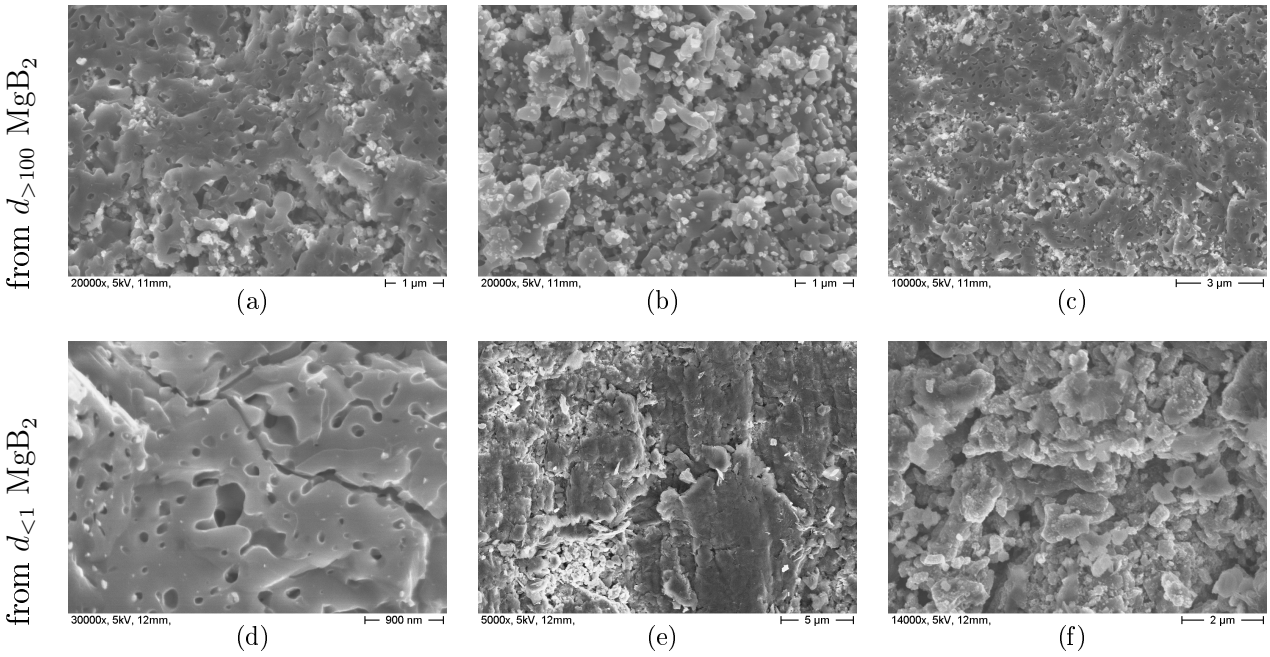


Figure 7.15: SEM images of fracture surfaces of resistively sintered samples produced from sedimented MgB_2 powders

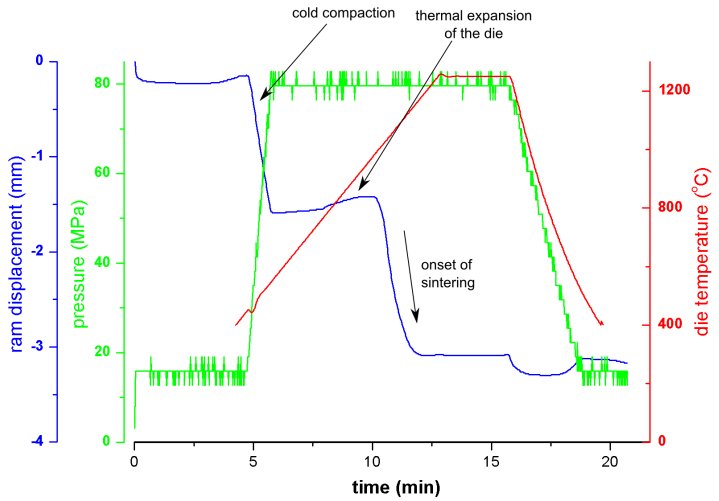
7.1.5 Summary

While resistive sintering produced MgB_2 bulks with a significantly higher density and hardness than pressureless heat-treatment for some of the powders, none attained full densification. However it was encouraging that denser material ($2.28\,g/cm^3$) could be produced without significant increase in impurity content (MgO content 7.8 wt.%) from the as-purchased MgB_2 powder. In order to produce denser MgB_2 bulk material and to gain greater control over the key parameters (atmosphere, temperature, heating rate and pressure), further pressure-assisted processes were investigated.

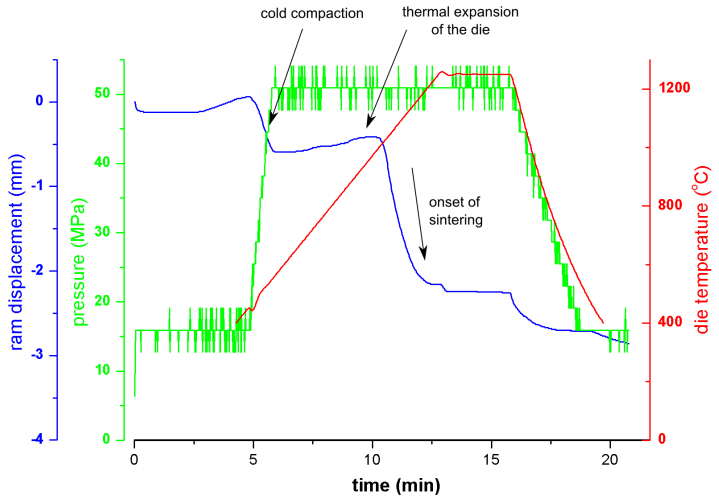
7.2 Spark Plasma Sintering

Spark plasma sintering was carried out at Queen Mary, University of London, with the assistance of Dr Haixue Yan. A typical run took only around 1 h per sample including pump down and cool down times. The main advantages of the SPS over the resistive sintering rig is that tests can be carried out in either vacuum or argon gas, the heating rate is much more responsive and rapid, the high vacuum can be obtained more quickly, the pressure can be varied over a wider range and a higher temperature can be obtained. In this work, the test temperatures were $1200 - 1350\,^{o}C$, and the applied pressure ranged from 16 MPa to 80 MPa. The lower limit is the lowest pressure which could be applied while still holding the die in position during heat-treatment.

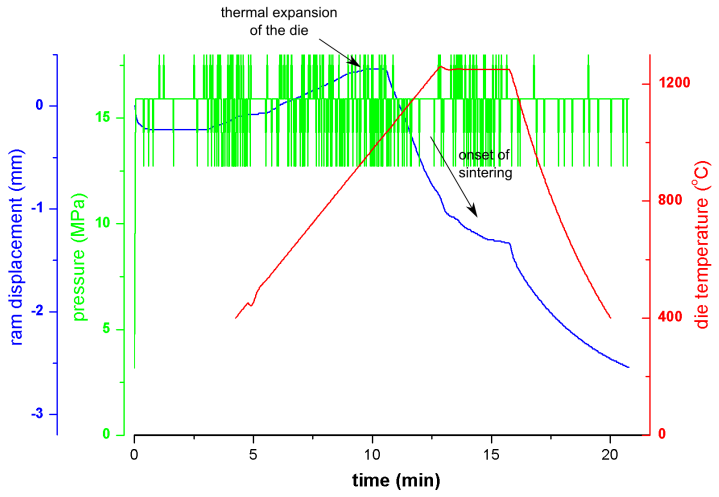
Graphs showing the logged temperature, applied pressure, and ram displacement are shown in Figures 7.16-7.19. The thermocouple could not accurately measure temperatures below $400\,^{o}C$, so temperatures below this temperature are excluded from the logged data. Samples were produced from the as-purchased powder and the powders ball milled for 8 h and 20 h. In order to assess the effect of different heat-treatment conditions on the properties of the bulk material, as-purchased MgB_2 powder was used to make a number of samples under different conditions. These were under vacuum or under argon gas, and under a range of applied pressures (16 MPa, 50 MPa and 80 MPa). The data logged during these runs is shown in Figure 7.16a-c. The data shows that the greatest ram displacement (indicative of the most extensive densification) occurred for the sample prepared under the highest pressure. All samples were produced using exactly the same mass of MgB_2 powder (3 g) loaded into the die and these samples were heated at the same temperature. In contrast to the resistive sintered sample produced from the same powder (Figure 7.1) the ram displacement falls after removal of the applied pressure; this is due to the ability in the SPS to move both the upper and lower plungers as pressure is removed, whereas in the resistive sintering rig only the upper plunger is moved.



(a) Maximum Applied Pressure 80 MPa, Maximum Temperature 1250 deg. C

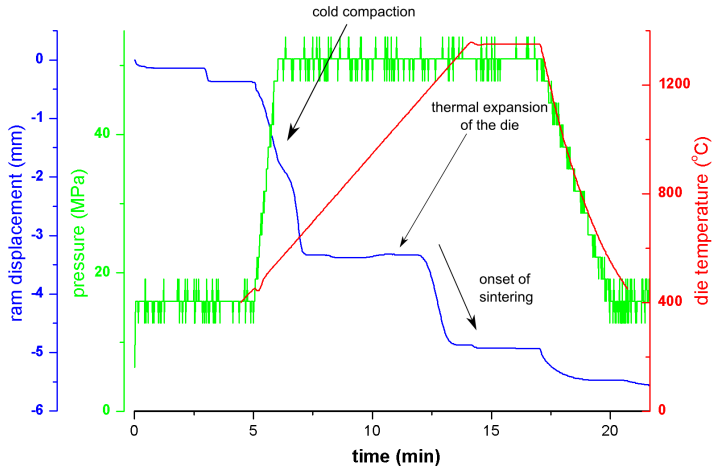


(b) Maximum Applied Pressure 50 MPa, Maximum Temperature 1250 deg. C

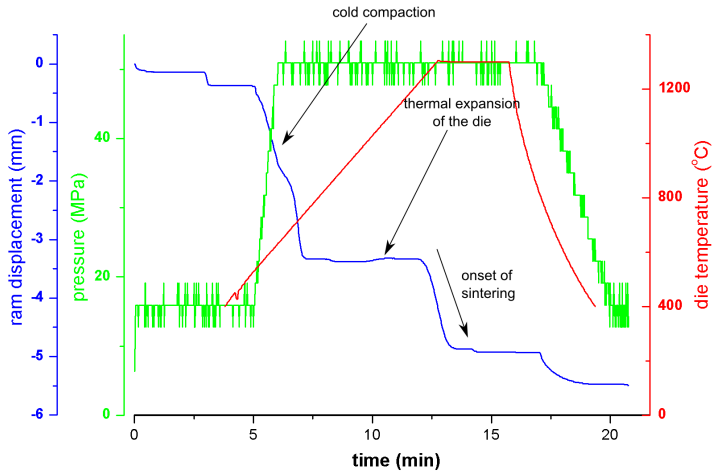


(c) Maximum Applied Pressure 16 MPa, Maximum Temperature 1250 deg. C

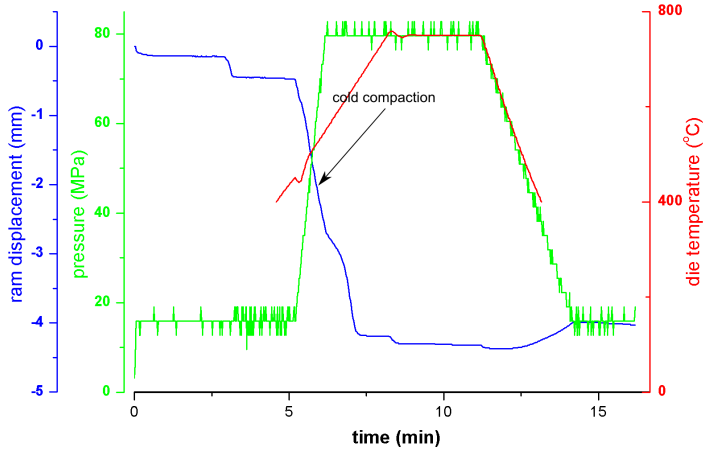
Figure 7.16: Variation in pressure, ram displacement and die temperature logged during spark plasma sintering of as-purchased MgB_2 powder in vacuum



(a) Initial Run, Maximum Pressure 50 MPa, Maximum Temperature 1350 deg. C



(b) Maximum Applied Pressure 50 MPa, Maximum temperature of 1350 deg.C



(c) Maximum Pressure 80 MPa, Maximum heat-treatment temperature of 750 deg.C

Figure 7.17: Variation in pressure, ram displacement and die temperature logged during spark plasma sintering in vacuum of MgB_2 powder ball milled for 20 h in isopropanol

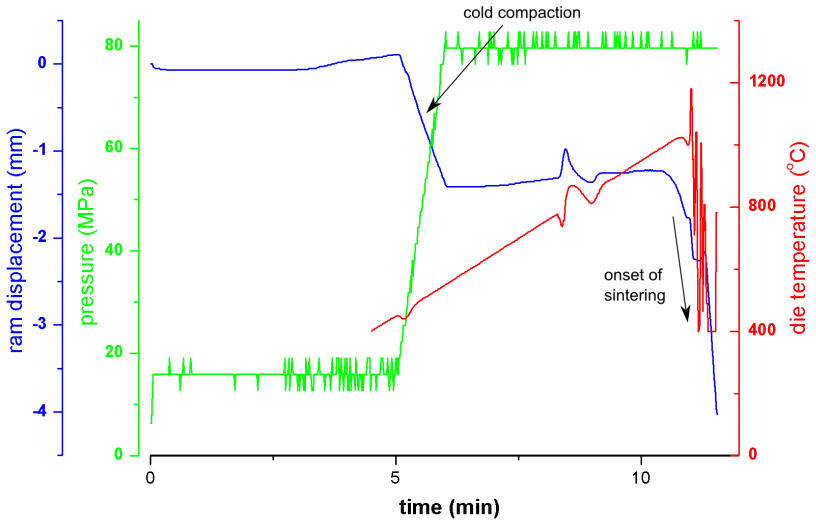


Figure 7.18: Variation in pressure, ram displacement and die temperature logged during spark plasma sintering of as-purchased MgB_2 powder in Ar gas. In Argon, Maximum Test conditions were applied pressure 80 MPa, maximum temperature 1250 °C.

The heat-treatment of the sample prepared by spark plasma sintering under Ar gas was aborted at 1200 °C, however significant densification still occurred so the structure of the sample was still studied. A very sudden rapid change in the ram height caused the instrument to indicate that the run should be aborted. Following the removal of the die from the SPS chamber, a white powder was found dispersed over the inside of the chamber. From previous experience of the heat-treatment of MgB_2 (as discussed in Chapter 4) this powder is likely to be MgO but the powder was too finely dispersed to be collected for analysis.

An initial test to establish a suitable peak temperature for heat-treatment involved producing a sample from the powder prepared by ball milling for 20 h in isopropanol. The data logged during this test indicated two critical temperatures at which rapid densification occurred, the first at around 750 °C and the second around 1350 °C. The data logged in this run is shown in Figure 7.17a. For this reason two further samples were produced with peak temperatures of 1350 °C (Figure 7.17b) and 750 °C (Figure 7.17c). Characterization of these two samples will aid determination of the effects of the two densification steps identified in Figure 7.17a.

The sample produced from MgB_2 powder which had been ball milled for 8 h in isopropanol/air was heat-treated at 1200 °C after initial tests to determine the approximate temperature at which rapid densification occurred. From Figure 7.19 densification appears to occur from around 1000 °C when the sample is under a load of 80 MPa, similarly to the sample produced from as-purchased MgB_2 (see Figure 7.16a). The change in ram displacement during preparation of this sample was lower than that for the samples produced from the other ball milled MgB_2 powder.

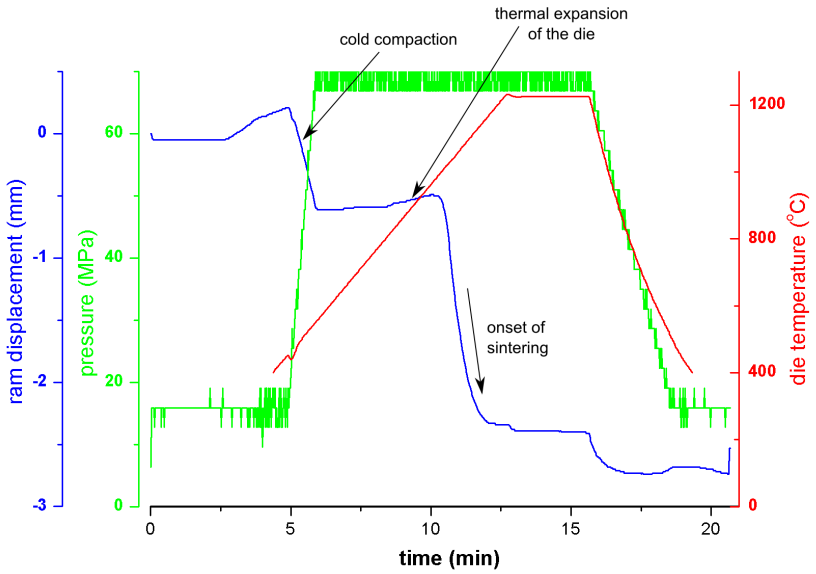


Figure 7.19: Variation in pressure, ram displacement and die temperature logged during spark plasma sintering in vacuum of MgB_2 powder ball milled for 8 h in isopropanol. Test conditions were applied pressure 80 MPa, maximum temperature 1200 °C.

7.2.1 Density

Following spark plasma sintering, the samples were ground using a flat bed grinder to remove the graphite foil which was in contact with the faces of the pellets during heat-treatment. The density was then measured using Archimedes' method and isopropanol as the immersion medium, and the results are shown in Figure 7.20. In all cases the densities of spark plasma sintered samples were higher ($> 2.0\,g/cm^3$) than those of equivalent pressureless heat-treated samples. The density of the samples produced from as-purchased MgB_2 powder in vacuum using pressures of 50 MPa or 80 MPa were very similar

at 2.65 g/cm^3, while the density of the samples produced in vacuum under the minimum pressure (16 MPa) and under argon gas with 50 MPa applied pressure were 2.52 g/cm^3 and 2.21 g/cm^3 respectively. For the samples produced from ball milled powders, the density of the sample produced at high temperature from powder milled for 20 h was 2.67 g/cm^3 (similar to the values from as-purchased MgB_2 powder produced under high pressure). The sample produced from the same powder at lower temperature had significantly lower density (2.13 g/cm^3) indicating that for full densification the temperature must be higher than 750 °C. The density of the sample produced from powder ball milled for 8 h was also lower at 2.28 g/cm^3 even at 80 MPa and 1200 °C.

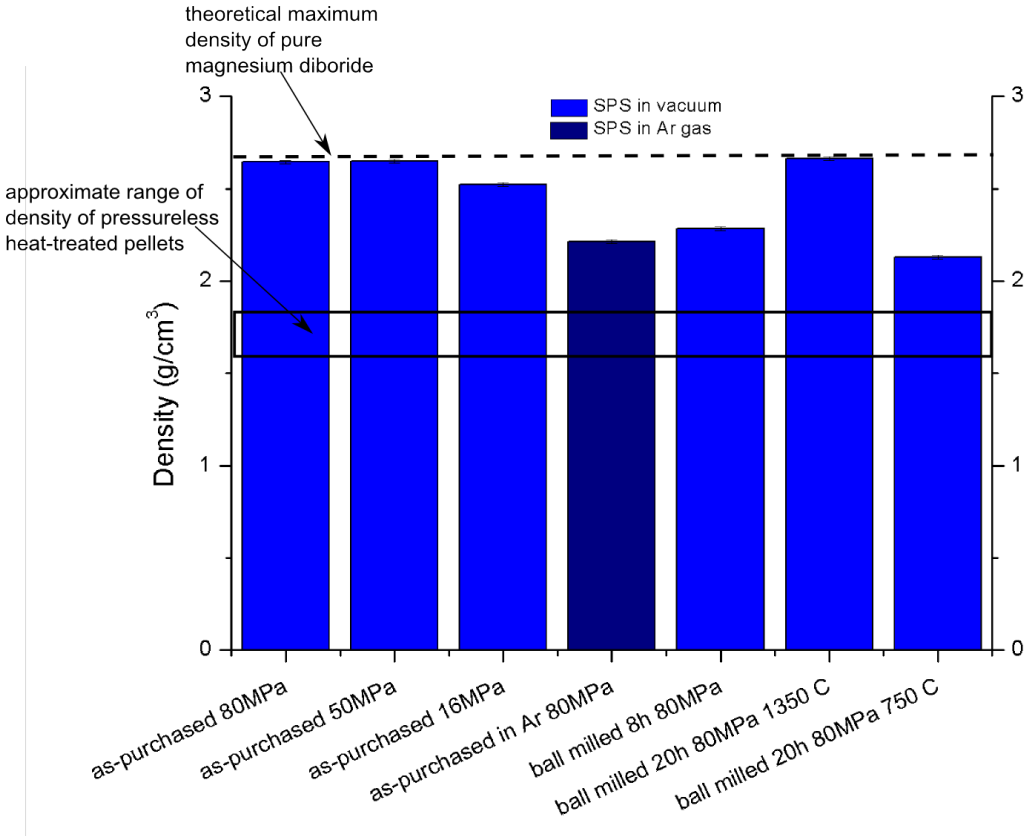


Figure 7.20: Density measured using Archimedes' method for all spark plasma sintered MgB_2 bulks

7.2.2 Hardness

The hardness of the samples was measured using Vickers hardness indentation with a 2 kg load. The results are shown in Figure 7.21. The hardest sample is that produced from powder which was ball milled for 20 h in air/isopropanol (heat-treated at 1350 °C), followed by the sample produced from powder ball milled for 8 h in air/isopropanol. The sample produced from 20 h ball milled powder and heat-treated at 750 °C had much lower hardness (233 HV/2) as full densification had not occured. The samples produced from as-purchased MgB_2 powder have lower hardness than those produced from the ball milled powder, but still much higher than those for pressureless heat-treatment. Of the four samples produced, the hardest is that for the sample produced in vacuum under 50 MPa pressure, closely followed by that of the sample produced in vacuum under 80 MPa pressure. The hardness of the sample produced in vacuum under 16 MPa pressure was significantly lower. Finally, the sample spark plasma sintered in argon under 50 MPa pressure has the lowest average hardness at 323 HV/2. but is very inhomogeneous with hardness values ranging from 42 HV/2 to 559 HV/2. For the low hardness values the average value was measured as 50 ± 7 HV/2, and for the harder regions as 505 ± 12 HV/2. Optical microscope images of indentations measured on this sample are shown in Figure 7.22.

7.2.3 Impurity Content

The impurity content was assessed using XRD $\theta - 2\theta$ scans. Figure 7.23 shows the spectra for the samples prepared from as-purchased MgB_2 powder by spark plasma sintering in vacuum or in Ar gas. The samples prepared under vacuum have similar XRD spectra, dominated by the MgB_2 peaks with small peaks due to MgO and MgB_4. The spectrum for the pellet prepared in Ar gas is dominated by peaks due to MgO, and contains very little MgB_2.

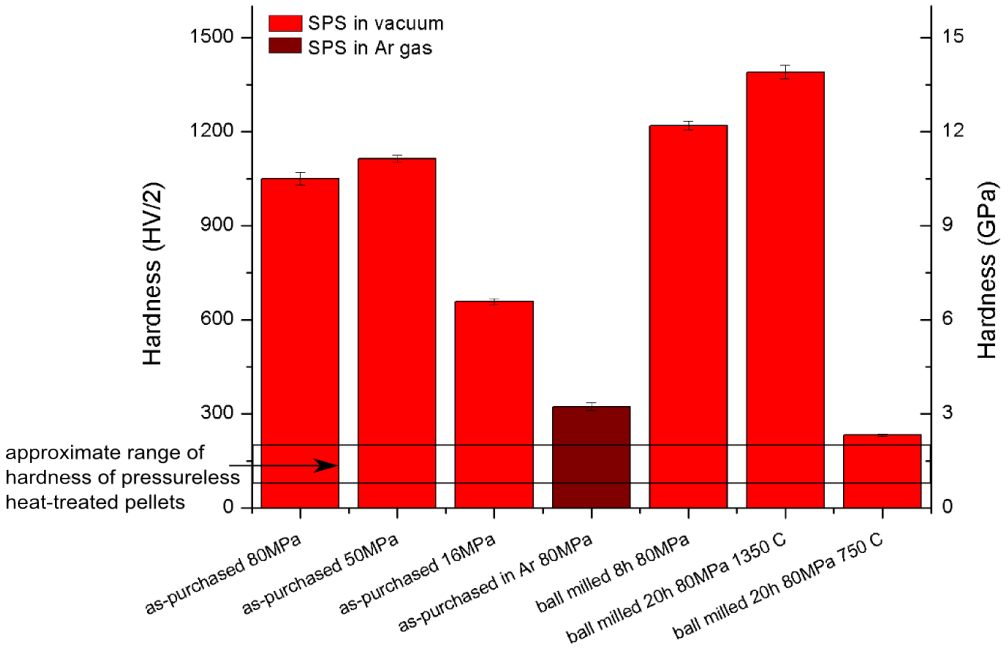
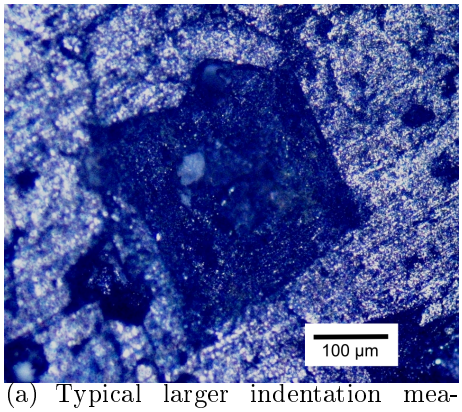
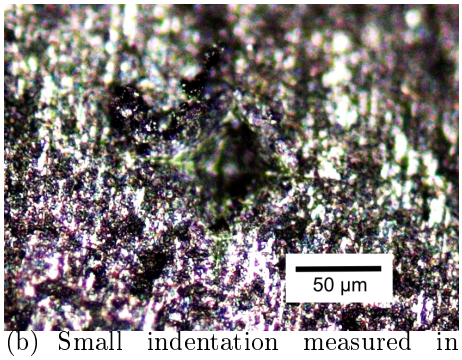


Figure 7.21: Hardness of all spark plasma sintered MgB_2 bulks



(a) Typical larger indentation measured in less hard region



(b) Small indentation measured in harder region

Figure 7.22: Pyramidal indentations on the surface of the inhomogeneous MgB_2 sample produced by spark plasma sintering of as-purchased MgB_2 powder in Ar gas

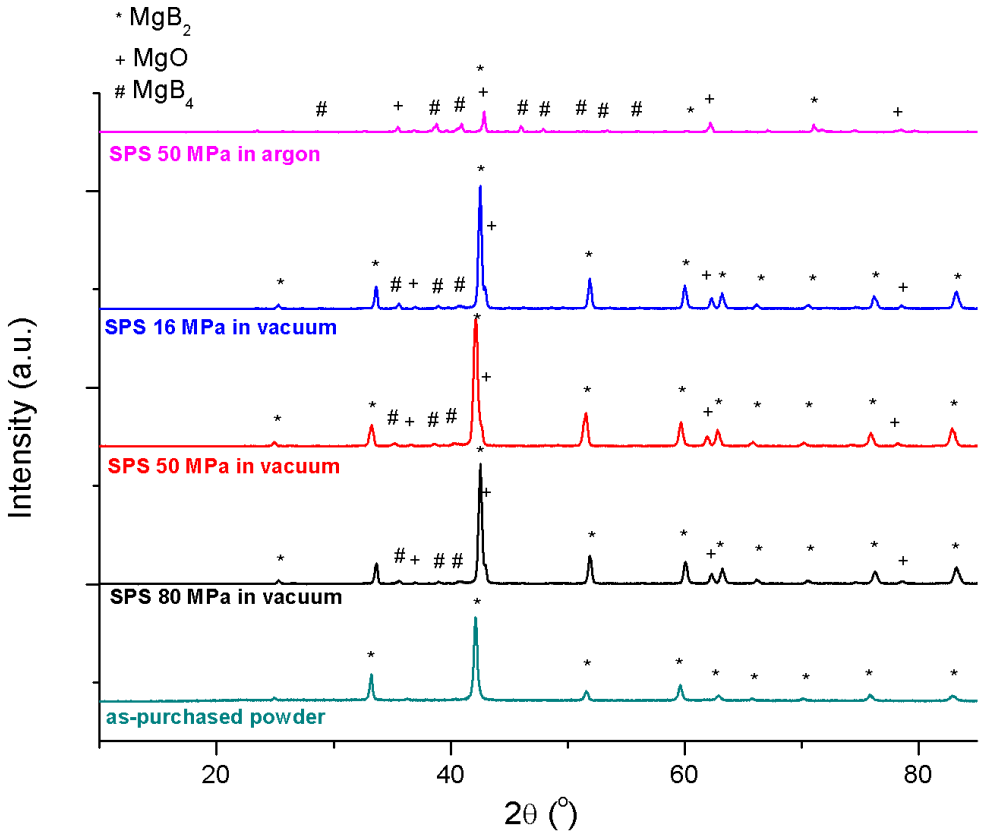


Figure 7.23: XRD spectra for the spark plasma sintered pellets produced from as-purchased MgB_2 powder and heat-treated in vacuum or in Ar. The spectrum for the starting powder is included for comparison.

Figure 7.24 compares the sample prepared by spark plasma sintering of powder ball milled in isopropanol for 8 h with the starting powder and samples prepared from the same powder by resistive sintering and pressureless heat-treatment at 950 °C and 1100 °C. The XRD spectrum of the sample produced by SPS is most similar to that of the sample produced by pressureless heat-treatment at 1100 °C, containing several peaks due to MgB_4 and MgO, including all the expected peaks due to MgB_2.

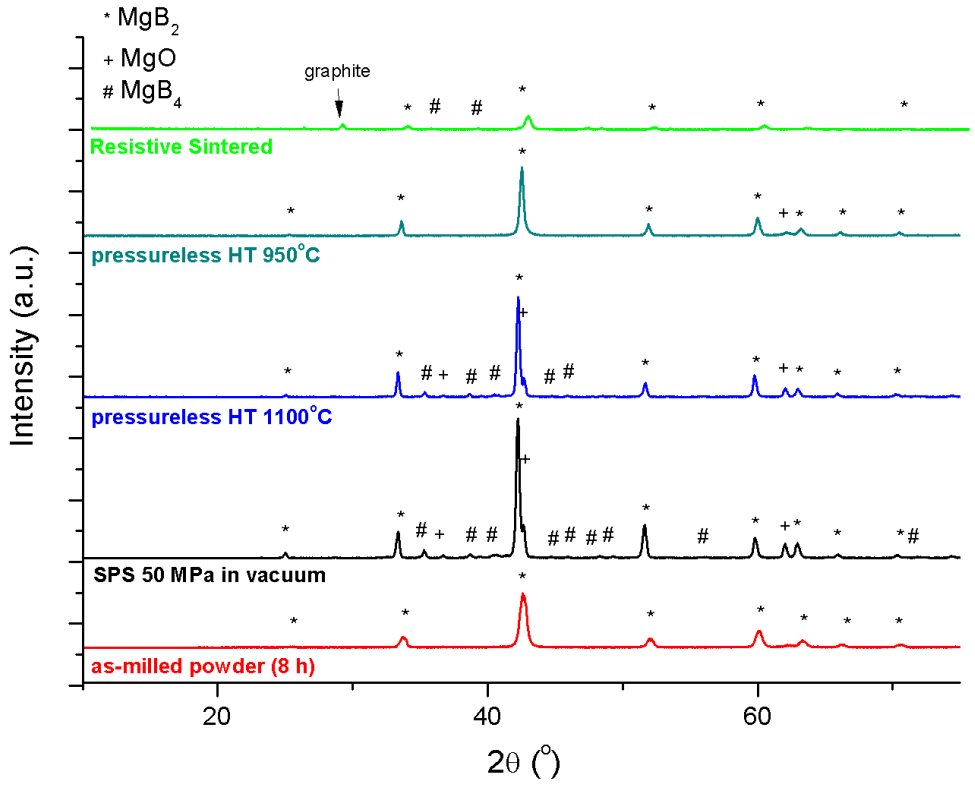


Figure 7.24: XRD spectra for the spark plasma sintered pellet produced from MgB_2 powder ball milled for 8 h and heat-treated in vacuum. The spectra for the starting powder, the resistively sintered pellet, and the pressureless sintered pellets heat-treated at 950 °C and 1100 °C produced from the same powder are included for comparison.

Figure 7.25 compares the samples prepared by spark plasma sintering of powder ball milled in isopropanol for 20 h with samples from the same powder prepared by resistive sintering and pressureless heat-treatment at 950 °C and 1100 °C, and with the starting as-milled powder. The XRD spectrum for the pellet produced by spark plasma sintering at 750 °C contains only peaks due to MgO and MgB_2, consistent with the observation made earlier in several samples that the MgB_4 forms at a higher temperature. The spectrum for the pellet spark plasma sintered at 1350 °C also contains peaks due to MgB_4, and is similar to the spectra for the pressureless heat-treated samples.

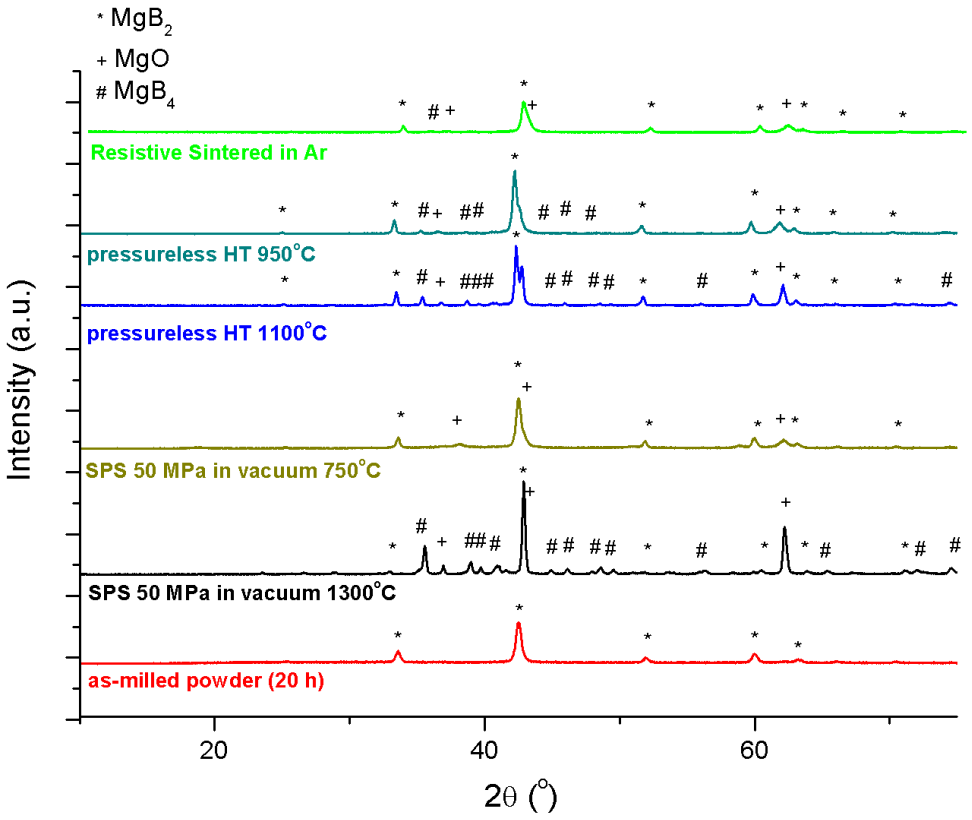


Figure 7.25: XRD spectra for the spark plasma sintered pellets produced from MgB_2 powder ball milled for 20 h and heat-treated in vacuum. The spectra for the starting powder, the resistive sintered pellet, and the pressureless sintered pellets heat-treated at 950 °C and 1100 °C produced from the same powder are included for comparison.

Table 7.3 shows the MgO content as a percentage of the MgB_2 content, calculated using the calibration curve in Chapter 4. The MgO content for the samples produced from as-purchased Alfa Aesar MgB_2 powder and spark plasma sintered in vacuum are similar at $7.3 - 8.6$ wt.%, indicating the the MgO content does not depend on the pressure used during spark plasma sintering. The MgO content of the sample prepared by spark plasma sintering of the same powder in Ar gas was calculated as 71.6 wt%, though, as discussed earlier, the MgO content calculations are less accurate for high MgO contents because the calibration curve flattens out in this region. As indicated in the XRD spectrum for this sample (Figure 7.23) this sample largely consists of MgO. The samples prepared by spark plasma sintering in vacuum from ball milled powders have higher MgO contents than those

prepared from as-purchased MgB_2 powder. Even the sample prepared from powder ball milled for 20 h in isopropanol and heat-treated at 750 °C contains 14.3 % MgO, indicating that amorphous impurities in the powder due to the ball milling form MgO during heat-treatment. This must be in addition to the MgO which forms in all samples along with the MgB_4 at high temperatures when oxygen is present [96]. The sample produced from MgB_2 ball milled for 20 h and heat-treated at 1350 °C mostly contains MgO, and the level was calculated as 83.8 %, the highest measured for a spark plasma sintered sample in this work.

Table 7.3: MgO content of spark plasma sintered MgB_2 bulks

Sample	MgO Content (as wt.% of MgB_2 content)	Density (g/cm^3)
SPS of as-purchased MgB_2 80 MPa in vacuum	8.2	2.65
SPS of as-purchased MgB_2 50 MPa in vacuum	7.3	2.65
SPS of as-purchased MgB_2 16 MPa in vacuum	8.6	2.52
SPS of as-purchased MgB_2 80 MPa in Ar gas	71.6	2.21
SPS of 8 h ball milled MgB_2 50 MPa in vacuum	14.3	2.28
SPS of 20 h ball milled MgB_2 50 MPa in vacuum, max. temperature 1350 °C	83.8	2.67
SPS of 20 h ball milled MgB_2 50 MPa in vacuum max. temperature 750 °C	31.3	2.13

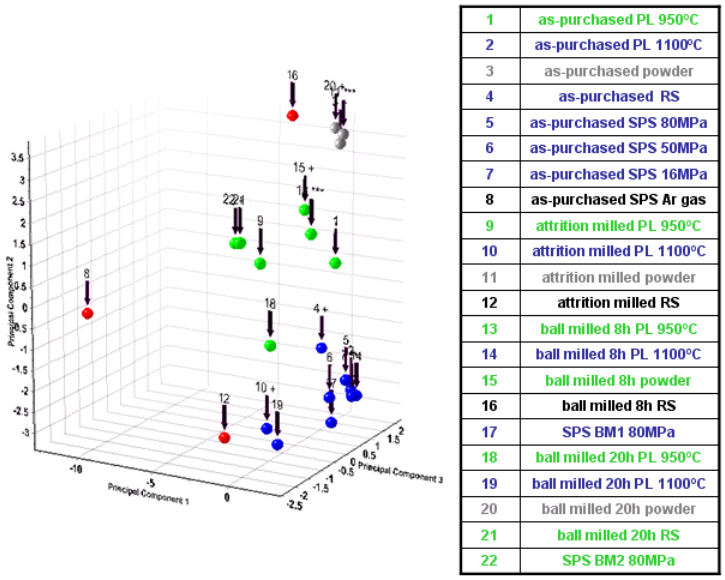
The relative densities of the samples are given in Table 7.4, calculated assuming that samples are composites of MgO and MgB_2 only. These calculations indicate that the pellets spark plasma sintered from as-purchased powder are very high in density. It is important to take into account the fact that maximum density of these MgB_2 bulks is lower than that of the MgB_2 phase, and can lead to misleading calculations of density. The impurity content is not taken into account in assessing the density of MgB_2 bulks in

the literature.

Table 7.4: Relative densities of spark plasma sintered MgB_2 bulks. Composite densities are calculated assuming that the samples consist only of MgB_2 and MgO

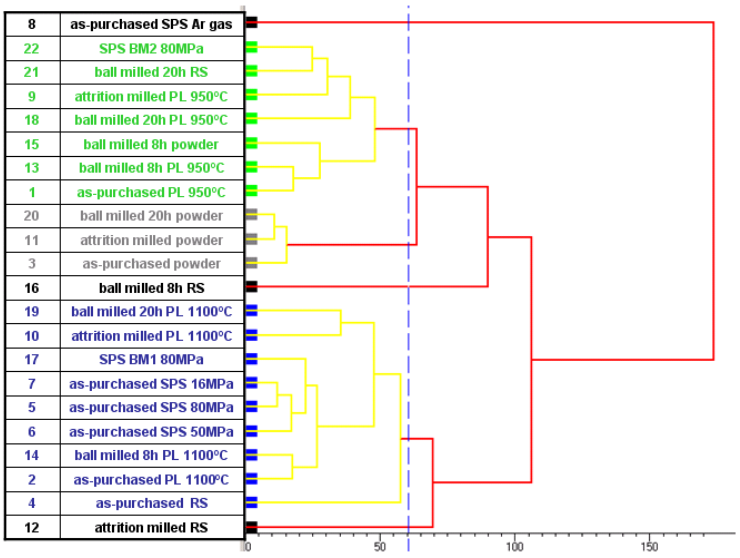
Sample	Relative Density (%)
SPS of as-purchased MgB_2 80 MPa in vacuum	97
SPS of as-purchased MgB_2 50 MPa in vacuum	97
SPS of as-purchased MgB_2 16 MPa in vacuum	92
SPS of as-purchased MgB_2 80 MPa in Ar gas	96
SPS of 8 h ball milled MgB_2 50 MPa in vacuum	81
SPS of 20 h ball milled MgB_2 50 MPa in vacuum, max. temperature 1350 °C	89
SPS of 20 h ball milled MgB_2 50 MPa in vacuum, max. temperature 750 °C	66

A cluster analysis was carried out on the XRD spectra for the spark plasma sintered pellets, along with those for the starting powder and the pellets produced by resistive sintering and pressureless heat-treatment (Figure 7.26). This indicates that the sample prepared from as-purchased MgB_2 powder spark plasma sintered in argon gas is most dissimilar to the other samples, adding evidence to the conjecture that this sample contains little to no MgB_2. Otherwise three main clusters are formed, of which two contain spectra taken from spark plasma sintered pellets. The spark plasma sintered samples prepared in vacuum from as-purchased MgB_2 powder and powder ball milled for 8 h in isopropanol are clustered with the samples prepared by pressureless heat-treatment at 1100 °C (blue cluster). The green cluster contains the sample produced by spark plasma sintering of MgB_2 powder ball milled for 20 h in isopropanol, with the resistively sintered sample prepared from the same powder, and the samples prepared by pressureless sintering of all powders.



1	as-purchased PL 950°C
2	as-purchased PL 1100°C
3	as-purchased powder
4	as-purchased RS
5	as-purchased SPS 80MPa
6	as-purchased SPS 50MPa
7	as-purchased SPS 16MPa
8	as-purchased SPS Ar gas
9	attrition milled PL 950°C
10	attrition milled PL 1100°C
11	attrition milled powder
12	attrition milled RS
13	ball milled 8h PL 950°C
14	ball milled 8h PL 1100°C
15	ball milled 8h powder
16	ball milled 8h RS
17	SPS BM1 80MPa
18	ball milled 20h PL 950°C
19	ball milled 20h PL 1100°C
20	ball milled 20h powder
21	ball milled 20h RS
22	SPS BM2 80MPa

(a) Principal Components Analysis



(b) Dendrogram

Figure 7.26: Cluster analysis of XRD spectra of spark plasma sintered MgB_2 samples, with starting powders, and bulks produced by resistive sintering and pressureless heat-treatment included for comparison.

7.2.4 Microscopy

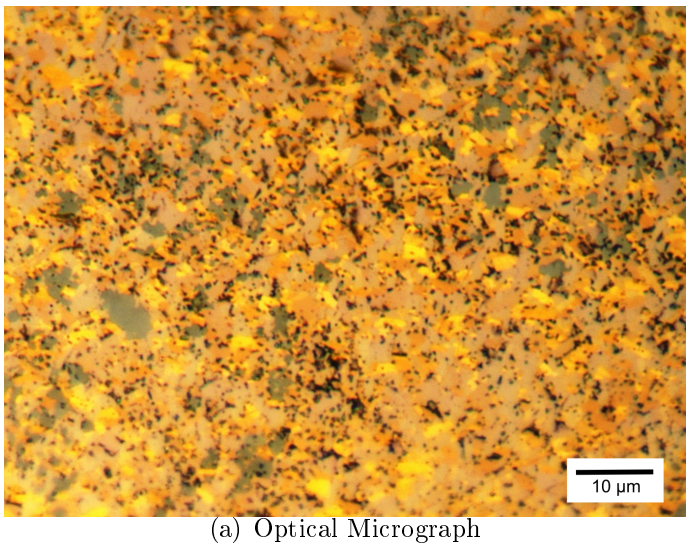
Optical and polarised light optical microscopy was carried out on polished sections of the spark plasma sintered samples. It was observed that samples which consisted of dense MgB_2 polished easily and attained a golden lustre. The sample prepared from powder

ball milled for 20 h in isopropanol and heat-treated at 1350 °C was the only sample which contained large amounts of MgO. When polished, this sample was dark grey in colour. The sample prepared from as-purchased MgB_2 spark plasma sintered in argon gas was not dense enough to withstand the polishing process.

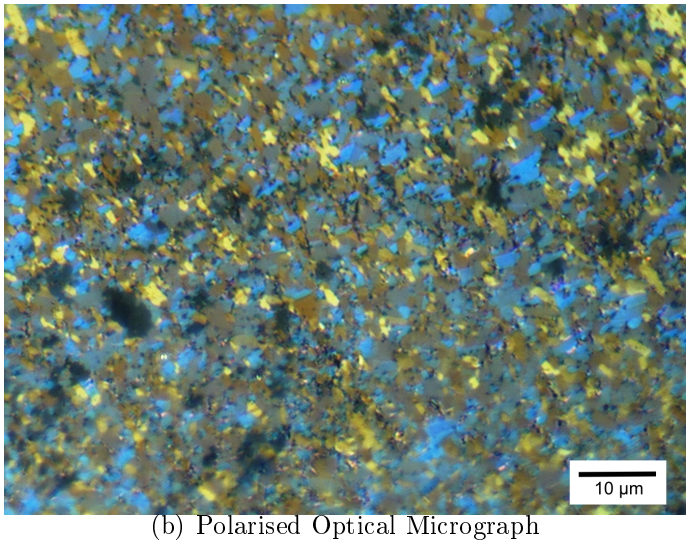
Figures 7.27, 7.28, and 7.29 show optical micrographs and the equivalent polarised light optical micrographs from the same regions for samples prepared by spark plasma sintering of as-purchased powder under increasing pressure. The polarised optical micrographs indicate that the grain size of the sample prepared under the lowest pressure (16 MPa) is around $2-3\,\mu$m in diameter. The grain sizes of the pellets prepared under higher pressure are smaller at around $1\,\mu$m in diameter. The grains are elongated in shape, similar to those observed in HIPed samples by Mikheenko *et al* [165]. This trend is commensurate with that of density for this set of samples. The density is high but some pores are still seen; this may be due to grain pull-out during polishing rather than to true porosity. It is certainly the case that these samples have undergone a great deal of sintering, particularly in comparison to the samples prepared by pressureless heat-treatment, developing a dense, well-connected microstructure.

Figure 7.30 shows optical micrographs and equivalent polarised optical micrographs for samples produced by spark plasma sintering of powder ball milled for 8 h in isopropanol. Two distinct regions were observed (see Figure 7.30a). The polarised optical images reveal that the two regions have similar grain size (note that scales of the two images are different) of around $2\,\mu$m in diameter. However Region 2 contains more porosity than Region 1, indicating that the sample is somewhat inhomogeneous.

The spark plasma sintered sample prepared from MgB_2 powder ball milled for 20 h in isopropanol had a very different appearance to that of the other samples. The pellet appeared grey/white in the optical image, and contained little colour variation in the polarised optical micrograph (Figure 7.31). The grain size is much more inhomogeneous with some large grains of around $8\,\mu$m clearly visible with smaller grains between them. This sample had a very high MgO content (83.8 wt.%) in comparison to the samples

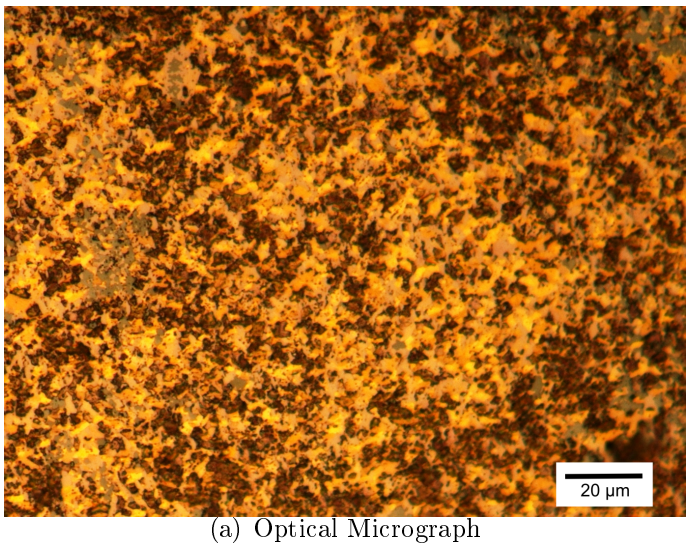


(a) Optical Micrograph

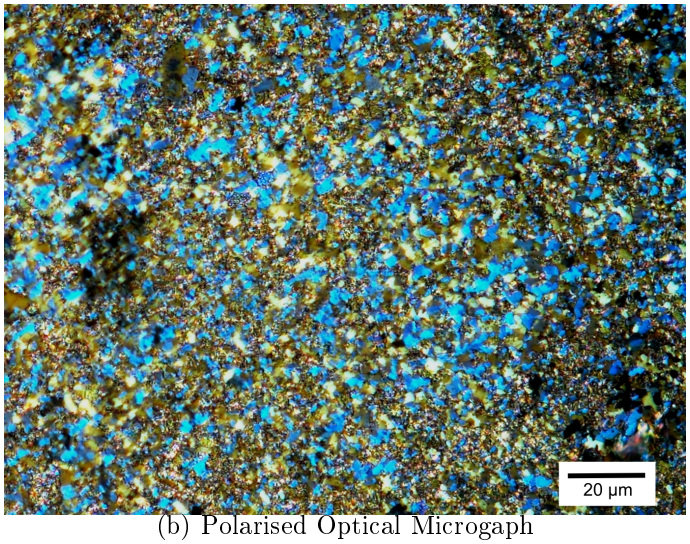


(b) Polarised Optical Micrograph

Figure 7.27: Optical and polarised-optical micrographs for spark plasma sintered sample produced from as-purchased MgB_2 at 80 MPa pressure. Images are of the polished top surface of the sample.

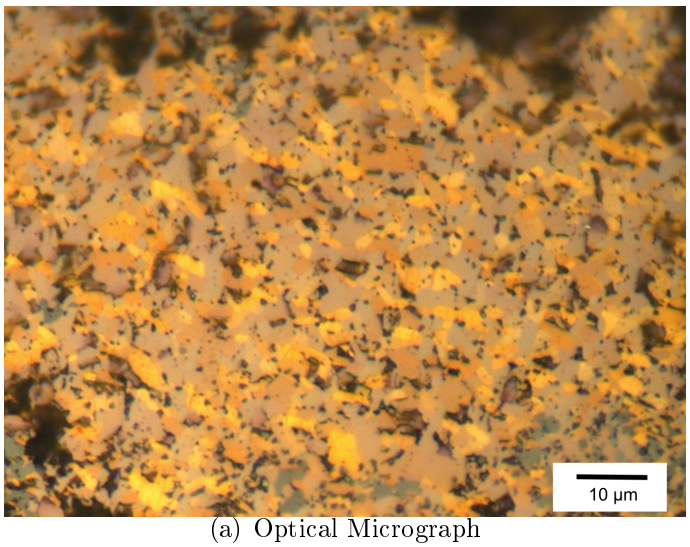


(a) Optical Micrograph

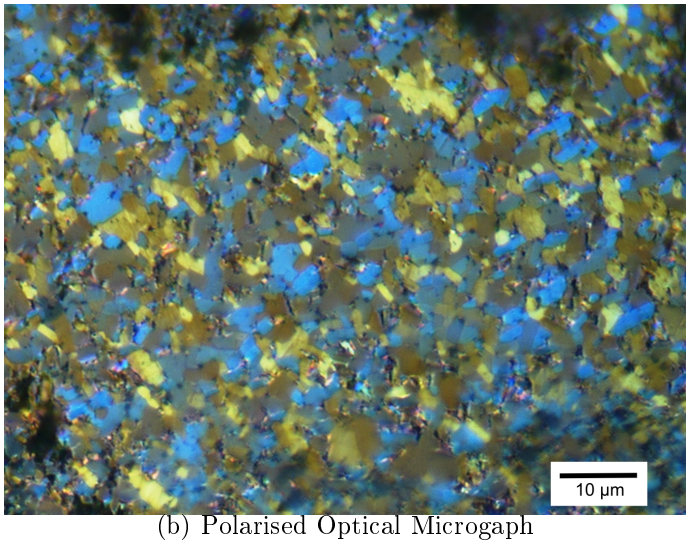


(b) Polarised Optical Micrograph

Figure 7.28: Optical and polarised-optical micrographs for spark plasma sintered sample produced from as-purchased MgB_2 at 50 MPa pressure. Images are of the polished top surface of the sample.

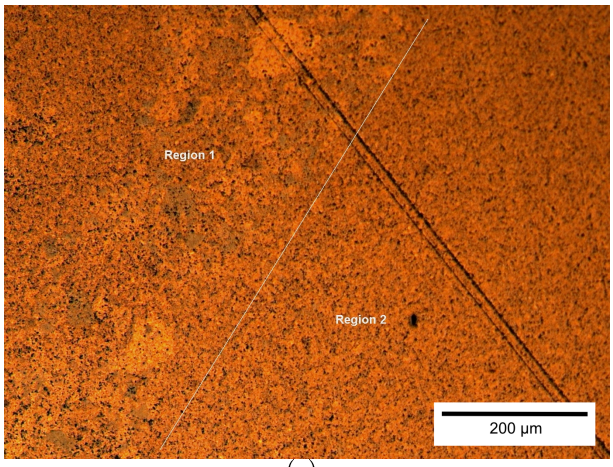


(a) Optical Micrograph

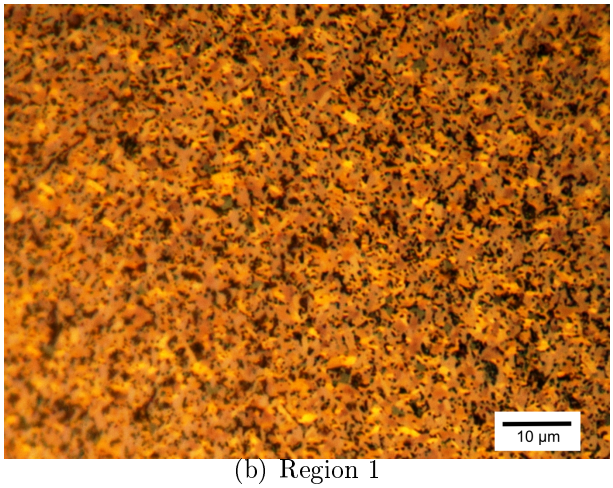


(b) Polarised Optical Micrograph

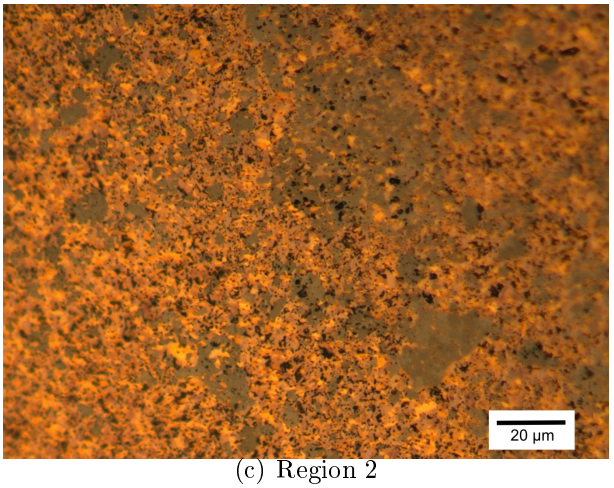
Figure 7.29: Optical and polarised-optical micrographs for spark plasma sintered sample produced from as-purchased MgB_2 at 16 MPa pressure. Images are of the polished top surface of the sample.



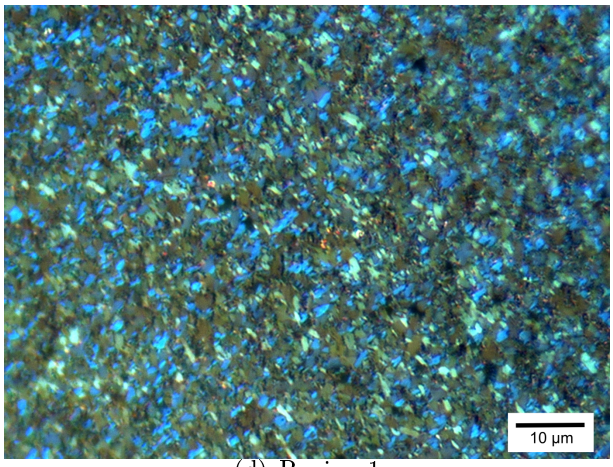
(a)



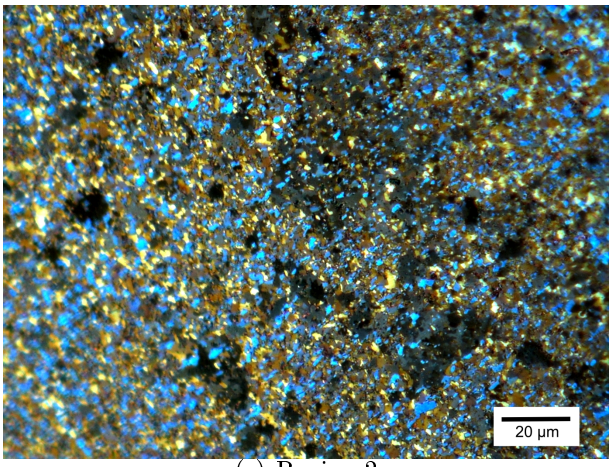
(b) Region 1



(c) Region 2



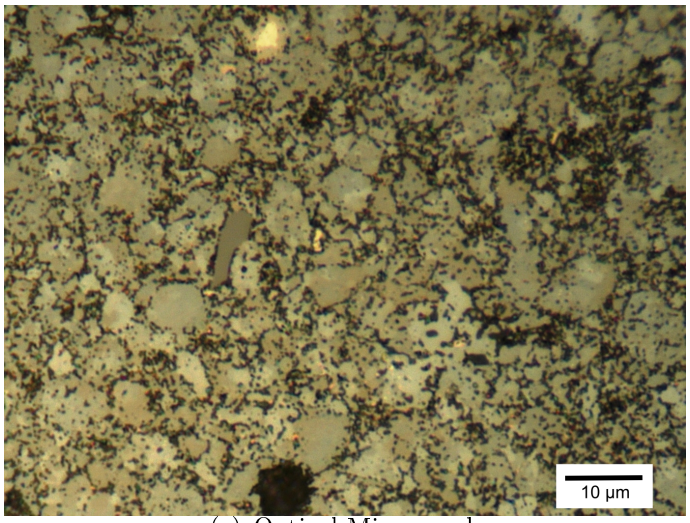
(d) Region 1



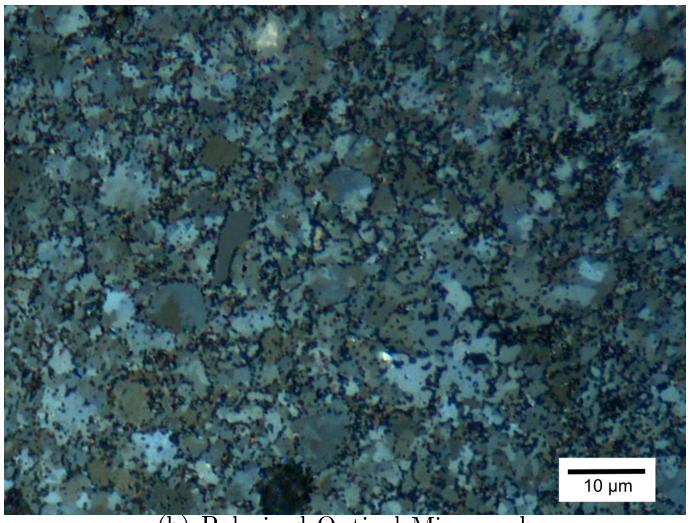
(e) Region 2

Figure 7.30: Optical and polarised-optical micrographs for spark plasma sintered sample produced from MgB_2 powder ball milled for 8 h and heat-treated at 50 MPa pressure. Images are of the polished top surface of the sample.

produced from as-purchased MgB_2 (see Table 7.3 on page 255).



(a) Optical Micrograph



(b) Polarised Optical Micrograph

Figure 7.31: Optical and polarised-optical micrographs for spark plasma sintered sample produced from MgB_2 powder ball milled for 20 h and heat-treated at 1350 °C and 50 MPa pressure. Images are of the polished top surface of the sample.

In addition to the optical micrographs, SEM images were taken of fracture surfaces of the spark plasma sintered samples. Figure 7.32 shows these images for the samples prepared from as-purchased MgB_2 powder by spark plasma sintering in vacuum. The samples heat-treated under 50 MPa and 80 MPa pressure are dense and consist of well connected grains with a few small spherical particles on the surfaces. These images are similar to those of Tampieri *et al* [158] for hot pressed bulk MgB_2 (see Figure 2.8). The

grains appear faceted and slightly elongated. The sample heat-treated under the minimum pressure of 16 MPa has a completely different appearance, consisting of rounded smooth regions with the appearance of partially sintered particles. It appears that densification has not completed for this sample, in line with the data for the density and hardness measurements compared to the samples prepared under higher pressures. This indicates the critical importance of the pressure in the production of dense MgB_2 bulk material.

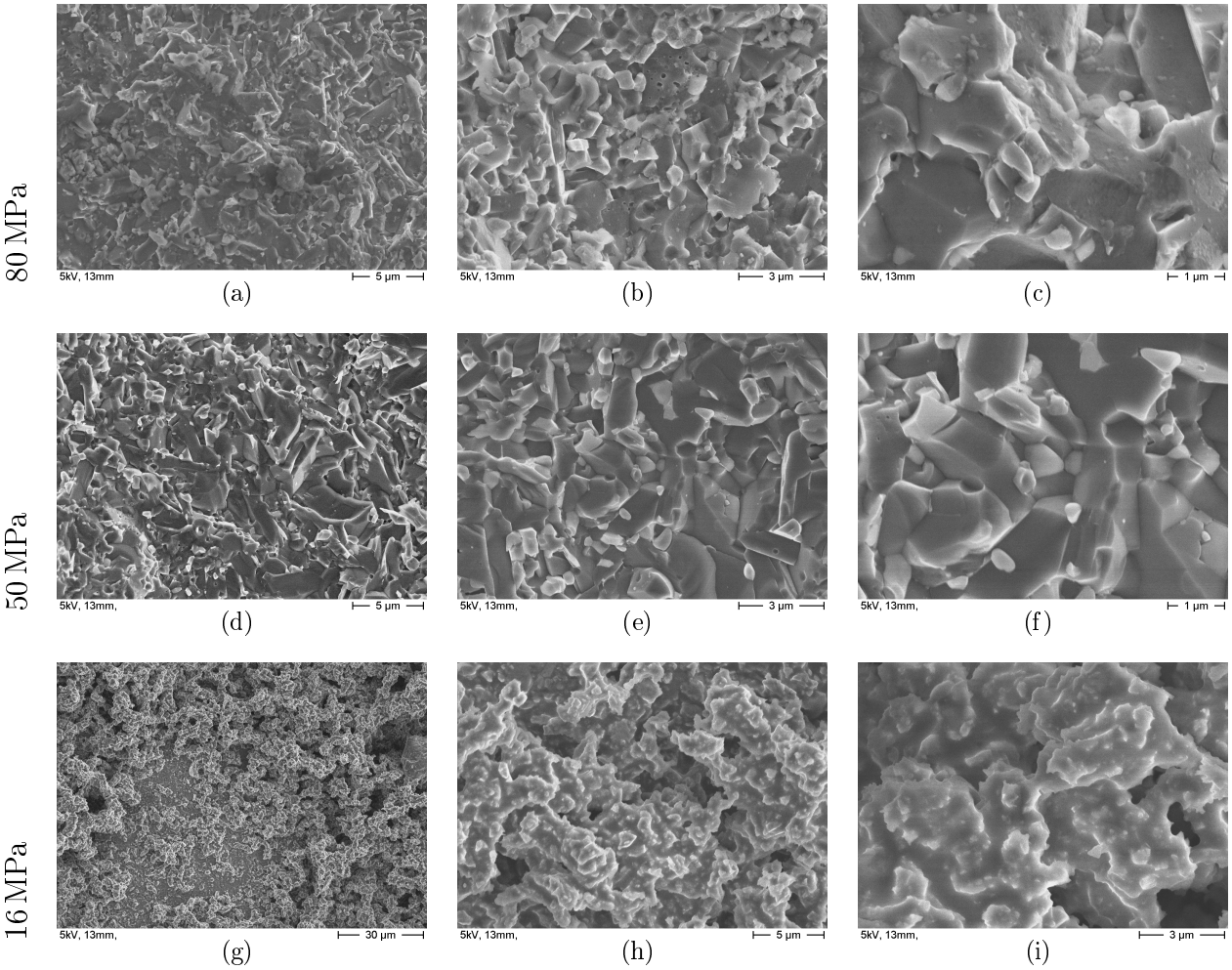


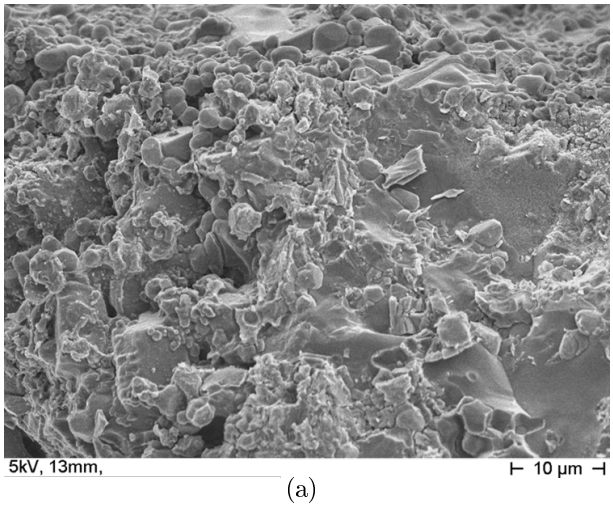
Figure 7.32: SEM images of fracture surfaces of the spark plasma sintered samples produced in vacuum from as-purchased MgB_2 powder

Figure 7.33 shows the SEM images of the fracture surface of the sample prepared from as-purchased MgB_2 powder spark plasma sintered in argon gas. This sample was highly inhomogeneous, as shown in Figure 7.33a. Some regions are smooth and densified (Figure 7.33b) while others are porous and powder-like (Figures 7.33c and 7.33d). Another region

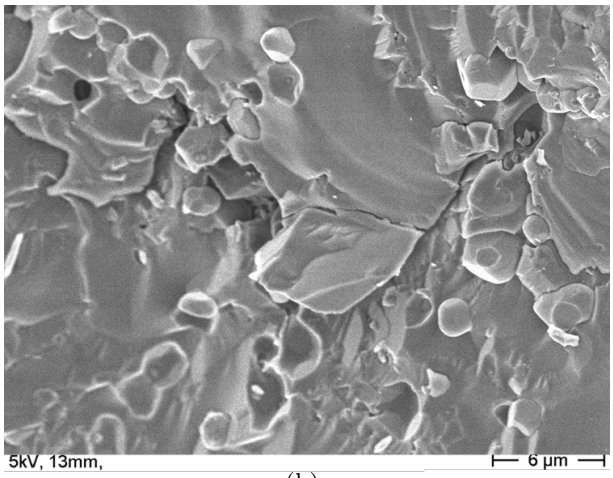
is smooth but contains many rounded holes (Figure 7.33e). This is due to the reaction during heat-treatment which caused the formation of a large quantity of Mg vapour which then formed MgO (71.6 wt.%, see Section 7.2.3). The inhomogeneity also explains the variation in the hardness data, with hard regions of around 500 HV/2, and soft regions similar to the sample prepared by pressureless heat-treatment at around 50 HV/2.

SEM images of the sample prepared by spark plasma sintering of powder ball milled for 8 h in isopropanol were difficult to obtain because the sample charged significantly, probably due to non-conducting impurities. The images obtained are shown in Figure 7.34. The sample is not as porous as those prepared by resistive sintering or pressureless heat-treatment of the same powder, with well connected grains. Some of these are elongated like those of the samples prepared from as-purchased MgB_2 powder by spark plasma sintering in vacuum. These grains can be seen in Figure 7.34c for this sample.

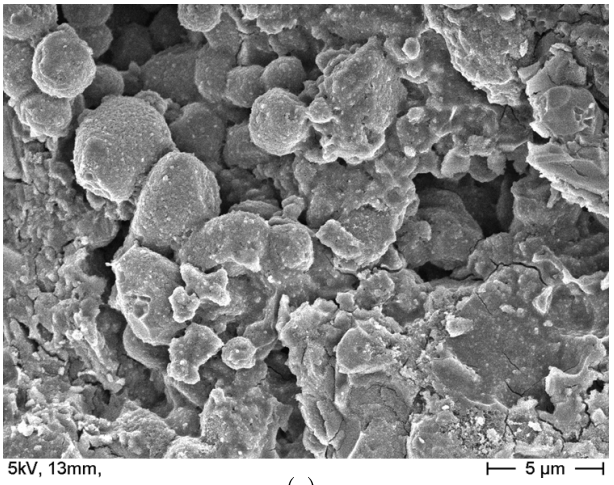
The SEM images (Figure 7.35) of the sample prepared by spark plasma sintering of MgB_2 powder which was ball milled for 20 h in isopropanol indicate that the surface is still rather porous, but contains regions where particles are clearly linked together. In addition, the spherical particles which have been seen in other samples with high measured MgO content are observed. Overall the sample appears well consolidated and this accounts for its high hardness and density despite the low MgB_2 content of the sample, which has an MgO content estimated at 83.8 wt.%. Comparison to the hardness of pure MgO is uninstructive due to the composite nature of these samples, and the well-established effects of hardness measuring technique, grain size, and porosity on hardness values.



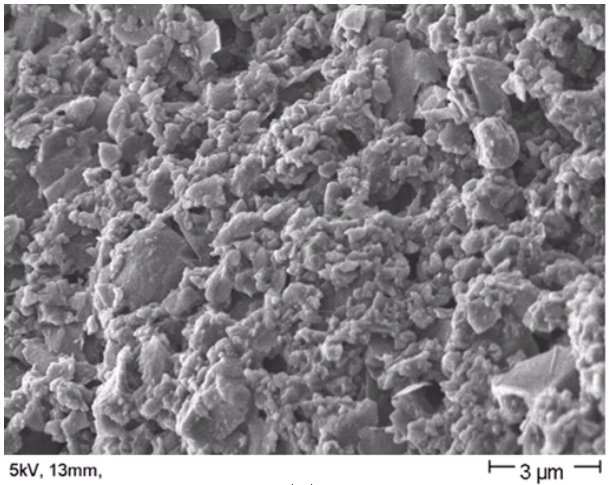
(a)



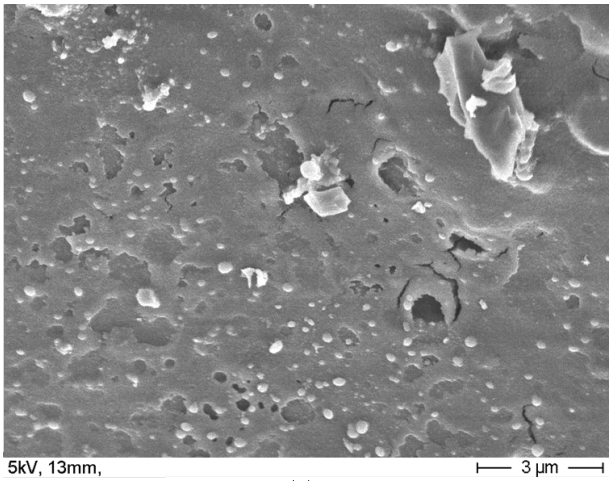
(b)



(c)

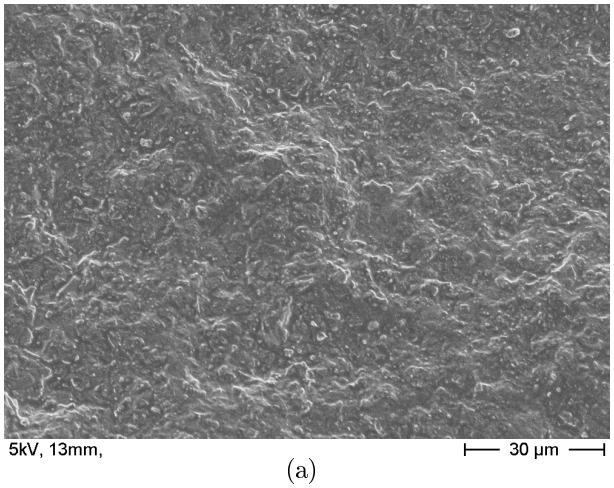


(d)

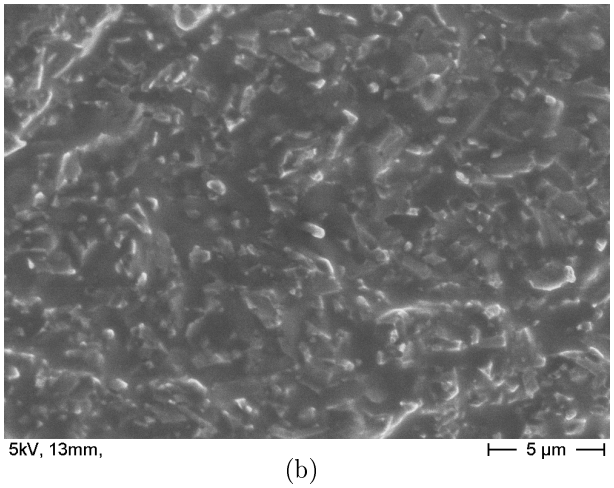


(e)

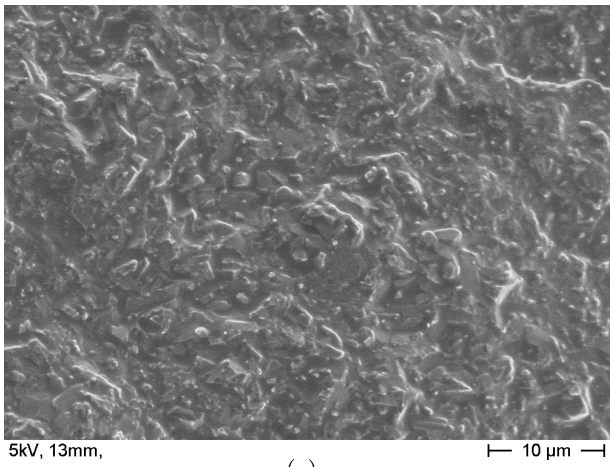
Figure 7.33: SEM images of fracture surface of the spark plasma sintered samples produced in Ar gas from as-purchased MgB_2 powder



(a)

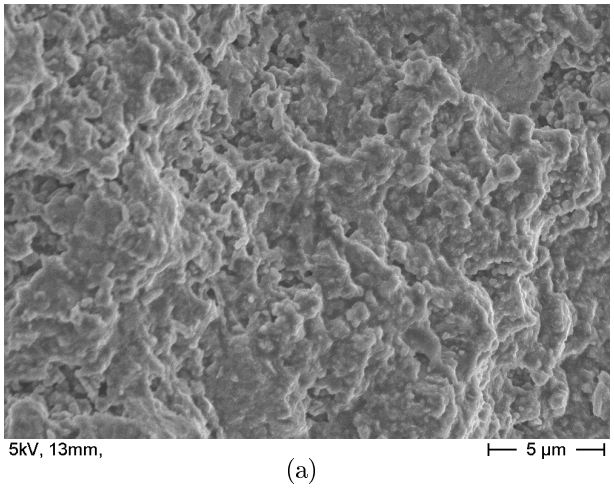


(b)

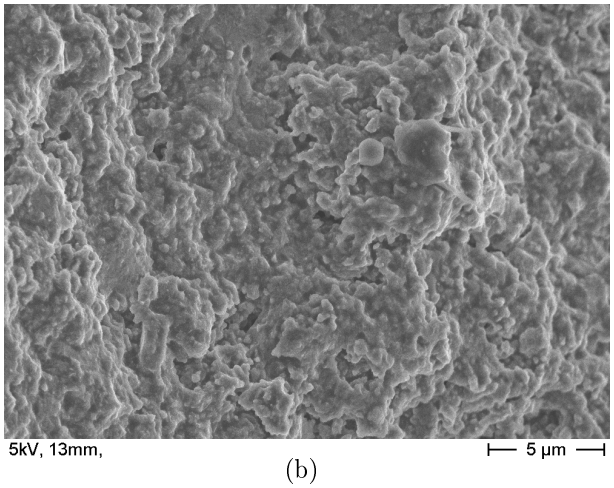


(c)

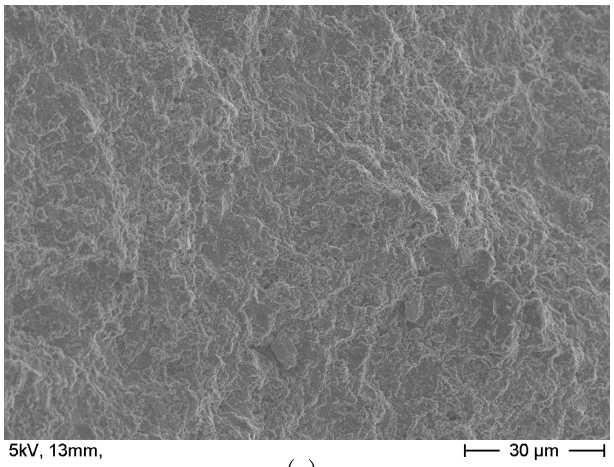
Figure 7.34: SEM images of fracture surface of the spark plasma sintered samples produced from MgB_2 powder ball milled for 8 h



(a)



(b)



(c)

Figure 7.35: SEM images of fracture surface of the spark plasma sintered samples produced from MgB_2 powder ball milled for 20 h

7.3 Hot Pressing

The hot press used was at the University of Oxford, and is a home-built rig. The hot press was out of action for much of the period during which I required it, and this is one reason why alternative processing techniques were sought at other institutions. In addition, as the hot press operates using argon gas, rather than vacuum, I was unsure whether it would give good results. For this reason only one sample was produced, using as-purchased MgB_2 powder, in order to compare a sample heat-treated under moderate pressure (30 MPa) in argon gas with the samples produced at various pressures in vacuum or argon using the spark plasma sintering or resistive sintering techniques.

Unlike the other two facilities used, the hot press does not have in-built monitoring equipment. The pressure was applied in three stages during the heat-up until it reached 30 MPa. The temperature was increased to approximately 1250 °C over the course of approximately 30 min as measured by a thermocouple placed close to the die wall. The hot press was then held under these conditions for approximately 30 min.

The pellet produced under these conditions appeared to be very dense MgB_2, with a light brown appearance, very similar in appearance to the sample produced by spark plasma sintering of as purchased MgB_2 powder in vacuum at 1250 °C. This indicates that using argon in the hot press did not seem to result in excessive formation of MgO unlike with the spark plasma sintering. This may be due to the fact that the hot press is open to the atmosphere, allowing the removal of volatile impurities and vapor more easily than in the pressurised environment of the spark plasma sintering furnace.

7.3.1 Density

The density of the hot pressed material was measured as previously using Archimedes' method, and the resulting measurement is plotted in Figure 7.36 along with the measured values for other samples produced from as-purchased MgB_2 powder by spark plasma sintering (in vacuum and in argon), pressureless heat-treatment in argon, and resistive

sintering in vacuum. The density varies significantly between these samples. The hot pressed sample has a similar density to that of the sample prepared by spark plasma sintering in vacuum with lowest pressure (16 MPa). There is a clear difference between the samples prepared with some applied pressure, and the samples prepared with no pressure applied, even at a high temperature of 1100 °C. In the spark plasma sintered samples where we have detailed information on the process of densification of the material, the initial decrease in ram displacement occurs when the pressure is applied. The subsequent densification occurs at and above 1000 °C, indicating that the temperature for the densification with pressure applied is close to the temperature attained during pressureless heat treatment.

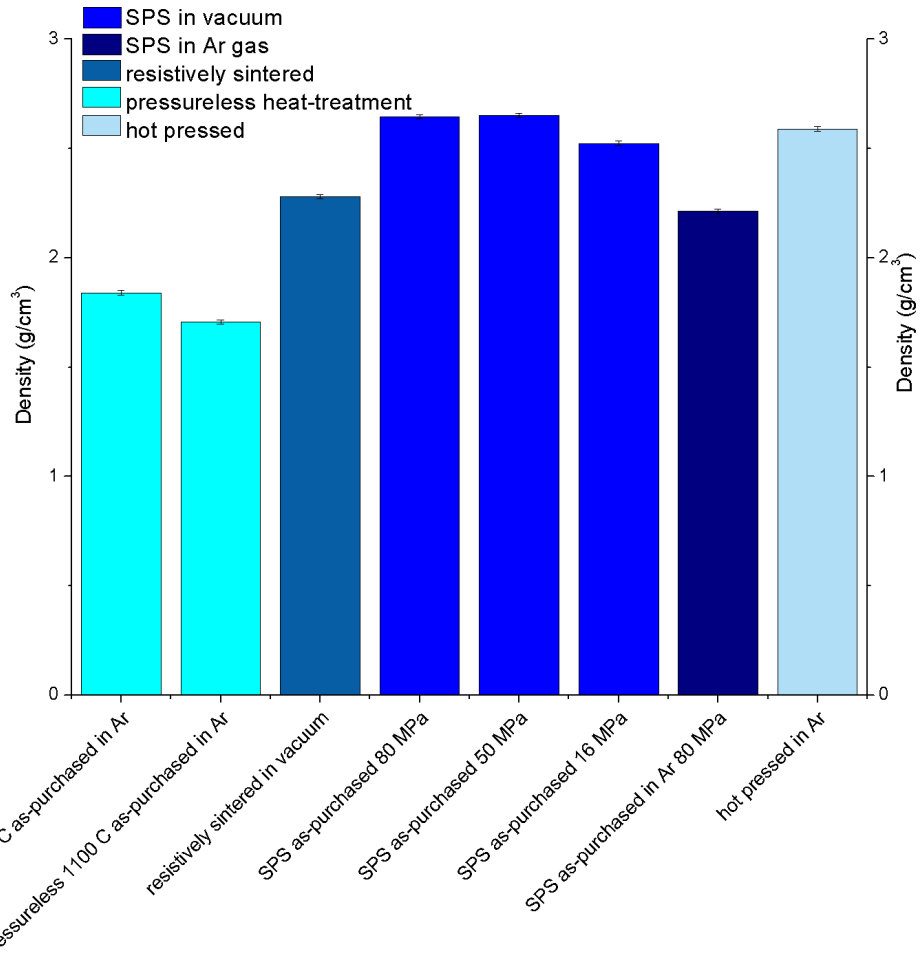


Figure 7.36: Density of MgB_2 bulks produced from as-purchased MgB_2 powder produced by all heat-treatment methods used in this work.

7.3.2 Hardness

The hardness of the hot pressed pellet was measured using a Vickers indenter, and is again similar to the hardness of the spark-plasma sintered sample produced at 16 MPa pressure in vacuum (see Figure 7.37). The hardest pellet prepared in this work was the resistively sintered pellet. This is not consistent with the density of the sample, which was lower than that for the spark plasma sintered sample. The explanation for this is not clear. It may be a size effect due to the very large difference in diameter and volume between the small pellets produced by resistive sintering (5 mm diameter, approximately $1-2$ mm height) and the larger ones produced by pressureless heat-treatment (9 mm diameter, $3-4$ mm height), spark plasma sintering (20 mm diameter, $2-3$ mm height) and hot pressing (25 mm diameter, 3 mm height). In particular, as the resistive sintered sample was produced in a graphite die, the region into which carbon may have diffused is a significantly larger proportion of the sample volume than for the other samples produced in graphite dies, and this may have affected the hardness and or the density for this material. In addition the error in the density is higher for the smaller pellets as the error in the measurement is a greater fraction of the total measured masses.

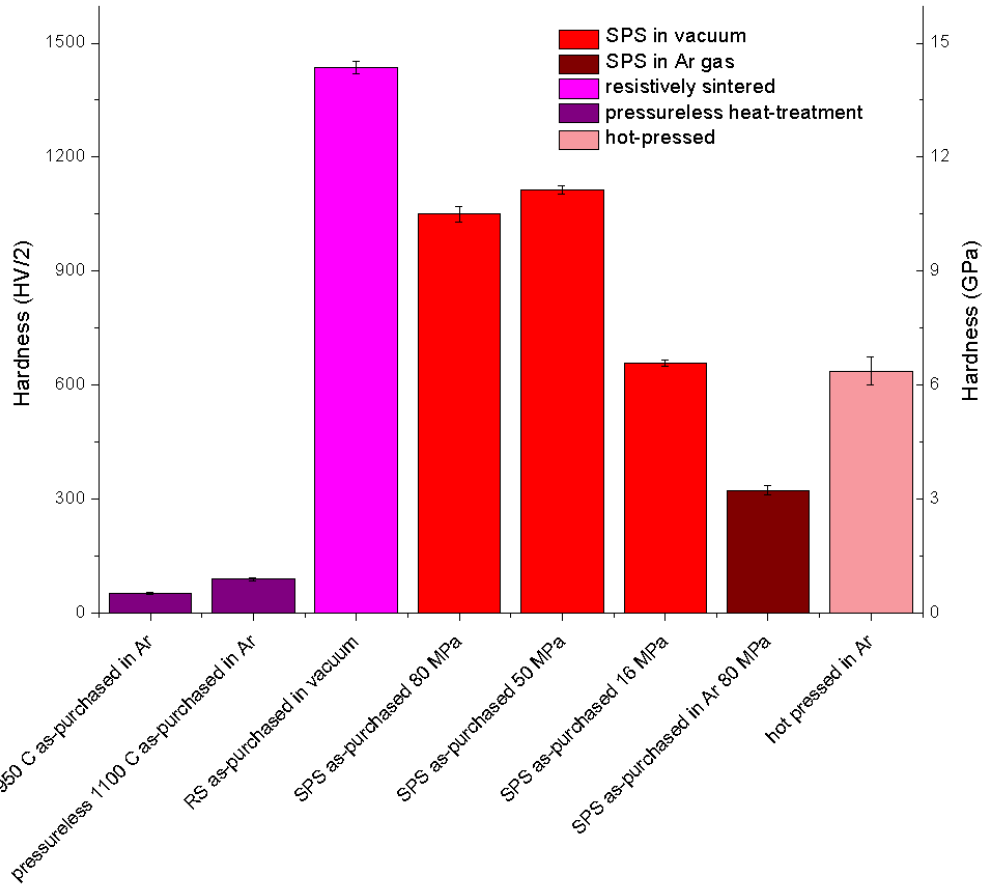


Figure 7.37: Hardness of MgB_2 bulks produced from as-purchased MgB_2 powder produced by all heat-treatment methods used in this work.

A comparison of the hardness and density has been made for all samples produced from as-purchased MgB_2 in this work (Figure 7.38). As can be seen, there is a very strong correlation between hardness and density for all these MgB_2 bulk samples. A similar relationship was also observed by Mukhopadhyay *et al* [223] for sialon and silicon nitride samples.

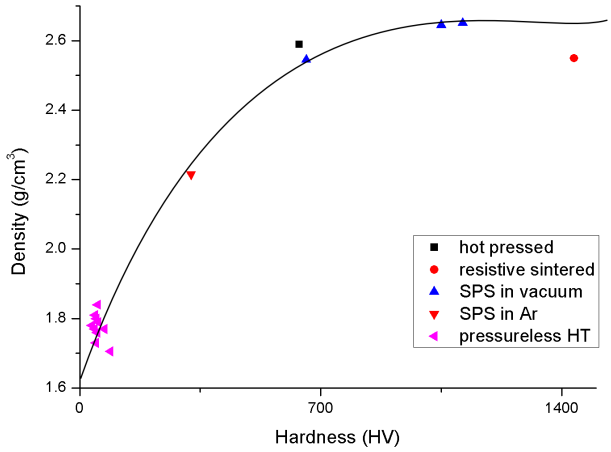


Figure 7.38: Correlation of hardness and density for bulk material produced from as-purchased MgB_2 powder

7.3.3 Impurity Content

The impurity content of the hot pressed sample was also measured using XRD $\theta - 2\theta$ analysis. Figure 7.39 shows the spectrum of the hot pressed sample, with the spectra for the starting powder, and the bulk samples made from the same powder by resistive sintering, spark plasma sintering and pressureless heat-treatment included for comparison. The XRD spectrum of the hot pressed sample has only peaks due to MgB_2, MgB_4 and MgO. The spectrum is again very similar to the sample produced by spark plasma sintering under 16 MPa pressure. The MgO content was measured from the peak area ratio as described in Chapter 4, and the hot pressed sample has a lower MgO content than all of the other samples produced under pressure at 6.0 wt%, though this is still higher than the MgO content of the sample produced by pressureless heat-treatment at 950 °C. The MgO contents of samples produced from as-purchased MgB_2 powder are given in Table 7.5. There is no correlation of density and MgO content.

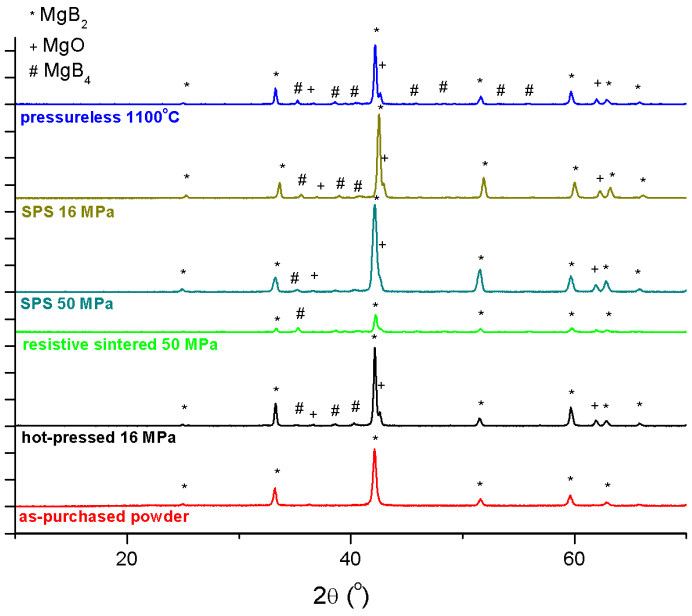


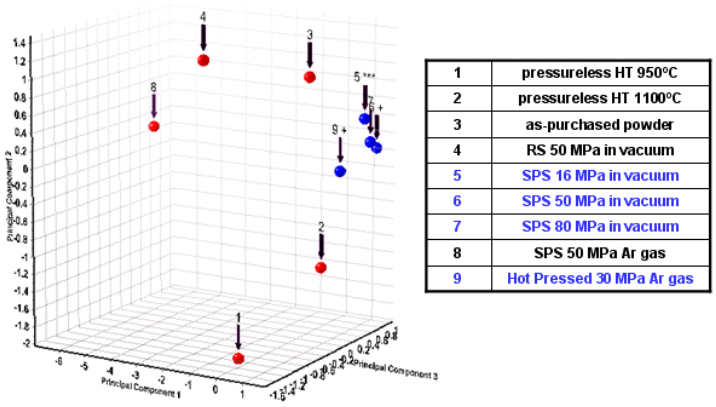
Figure 7.39: XRD spectrum for the hot pressed pellet produced from MgB_2 powder. The spectra for the starting powder, the spark plasma sintered pellets produced at 50 MPa and 16 MPa, the resistively sintered pellet, and the pressureless sintered pellets heat-treated at 950 °C and 1100 °C produced from the same powder are included for comparison.

Table 7.5: MgO content of bulk MgB_2 samples produced from as-purchased powder

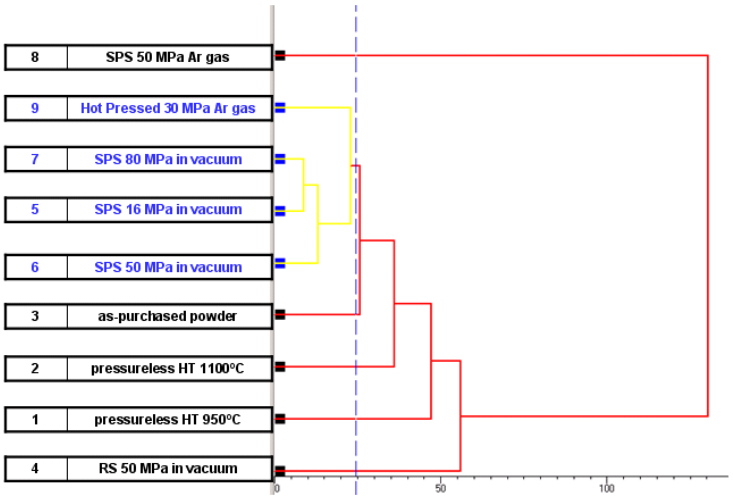
Sample	MgO Content (as wt.% of MgB_2 content)	Density (g/cm^3)
SPS in Vacuum, 80 MPa	8.2	2.65
SPS in Vacuum, 50 MPa	7.3	2.65
SPS in Vacuum, 16 MPa	8.6	2.52
SPS in Argon Gas	71.6	2.21
Resistive Sintered in Argon Gas	7.8	2.28
Pressureless Heat-Treated at 950 °C	5.1	1.84
Pressureless Heat-Treated at 1100 °C	7.3	1.71
Hot Pressed	6.0	2.59

A cluster analysis was carried out using the XRD spectra of the samples produced from as-purchased MgB_2 in this work. The principal components analysis and the cluster

analysis are shown in Figure 7.40. The only cluster formed (blue) consists of the XRD spectra of the three spark plasma sintered samples prepared in vacuum with the hot pressed sample, as would be expected from the calculated MgO contents.



(a) Principal Components Analysis



(b) Dendrogram

Figure 7.40: Cluster analysis of XRD spectra of MgB_2 samples including hot pressed MgB_2 bulk

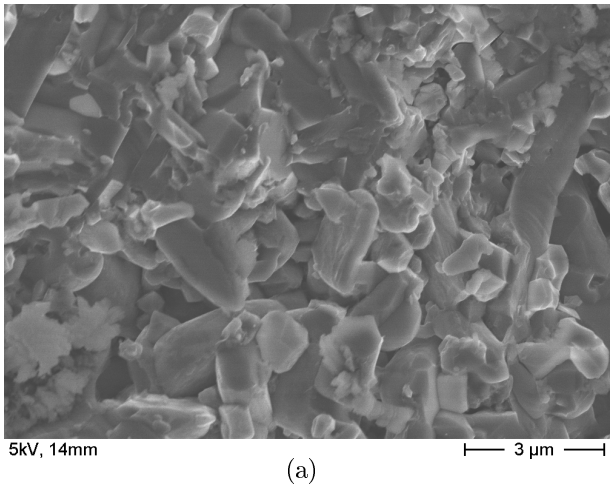
7.3.4 Microscopy

The hot pressed pellet was fractured and examined using SEM. In this case, the fracture surface is more similar to one of the spark plasma sintered sample heat-treated under high pressure, and quite unlike the sample heat-treated at the lowest pressure. The grains are mostly elongated with sharp angular connections between grains (Figure 7.41c). The

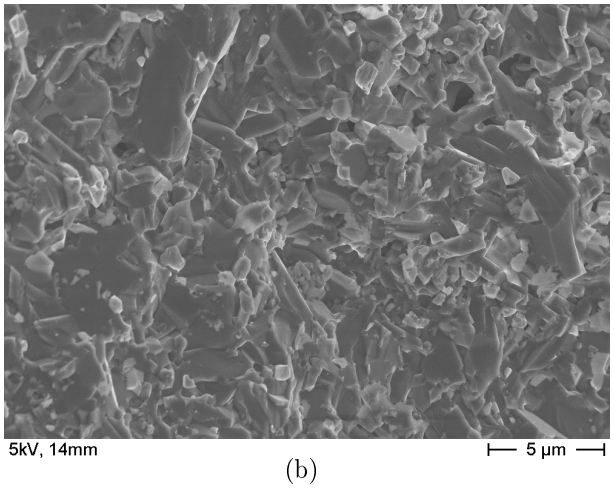
sample appears more porous than the spark plasma sintered sample prepared at 50 MPa or above. Some spherical particles (thought to be due to impurity phase formation) are visible in Figure 7.41a. The inhomogeneous structure of the fracture surface is demonstrated by Figure 7.41b. Overall these images are again similar to those of Tampieri *et al* [158] for hot pressed MgB_2 (see Figure 2.8 on page 39).

7.4 Summary

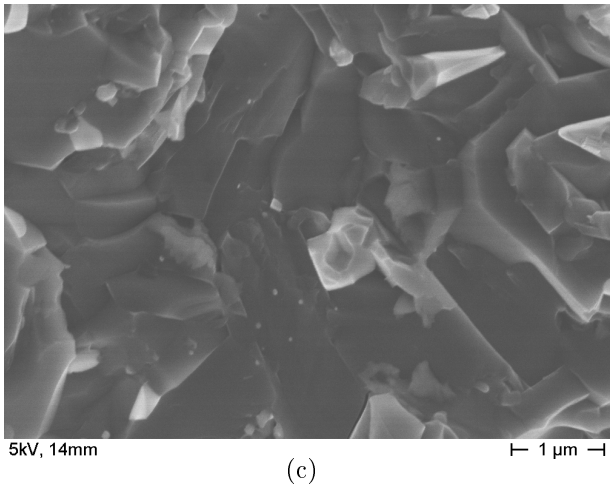
Heat-treatment combined with the application of pressure produces dense MgB_2. The densest samples were produced using spark plasma sintering with applied pressure $>$ 50 MPa and by hot pressing at 30 MPa. Impurity content was generally low ($<$ 10 wt.% MgO) for samples produced from as-purchased Alfa Aesar MgB_2. Some of the bulk samples, particularly those produced from the attrition milled powder and the powder ball milled for 20 h in isopropanol/air contained very high MgO content. As this was also seen in samples prepared from these powders by pressureless heat-treatment (Chapter 6) this is probably due to the formation of an amorphous compound which forms MgO during heat-treatment. The densest samples were also those with the lowest impurity content, indicating that careful control of the starting powder is necessary to obtain dense MgB_2 with low impurity content.



(a)



(b)



(c)

Figure 7.41: SEM images of fracture surface of the hot pressed sample produced in Ar gas from as-purchased MgB_2 powder

8 Conclusions and Suggestions for Further Work

8.1 Conclusions

I have shown that as-purchased Alfa Aesar MgB_2 powder is highly agglomerated, and the measurement of particle size depends strongly on the degree of dispersion carried out prior to examination. This has not previously been demonstrated by other studies. The powder can be de-agglomerated using ultrasound to give a reasonably fine size distribution. Variation of agglomeration and particle size between batches of Alfa Aesar MgB_2 powder is likely to account for some of the variation in results between research groups working on similar samples. Drying of MgB_2 powders by evaporation following long exposure to isopropanol leads to the formation of harder agglomerates than in the starting powder, which could not be easily broken up by ultrasonication.

Without careful protection during heat-treatment the impurity content of MgB_2 artefacts can reach very high levels, even during heat-treatment at relatively modest temperatures. Using a protective MgB_2 powder bed this can be kept down to around 5 wt.% for heat-treatment at 950 °C (typically used for *ex situ* PIT wires), or 7 wt.% for heat-treatment at 1100 °C.

XRD can be used to assess the MgO content of MgB_2 following calibration. The detection limit of MgO content is 5 wt.% using this method. EDX can only be used to accurately measure the MgO content of samples where the MgO is distributed homoge-

neously through the sample, otherwise the errors are too large to differentiate the two phases. It is difficult to distinguish between the three magnesium-containing materials most commonly found in these samples; MgB_2, MgO and MgB_4, because of difficulties in the detection of light elements.

Pressureless heat-treatment of MgB_2 at temperatures up to 1100 °C resulted in very limited sintering. An increase in hardness was observed, but this was not accompanied by a change in density, indicating that sintering was in its very early stages. Samples produced by pressureless heat-treatment had high $J_{c,mag}$ at low magnetic fields, but poor flux pinning and connectivity meant $J_{c,mag}$ decreased rapidly with increasing applied magnetic field.

Modification of MgB_2 powder is difficult because the powder is sensitive to exposure to dispersing solvents, and the powder agglomerates readily. Attrition milling resulted in contamination by ZrO_2, but ball milling did not, even when milling was carried out for 20 h. Many of the dense bulk samples produced from modified powders had high impurity content, and the densest samples were those which had the lowest impurity content.

Samples produced from MgB_2 powder modified by attrition milling increased in density during pressureless heat-treatment at all temperatures. However, as the MgO content increased considerably for all heat-treatment temperatures, it is difficult to separate the effect of the change in particle size on the densification from the that due to the reaction to form MgO. The green density of these samples was around 64 % of the theoretical density of MgB_2, while the density after heat-treatment was $70 - 77$ % of the theoretical density of MgB_2/MgO (calculated based on the composite density according to the MgO content from XRD measurements). For samples pressureless heat-treated at 1100 °C, $H_{c2}(4\,\mathrm{K})$ increased from 4.2 T for bulk produced from as-purchased MgB_2 to 6.6 T for bulk produced from attrition milled MgB_2. This is indicative of a true increase in connectivity in the material.

By combining the results for pressureless and pressure-assisted heat-treatments, a clear correlation between hardness and density has been established for MgB_2 samples. This

will be invaluable for assessing density in composite materials such as PIT wires, where the density is difficult to measure accurately by Archimedes' method due to the presence of the metal sheath.

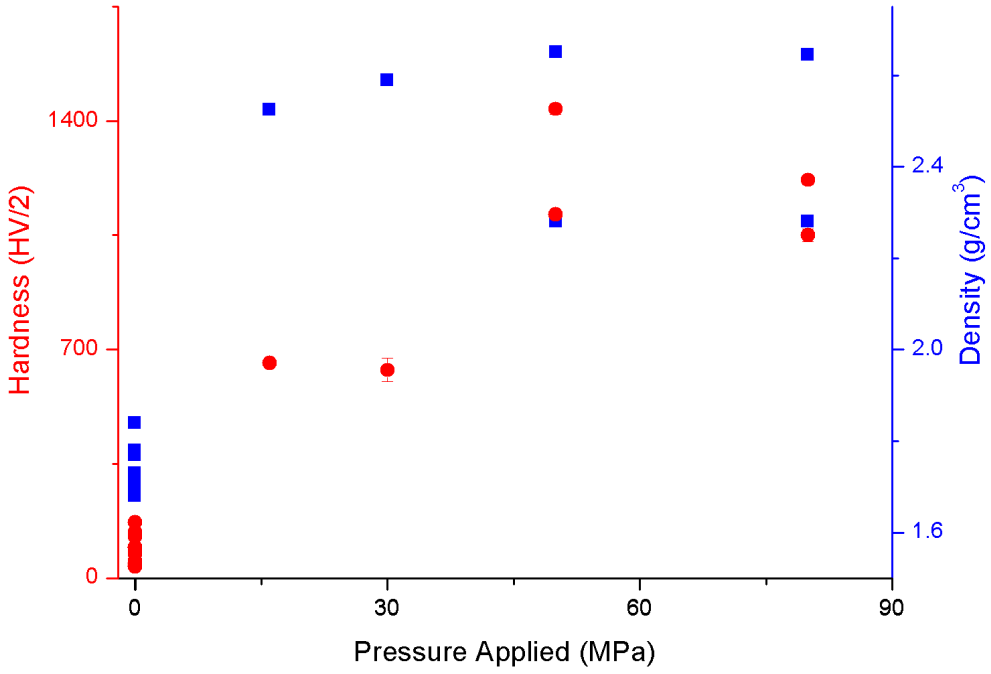


Figure 8.1: Pressure versus density and hardness for a range of samples prepared in this work consisting of ≤20 wt.% MgO

A plot of pressure versus both hardness and density for all samples is shown in Figure 8.1, and indicates a clear correlation; application of high pressure during heat-treatment leads to high hardness and density. The correlation of high density and good superconducting properties has been established by the work of other research groups. For example, Shim *et al [146]* produced dense MgB_2 bulk by spark plasma sintering with $J_{c,mag} = 5 \times 10^5\,\mathrm{A/cm^2}$ at 5 K and 1 T, more than one order of magnitude higher than that of pressureless heat-treated samples produced in this work, which achieved $J_{c,mag} = 3 \times 10^4\,\mathrm{A/cm^2}$ under the same conditions. A similar plot of temperature versus both hardness and density (Figure 8.2) shows no correlation (samples with very high MgO content have been excluded from these analyses). This indicates that the application

of high pressure during heat-treatment is critical and leads to highly dense MgB_2 bulk material with a small grain size, which is important for obtaining good superconducting properties as the high concentration of grain boundaries increases the flux pinning in high applied magnetic fields [159; 160]. Hot pressing causes an increase in the driving force for densification in ceramics, as the externally applied uniaxial pressure counters the internal pore pressure [50]. This means that dense material can rapidly be obtained. In the case of MgB_2 a rapid heat-treatment at as low a temperature as possible is crucial in order to prevent the formation of excessive impurity content, as magnesium is very volatile and reactive.

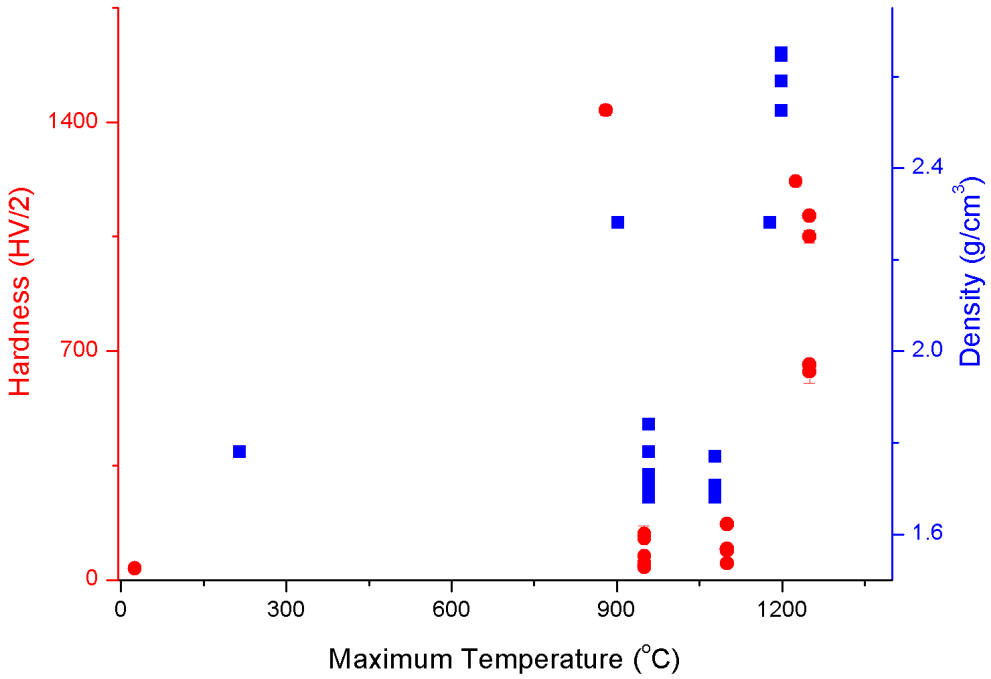


Figure 8.2: Temperature versus density and hardness for a range of samples prepared in this work consisting of ≤ 20 wt.% MgO. No real correlation is observed.

8.2 Further Work

Modified powders would be more useful if the impurity content could be minimised; in addition this would establish whether the enhancement in densification seen in the

samples produced from attrition milled MgB_2 powder was due to an increase in MgO content or to true densification due to reduced particle size. The effect of milling in liquid and non-liquid protective atmospheres should be established in order to achieve this. In addition, the use of drying techniques such as critical point drying should be investigated to decrease the degree of agglomeration in these powders. Alternatively, the production of MgB_2 bulk by slip casting would allow more extensive particle motion without drying the modified powders, reducing agglomeration and increasing bulk density.

Optimisation of heat-treatment schedules for the pressure-assisted methods may allow the growth of MgB_2 bulk with significantly smaller grain size. This will enhance flux pinning at high magnetic fields. In addition, careful experimentation coordinating the onset of sintering with the temperature would allow maximum sintering to occur whilst minimising the temperature and hence the impurity content. In-line monitoring of temperature, pressure and ram displacement is required in order to design the optimum process to produce dense MgB_2 with low impurity content. Understanding of the relationship between the heat-treatment temperature, pressure and duration by establishing the nature of the stress- and thermally-activated deformation mechanisms will aid the application of this work to PIT wires with optimised properties.

References

[1] Kamerlingh Onnes H. *Proceedings of the Koninklijke Nederlandse Akademie van Wetenschappen* **13**:p. 1274 (1912)

[2] Kamerlingh Onnes H. *Proceedings of the Koninklijke Nederlandse Akademie van Wetenschappen* **14**:p. 113 (1911)

[3] Kamerlingh Onnes H. *Proceedings of the Koninklijke Nederlandse Akademie van Wetenschappen* **14**:p. 818 (1912)

[4] Kamerlingh Onnes H. *Proceedings of the Koninklijke Nederlandse Akademie van Wetenschappen* **16**:p. 987 (1914)

[5] Young H., Freedman R. *University Physics.* Addison-Wesley Series in Physics, 9th ed. Addison-Wesley, Reading, Massachusetts (1996)

[6] Rose-Innes A., Rhoderick E. *Introduction to Superconductivity.* 2nd ed. Pergamon Press, Oxford (1978)

[7] Meissner W., Ochsenfeld R. *Naturwissenschaften* **21**:p. 787 (1933)

[8] Buckel W., Kleiner R. *Superconductivity: Fundamentals and Applications.* 2nd ed. Wiley-VCH, Weinheim (2004)

[9] Evetts J. (ed.). *Concise Encyclopedia of Magnetic and Superconducting Materials.* 1st ed. Pergamon Press, Oxford (1992)

[10] Cyrot M., Pavuna D. *Introduction to Superconductivity and High-Tc Materials.* 1st ed. World Scientific (1995)

[11] Sheahen T.P. *Introduction to High-Temperature Superconductivity.* Plenum Press, New York (1994)

[12] Goodrich L., Bray S. *Cryogenics* **30**:pp. 667 (August 1990)

[13] Wisniewski A., Puzniak R., Judek J., Krutzler C., Eisterer M., Weber H., Jun J., Kazakov S., Karpinski J. *Superconductor Science and Technology* **20**:p. 256 (2007)

[14] Bean C. *Reviews of Modern Physics* **36**:p. 31 (1964)

[15] Hsieh C., Chang C., Chang C., Sou U., Sheu H., Hsu H., Yang H. *Solid State Communications* **137**:p. 97 (2006)

[16] Kovac P., Husek I., Grovenor C., Salter C. *Superconductor Science and Technology* **16** (2):p. 292 (2003)

[17] Wang X.L., Soltanian S., James M., Qin M.J., Horvat J., Yao Q.W., Liu H.K., Dou S.X. *Physica C* **408-10**:p. 63 (2004)

[18] Waldram J. *Superconductivity of Metals and Cuprates.* 1st ed. IoP Publishing, Bristol, UK (1996)

[19] Bardeen J., Cooper L., Schrieffer J. *Physical Review* **106**:p. 162 (1957)

[20] Godeke A., Cheng D., Dietderich D., Ferracin P., Prestemon S., Sabbi G., Scanlan R. *IEEE Transactions on Applied Superconductivity* **17** (2):pp. 1149 (2007)

[21] Bednorz J., Muller K. *Zeitschrift fur Physik B - Condensed Matter* **64**:p. 189 (1986)

[22] Vase P., Flukiger R., Leghissa M., Glowacki B. *Superconductor Science and Technology* **13**:p. R71 (2000)

[23] American Superconductor . *http://www.amsc.com* (accessed 1st April 2008)

[24] THEVA . *http://www.theva.com* (accessed 1st April 2008)

[25] SuperPower . *http://www.superpower-inc.com* (accessed 1st April 2008)

[26] Solozhenko V.L., Turkevich V.Z., Holzapfel W.B. *Journal of Physical Chemistry B* **103** (38):p. 8137 (1999)

[27] Sundaram V., Logan K.V., Speyer R.F. *Journal of Materials Research* **12** (10):p. 2657 (1997)

[28] Gillan E.G., Kaner R.B. *Chemistry of Materials* **8** (2):p. 333 (1996)

[29] Nagamatsu J., Nakagawa N., Muranaka T., Zenitani Y., Akimitsu J. *Nature* **410** (6824):p. 63 (2001)

[30] Yamamoto A., Takao C., Masui T., Izumi M., Tajima S. *Physica C* **383**:p. 197 (2002)

[31] Bud'ko S.L., Lapertot G., Petrovic C., Cunningham C.E., Anderson N., Canfield P.C. *Physical*

Review Letters **86** (9):p. 1877 (2001)
[32] Souma S., Machida Y., Sato T., Takahashi T., Matsui H., Wang S.C., Ding H., Kaminski A., Campuzano J.C., Sasaki S., Kadowaki K. *Nature* **423** (6935):p. 65 (2003)
[33] Buzea C., Yamashita T. *Superconductor Science and Technology* **14** (11):p. R115 (2001)
[34] Columbus Superconductors . *http://www.columbussuperconductors.com/news.htm* (accessed 31st October 2007)
[35] Stenvall A., Hiltunen I., Korpela A., Lehtonen J., Mikkonen R., Viljamaa J., Grasso G. *Superconductor Science and Technology* **20**:p. 336 (2007)
[36] Nakane T., Kitaguchi H., Kumakura H. *Superconductor Science and Technology* **19**:p. 528 (2006)
[37] Alessandrini M., Fang H., Hanna M., Putman P., Zhou Y.X., Salama K. *Superconductor Science and Technology* **19**:p. 129 (2006)
[38] Birajdar B., Braccini V., Tumino A., Wenzel T., Eibl O., Grasso G. *Superconductor Science and Technology* **19** (9):p. 916 (2006)
[39] Jones M., Marsh R. *Journal of the American Chemical Society* **76**:p. 1434 (1954)
[40] Birkedal H., Van Beek W., Emerich H., Pattison P. *Journal of Materials Science Letters* **22** (15):p. 1069 (2003)
[41] Budworth D. *An Introduction to Ceramic Science.* 1st ed. Pergamon Press, Oxford (1970)
[42] Brook R.V., Cahn R., Haasen P., Kramer E.S. (eds.). *Materials Science and Technology: Vol. 17A Processing of Ceramics (Part I).* 1st ed. VCH Publishers Inc., New York (1996)
[43] Prikhna T.A., Gawalek W., Savchuk Y.M., Surzhenko A.B., Zeisberger M., Moshchil V.E., Dub S.N., Melnikov V.S., Sergienko N.V., Habisreuther T., Litzkendorf D., Abell S., Nagorny P.A. *IEEE Transactions on Applied Superconductivity* **13** (2):pp. 3506 (2003)
[44] Ashby M.F., Jones D.R.H. *Engineering Materials 1.* 1st ed. Pergamon Press, Oxford (1980)
[45] Brook R.V., Cahn R., Haasen P., Kramer E.S. (eds.). *Materials Science and Technology: Vol. 17B Processing of Ceramics (Part II).* 1st ed. VCH Publishers Inc., New York (1996)
[46] Kingery W. *Introduction to Ceramics.* 1st ed. John Wiley & Sons (New York) (1965)
[47] Rahaman M. *Sintering of Ceramics.* 1st ed. CRC Press, Boca Raton, USA (2008)
[48] Edwards E., Endean M. (eds.). *Manufacturing with Materials.* Materials in Action, 1st ed. Butterworth-Heinemann, Oxford (1990)
[49] Ashby M., Jones D. *Engineering Materials 2: An Introduction to Microstructures, Processing and Design.* International Series on Materials Science and Technology, 1st ed. Pergamon Press, Oxford (1986)
[50] Reed J. *Principles of Ceramic Processing.* 2nd ed. Wiley-Interscience, New York (1995)
[51] Weiser M., de Jonghe L. *Journal of the American Ceramic Society* **69** (11):pp. 822 (1986)
[52] Frost H.J., Ashby M.F. *Deformation-Mechanism Maps.* 1st ed. Pergamon Press, Oxford (1982)
[53] Kolemen U., Uzuna O., Aksan M., Guclu U., Yakinci E. *Journal of Alloys and Compounds* **415**:p. 294 (2006)
[54] Fu M., Chen J., Jiao Z., Kumakura H., Togano K., Ding L., Zhang Y., Chen Z., Han H., Chen J. *Physica C* **406**:p. 53 (2004)
[55] Yamamoto K., Osamura K., Balamurugan S., Nakamura T., Hoshino T., Muta I. *Superconductor Science and Technology* **16**:pp. 1052 (2003)
[56] Ichitsubo T., Ogia H., Setoa T., Hiraoa M., Inuib H. *Materials Letters* **57**:p. 3910 (2003)
[57] Nesterenko V.F., Gu Y. *Applied Physics Letters* **82** (23):pp. 4104 (2003)
[58] Balducci G., Brutti S., Ciccioli A., Gigli G., Manfrinetti P., Palenzona A., Butman M., Kudin L. *Journal of Physics and Chemistry of Solids* **66**:p. 292 (2005)
[59] Lide D. (ed.). *Handbook of Chemistry and Physics.* 73rd ed. CRC Press, Boca Raton ,USA (1992)
[60] Takano Y., Takeya H., Fujii H., Kumakura H., Hatano T., Togano K., Kito H., Ihara H. *Applied Physics Letters* **78** (19):p. 2914 (2001)
[61] Product data sheet - magnesium diboride. Available online at http://www.hcstarck.de (2005). Issued 15/08/05
[62] Gao Y.D., Ding J., Rao G.V.S., Chowdari B.V.R., Sun W.X., Shen Z.X. *Physica Status Solidi A* **191** (2):p. 548 (2002)
[63] Li S., White T., Plevert J., Sun C.Q. *Superconductor Science and Technology* **17** (9):p. S589 (2004)
[64] Goldacker W., Schlachter S.I., Liu B., Obst B., Klimenko E. *Physica C* **401** (1-4):p. 80 (2004)
[65] Flukiger R., Lezza P., Beneduce C., Musolino N., Suo H.L. *Superconductor Science and Technology* **16** (2):p. 264 (2003)

[66] Vogt T., Schneider G., Hriljac J.A., Yang G., Abell J.S. *Physical Review B* **6322** (22) (2001)
[67] Kovac P., Hugek I., Meligek T., Grivel J.C., Pachla W., Strbik V., Diduszko R., Homeyer J., Andersen N.H. *Superconductor Science and Technology* **17** (10):p. L41 (2004)
[68] Aswal D.K., Muthe K.P., Singh A., Sen S., Shah K., Gupta L.C., Gupta S.K., Sahni V.C. *Physica C* **363** (3):p. 208 (2001)
[69] Senkowicz B., Perez Moyet R., Mungall R., Hedstrom J., Uwakweh O., Hellstrom E., Larbalestier D. *Superconductor Science and Technology* **19**:p. 1173 (2006)
[70] Paranthaman M., Thompson J., Christen D. *Physica C* **355**:p. 1 (2001)
[71] Cooley L.D., Kang K., Klie R.F., Li Q., Moodenbaugh A.M., Sabatini R.L. *Superconductor Science and Technology* **17** (7):p. 942 (2004)
[72] Yavas M., Okur S., Egilmez M., Kalkanci M., Ozyuzer L. *Journal of Optoelectronics and Advanced Materials* **7** (1):p. 407 (2005)
[73] Shi L.A., Gu Y.L., Qian T., Li X.G., Chen L.Y., Yana Z.H., Ma J.H., Qian Y.T. *Physica C* **405** (3-4):p. 271 (2004)
[74] Yoshii K., Abe H. *Physica C* **388**:p. 113 (2003)
[75] Yoshii K., Abe H. *Superconductor Science and Technology* **15** (10):p. L25 (2002)
[76] Iijima Y., Kikuchi A., Yoshida Y., Takeuchi T., Banno N., Inoue K. *Physica C* **407** (1-2):p. 44 (2004)
[77] Kikuchi A., Yoshida Y., Iijima Y., Banno N., Takeuchi T., Inoue K. *Superconductor Science and Technology* **17** (6):p. 781 (2004)
[78] Jiang C.H., Hatakeyama H., Kumakura H. *Superconductor Science and Technology* **18** (5):p. L17 (2005)
[79] Kovac P., Melisek T., Dhalle M., den Ouden A., Husek I. *Superconductor Science and Technology* **18**:p. 1374 (2005)
[80] Zhou S., Pan A., Liu H., Dou S. *Physica C* **382**:p. 349 (2002)
[81] Grinenko V., Krasnoperov E., Stoliarov V., Bush A., Mikhajlov B. *Solid State Communications* **138**:p. 461 (2006)
[82] Varin R., Chiu C. *Journal of Alloys and Compounds* (in press - available online) (2005)
[83] Perner O., Eckert J., Hassler W., Fischer C., Muller K.H., Fuchs G., Holzapfel B., Schultz L. *Superconductor Science and Technology* **17** (10):p. 1148 (2004)
[84] Fang H., Padmanabhan S., Zhou Y.X., Salama K. *Applied Physics Letters* **82** (23):p. 4113 (2003)
[85] Hassler W., Rodig C., Fischer C., Holzapfel B., Perner O., Eckert J., Nenkov K., Fuchs G. *Superconductor Science and Technology* **16** (2):p. 281 (2003)
[86] Glowacki B.A., Majoros M., Vickers M.E., Zeimetz B. *Physica C* **372**:p. 1254 (2002)
[87] Haessler W., Herrmann M., Birajdar B.and Rodig C., Schubert M., Holzapfel B., Eibl O., Schultz L. *IEEE Transactions on Applied Superconductivity* **17(2)**:pp. 2919 (June 2007)
[88] Chen S., Glowacki B. *Superconductor Science and Technology* **19**:p. 116 (2006)
[89] Jiang J., Senkowicz B., Larbalestier D., Hellstrom E. *Superconductor Science and Technology* **19**:p. L33 (2006)
[90] Birajdar B., Wenzel T., Manfrinetti P., Palenzona A., Putti M., Eibl O. *Superconductor Science and Technology* **18**:p. 572 (2005)
[91] Kumakura H., Takano Y., Fujii H., Togano K., Kito H., Ihara H. *Physica C* **363**:p. 179 (2001)
[92] Yeoh W., Kim J., Horvat J., Dou S., Munroe P. *Superconductor Science and Technology* **19**:p. L5 (2006)
[93] Yeoh W., Kim J., Horvat J., Xu X., Qin M., Dou S., Jiang C.H., Nakane T., Kumakura H., Munroe P. *Superconductor Science and Technology* **19**:p. 596 (2006)
[94] Hossain M., Kim J., Wang X., Xu X., Peleckis G., Dou S. *Superconductor Science and Technology* **20**:p. 112 (2007)
[95] Chen S., Yates K., Blamire M., MacManus-Driscoll J. *Superconductor Science and Technology* **18**:p. 1473 (2005)
[96] Luo H., Wu X.F., Lee C.M., Yang T., Leng X., Liu Y., Qiu L., Luo H.M., Wang Z.H., Ding S.Y. *Superconductor Science and Technology* **15**:p. 370 (2002)
[97] Agrestini S. Metallo C.F.M.C.G.S.C.d.N.S.G.M.S.A.L.A.B.A. *Journal of Physics and Chemistry of Solids* **65**:p. 1479 (2004)
[98] Jung C.U., Park M.S., Kang W.N., Kim M.S., Kim K.H.P., Lee S.Y., Lee S.I. *Applied Physics Letters* **78** (26):p. 4157 (2001)

[99] Chen S.K., Glowacki B.A., MacManus-Driscoll J.L., Vickers M.E., Majoros M. *Superconductor Science and Technology* **17** (2):p. 243 (2004)
[100] Lee S.Y., Yoo S.I., Kim Y.W., Hwang N., Kim D.Y. *Journal of the American Ceramic Society* **86**:p. 1800 (2003)
[101] Penco R., Grasso G. *IEEE Transactions on Applied Superconductivity* **17** (2):pp. 2291 (June 2007)
[102] Canfield P.C., Finnemore D.K., Bud'ko S.L., Ostenson J.E., Lapertot G., Cunningham C.E., Petrovic C. *Physical Review Letters* **86** (11):p. 2423 (2001)
[103] Glowacki B.A., Majoros M., Vickers M., Evetts J.E., Shi Y., McDougall I. *Superconductor Science and Technology* **14** (4):p. 193 (2001)
[104] Goto T., Katoh H. *Physica C* **378**:p. 903 (2002)
[105] Goto T., Katoh H., Watanabe K. *IEEE Transactions on Applied Superconductivity* **13** (2):p. 3229 (2003)
[106] Ma R.Z., Bando Y., Mori T., Golberg D. *Chemistry of Materials* **15** (16):p. 3194 (2003)
[107] Wu J.Z., Yun S.H., Dibos A., Kim D.K., Tidrow M. *Microelectronics Journal* **34** (5-8):p. 463 (2003)
[108] Wu Y.Y., Messer B., Yang P.D. *Advanced Materials* **13** (19):p. 1487 (2001)
[109] Giunchi G., Ceresara S., Ripamonti G., Di Zenobio A., Rossi S., Chiarelli S., Spadoni M., Wesche R., Bruzzone P.L. *Superconductor Science and Technology* **16** (2):p. 285 (2003)
[110] Dou S., Liu H. *Superconductor Science and Technology* **6**:p. 297 (1993)
[111] Shimoyama J., Hanafusa K., Yamamoto A., Katsura Y., Horii S., Kishio K., Kumakura H. *Superconductor Science and Technology* **20**:p. 307 (2007)
[112] Kumar R.G.A., Vinod K., Varghese N., Syamaprasad U. *Superconductor Science and Technology* **20**:p. 222 (2007)
[113] Shcherbakova O., Pan A., Soltanian S., Dou S., Wexler D. *Superconductor Science and Technology* **20**:p. 5 (2007)
[114] Song K.J., Kim S.W., Park C., Joo J.H., Choi S.J., Ko R.K., Ha H.S., Ha D.W., Oh S.S. *Physica C* **407** (1-2):p. 17 (2004)
[115] Suo H.L., Beneduce C., Dhalle M., Musolino N., Genoud J.Y., Flukiger R. *Applied Physics Letters* **79** (19):p. 3116 (2001)
[116] Serquis A., Civale L., Hammon D.L., Liao X.Z., Coulter J.Y., Zhu Y.T., Peterson D.E., Mueller F.M. *Journal of Applied Physics* **94** (6):p. 4024 (2003)
[117] Jiang C.H., Nakane T., Kumakura H. *Applied Physics Letters* **87**:p. 252505 (2005)
[118] Grasso G., Malagoli A., Marre D., Bellingeri E., Braccini V., Roncallo S., Scati N., Siri A.S. *Physica C* **378**:p. 899 (2002)
[119] Kovac P., Husek I., Pachla W., Melisek T., Diduszko R., Frohlich K., Morawski A., Presz A., Machajdik D. *Superconductor Science and Technology* **15** (7):p. 1127 (2002)
[120] Majoros M., Glowacki B.A., Vickers M.E. *Superconductor Science and Technology* **15** (2):p. 269 (2002)
[121] Hassler W., Birajdar B., Gruner W., Herrmann M., Perner O., Rodig C., Schubert M., Holzapfel B., Eibl O., Schultz L. *Superconductor Science and Technology* **19**:p. 512 (2006)
[122] Grasso G., Malagoli A., Ferdeghini C., Roncallo S., Braccini V., Siri A.S., Cimberle M.R. *Applied Physics Letters* **79** (2):p. 230 (2001)
[123] Kovac P., Husek I., Melisek T. *Superconductor Science and Technology* **15** (9):p. 1340 (2002)
[124] Braccini V., Nardelli D., Malagoli A., Tumino A., Fanciulli C., Bernini C., Siri A.S., Grasso G. *IEEE Transactions on Applied Superconductivity* **15** (2):p. 3211 (2005)
[125] Fujii H., Kumakura H., Togano K. *Journal of Materials Research* **17** (9):p. 2339 (2002)
[126] Grovenor C.R.M., Goodsir L., Salter C.J., Kovac P., Husek I. *Superconductor Science and Technology* **17** (3):p. 479 (2004)
[127] Kumakura H., Matsumoto A., Fujii H., Togano K. *Applied Physics Letters* **79** (15):p. 2435 (2001)
[128] Lezza P., Gladyshevskii R., Suo H.L., Flukiger R. *Superconductor Science and Technology* **18** (5):p. 753 (2005)
[129] Eyidi D., Eibl O., Wenzel T., Nickel K.G., Schlachter S.I., Goldacker W. *Superconductor Science and Technology* **16** (7):p. 778 (2003)
[130] Grasso G., Malagoli A., Modica M., Tumino A., Ferdeghini C., Siri A.S., Vignola C., Martini L., Previtali V., Volpini G. *Superconductor Science and Technology* **16** (2):p. 271 (2003)
[131] Goldacker W., Schlachter S.I., Zimmer S., Reiner H. *Superconductor Science and Technology* **14** (9):p. 787 (2001)

[132] Vinod K., Abhilash Kumar R., Syamaprasad U. *Superconductor Science and Technology* **20**:p. R1 (2007)
[133] Flukiger R., Suo H.L., Musolino N., Beneduce C., Toulemonde P., Lezza P. *Physica C* **385** (1-2):p. 286 (2003)
[134] Allen T. *Powder Sampling and Particle Size Determination.* 1st ed. Elsevier, Amsterdam (2003)
[135] Lezza P., Gladyshevskii R., Senatore C., Cusanelli G., Suo H.L., Flukiger R. *IEEE Transactions on Applied Superconductivity* **15** (2):p. 3196 (2005)
[136] Lezza P., Abacherli V., Clayton N., Senatore C., Uglietti D., Suo H.L., Flukiger R. *Physica C* **401** (1-4):p. 305 (2004)
[137] Matsumoto Y., Terasaki Y., Abiru T., Akune T., Sakamoto N. *Physica C* **378**:p. 564 (2002)
[138] Ring T. *Fundamental of Ceramic Processing and Synthesis.* 1st ed. Academic Press (London) (1996)
[139] Jones W. *Fundamental Principles of Powder Metallurgy.* 1st ed. Edward Arnold (1960)
[140] Grasso G., Flukiger R. *Superconductor Science and Technology* **10**:pp. 223 (1997)
[141] Kovac P., Husek I., Melisek T., Dhalle M., Muller M., Ouden A.D. *Superconductor Science and Technology* **18** (5):p. 615 (2005)
[142] Husek I., Kovac P., Grovenor C.R.M., Goodsir L. *Superconductor Science and Technology* **17** (8):p. 971 (2004)
[143] Pachla W., Kovac P., Diduszko R., Mazur A., Husek I., Morawski A., Presz A. *Superconductor Science and Technology* **16** (1):p. 7 (2003)
[144] Tampieri A., Celotti G., Sprio S., Caciuffo R., Rinaldi D. *Physica C* **400**:pp. 97 (July 2004)
[145] Schmidt J., Schnelle W., Grin Y., Kniep R. *Solid State Sciences* **5**:p. 535 (2003)
[146] Shim S., Shim K., Yoon J.W. *Journal of the American Ceramic Society* **88** (4):p. 858 (2005)
[147] Bernard F., le Gallet S., Spinassou N., Paris S., Gaffet E., Woolman J., Munir Z. *Science of Sintering* **36**:pp. 155 (2004)
[148] Suo H., Wang Y., Ma H., Ma L., Liu M., Zhao Y., Zhou M. *Physica C* **460-462**:pp. 620 (May 2007)
[149] Indrakanti S.S., Nesterenko V.F., Maple M.B., Frederick N.A., Yuhasz W.H., Li S. *Philosophical Magazine Letters* **81** (12):p. 849 (2001)
[150] Maple M.B., Taylor B.J., Frederick N.A., Li S., Nesterenko V.F., Indrakanti S.S., Maley M.P. *Physica C* **382** (1):p. 132 (2002)
[151] Shields T.C., Kawano K., Holdom D., Abell J.S. *Superconductor Science and Technology* **15** (2):p. 202 (2002)
[152] Sung G.Y., Kim S.H., Kim J., Yoo D.C., Lee J.W., Lee J.Y., Jung C.U., Park M.S., Kang W.N., Du Z.L., Lee S.I. *Superconductor Science and Technology* **14** (10):p. 880 (2001)
[153] Jung C.U., Park M.S., Kang W.N., Kim M.S., Lee S.Y., Lee S.I. *Physica C* **353** (3-4):p. 162 (2001)
[154] Frederick N.A., Li S., Maple M.B., Nesterenko V.F., Indrakanti S.S. *Physica C* **363** (1):p. 1 (2001)
[155] Serquis A., Zhu Y.T., Peterson D.E., Mueller F.M., Schulze R.K., Nesterenko V.F., Indrakanti S.S. *Applied Physics Letters* **80** (23):p. 4401 (2002)
[156] Liao X.Z., Serquis A., Zhu Y.T., Civale L., Hammon D.L., Peterson D.E., Mueller F.M., Nesterenko V.F., Gu Y. *Superconductor Science and Technology* **16** (7):p. 799 (2003)
[157] Serquis A., Civale L., Hammon D.L., Liao X.Z., Coulter J.Y., Zhu Y.T., Jaime M., Peterson D.E., Mueller F.M., Nesterenko V.F., Gu Y. *Applied Physics Letters* **82** (17):p. 2847 (2003)
[158] Tampieri A., Celotti G., Sprio S., Rinaldi D., Barucca G., Caciuffo R. *Solid State Communications* **121** (9-10):p. 497 (2002)
[159] Toulemonde P., Musolino N., Flukiger R. *Superconductor Science and Technology* **16** (2):p. 231 (2003)
[160] Cimberle M.R., Novak M., Manfrinetti P., Palenzona A. *Superconductor Science and Technology* **15** (1):p. 43 (2002)
[161] Bhatia M., Sumption M.D., Collings E.W., Dregia S. *Applied Physics Letters* **87** (4) (2005)
[162] Bhatia M., Sumption M.D., Collings E.W. *IEEE Transactions on Applied Superconductivity* **15** (2):p. 3204 (2005)
[163] Martinez E., Angurel L.A., Navarro R., Millan A., Rillo C., Artigas M. *IEEE Transactions on Applied Superconductivity* **13** (2):p. 3210 (2003)
[164] Senkowicz B.J., Giencke J.E., Patnaik S., Eom C.B., Hellstrom E.E., Larbalestier D.C. *Applied Physics Letters* **86** (20) (2005)

[165] Mikheenko P., Martinez E., Bevan A., Abell J., MacManus-Driscoll J. *Superconductor Science and Technology* **20**:p. S264 (2007)
[166] Massalski T. (ed.). *Binary Alloy Phase Diagrams.* 2nd ed. ASM International, Ohio, USA (1990)
[167] Brutti S., Ciccioli A., Balducci G., Gigli G. *Applied Physics Letters* **80** (16):p. 2892 (2002)
[168] Brutti S., Balducci G., Gigli G., Ciccioli A., Manfrinetti P., Palenzona A. *Journal of Crystal Growth* **289**:p. 578 (2006)
[169] Fan Z.Y., Hinks D.G., Newman N., Rowell J.M. *Applied Physics Letters* **79** (1):p. 87 (2001)
[170] Yang D.L., Sun H.W., Lu H.X., Guo Y.Q., Li X.J., Hu X. *Superconductor Science and Technology* **16** (5):p. 576 (2003)
[171] Liao X.Z., Serquis A., Zhu Y.T., Peterson D.E., Mueller F.M., Xu H.F. *Superconductor Science and Technology* **17** (8):p. 1026 (2004)
[172] Fujii H., Kumakura H., Togano K. *Physica C* **363** (4):p. 237 (2001)
[173] Jiang C.H., Hatakeyama H., Kumakura H. *Physica C* **423** (1-2):p. 45 (2005)
[174] Berenov A., Serquis A., Liao X.Z., Zhu Y.T., Peterson D.E., Bugoslavsky Y., Yates K.A., Blamire M.G., Cohen L.F., MacManus-Driscoll J.L. *Superconductor Science and Technology* **17** (10):p. 1093 (2004)
[175] Wilke R., Bud'ko S.L., Canfield P.C., Finnemore D.K., Suplinskas R., Hannahs S. *Physical Review Letters* **92** (21):p. 217003 (2004)
[176] Cava R.J., Zandbergen H.W., Inumaru K. *Physica C* **385** (1-2):p. 8 (2003)
[177] Zhao Y.G., Zhang X.P., Qiao P.T., Zhang H.T., Jia S.L., Cao B.S., Zhu M.H., Han Z.H., Wang X.L., Gu B.L. *Physica C* **361** (2):p. 91 (2001)
[178] Ahn J.S., Kim Y.J., Kim M.S., Lee S.I., Choi E.J. *Physical Review B* **65** (17) (2002)
[179] Dou S.X., Soltanian S., Yeoh W.K., Zhang Y. *IEEE Transactions on Applied Superconductivity* **15** (2):p. 3219 (2005)
[180] Cheng C.H., Zhang H., Zhao Y., Feng Y., Rui X.F., Munroe P., Zeng H.M., Koshizuka N., Murakami M. *Superconductor Science and Technology* **16** (10):p. 1182 (2003)
[181] Matsumoto A., Kumakura H., Kitaguchi H., Hatakeyama H. *Superconductor Science and Technology* **16** (8):p. 926 (2003)
[182] Kumar D., Pennycook S.J., Narayan J., Wang H., Tiwari A. *Superconductor Science and Technology* **16** (4):p. 455 (2003)
[183] Zhao Y., Cheng C.H., Machi T., Koshizuka N., Murakami M. *Applied Physics Letters* **80** (13):p. 2311 (2002)
[184] Cheng C.H., Zhao Y., Feng Y., Zhu X.T., Koshizuka N., Murakami M. *Superconductor Science and Technology* **16** (1):p. 125 (2003)
[185] Cheng C.H., Zhao Y., Machi T., Koshizuka N., Murakami M. *Physica C* **385** (4):p. 449 (2003)
[186] Zhao Y., Cheng C.H., Feng Y., Machi T., Huang D.X., Zhou L., Koshizuka N., Murakami M. *Physica C* **386**:p. 581 (2003)
[187] Haigh S., Kovac P., Prikhna T.A., Savchuk Y.M., Kilburn M.R., Salter C., Hutchison J., Grovenor C. *Superconductor Science and Technology* **18** (9):p. 1190 (2005)
[188] Kovac P., Husek I., Melisek T., Grovenor C.R.M., Haigh S., Jones H. *Superconductor Science and Technology* **17** (11):p. 1225 (2004)
[189] Kang S.J.L. *Sintering: Densification, Grain Growth and Microstructure.* 1st ed. Elsevier Butterworth-Heinemann (Oxford) (2005)
[190] Bugoslavsky Y., Cohen L.F., Perkins G.K., Polichetti M., Tate T.J., Gwilliam R., Caplin A.D. *Nature* **411** (6837):p. 561 (2001)
[191] Dou S.X., Horvat J., Soltanian S., Wang X.L., Qin M.J., Zhou S.H., Liu H.K., Munroe P.G. *IEEE Transactions on Applied Superconductivity* **13** (2):p. 3199 (2003)
[192] Soltanian S., Wang X.L., Horvat J., Dou S.X., Sumption M.D., Bhatia M., Collings E.W., Munroe P., Tomsic M. *Superconductor Science and Technology* **18** (5):p. 658 (2005)
[193] Larbalestier D., Gurevich A., Feldmann D.M., Polyanskii A. *Nature* **414** (6861):p. 368 (2001)
[194] Wang J., Bugoslavsky Y., Berenov A., Cowey L., Caplin A.D., Cohen L.F., MacManus-Driscoll J.L., Cooley L.D., Song X., Larbalestier D.C. *Applied Physics Letters* **81** (11):p. 2026 (2002)
[195] Wang X.L., Zhou S.H., Qin M.J., Munroe P.R., Soltanian S., Liu H.K., Dou S.X. *Physica C* **385** (4):p. 461 (2003)
[196] Nakane T., Takeya H., Fujii H., Kumakura H. *Superconductor Science and Technology* **18** (4):p. 521 (2005)

[197] Shekhar C., Giri R., Tiwari R.S., Srivastava O.N. *Crystal Research and Technology* **39** (8):p. 718 (2004)
[198] Soltanian S., Horvat J., Wang X.L., Munroe P., Dou S. *Physica C* **390** (3):p. 185 (2003)
[199] Trociewitz U.P., Sastry P., Wyda A., Crockett K., Schwartz J. *IEEE Transactions on Applied Superconductivity* **13** (2):p. 3320 (2003)
[200] Goto D., Machi T., Zhao Y., Koshizuka N., Murakami M., Arai S. *Physica C* **392**:p. 272 (2003)
[201] Hyslop D. *Novel Refinement Technique and Microstructural Characterisation of MgB_2.* Part II Thesis, Department of Materials, University of Oxford (2005)
[202] Coulson J., Richardson J. *Chemical Engineering Vol.2 Unit Operations.* 5th ed. Pergamon Press, Oxford (1962)
[203] Woan G. *The Cambridge Handbook of Physics Formulas.* 1st ed. Cambridge University Press, Cambridge (2000)
[204] Pryor E. *An Introduction to Mineral Dressing.* 1st ed. Mining Publications, London (1955)
[205] Mikheenko P., Bevan A., Abell J. *Journal of Physics: Conference Series* **43**:p. 535 (2006)
[206] Sumitomo Coal Mining Company Inc . *http://www.scm-sps.com/index.html* (Accessed on13th April 2008)
[207] John V. (ed.). *Macmillan Dictionary of Materials and Manufacturing.* 1st ed. Macmillan Press Ltd, London (1990)
[208] Robinson P., Bradbury S. *Qualitative Polarized-Light Microscopy.* Royal Microscopical Society Microscopy Handbooks 09. Oxford Univeristy Press, Oxford (1992)
[209] Flewitt P., Wild R. *Physical Methods for Materials Characterisation.* Series in Materials Science and Engineering, 2nd ed. Institute of Physics Publishing, Bristol and Philadelphia (2003)
[210] Smallman R.E., Bishop R.J. *Modern Physical Metallurgy and Materials Engineering.* 6th ed. Butterworth-Heinemann (Oxford) (1999)
[211] Goodhew P., Humphreys J., Beanland R. *Electron Microscopy and Analysis.* 3rd ed. Taylor Francis, London (2001)
[212] Reimer L. *Scanning Electron Microscopy: Physics of Image Formation and Microanalysis.* 2nd ed. Springer-Verlag, Berlin (1998)
[213] Hirsch P., Howie A., Nicholson R., Pashley D., Whelan M. *Electron Microscopy of Thin Crystals.* 2nd ed. Robert E. Kreiger Publishing Company, Malabar, Florida (1977)
[214] Williams D., Carter C. *Transmission Electron Microscopy*, vol. I-IV. 1st ed. Plenum Press (1996)
[215] Cullity B., Stock S. *Elements of X-Ray Diffraction.* 3rd ed. Prentice-Hall, London (2001)
[216] Briggs D., Seah M. *Practical Surface Analysis.* 2nd ed. Wiley, Chichester (1990)
[217] Prikhna T., Gawalek W., Savchuk Y., Habisreuther T., Wendt M., Sergienko N., Moshchil V., Nagorny P., Schmidt C., Dellith J., Dittrich U., Litzendorf D., Melnikov V., Sverdun V. *Superconductor Science and Technology* **20**:pp. S257 (2007)
[218] Marchi J., Bressiani J., Bressiani A. *Materials Research* **4**:pp. 231 (2001)
[219] Pachla W., Presz A., Kovac P., Husek I., Diduszko R. *Superconductor Science and Technology* **17** (11):p. 1289 (2004)
[220] Braccini V., Malagoli A., Tumino A., Vignolo M., Bernini C., Fanciulli C., Romano G., Tropeano M., Siri A.S., Grasso G. *IEEE Transactions on Applied Superconductivity* **17** (2, Part 3):pp. 2766 (2007)
[221] Epstein N., Young M.J. *Nature* **196**:pp. 885 (1962)
[222] Andreasen A., Anderson J. *Colloid and Polymer Science* **50**:pp. 217 (1930)
[223] Mukhopadhyay A., Datta S., Chakraborty D. *Ceramics International* **17**:p. 121 (1991)